



HAL
open science

Mechanistic studies of metal-catalyzed reactions : predicting tools for reaction optimization

Pierre-Adrien Payard

► **To cite this version:**

Pierre-Adrien Payard. Mechanistic studies of metal-catalyzed reactions: predicting tools for reaction optimization. Theoretical and/or physical chemistry. Université Paris sciences et lettres, 2019. English. NNT : 2019PSLEE009 . tel-02426249

HAL Id: tel-02426249

<https://theses.hal.science/tel-02426249>

Submitted on 2 Jan 2020

HAL is a multi-disciplinary open access archive for the deposit and dissemination of scientific research documents, whether they are published or not. The documents may come from teaching and research institutions in France or abroad, or from public or private research centers.

L'archive ouverte pluridisciplinaire **HAL**, est destinée au dépôt et à la diffusion de documents scientifiques de niveau recherche, publiés ou non, émanant des établissements d'enseignement et de recherche français ou étrangers, des laboratoires publics ou privés.



THÈSE DE DOCTORAT
DE L'UNIVERSITÉ PSL

Préparée à L'Ecole Normale Supérieure

**Mechanistic Studies of Metal-Catalyzed Reactions:
Predicting Tools for Reaction Optimization**

**Etudes de mécanismes de réactions catalytiques : développement de
nouveaux outils et application à l'optimisation de réactions.**

Soutenue par

Pierre-Adrien Payard

Le 20 septembre 2019

Ecole doctorale n° 388

**Chimie Physique et Chimie
Analytique de Paris-Centre**

Spécialité

Chimie Physique

Composition du jury :

Pr Christophe COPERET Professeur, Ecole Polytechnique Fédéral de Zürich	<i>Président du jury</i>
Dr Karinne MIQUEU Directeur de recherche, Université de Pau	<i>Rapporteur</i>
Dr Nicolas MEZAILLES Directeur de recherche, Université P. Sabatier	<i>Rapporteur</i>
Dr Laurence GRIMAUD Directeur de recherche, ENS	<i>Directeur de thèse</i>
Dr Marc PERA-TITUS Chargé de recherche, UMI E2P2	<i>Co-directeur de thèse</i>



« FAUST : Rien ! En vain j'interroge, en mon ardente veille, La nature et le Créateur; [...]
Je ne vois rien ! Je ne sais rien ! [...] A moi, Satan ! à moi !
MEPHISTOPHELES : Me voici ! [...] A nous deux, cher Docteur,
Qu'attendez-vous de moi ? Par où commencerai-je ? »

Faust, C. Gounod (libretto J. Barbier, M. Carré, after J. W. von Goethe)

Remerciements

En premier lieu, je tiens à remercier Mme Karine Miqueu et M Nicolas Mézailles pour avoir accepté de rapporter cette thèse ainsi que M Christophe Copéret qui m'a fait l'honneur de présider ce jury. Merci à tous les trois pour la discussion particulièrement vivante et riche scientifiquement qui a suivi ma présentation.

Je remercie chaleureusement mes deux directeurs de thèse Mme Laurence Grimaud et M Marc Pera-Titus. Chacun à sa façon a contribué non seulement à m'offrir une formation de qualité mais aussi un cadre de travail confortable ; l'un et l'autre ont su faire montre de leurs grandes qualités humaines. Non moins chaleureusement je remercie mes encadrants « officieux » mais également actifs et bienveillants : Mme Ilaria Ciofini et M Raphael Wischert. Merci également à Mme Anny Jutand et M Christian Amatore pour les discussions scientifiques particulièrement fructueuses que nous avons pu avoir.

Merci aux doctorants et docteurs avec qui j'ai travaillé au quotidien pour l'ambiance toujours excellente, le soutien constant, la bonne humeur et, parfois aussi, le travail en commun : Lena Beauzamy, Antoine Bohn, Indira Fabre, Baptiste Haddou, Hakim Lakhmini, Aude Nyadanu, Luca A. Perego, Adnan Sayeg, Aurélien Bailly, Khaoula Jhaoudi, Na Pan, Justine Pandard, Jules Schleinitz. Parmi eux je me dois d'adresser un remerciement particulier à M Luca A. Perego qui m'a encadré pendant mon stage de M2 et avec qui j'ai pu travailler de nouveau pendant ma première année de thèse : il a contribué de façon majeure à ma formation scientifique.

J'adresse un remerciement spécial aux étudiants que j'ai pu encadrer dans le cadre de stages, Sanaa Ajig, Célia Bresson, Léa Chocron, Annie Dethoor, Emile Escoude, Khaoula Jhaoudi, Laurélia Guichard, Johanne Lebrun-Thauront, Aude Salamé et Damien Tocqueville. J'ignore si ma formation leur a été utile mais eux m'ont beaucoup appris ! Ils ont réalisé une partie non négligeable des travaux présentés ici, ce fut un réel plaisir de travailler avec eux et je leur souhaite la plus grande réussite dans la suite de leurs études. Je remercie également l'ensemble des membres du départements et en particulier ceux qui m'ont apporté une aide technique directe : Mme Anne Boutin, M Rodolphe Vuilleumier, M Eric Ait, M Fabien Ferrage, M Fabien Lacomba, M Thomas Le Saux, M Philippe Pelupessy et M Ari Seitsonen.

Une thèse c'est aussi une mission pédagogique et je tiens par conséquent à remercier les personnes qui m'ont accordé leur confiance en me permettant d'assurer des enseignements, Mme Clothilde Policar, M Nicolas Levy, Mme Anne-Sophie Bernard, M Ludovic Jullien, M Laurent Thouin et M Éric Labbe, ainsi que tous les membres de l'équipe pédagogique de l'ENS qui ont pu me guider dans mes débuts d'enseignant et en particulier M Frédéric Lemaitre.

Merci également aux membres ou anciens membres du laboratoire E2P2 de Shanghai pour leur accueil lors de mon trop bref séjour parmi eux et en particulier à MM Armin Liebens, Matthieu Corbet et Stéphane Streiff pour la confiance qu'ils m'ont accordée en choisissant de soutenir cette thèse en complément de l'Ecole Normale Supérieure de Paris-Saclay qui m'a attribué une bourse de thèse pour ces trois années.

Merci enfin à toutes les personnes extérieures avec qui j'ai eu la chance de collaborer, M Laurent Bonneviot, M Lhoussain Khrouz, Mme Carine Michel et M Philippe Sautet (ENS Lyon), M Laurent Binet et Mme Nadia Touati (Chimie Paris), M Simon Wagshal (Jansen), Mme Isabelle Gillaizeau (Univ Orléans) et Mme Carmen Galan (Univ Bristol).

Table of contents

TABLE OF CONTENTS	3
ABBREVIATIONS	7
GENERAL INTRODUCTION	9
CHAPTER I - MECHANISTIC STUDIES TOWARD GREENER PROCESSES: CHALLENGES AND TOOLS	11
1.What is a chemical mechanism?	12
2.Experimental techniques for mechanistic investigation	12
2.1. Kinetics and reactivity	12
2.2. Electrochemistry	15
2.3. Nuclear Magnetic Resonance spectroscopy of heteronuclei	21
2.4. Electron Paramagnetic Resonance (EPR) spectroscopy	24
3.Theoretical Tools	30
3.1. Theoretical foundations	30
3.2. The Born-Oppenheimer approximation and nuclear energy	31
3.3. Electronic energy and Slater approximation	32
3.4. How to evaluate the electronic energy?	33
3.5. The Density Functional Theory (DFT)	34
3.6. Choice of the basis set and functional	36
3.7. Empirical dispersion corrections	39
3.8. Modelization of solvent effects.....	39
3.9. Calculation of thermodynamic parameters	40
3.10. Charge and bond analyses.....	41
3.11. Indicators of chemical reactivity: electronegativity, global and local hardness, Fukui functions and global electrophilicity index	42
3.12. Conclusion	44

CHAPTER II - BORON-TO-TRANSITION-METALS TRANSMETALLATION: MECHANISTIC STUDIES	45
1.Context of the Study	46
1.1. Transition-metal catalyzed coupling reactions.....	46
1.2. Generalities on the mechanism of the Suzuki-Miyaura cross- coupling reaction	50
1.3. The Palladium-to-Boron Transmetallation Step	51
2.Transmetallation from Boron to Nickel.....	55
2.1. Previous works	55
2.2. Choice of the model reaction	55
2.3. Formation of hydroxo-bridged dinuclear complexes	56
2.4. Decomposition of the complex with excess base	62
2.5. Interaction of PhB(OH)_3^- with complex 1	63
2.6. Effect of the $\text{OH}^-/\text{PhB(OH)}_2$ ratio on the kinetics of TM and RE.....	67
2.7. Influence of Br^- and PPh_3 on the rate of TM and RE.....	70
2.8. Mechanism of the TM step	71
2.9. Mechanism of the RE step	73
2.10. Electronic Effects of TM.....	75
2.11. Effects of the conter-ion.....	77
2.12. Effects of the nature of the halide and of the phosphine.....	78
2.13. Conclusions	81

CHAPTER III - LEWIS ACID AND REDOX CATALYTIC PROPERTIES OF TRIFLATE AND TRIFLIMIDE SALTS	83
1. Triflate and triflimide salts in catalysis	84
1.1. Lewis acidity: definition and quantification	84
1.2. Triflate and triflimide salts: history, preparation and characterization	86
1.3. Application of triflate and triflimides in synthesis	88
2. Mechanistic study of a model reaction: Al(OTf) ₃ -catalyzed amination of alcohol	91
2.1. Description of the model reaction and solvent effects	91
2.2. Nature of Al(OTf) ₃ in nitromethane and coordination of BnOH	92
2.3. Deactivation of Al(OTf) ₃ by aniline in nitromethane	95
2.4. Competition between BnOH and aniline for Al in toluene	98
2.5. Validation of the DFT methodology	100
2.6. Determination of the structure of the catalyst by DFT calculations	102
2.7. Amination Mechanism	106
2.8. Conclusions	109
3. Rational design of Lewis acids for the direct amination of alcohols	110
3.1. Experimental trends for amination within a series of Lewis acids	110
3.2. Experimental descriptors of Lewis acidity	111
3.3. Structures of metal triflate and triflimides salts	114
3.4. Theoretical descriptors of Lewis acidity	125
3.5. Fukui functions and local hardness	134
3.6. "In silico Child's method"	136
3.7. Synthesis and characterization of titanium triflimide	140
3.8. Catalytic activity of 4	145
3.9. Mechanistic insights	149
3.10. Conclusions	157
4. Iron triflate salts for oxidation of cyclohexane	158
4.1. Industrial synthesis of cyclohexanone and cyclohexol	158
4.2. Iron catalyzed oxidation	159
4.3. Cyclohexane oxidation using TBHP as oxidizing agent	160
4.4. EPR investigation	165
GENERAL CONCLUSIONS AND PERSPECTIVES	174
EXPERIMENTAL SECTION	177

Abbreviations

AA	Adipic Acid	LB	Lewis Base
AO	Atomic Orbital	LCAO	Linear Combination of Atomic Orbital
Ar	Aryl group	LDA	Local Density Approximation
Bn	Benzyl	LSA	Lewis SuperAcid
BnOH	BenzylAlcohol	MO	Molecular Orbitals
bpy	2,2'-bipyridyl	NBO	Natural Bounding Orbital
CE	Counter Electrode	NMR	Nuclear Magnetic Resonance
CV	Cyclic Voltamogramme (or Cyclic Voltametry)	N ⁺ Tf ₂	N(SO ₃ CF ₃) ₂
Cy	Cyclohexyl	OA	Oxidative Addition
CyH	Cyclohexane	OTf	SO ₃ CF ₃
CyONE	Cyclohexanone	PCM	Polarizable Dielectric Continuum
DFT	Density Functional Theory	Ph	Phenyl
DMF	DiMethylFormamide	RDS	Rotating Disk electrode
DMPO	5,5-Dimethyl-1-pyrroline <i>N</i> -oxide	RE	Reference Electrode
DMSO	DiMethylSulfOxide	RE	Reductive Elimination
dppb	1,4-bis(diphenylphosphino)butane	SCE	Saturated Calomel Electrode
dppe	1,2-bis(diphenylphosphino)ethane	SCF	Self Consistent Field
dppf	1,1'-bis(diphenylphosphino)ferrocene	SHE	Standard Hydrogen Electrode
dppm	1,1-bis(diphenylphosphino)methane	S-M	Suzuki-Miyaura
dppp	1,3-bis(diphenylphosphino)propane	STO	Slater -Type Orbital
EA	Electronic Affinity	TBA	TetraButylAmmonium
ECP	Effective Core Potential	TBHP	TerButylHydroPeroxide
EPR	Electron Paramagnetic Resonance	THF	TetraHydroFurane
ESI-MS	Electro-Spray Ionization Mass Spectroscopy	TM	TransMetalation
FIA	Fluorine Ion Affinity	TMS	TetraMethylSilane
GGA	Generalized Gradient Approximation	TOF	TurnOver Frequency
GIE	Global Electrophilicity Index	Tol	Tolyl
GTO	Gaussian-Type Orbital	TON	TurnOver Number
HIA	Hydride Ion Affinity	TS	Transition State
HSAB	Hard and Soft Acids and Basis	UME	UltraMicroElectrode
IE	Ionization Energy	WE	Working Electrode
LA	Lewis Acid	Xyl	Xylyl
		ZPS	Zero-Field Splitting

General introduction

The development and optimization of new reactions can be the results of serendipity as well as of rational design inspired from mechanistic studies and predictive tools. If Artificial Intelligence is to be the future of organic chemistryⁱ the role of the chemist would be no more to set-up “cooking recipes” but rather to find out general rules and indicators, physical (chemical) laws, to minimize the time lost in trial-and-error. The aim of this thesis is not only to provide rational to understand and provide keys for optimization of known reactions but also to develop new methodologies to explain the catalytic properties and eventually predict catalytic performances.

After describing in Chapter I the main experimental and theoretical technics used in this thesis we will present in detail two projects using the same *modus operandi*. Chapter II is dedicated to the detail mechanistic study of the key-step of transmetalation from boron to nickel complexes. In Chapter III we endeavor to set-up a scale of Lewis affinity to predict the catalytic properties of Lewis superacids for the reaction of direct amination of alcohols.

More in detail, in Chapter II, the mechanism of boron-to-metal transmetalation, the key step of the nickel-catalyzed Suzuki-Miyaura coupling, is examined both experimentally and theoretically. We evidenced the formation of dinuclear μ -hydroxo-bridged complexes responsible for the catalyst deactivation. The base/boronic acid ratio is the crucial parameter to tune this reaction, as it modulates the extent of formation of these species. Counter anions and electronic effects have been studied and the full energy profile was DFT-calculated. These findings explain some limitations encountered in practical applications of Ni-catalyzed couplings and suggest how to tailor the experimental conditions to overcome these difficulties.

Chapter III is dedicated to the optimization of the direct amination of alcohol catalyzed by Lewis superacids. A model system using $\text{Al}(\text{OTf})_3$ was studied, detailed insights into the structure and reactivity of the catalyst under working conditions in both nitromethane and toluene as solvent were obtained. Competition between reactants for Al binding in the two solvents explains the different reactivities observed. The effect of the metal salts was then rationalized using a new approach that we called “*in silico* Beckett-Childs method”. This method affords a handy descriptor of Lewis acidity based on the partial charge build-up on phosphine oxide coordinated to a Lewis acid. When applied to a broad series of metal triflate and triflimide salts, this descriptor afforded good correlation with the catalytic activity. It allows to predict a high activity for unprecedented titanium triflimide, which was experimentally confirmed. Lastly, the interest of Lewis Superacids in redox catalysis was demonstrated for the oxidation of cyclohexane and the nature of the $\text{Fe}(\text{OTf})_3$ catalyst under reaction conditions was studied using EPR combined with DFT.

ⁱ J. M. Brunel, F. Peiretti, *ACS Omega*, **2018**, 3, 10, 13263-13266; Z. Li, S. Wang, H. Xin, *Nature Cat.*, **2018**, 1, 641-642; M. H. S. Segler, M. Preuss, M. P. Waller, *Nature*, **2018**, 555, 604-610.

CHAPTER I

Mechanistic Studies toward Greener Processes:

Challenges and Tools

“PHILINTE - Ah ! qu'en termes gallants ces choses là sont mises !

ALCESTE - Morbleu ! Vil complaisant, vous louez des sottises ?”

Molière, Le Misanthrope

1. What is a chemical mechanism?

A reaction mechanism is defined in the IUPAC goldbook as “A detailed description of the process leading from the reactants to the products of a reaction, including a characterization as complete as possible of the composition, structure, energy and other properties of reaction intermediates, products and transition states.” In other words, the mechanism is a chemical reaction followed at the molecular scale: the description of the geometrical transformation of the reactants into the product generally through intermediate compounds.

As there is no available way to directly follow the molecular motion during a reaction the chemist have to propose an acceptable mechanism, consistent with as set of indirect experimental proofs based on structural characterization of intermediates, rate laws, etc. A brief description of some of these techniques will be given in the first part of this section. To help the interpretation of these data, as well as to access structural details about non-isolated intermediates and predict their reactivity, theoretical tools have been developed that will be discussed in the second part of this section.

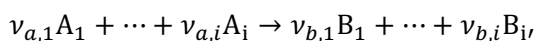
2. Experimental Techniques for Mechanistic Investigation

2.1. Kinetics and reactivity²

The measure of reaction rate is one of the most powerful method to get some insights into the mechanism of a reaction. The important parameters are the reaction order, activation energy, solvent and electronic effects.

a) Orders of reaction and elementary reactions

Any complex reaction may be decomposed into a succession of *elementary reactions*. Each elementary reaction is supposed to take place as a single process (i.e. to have a single transition state between reactant and product). As a consequence of this definition, the rate law (r) of an elementary reaction will be directly proportionate to the concentration of the reactants ($[A_n]$) times the stoichiometric coefficient ($\nu_{a,n}$):



$$r = \prod_{n=1}^i k_a [A_n]^{\nu_{a,n}}$$

Due to the low probability of having a large number of reactant molecules in a reduced space, elementary reactions are generally mono- or bimolecular processes. For instance, simple

² T. H. Lowry, K. S. Richardson, *Mechanism and Theory in Organic Chemistry*, 1987 (third ed.), Harper.

reactions such as bond breaking (dissociation), bond formation (association), concerted breaking and dissociation (substitution), isomerisation ... may be elementary reactions.

In most cases, however, reactions are not elementary steps and the mechanism can be decomposed into a succession of elementary reactions. In the general case, the reaction rate may be written as:

$$r = \prod_{n=1}^i k_a [A_n]^{v'_{a,n}} [B_i]^{v'_{b,n}}$$

The experimental coefficients v'_n (*a priori* different from the stoichiometry coefficients, v_n) are called the orders of the reaction with respect to A_i .³ These values provide information about the role played by the molecule A_i in the mechanism. In order to interpret such complex rate laws, one needs to formulate a hypothesis about the relative rate of the elementary reactions. The two most current hypotheses are:

- Rate determining step (RDS): if an elementary step has a high activation energy compared to the other steps the reaction rate may be approximate to the rate of this step.⁴
- Rapid pre-equilibrium: if one of the steps is a reversible process with low activation energy (compared to the rate determining one) it may be treated as a quasi-equilibrium.⁵
- Steady state approximation: if an unstable intermediate is present only at a low concentration its rate law can be approximately set to zero.

Note that in some cases, reactions may have no order, if several steps are in competition. Experimentally the order of a reaction with respect to the different reactants may be obtained by the method of flooding. If all reagents one excepted ($A_i, i > 1$) are put in excess, the rate law becomes:

$$r = \left(\prod_{n=2}^i k_a [A_n]_0^{v'_{a,n}} [B_i]^{v'_{b,n}} \right) [A_1]^{v'_{a,1}} = k_{app} [A_1]^{v'_{a,1}}$$

And the determination of each order becomes possible.

b) Transition state theory

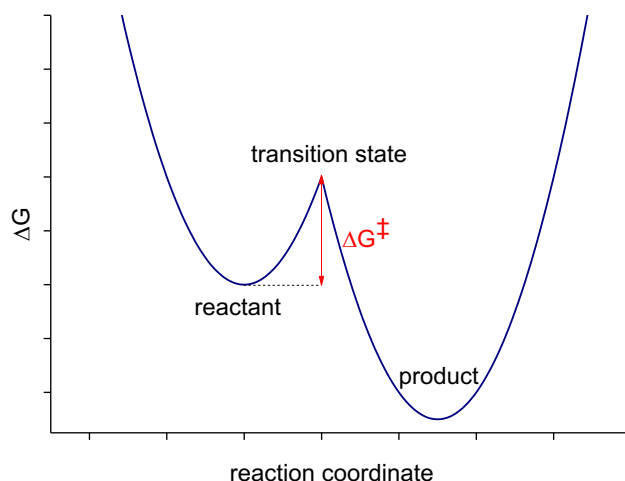
The deformation of the reactant to access the product required a minimal amount of energy, called the activation energy (E_a). It is convenient to project the N dimension energy surface corresponding to the modification of the N geometric coordinates of the reactant system of

³ A. D. McNaught and A. Wilkinson, *Compendium of Chemical Terminology (the "Gold Book")*, 1997 (2nd ed.), Blackwell Scientific Publications.

⁴ IUPAC definition is: "rate-controlling (rate-determining or rate-limiting) step in a reaction occurring by a composite reaction sequence is an elementary reaction the rate constant for which exerts a strong effect — stronger than that of any other rate constant — on the overall rate."

⁵ IUPAC definition: "A rapidly reversible step preceding the rate-limiting step in a stepwise reaction."

atoms to a two-dimension pathway. Any geometric parameter modified during the course of the reaction may be used for the 2D representation of the reaction pathway (**Scheme 1**), this parameter is called a *reaction coordinate*. In the transition state theory, the reaction coordinate is the curvilinear coordinates leading from the reactants to the products through the lowest energy pathway. The set of coordinates of maximal energy is called the transition state (TS). This zero gradient point has all its secondary derivate positive except one, negative and collinear with the reaction coordinate at the TS (saddle point).



Scheme 1 - Reaction pathway.

In the transition state theory, the kinetic constant of a reaction is given by:

$$k = \frac{k_B T}{h} \exp\left(\frac{\Delta S^\ddagger}{R}\right) \exp\left(-\frac{\Delta H^\ddagger}{RT}\right)$$

With k_B the Boltzmann constant, h the Planck constant, T the temperature, R the gas constant, ΔS^\ddagger the activation entropy and ΔH^\ddagger the activation enthalpy. The determination of ΔS^\ddagger and ΔH^\ddagger is possible by plotting the logarithm of the k constant as a function of $1/T$.

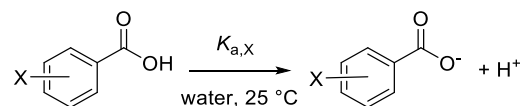
c) Electronic effects⁶

Using the Hammett definition, the electron withdrawing ability of an X moiety on a benzene ring is defined as:

$$\sigma_X = \log\left(\frac{K_{a,X}}{K_{a,H}}\right)$$

With $K_{a,X}$ the acidity constant of the benzoic acid derivative:

⁶ H. H. Jaffé, *Chem. Rev.* **1953**, 53, 2, 191-261.



Some values for classical substituents at the para position are reported in **Table 1**:

Table 1 – Hammett coefficient (σ_X) for some classical functional group.⁷

X	σ_X	X	σ_X
OMe	-0.27	I	0.18
CH ₃	-0.17	Cl, Br	0.23
H	0.00	CHO	0.35
F	0.06	CN	0.66

The plot of $\log\left(\frac{k_X}{k_H}\right)$ (with k_X the kinetic constant for a given reaction for an X moiety) versus the coefficient σ_X provides information about the effect of the electronic demand on the activation energy. The slope is noted ρ , a positive value of ρ indicates a decrease of the positive partial charge located on the aromatic ring between the reactant and transition state (electrophilic behaviour) while a negative value corresponds to an increase of the positive partial charge (nucleophilic behaviour). Finally, a change in the slope indicates a change in the mechanism or in the rate-determining step of the mechanism between electron-donating and electron-withdrawing substituents.

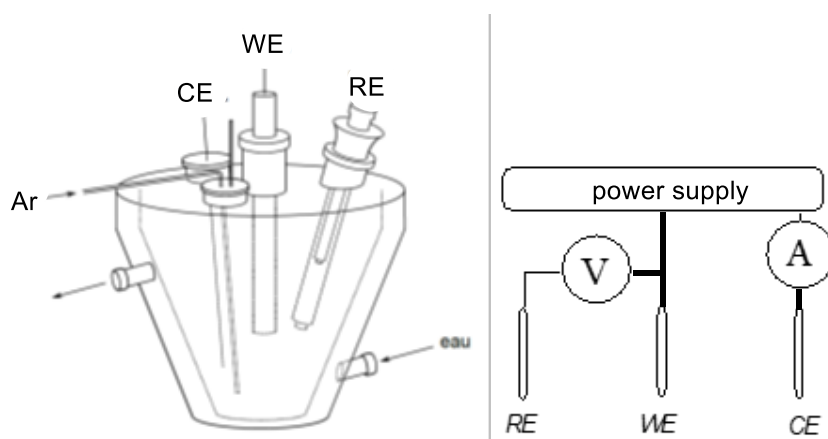
2.2. Electrochemistry⁸

a) Definitions and description of the apparatus

Definition. Electrochemistry may be viewed as any technic involving the coupling between an electric current and a chemical reaction. The electron exchange between the chemical system and the circuit takes place at the electrode and may be used either as a way to convert electronic energy to chemical energy (electrolysis, electrosynthesis) or chemical energy to electronic energy (battery). Finally, electrochemistry may also be used as an analytical tool: i) the current will give information related to the kinetic of the electron transferred and thus - under controlled conditions - to the concentration of redox active species ii) the potential is characteristic of the redox species. This analytical technic will be particularly useful in the case of metal catalyzed reaction, in order to characterize the oxidation state and concentration of the catalyst.

⁷ C. Hansch, A. Leo, R. W. Taft, *Chem. Rev.* **1991**, *91*, 2, 165-195.

⁸ *Electrochimie - Des concepts aux applications*, F. Miomandre, S. Sadki, P. Audebert, R. Méallet-Renault, **2014**, (3rd edition), Dunond; *Analytical and Physical Electrochemistry*, H. Girault, **2004** (1st edition), EPFL Press.



Scheme 2 – **Left:** the three electrodes set-up (WE: Working Electrode, CE: Counter Electrode, RE: Reference Electrode), **Right:** equivalent electronic circuit.

Three electrode set-up. In order to have access to both the current and potential of a given electrode, a three-electrode setup is generally used (**Figure 2**). The set-up is made of:

- i) **the working electrode:** the most important one, which is the electrochemical probe. In the present work, a steady glassy carbon or gold disk electrode was generally used.
- ii) **the reference electrode:** this electrode must have a fixed potential and will be used as a reference to measure the potential of the working electrode. The universal reference electrode recommended by IUPAC is the Standard Hydrogen Electrode⁹ based on the electrochemical couple $\text{H}^+_{(\text{aq})}/\text{H}_{2(\text{g})}$. For practical reasons, other reference electrodes are generally used such as the Saturated Calomel Electrode (SCE) or the $\text{Ag}_{(\text{s})}/\text{AgCl}_{(\text{s})}$ electrode, whose potentials are respectively $E(\text{Hg}_2\text{Cl}_{2(\text{s})}/\text{Hg}_{(\text{l})}) = +0.244 \text{ mV vs SHE}$ (saturated KCl, 298 K) and $E(\text{Ag}_{(\text{s})}/\text{AgCl}_{(\text{s})}) = +207 \text{ mV vs SHE}$ ($C_{\text{KCl}} = 3.0 \text{ mol L}^{-1}$, 298 K).¹⁰ The reference electrode is separated from the solution by a bridge containing the solvent and the supporting electrolyte.
- iii) **the counter-electrode:** this electrode generally consists of a platinum wire and allows to close the electronic circuit. The use of a counter electrode avoids to polarize the reference electrode (i.e. to stay at a fixed potential).

When a potential different from the equilibrium one is applied at the working electrode, a current is measured that may be due either to a chemical reaction (Faradic current) or to the resistive behaviors of the cell (ohmic drop). The proportion of ohmic drop may be reduced by using a supporting electrolyte. In the case of polar organic solvents (acetonitrile, 1,4-dioxane, DMF, nitromethane, THF, etc) $n\text{Bu}_4\text{NBF}_4$ was generally used with a concentration around 0.3 M (the concentration should be high compared to the one the redox active species, *vide infra*). The use of highly resistive and apolar solvents such as toluene is more challenging, in this case

⁹ Pure and Applied Chemistry, **1986**, 58, p 955; Note that this is only a theoretical reference, the real hydrogen-based reference is called the Normal Hydrogen Electrode (NHE).

¹⁰ Metrohm®, reference electrode documentation, 8.109.8050EN.

$n\text{Hex}_4\text{NBF}_4$ was used (saturation at 0.06 M) in combination with a UltraMicroElectrode (UME) to limit the impact of the ohmic drop.¹¹

b) Limitation by charge or mass transfer

The electrochemical current obtained may be easily related with the kinetics of the redox reaction by derivation of the Faraday law:

$$q = Fnz$$
$$I = \frac{\partial q}{\partial t} = Fzv$$

with q the charge transferred, F the faraday constant (96485 C mol^{-1}), n the amount of the substance, z its charge, I the electronic current and v the reaction rate. Thus, the measure of the current obtained for an applied potential can give us information about the redox reaction rate.

The redox reaction may be limited either by

i) the kinetics of the **electron transfer**: a redox couple may be *fast* or *slow* depending on the intrinsic activation energy for the reaction: $\text{Red} + \text{Ox} = \text{Ox} + \text{Red}$.¹² In the case of simple electron transfer (no fragmentation or condensation coupled with the electron transfer), the solvent reorganization is generally the limiting process.¹³

ii) the kinetics of the **mass transfer**: as the redox reaction must take place at the electrode (i.e. on a surface) the kinetics of the reaction is influenced by the transportation phenomenon in solution, namely, convection (macroscopic motion of the solvent), migration (charge migration under an electrochemical field) and diffusion. In the presence of a supporting electrolyte, migration of redox active species is negligible with respect to the one of the electrolytes (in our case roughly more than one hundred times more concentrated). Thanks to the solvent viscosity, the convection may also be insignificant around the electrode, in the diffusion layer (approximately $10 \mu\text{m}$).

c) Description of Electrochemical technics used in the present work

Chronoamperometry. The simplest electrochemical sequence is to apply a potential and measure the current at the working electrode as a function of time, this is called chronoamperometry. When this experiment is performed on a macroscopic disk electrode (more than $100 \mu\text{m}$, *vide infra* definition of micro electrodes) the diffusion limits the current, which decreases as (**Scheme 3**):⁷

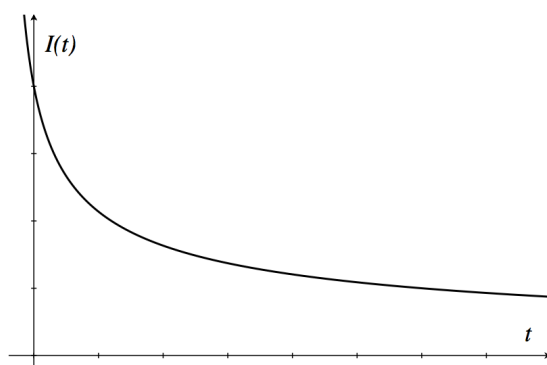
¹¹ C. Amatore, F. Pfluger, *Organometallics*, **1990**, *98*, 2276-2282.

¹² The reversible and non-reversible nomenclature is also used instead of fast and slow however for clarity reason we will use preferentially the above-mentioned terminology.

¹³ T. H. Lowry, K. S. Richardson, *Mechanism and Theory in Organic Chemistry* (3rd Edition), chapter 2.

$$I(t) = nFSC \sqrt{\frac{D}{\pi t}}$$

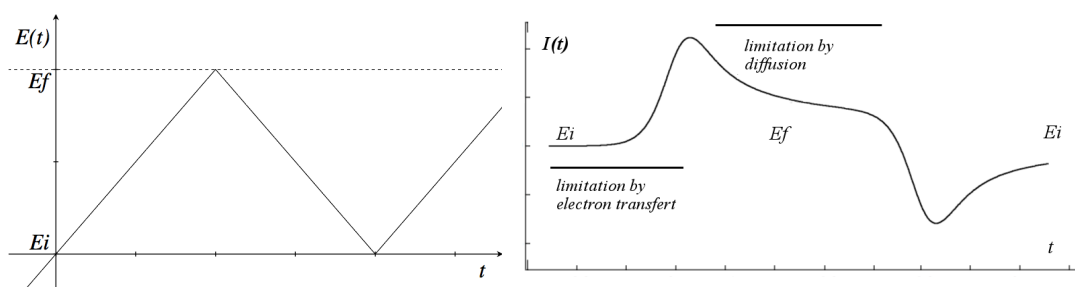
with $I(t)$ the current, n the number of electrons, F the faraday constant, S the surface of the electrode, C the concentration of the electroactive species, D the diffusion coefficient and t the time. This equation is called the *Cottrell Law*.



Scheme 3 – Schematic pattern of a chronoamperogram following the Cottrell Law.

The use of a rotating disk electrode allows to control the size of the diffusion layer. In this case, the current is simply proportionate to the concentration of the redox active species, allowing to monitor the kinetics of a reaction (as a first approximation the time resolution of this technic is limited by the rotation speed of the electrode).¹⁴

Cyclic voltammetry on disk electrodes. In the case of cyclic voltammetry (CV), a linearly increasing potential is applied at the working electrode (**Scheme 4**, left). Starting from an initial potential E_i , at which no reaction occurs, the potential reaches E_f . The obtained voltammogram is called cyclic if the potential reaches E_i again at the end of the measurement. The current increases exponentially when the oxidation (or reduction) potential of a species present in the media is reached, until the diffusion becomes the limiting process resulting in a decrease of the current (following the Cottrell law, *vide supra*).

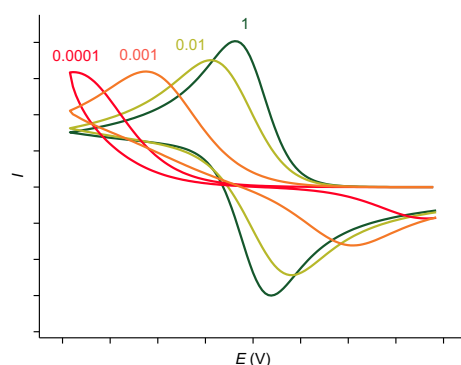


Scheme 4 – Cyclic voltammetry, applied potential.

¹⁴ A. Jutand, *Chem. Rev.*, **2008**, *10*, 87, 2300-2347

The pattern of a CV is characteristic of a redox couple and may be useful to understand the product formed at the electrode after the electron transfer. Thus, the simplest cases will be described herein.

Reversible systems: a redox couple is chemically reversible if the species formed after the electron transfer at the electrode is stable. In this case, the current corresponding to back transfer is observed when going back from E_f to E_i and the CV is symmetrical (**Scheme 5**).



Scheme 5 - CV for reversible fast or slow couples (k^0 constants, cm s^{-1} , related to the kinetics of the electron transfer are reported on the graph, diffusion constant D_k set to $10^{-5} \text{ cm}^2 \text{ s}^{-1}$ for both Ox and Red, transfer coefficient α set to 0.5, scan rate 0.1 V s^{-1} , simulated using DigiElch©).

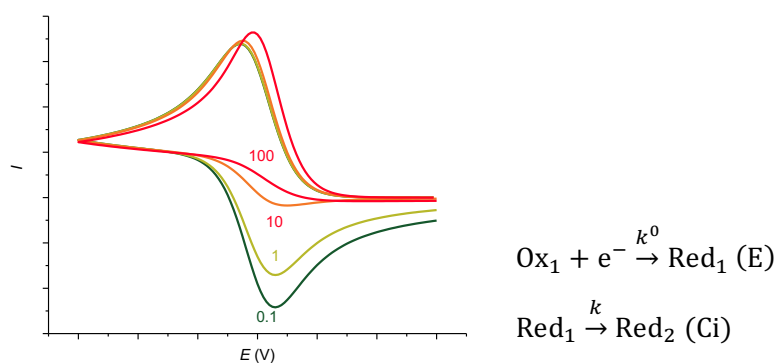
For a fast couple, the current peak in this case is given by:

$$I_p = 0.4463 nFSC \sqrt{\frac{nFvD}{RT}}$$

with I_p the current, n the number of electrons, F the faraday constant, S the surface of the electrode, C the concentration of the active species, v the scan rate, D the diffusion coefficient, R the gas constant and T the temperature. This equation is called the *Randles-Sevcik* equation.

In the case of slow couples a symmetrical pattern is also observed but the oxidation and reduction peaks are more discarded (**Scheme 5**). The peak current is still proportionate to the concentration of the redox active species, allowing kinetic measurement.

Non-reversible systems (ECi): If the species formed (Red_1) after the electron transfer decomposes or reacts with a third species to give Red_2 , the system becomes chemical irreversible. The formed species cannot be detected at low scan rate and the shape of the CV is modified as shown below (**Scheme 6**), on the contrary at high scan the reversibility can be restored.

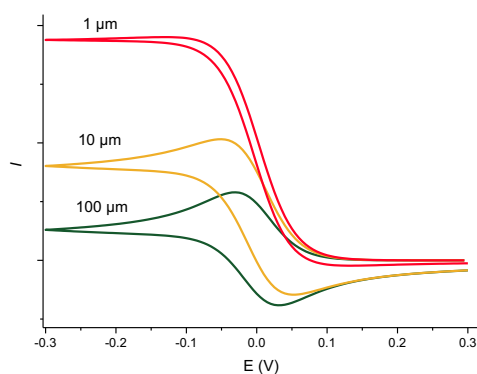


Scheme 6 - CV for reversible or irreversible fast couples ($k^0 = 10^4 \text{ cm s}^{-1}$, the k constant values (s^{-1}) of the reaction $\text{Red}_1 \rightarrow \text{Red}_2$ are reported on the graph, diffusion constant D_k set to $10^{-5} \text{ cm}^2 \text{ s}^{-1}$ for both Ox_1 and Red_1 , transfer coefficient α set to 0.5, scan rate 0.1 V s^{-1} , simulated using DigiElch©).

Cyclic Voltammetry on UME. In the case of highly resistive solvent it is preferable to use UME (vide supra), but the voltammogram obtained in this case is very different. When the diameter of the electrode become non-negligible with respect with the size of the diffusion layer (i.e. between 1 and $25 \mu\text{m}$) the radial diffusion becomes significant:

$$\frac{1}{\delta} = \frac{1}{r} + \frac{1}{\sqrt{\pi D t}}$$

for time $t \gg \frac{r^2}{\pi D}$ the diffusion layer (and thus the diffusion current) becomes independent of the time. Thus, using a scan rate slow enough, a quasi-stationary behaviour should be obtained. In this case, using a low scan rate compared to the diffusion time, the CV has a sigmoid shape independently of the reactions following the electron transfer (see **Scheme 7**).



Scheme 7 - Cyclic voltammogram of a solution of Ox ($k^0 = 10^4 \text{ cm s}^{-1}$, the diameters of the hemispherical UME are reported on the figure, diffusion constant D_k set to $10^{-5} \text{ cm}^2 \text{ s}^{-1}$ for both Ox and Red , transfer coefficient α set to 0.5, scan rate 10 mV s^{-1} , simulated using DigiElch©).

d) Electrochemistry to study reaction mechanisms¹⁵

Electrochemistry is a powerful tool for mechanistic studies. It can be used as a traditional analytical technic, providing information about the concentration of redox active species (both CV and chronoamperometry may yield currents proportionate to the concentration under appropriate conditions). It is thus possible to estimate thermodynamic (equilibrium constants) as well as kinetic data. Electrochemistry has a high sensitivity (100 μM concentration is enough to obtain correct data) and high time-resolution (1 ms on UME). More specifically, electrochemistry can provide information about the redox state of the system it is thus particularly interesting to study metal-catalyzed processes.

Finally, electrochemistry is a dynamic analytical technic, i.e. the electron transfer can be used to locally modify the chemical mixture and to study the answer of a system. For instance, it is possible to shift an equilibrium by oxidation/reduction of one of the molecules involved in the equilibrium (allowing the measure of kinetics of rapid equilibrium) or to generate an active species (metal complex with a low or high oxidation state or organic radical) and to study its reactivity.

2.3. Nuclear magnetic resonance spectroscopy of heteronuclei**a) Principle**

Nuclear Magnetic Resonance (NMR) has been developed in the 40's by E. M. Purcell and F. Block. This technique uses the interaction of a nuclear spin (\vec{S}) with a magnetic field (\vec{B}) to obtain structural data on organic and inorganic compounds.

A nuclear magnetic moment ($\vec{\mu} = \gamma \vec{S}$) interacts with a magnetic field following:¹⁶

$$H_{magn} = -\vec{\mu} \cdot \vec{B} = -\gamma \vec{S} \cdot \vec{B}$$

This interaction leads to the splitting of the $|Ms\rangle$ electronic sublevels proportionate to the extent of the magnetic field and of the gyromagnetic ratio (γ). All non-zero spin nuclei may a priori be detected using NMR. The sensitivity of a nucleus is related to the gyroscopic ratio (the sensitivity increases with the energetic gap between the spin levels) and to the natural abundance. In this work, the following nuclei are used:

¹⁵ C. Sandford, M. A. Edwards, K. J. Klunder, D. P. Hickey, M. Li, K. Barman, M. S. Sigman, H. S. White, S. D. Minter, *Chem. Sci.*, **2019**, DOI 10.1039/C9SC01545K; A. Jutand, *Chem. Rev.*, **2008**, *1087*, 2300-2347.

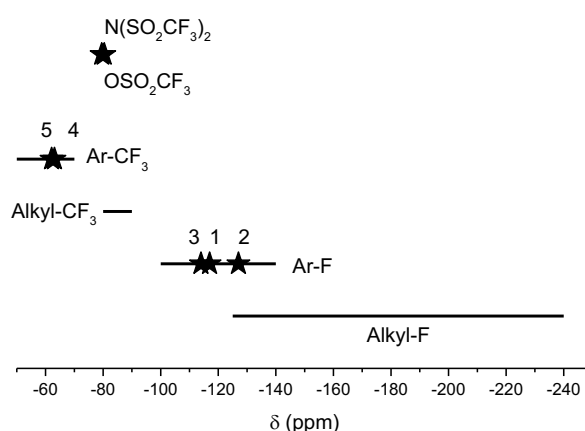
¹⁶ S. A. Smith, W. E. Palke, J. T. Gerig, *Concepts Magn Reson*, **1992**, *4*, 107-144.

Table 2 – Gyroscopic ratio, natural abundance and sensitivity related to ^1H NMR.

	γ (10^{-7} rad s^{-1})	Natural abundance (%)	Sensitivity ^a	Frequenc ^b (MHz)	Range (ppm)
^1H	26.75	99.98	100	300	13
^{11}B	8.58	80.42	16.5	96	210
^{19}F	25.16	100.0	83.3	282	700
^{31}P	10.82	100.0	6.63	121	430

^a with respect to ^1H NMR.^b On a standard NMR instrument in which ^1H resonates at 300 MHz.**b) ^{19}F and ^{31}P NMR**

^{19}F NMR has a sensitivity nearly as good as the proton one due to its high gyroscopic ratio and high abundance, it also has a very large range of chemical shift (**Scheme 8**). Due to these points, fluorine NMR may be used as an atomic probe to monitor any structural change in fluorine-tagged complexes as well as to follow kinetics of reactions (using a 10 mM sample only 16 s are required to get a spectrum with a correct signal to noise ratio allowing to study reactions with $t_{1/2}$ as low as 100 s).¹⁷

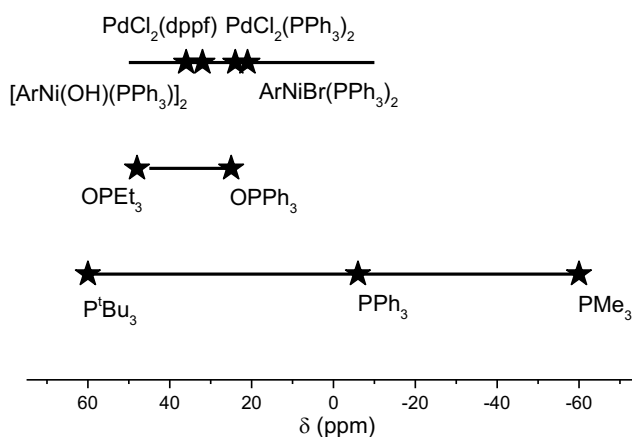


Scheme 8 – Chemical shift range of some organic fluorine derivatives. Some of the fluorinated compounds used in the present work are indicated by stars (1: 4-F-2-Me-1,1'-biphenyl, 2: (*p*-F-*o*-Me-C₆H₃)NiBr(PPh₃)₂, 3: fluorobenzene, 4: (*p*-CF₃-C₆H₄)NiCl(PCy₃)₂ and 5: α,α,α -trifluorotoluene).

In organometallic and coordination chemistry, ^{31}P NMR is a major tool for the study of metal complexes featuring phosphorus ligands. Its sensitivity is quite low compared to ^1H and ^{19}F NMR (**Table 2**), however the use of proton-decoupled sequences allows to enhance the signal

¹⁷ The group of Prof G. Lloyd-Jones has recently developed stop-flow NMR-monitored experiments allowing to measure half-life as low as the millisecond, P. A. Cox, M. Reid, A. G. Leach, A. D. Campbell, E. J. King, G. C. Lloyd-Jones, *J. Am. Chem. Soc.*, **2017**, 139, 37, 13156-13165; A. B. Jones, G. C. Lloyd-Jones, D. Uhrin, *Anal. Chem.* **2017**, 89, 18, 10013-10021.

to noise ratio. $^{31}\text{P}\{^1\text{H}\}$ NMR is routinely used for the characterization of stable compounds as well as to evidence short-lived reaction intermediates.¹⁸ Therefore, this technique is particularly useful to elucidate the mechanisms of catalytic reactions and to help to the development of new transformations¹⁹ promoted by phosphine-ligated metal catalysts. ^{31}P nuclei yield easily observable and sharp NMR signals over a wide range of chemical shift, providing valuable chemical information due to their high chemical shift sensitivity even to minor structural changes (Scheme 9).¹⁸



Scheme 9 – Chemical shift range of phosphines, phosphine oxides and phosphines in transition metal complexes.

Unfortunately, while the chemical shifts of ^1H or ^{13}C in organic molecules have been traditionally estimated by the use of empirical correlation tables,²⁰ ^{31}P NMR chemical shifts are notoriously difficult to predict based only on qualitative considerations and tabulated data.^{18,21} Indeed, whereas ^1H and ^{13}C NMR spectroscopies are mainly concerned with contributions due to σ -bonding or to well-defined and recurring π bonded structural elements, the influence of π -bonding in ^{31}P NMR is larger in magnitude, more frequent and less transferable from one compound to another.¹⁸

c) Quantitative NMR

NMR spectrum can be used to determine thermodynamic as well as kinetic data, this requires however the signal to be proportionate to the concentration of the sample and to determine the proportionality coefficient.

¹⁸ P. S. Pregosin, R. W. Kunz, *^{31}P and ^{13}C NMR of Transition Metal Phosphine Complexes*, 1979, Springer; O. Kühl, *Phosphorus-31 NMR Spectroscopy: A Concise Introduction for the Synthetic Organic and Organometallic Chemist*, 2008, Springer.

¹⁹ D. S. Glueck, *Coord. Chem. Rev.* **2008**, 252, 2171-2179.

²⁰ M. Hesse, H. Meier, B. Zeeh, *Spectroscopic Methods in Organic Chemistry*, 2007 (2nd edition), Springer.

²¹ J. Tong, S. Liu, S. Zhang, S. Z. Li, *Spectrochimica Acta Part A: Molecular and Biomolecular Spectroscopy*, **2007**, 67, 837-846.

It is convenient to use proton-decoupled sequences noted, $^{19}\text{F}\{\text{H}\}$ and $^{31}\text{P}\{\text{H}\}$. These sequences, however, produces an increase of the signal of heteronuclei, through the so-called Nuclear Overhauser Effect (NOE), roughly proportionate to the number of spatially close protons. The use of inverse-gated decoupling allows to prevent this problem.²²

Another problem is the relaxation delay (generally written d_1), the d_1 must be at least five times the spin lattice relaxation time (T_1). T_1 can be measured using a sequence called inversion-recovery.²³ In our case a ^{19}F nucleus in an organometallic complex relaxes nearly 10 times faster than one in an organic molecule and a d_1 of 10 s was required.

Finally, an internal reference is needed, in our case fluorobenzene and/or phosphoric acid were added in a glass capillary filled with deuterated DMSO, allowing to lock and shim (without waste of deuterated solvent) as well as to have a reference.

2.4. Electron paramagnetic resonance spectroscopy²⁴

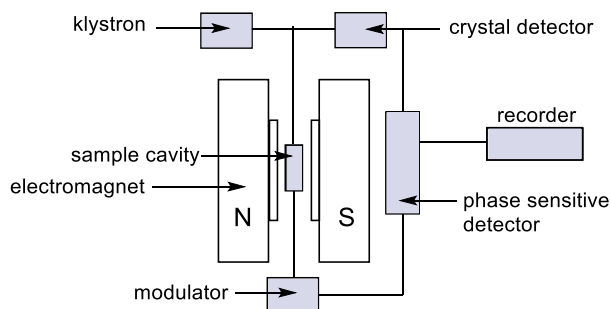
a) Zeeman effect and description of the apparatus

Any unpaired electron – characterized by an intrinsic magnetic moment $\vec{\mu}_e$ – placed in a magnetic field (\vec{B}) interacts with it through a dipolar-dipolar interaction. This interaction leads to a splitting of the $|Ms\rangle$ electronic sublevels proportionate to the extent of this field:

$$\hat{H}_{magn} = -\vec{\mu}_e \cdot \vec{B}$$

$$\hat{H}_{magn} = g_e \beta \cdot \vec{S} \cdot \vec{B}$$

With β the Bohr magneton ($\beta = 9.27400949 \cdot 10^{-24} \text{ J T}^{-1}$) and g_e the free-electron Zeeman factor ($g_e = 2.0023$). The Electron Paramagnetic Resonance (EPR) Spectroscopy values this phenomenon to study the chemical structure of paramagnetic molecule (organic radicals or transition metal complexes). **Scheme 10** shows a schematic representation of the EPR apparatus.



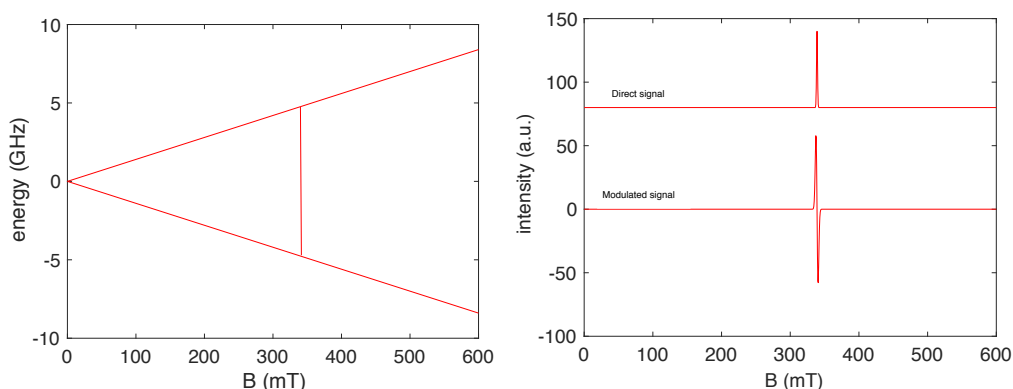
Scheme 10 – Principe of the EPR spectrometer.

²² D. Soulsby, *NMR Spectroscopy in the Undergraduate Curriculum*, 2013, American Chemical Society.

²³ T. J. Williams, A. D. Kershaw, V. Li, X. Wu, *J Chem Educ.*, 2011, 88, 5, 665–669.

²⁴ P. Bertrand, *Spectroscopie de résonance paramagnétique électronique*, 2010, EDP Science; W. R. Hagen, *Biomolecular EPR spectroscopy*, 2009, Taylor & Francis.

The sample is placed in a cavity in the center of the magnetic field. For a magnetic field of 0.3 T, a microwave of around 10 GHz is suitable to study the spin transition ($\nu = g \beta B/h$, with h the Planck constant). Due to technical reasons, related to the difficulty to have a variable-frequencies microwave source, the spectrometer works at fixed frequency (usually 10 GHz ‘X band’ or 35 GHz ‘Q band’) while the magnetic field is variable. An absorption of the μ -wave signal is observed for the adapted magnetic field (**Scheme 11**).



Scheme 11 - **Left**: Zeeman effect for a single electron, **Right**: Simulated EPR signal for the same systems on a 9.39 GHz spectrometer (direct and using frequency modulation, simulated using Easyspin toolbox on Matlab©).

Compared to NMR spectra, EPR spectra seem to be “ill-phased”, this is due to the signal acquisition technic: in order to increase the signal to noise ratio the microwave signal is frequency modulated by a small sinusoidale component:

$$B_z(t) = B^0 + B_m \cos(2\pi\nu_m t)$$

The detected time variable component is proportionate to the first derivate of the signal (**Scheme 11**):

$$I(B_z) \approx I(B^0) + I'(B^0) \cdot B_m \cos(2\pi\nu_m t)$$

b) Hamiltonian and transition rules

The electronic transitions observed in EPR spectroscopy are due to the interaction of a second magnetic field (\vec{B}_1), perpendicular to the first one, with the magnetic momentum of the electron. The Fermi gold rule is thus written in this case:

$$T_{i \rightarrow f} = |\langle \Phi_f | \vec{B}_1 \cdot \vec{\mu}_e | \Phi_i \rangle|^2$$

The $T_{i \rightarrow f}$ quantity is proportionate to the probability of the transition, Φ_i the initial wave function of the system and Φ_f the final state. As there is no change in the spatial part $|\Psi_i\rangle$ of the wave function:

$$|\Phi_i\rangle = |\Psi_i\rangle|\chi_i\rangle \text{ and } |\Phi_f\rangle = |\Psi_i\rangle|\chi_f\rangle$$

With $|\chi_i\rangle$ and $|\chi_f\rangle$ the spin part. The probability may be re-written as:

$$T_{1 \rightarrow 2} = \langle \Psi_i | \Psi_i \rangle \cdot \langle \chi_f | \vec{B}_1 \cdot \vec{\mu}_e | \chi_i \rangle$$

After projection along the Cartesian axis:

$$T_{i \rightarrow f} = g \cdot \beta (\langle \chi_f | B_{1,x} \cdot S_x | \chi_i \rangle + \langle \chi_f | B_{1,y} \cdot S_y | \chi_i \rangle + \langle \chi_f | B_{1,z} \cdot S_z | \chi_i \rangle)$$

The term $\langle \chi_f | B_z \cdot S_z | \chi_i \rangle$ is zero, as $|\chi_i\rangle$ and $|\chi_f\rangle$ are orthogonate. On the contrary, the two other terms may be non-zero, only if $|\chi_f\rangle$ is not orthogonate to $\hat{S}^+ |\chi_i\rangle$ (or $\hat{S}^- |\chi_i\rangle$) with \hat{S}^+ and \hat{S}^- the Ladder operators, as \hat{S}_x and \hat{S}_y may be written as:

$$\hat{S}_x = \frac{1}{2} (\hat{S}^+ + \hat{S}^-); \hat{S}_y = \frac{1}{2i} (\hat{S}^+ - \hat{S}^-)$$

As a conclusion, the only transition rule allowed in perpendicular mode of EPR is: $\Delta S = \pm 1$

c) The zero field splitting and effective magnetic Hamiltonian

In practice several supplementary dipolar interactions, besides the main one between the electronic spin and the magnetic fields, can affect the aspect of an EPR spectra. These interactions are listed in **Table 3**:

Table 3 – List of magnetic dipolar interactions than can affect the aspect of an EPR scepra.

Interaction	Phenomenon	Example
SS	Spin-spin (fine structure also called Zero Field Splitting)	In high spin system (fine structure) In cluster (fine structure or broadening)
SB	Zeeman effect	Basic EPR
SO	Spin-orbit (g anisotropy and fine structure)	In metal complexes
SI	Electronic spin - nuclear spin interaction (Hyperfine and superhyperfine structure)	With non-zero nuclear spin metals (^{57}Fe , ^{63}Cu , etc) or non-zero nuclear spin ligand (^1H , ^{14}N , etc)

Considering all these interactions (except the one between the electronic and nuclear spin), the *effective* magnetic Hamiltonian can be written as

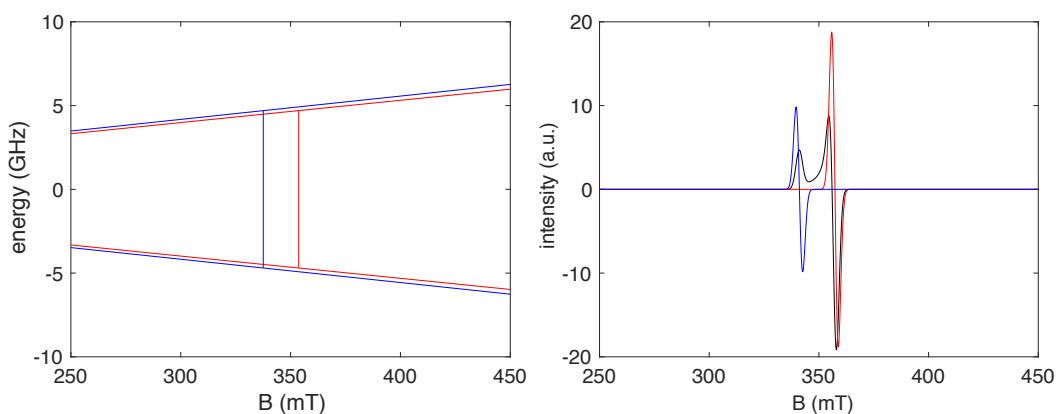
$$\hat{H}'_{magn} \approx -\beta \cdot \tilde{g} \cdot \vec{S} \cdot \vec{B} + S \cdot \tilde{D} \cdot S$$

with \tilde{g} the *effective* magnetic tensor and \tilde{D} the ZFS tensor, formally a spin-spin interaction independent of the magnetic field intensity and thus called ‘zero field splitting’ (FZS):

$$\hat{H}_{\text{ZFS}} = \mathbf{S} \cdot \tilde{\mathbf{D}} \cdot \mathbf{S} = D \left[S_z^2 - \frac{S(S+1)}{3} \right] + E(S_x^2 - S_y^2)$$

This term lead to supplementary transitions. D and E are two scalars characterizing the ZFS interaction: D measures the extent of the interaction while E is related to the symmetry of the interaction.

The effective magnetic tensor $\tilde{\mathbf{g}}$ is the analogue of the chemical shift in NMR spectroscopy, contrary to the chemical shift, it is generally not possible to predict its evolution using qualitative reasoning. Spin-orbit interactions are mainly responsible for the modification of $\tilde{\mathbf{g}}$ compared to $\tilde{\mathbf{g}}_e$ ($\tilde{\mathbf{g}}_e = g_e \tilde{\mathbf{1}}$).²⁵ The values of g_x , g_y and g_z provide information about the symmetry of the paramagnetic center. $g_x = g_y = g_z$ corresponds to an isotropic system, $g_x = g_y \neq g_z$ to an axial system (typically a Jahn-Teller distorted system) and $g_x \neq g_y \neq g_z$ to a rhombic system. These values can be extracted from the spectra by fitting (**Scheme 12**).



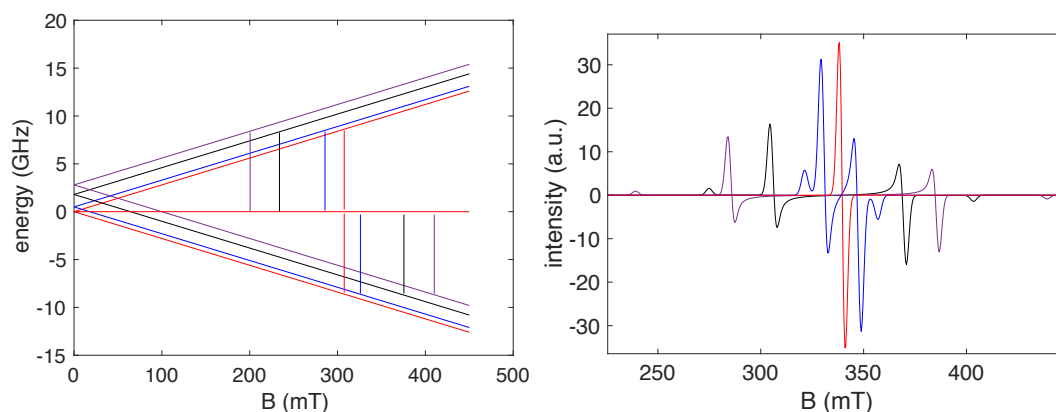
Scheme 12 – Left: Zeeman effect for an hypothetical $S = \frac{1}{2}$ system, with $g_x = 1.90$, $g_y = 1.90$ (red) and $g_z = 1.99$ (blue), Right: Simulated EPR signal (black) for the same systems on a 9.39 GHz spectrometer (simulated using Easyspin toolbox on Matlab©), axial (blue) and equatorial contribution (red) are indicated.

For the same reasons, D and E values are non-easily predictable without DFT (*vide infra*). In organic molecules D varies between 0.1 and 1 cm^{-1} ,²⁶ while for transition metal complexes it is usually between 0.1 and 10 cm^{-1} .²⁷ The E/D value varies between 0 (for an axially symmetrical complex $D_x = D_y$) and 1/3 for strongly distorted structures. **Scheme 13** shows a schematic representation of ZFS effect on an EPR spectra (for an axial system), the signal become splitted and the split is proportionate to D .

²⁵ As a consequence, the *effective* magnetic tensor is generally very close to the $\tilde{\mathbf{g}}_e$ for organic molecules with low spin-orbit interactions, on the contrary paramagnetic transition metal complexes display important shifts.

²⁶ Mainly due to spin-spin interactions.

²⁷ Mainly due to spin-orbit interactions.



Scheme 13 – Left: Zeeman effect for an hypothetical $S = 1$ system (with $\tilde{g} = \tilde{g}_e$) with increasing initial splitting ($D = 0$ (red), 0.5 (blue), 1.8 (black) and 2.8 GHz (purple)), Right: Simulated EPR signal for the same systems on a 9.39 GHz spectrometer (simulated on a perfectly axially symmetrical system, $E = 0$, using Easyspin toolbox on Matlab©).

d) Prediction of spectroscopic parameters by DFT

As stated before, changes in the effective \tilde{g} are due mainly to the spin-orbit coupling, \tilde{g} may be estimated starting from the electronic wave-function in the absence of coupling with the help of the perturbation theory, by considering the interaction with electronic excited states. The perturbation Hamiltonian is:

$$\hat{H}_{pert} = \beta \cdot (g \cdot \vec{S} + \vec{l}_e) \cdot \vec{B} + \vec{S} \cdot \vec{l}_e$$

under the projected from:

$$\hat{H}_{pert} = g_e \beta \vec{B} \cdot \vec{S} + [L_x(\lambda S_x + \beta B_x) + L_y(\lambda S_y + \beta B_y) + L_z(\lambda S_z + \beta S_z)]$$

The first order contribution is zero since we have:

$$\langle \Phi_1 | \hat{L}_x | \Phi_1 \rangle = \langle \Phi_1 | \hat{L}_y | \Phi_1 \rangle = \langle \Phi_1 | \hat{L}_z | \Phi_1 \rangle = 0$$

Need to go up to the second order and considered the contribution of the k excited states:

$$\tilde{g} = \begin{bmatrix} g_e & -\lambda \sum_k \frac{2\langle \Phi_1 | \hat{L}_x | \Phi_k \rangle \langle \Phi_k | \hat{L}_y | \Phi_1 \rangle}{E_k - E_1} & -\lambda \sum_k \frac{2\langle \Phi_1 | \hat{L}_x | \Phi_k \rangle \langle \Phi_k | \hat{L}_z | \Phi_1 \rangle}{E_k - E_1} \\ \dots & g_e & \dots \\ \dots & \dots & g_e \end{bmatrix}$$

Using this approach,²⁸ the calculation of the g-tensor is quite easy to perform using the EPR module of ORCA for instance.²⁹ Compared to NMR prediction no specific basis set and functional are needed for these calculations.

²⁸ F. Neese, *J. Chem. Phys.*, **2005**, 122, 034107.

²⁹ ORCA - An ab initio, DFT and semiempirical SCF-MO package - Version 4.0.1, manual, F. Neese et al.; F. Neese, *WIREs Comput Mol Sci*, **2012**, 2, 73-78.

The Zero Field Splitting contribution is trickier to estimate, one needs to estimate both the spin-orbit and spin-spin contribution. Concerning the spin-orbit contribution several methods have been developed,³⁰ we used the QRO approach.³¹ The calculation of the spin-spin coupling contribution was done using the restricted spin density obtained from the singly occupied unrestricted natural orbitals.³²

³⁰ The coupled-perturbed method is recommended by F. Neese (F. Neese, *J. Chem. Phys.*, **2007**, *127*, 164112.) however, in our hands, it proved to have convergence problems on high spin iron triflate.

³¹ F. Neese, E. I. Solomon, *Inorg. Chem.*, **1998**, *37*, 6568-6582; F. Neese, *J. Am. Chem. Soc.*, **2006**, *128*, 10213-10222.

³² S. Sinnecker, F. Neese, *J. Phys. Chem. A*, **2006**, *110*, 12267-12275; C. Riplinger, J. P. Y. Kao, G. M. Rosen, V. Kathirvelu, G. R. Eaton, S. S. Eaton, A. Kutateladze, F. Neese, *J. Am. Chem. Soc.*, **2009**, *131*, 10092-10106.

3. Theoretical Tools

NB: Atomic units are used all along this subsection, $m_e = 1$, $\hbar = 1$, $e = 1$, $\frac{1}{4\pi\epsilon} = 1$

3.1. Theoretical foundations and classical approximations

Quantum mechanics is founded on the postulate that any particle (electron, nucleus, etc) may be completely described by a wave function $|\Psi\rangle$ which is a function of the space coordinate ($\mathbf{r}_1 \dots \mathbf{r}_N$) and spin coordinate of the N particles of the system. This function is obtained by solving the Schrödinger equation:

$$\hat{H}|\Psi\rangle = E|\Psi\rangle$$

where \hat{H} is called the Hamiltonian of the system, i.e. the energy operator.³³ The fundamental energy (E) is the lowest eigenvalue of this equation. This function has no physical meaning in itself, however partial integration of it leads to the probability for the particle to occupy an infinitesimal volume $d\tau$ around \mathbf{r}_1 :

$$\rho(r_1) = \langle\Psi|\Psi\rangle_{2\dots N} = \int_{r_2} \dots \int_{r_N} |\Psi|^2 dr_2 \dots dr_N$$

The complete integral of this function is normalized:

$$\langle\Psi|\Psi\rangle_{1\dots N} = \int_{r_1} \dots \int_{r_N} |\Psi|^2 dr_1 \dots dr_N = 1$$

Any physical property (“observable”) of the system (energy, etc) can be obtained from this function by using the adapted operator, the observable being the eigenvalues.

The non-relativistic Hamiltonian can be written as:³⁴

$$\hat{H} = \hat{T}_N + \hat{V}_{NN} + \hat{T}_e + \hat{V}_{Ne} + \hat{V}_{ee}$$

With \hat{T}_N and \hat{T}_e the kinetic energy of the nuclei and electrons respectively:

$$\hat{T}_N = \sum_n^{nuclei} -\frac{1}{2} \nabla_n^2 ; \hat{T}_e = \sum_i^{e^-} -\frac{1}{2} \nabla_i^2$$

And \hat{V}_{NN} , \hat{V}_{eN} and \hat{V}_{ee} the nuclei-nuclei, nuclei-electrons and electrons-electrons potential energy operators:

³³ This equation is correct only for time-independent system, for time-dependent system the Schrödinger equation is written: $\hat{H}|\Psi\rangle = i \frac{\partial|\Psi\rangle}{\partial t}$

³⁴ Relativistic corrections are required in order to correctly describe the core electrons of heavy nuclei.

$$\hat{V}_{NN} = \sum_n^{\text{nuclei}} \sum_{m < n} \frac{Z_n Z_m}{r_{n,m}}; \hat{V}_{Ne} = - \sum_n^{\text{nuclei}} \sum_i^{e^-} \frac{Z_n}{r_{n,i}}; \hat{V}_{ee} = \sum_i^{e^-} \sum_{j < i} \frac{1}{r_{i,j}}$$

This equation cannot be solved for a system with more than two corps (i.e. the hydrogen atom), for this reason several semantic approximations have been adopted.

3.2. The Born-Oppenheimer approximation and nuclear energy

As the nuclei move much slower than electrons, due to the mass dissimilarity ($m_e/m_p = 1836$), it is possible to neglect the coupling between the electronic and nuclear motions. It is a good approximation to consider that electrons adapt instantly to any move of the nuclei. This is called the Born-Oppenheimer principle. The wave function may be splitted into a nuclei wave function $|\chi(R_N)\rangle$ and an electronic wave function $|\Phi(r_i, R_N)\rangle$:

$$|\Psi(R_n, r_i)\rangle = |\chi(R_N)\rangle |\Phi(r_i, R_N)\rangle$$

the electronic wave function $|\Phi(r_i, R_N)\rangle$ is a solution of the electronic Hamiltonian \hat{H}_e for a given nuclear conformation (nuclei fixed, the positions R_N are *parameters*):

$$\hat{H}_e = \hat{T}_e + \hat{V}_{Ne} + \hat{V}_{ee}$$

$$\hat{H}_e |\Phi(r_i, R_N)\rangle = E_e |\Phi(r_i, R_N)\rangle$$

The electronic energy $E_e(R_N)$ depends on the nuclear conformation R_N and consequently the total potential energy affecting the nuclei is of the form: ³⁵

$$\hat{U}_N = \hat{V}_N + E_e(R_N)$$

Finally, the nuclear wave function is a solution of:

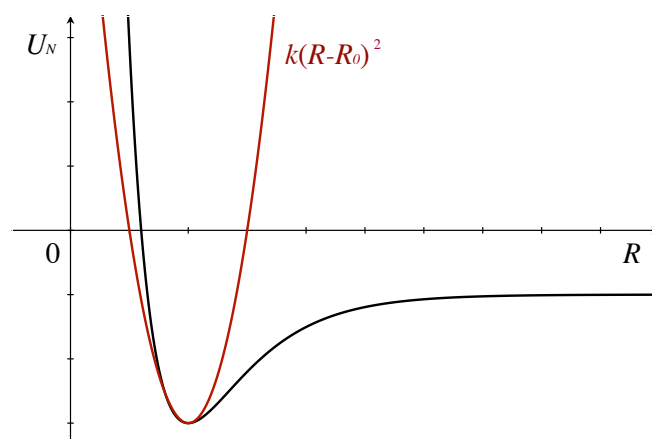
$$\hat{H}_N |\chi(R_N)\rangle = E |\chi(R_N)\rangle$$

$$\hat{H}_N = \hat{T}_N + \hat{V}_N + E_e(R_N)$$

For a diatomic molecule, the potential energy of a diatomic molecule is reproduced on **Scheme 14**. It is convenient to reduce this energy surface to an harmonic oscillator around the equilibrium position of the nuclei (R_0):

$$U_{N,approx} = \frac{1}{2} k(R - R_0)^2$$

³⁵ Adiabatic theorem: to study the nuclei energy we suppose that there is no change in the electronic state (i.e. a modification of the position of the nuclei cannot induce a change in the electronic state).



Scheme 14 – Potential energy (U_N) of a diatomic molecule as a function of the internuclear distance (R).

This can be generalized to polyatomic molecules; the surface energy can be decomposed to $3N-6$ ³⁶ harmonic vibration modes. The total nuclear energy can be approximated to:

$$\hat{H}_N = \hat{U}_N + \hat{T}_N$$

with:

$$\hat{U}_N = \sum_{n=1}^{3N-6} \frac{1}{2} k_n (R_n - R_{n,0})^2$$

The fundamental eigenvalues of this Hamiltonian are:

$$U_N = \sum_{n=1}^{3N-6} \frac{1}{2} \sqrt{\frac{k_n}{m_n}}$$

with m_n the reduce mass associated to the vibration mode.

3.3. Electronic energy and Slater approximation

In order to estimate the electronic wave function, it is convenient to consider that each electron can be described by an independent wave function $|\varphi_i(r_i)\rangle$, the polyelectronic wave function being the product of the mono-electronic ones:

$$|\Phi(r_i)\rangle = \prod_i^{e^-} |\varphi_i(r_i)\rangle$$

This expression, however, cannot reproduce the fermionic behaviour of electrons, i.e. the polyelectronic wave function must be antisymmetric with respect to the exchange of two electrons. A convenient way to obtain such antisymmetric polyelectronic functions, for I electrons, based on mono-electronic function is to write the Slater determinant:

³⁶ For a non-linear molecule.

$$|\Phi(r_i)\rangle = \frac{1}{\sqrt{I!}} \begin{vmatrix} \varphi_1 & \dots & \varphi_1 \\ \dots & \ddots & \dots \\ \varphi_I & \dots & \varphi_I \end{vmatrix}$$

The polyelectronic Hamiltonian can also be expressed as a sum of mono-electronic ones, plus an electrons-electrons repulsion term:

$$\hat{H}_e = \sum_i^I h_i + \sum_{i<j}^I \frac{1}{r_{i,j}}$$

with

$$\hat{h}_i = -\frac{1}{2}\nabla_i^2 + \sum_n^{\text{nuclei}} \frac{Z_n}{r_{i,n}}$$

The value of this Hamiltonian on the polyelectronic wave function can be decomposed into several terms whose physical meaning will be discussed:

$$E_e = \sum_i^I h_i + \frac{1}{2} \sum_i^I \sum_j^I [J_{i,j} - K_{i,j}]$$

with h_i the one-electron energy (the Coulomb integrals):

$$h_i = \langle \varphi_i | \hat{h}_i | \varphi_i \rangle$$

and $[J_{i,j} - K_{i,j}]$ the part of the electron-electron interaction energy, it is constituted of two parts, $J_{i,j}$ is a classical electron-electron repulsion:

$$J_{i,j} = \langle \varphi_i \varphi_j | \frac{1}{r_{i,j}} | \varphi_i \varphi_j \rangle$$

while $K_{i,j}$ is a purely quantum term called exchange energy:

$$K_{i,j} = \langle \varphi_i \varphi_j | \frac{1}{r_{i,j}} | \varphi_j \varphi_i \rangle$$

3.4. How to evaluate the electronic energy?

a) Semi-empirical approach

The simplest method to evaluate the electronic energy is to parameterize the Coulomb and exchange integrals based on experimental data. The simplest parameterization is the Hückel method: in this case both Coulomb and exchange integrals have fixed values.

More advanced semi-empirical methods have been developed such as the Austin Model 1 (AM1)³⁷ or PM3³⁸/PM6.³⁹ Semi-empirical methods have very low computational cost and provide generally correct geometry optimization for organic molecule. They are also useful to provide a first guess to iterative resolution methods (*vide infra*).

b) Hartree-Fock and post-Hartree-Fock methods

The Hartree-Fock approach consists in a Self-Consistent Field (SCF) method. The one electron Fock operator is written:

$$\hat{f}_i = \hat{h}_i + \hat{V}_i^{HF}$$

with \hat{V}_i^{HF} the Hartree-Fock potential, i.e. the potential energy average interaction with the other electrons. As this operator depends on the other mono-electronic wave functions the set of equations has to be solved iteratively. This technique is called the self-consistent field (SCF) procedure.

However, the obtained wave-function is not the exact wave-function due to the approximation of considering the electron as a mean field and not as individual particles. Therefore, a part of the electron correlation is missing. Several methods (MP2, MP3 etc)⁴⁰ have been developed to solve this problem by using a linear combination of Slater determinants instead of a single one leading to great improvement in the accuracy of the electronic energy evaluation. These methods however have a very high computational cost and thus cannot be applied on large molecular systems.

3.5. The Density Functional Theory (DFT)⁴¹

Instead of dealing with the polyelectronic wave function – without direct physical meaning – one should prefer to rather consider the simple electron density:

$$\rho(r_1) = I. \langle \Phi | \Phi \rangle_{2...I}$$

The Hohenberg and Kohn theorems state that:

1- The electronic energy⁴² can be expressed as a functional of the electronic density:

$$E_e = E[\rho(r)]$$

2- The ground state electronic density corresponds to the minimal electronic energy.

³⁷ M. J. S. Dewar, E. G. Zoebisch, E. F. Healy, J. J. P. Stewart, *J. Am. Chem. Soc.*, **1985**, 107, 3902-3909.

³⁸ J. J. P. Stewart, *J. Comp. Chem.*, **1989**, 10, 209–220.

³⁹ J. J. P. Stewart, *J Mol. Mod.*, **2007**, 13, 1173–1213.

⁴⁰ V. Magnasco, *Post- Hartree-Fock Methods. In Methods of Molecular Quantum Mechanics*, **2009**, Wiley.

⁴¹ R. G. Parr, W. Yang, *Density-Functional Theory of Atoms and Molecules*, **1989**, Oxford University Press.

⁴² And any other electronic properties of the system.

The difficulty is that there is no exact analytical way to express this functional. It can be decomposed into a sum of several functionals:

$$E[\rho] = V_{Ne}[\rho] + T_e[\rho] + V_{ee}[\rho]$$

The first term can be easily estimated:

$$V_{Ne}[\rho] = \int \rho(r)V(r)dr$$

The second one, the kinetic energy of the electrons, can be estimated using the Kohn-Sham method.⁴³ For non-interacting electrons described by single monoelectronic wave functions:

$$T_{e,mono}[\rho] = -1/2 \sum_i^{e^-} \langle \varphi_i | \nabla^2 | \varphi_i \rangle$$

Part of the third term can be estimated easily, the classical electrons-electrons repulsion interaction:

$$V_{ee}[\rho] = J[\rho] + E_{NC}[\rho]$$

with:

$$J[\rho] = 1/2 \sum_{i,j} \int \frac{1}{r_{ij}} \rho(r_i)\rho(r_j)dr_i dr_j$$

and $E_{NC}[\rho]$ a non-classical term, corresponding mainly to the exchange-correlation energy. The total functional can be expressed again as:

$$E[\rho] = V_{Ne}[\rho] + T_{e,mono}[\rho] + J[\rho] + E_{XC}[\rho]$$

with $E_{XC}[\rho]$ the total exchange and correlation energy, coming partly from the electron-electron repulsion potential ($E_{NC}[\rho]$) and partly from the missing kinetic energy due to the Kohn-Sham approximation (*vide supra*). There is no analytical form for this term, however, it can be estimated using approximations. This functional can be decomposed into an exchange part and a correlation part:

$$E_{XC}[\rho] = E_X[\rho] + E_C[\rho]$$

The simplest way to evaluate this term is to consider that the exchange and correlation energy depend only of the value of the electronic density in each point of space. The energy value in each point is obtained by considering locally a uniform electron gas. This method called the Local Density Approximation (LDA) is not accurate enough for molecular modelling but can be applied successfully to material system.

To improve the quality of the calculations, one needs to consider also the gradient effect (the inhomogeneity of the electronic density), these methods are called generalized gradient approximation (GGA). Among the most popular GGA corrections, we can cite the exchange

⁴³ W. Kohn and L. J. Sham, *Phys. Rev.*, **1965**, *140*, A1133-A1138.

functional developed by Becke (indicated by the letter ‘B’ in the name of the functionals)⁴⁴ and the correlation functionals proposed by Lee, Yang and Parr (and noted ‘LYP’)⁴⁵ or by Perdew (‘P86’,⁴⁶ ‘PW91’,⁴⁷ ‘PBE’⁴⁸). For instance, the BP86 functional used in CHAPTER III used the Becke correction to evaluate the exchange term and the Perdew’s one to the correlation energy.

The evaluation of the exchange term can be improved by addition of a percentage of the exact Hartree-Fock exchange. These functionals are called ‘hybrid functionals’, for instance B3LYP (20% of HF exchange) and PBE0 (25%), used in CHAPTER III.

Finally, the GGA approximation can be completed by taking into account the kinetic energy density in addition to the density and density gradients. These functionals are called metaGGA and perform better than classical hybride ones for the description of dispersion forces (see section 3.7).

Table 4 – Functionals used in this thesis.

Functional	Exact	
	Hartree-Fock exchange (%)	Class
BP86 ^{44, 46}	0	GGA
B3LYP ⁴⁹	20	Hybrid, GGA
PBE0 ⁵⁰	25	Hybrid, GGA
M06 ⁵¹	27	Meta, Hybrid, GGA

3.6. Choice of the basis set and functional

A molecular wave function can be expressed as an infinite linear combination of atom-centered mono-electronic wave functions (LCAO method). For practical reasons only a finite set of functions is considered. Unfortunately, the exact hydrogen-based orbitals (Slater type, STO):

⁴⁴ A. D. Becke, *Phys. Rev. A*, **1988**, *38*, 3098–3100.

⁴⁵ C. Lee, W. Yang R. G. Parr, *Phys. Rev. B*, **1988**, *37*, 785-789.

⁴⁶ J. P. Perdew, *Phys. Rev. B*, **1986**, *33*, 8822-8824.

⁴⁷ J. P. Perdew (Eds.: P. Eschrig, H. Ziesche), in *Electron. Struct. Solids '91*, **1991**, Akademie Verlag, p 11-20.

⁴⁸ J. P. Perdew, K. Burke, M. Ernzerhof, *Phys. Rev. Lett.*, 1996, *77*, 3865-3868; J. P. Perdew, K. Burke, M. Ernzerhof, *Phys. Rev. Lett.*, **1997**, *78*, 1396. M. Ernzerhof, G. E. Scuseria, *J. Chem. Phys.* 1999, **110**, 5029-5036.

⁴⁹ A. D. Becke, *J. Chem. Phys.*, **1993**, *98*, 5648-5652.

⁵⁰ C. Adamo and V. Barone, *J. Chem. Phys.*, **1999**, *110*, 6158-6169.

⁵¹ Y. Zhao and D. G. Truhlar, *Theor. Chem. Acc.*, **2008**, *120*, 215-41.

$$\vartheta_{abc}^{STO}(xyz) = Nx^a y^b z^c e^{-\zeta r}$$

are not fitted for practical use (bielectronic integrals are too long to calculate) and it is more convenient to consider a linear combination of Gaussian Type Orbital (GTO):

$$\vartheta_{abc}^{GTO}(xyz) = Nx^a y^b z^c e^{-\zeta r^2}$$

in order to mimic STO orbitals. Each orbital is described by one (single zeta), two (double zeta), three (triple zeta) or four (quadruple zeta etc) functions and each function is composed of a linear combination of Gaussian. Generally *split-valence* basis sets are used, in this case the core-electrons are described by a single function (as they do not impact the chemistry) and valence electrons by a larger set. To describe the polarizability of atoms it is necessary to add polarization functions (functions of high angular momentum, usually **d** or **f** functions). This is important for atoms featuring lone pairs. For instance, if we consider the basis set used in this thesis:

- **Pople’s basis set:** the double zeta functions are noted X-YZg, with X the number of Gaussians used to describe the core orbitals, Y and Z are the number of Gaussians used to describe the valence orbitals. Polarization functions are noted * and diffusion functions (d) or +.

Ex: The 6-31G basis use core orbitals made of 6 Gaussians, and valence orbitals are described by two functions: one made of 3 Gaussians, and one made of a single one. The triple and quadruple zeta are noted 6-311G and 6-3111G respectively. 6-31+G(d) is completed with polarization and diffusion functions (for instance on C: 6-31G* also noted 6-31G(d,p) have a supplementary **d** function compared to 6-31G, 6-31+G has a very diffuse (low ζ value) supplementary **p** function).

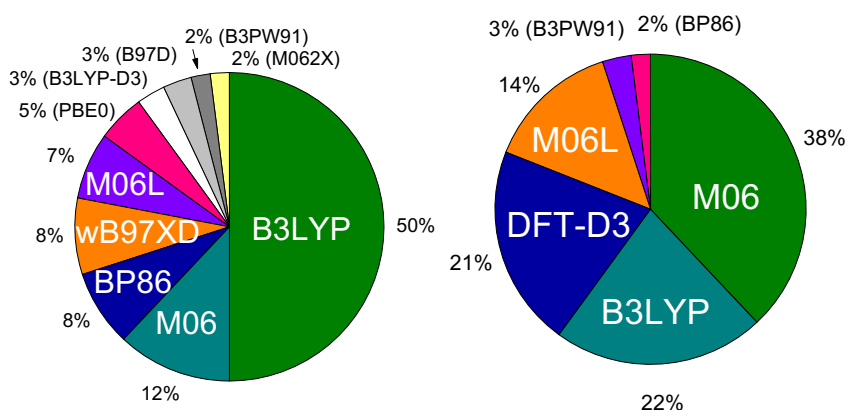
- **Karlsruhe basis set:** the second generation of these basis is noted ‘def2’, SV for split-valence, TZ for triple-zeta, QZ for quadruple-zeta. D for diffuse functions and P for polarization functions. The number of primitive Gaussians used by functions changes according to the atom described, ex: for the def2-SVP s orbitals, H-He: 3, Li-Ar: 5, K-Kr: 6. This basis set has associated pseudo-potentials for heavier atoms (*vide infra*).

Ex: def2-SVP (split-valence with polarization functions), def2-TZVP (valence triple-zeta with polarization functions).

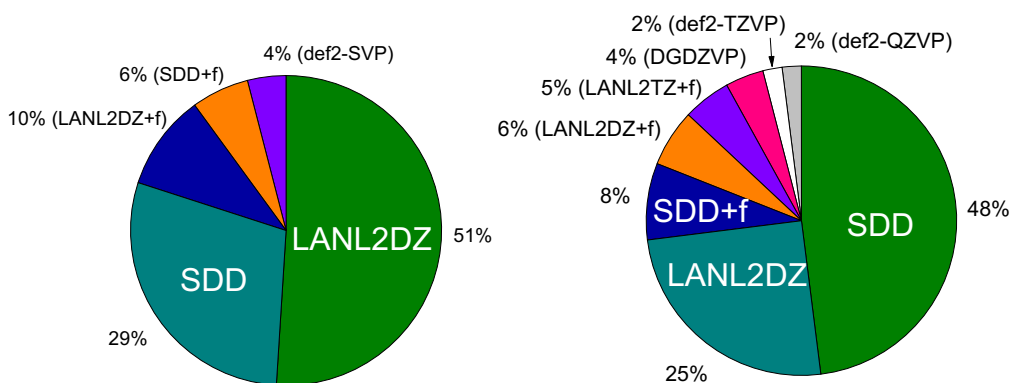
- **Effective Core Potential (ECP):** Core electrons have no direct impact on the chemical reactivity and are not significantly affected by the formation/breaking of chemical bonds. It is thus convenient to model core electrons by a fixed potential energy (the ECP). This approach allows also to take into account the relativistic effects that are non-negligible on core-electrons of heavy element. In CHAPTER II the Los Alamos effective core potential LANL2 has been used in combination with the corresponding basis set. In Chapter III the def2-SVP and TZVP associated with ECP have been used.

There are two classical ways to optimize the choice of the basis set and functional: using a set of experimental data or using high level theoretical calculations (for instance coupled-cluster methods, CCSD⁵²).⁵³

Alternatively, it may also be interesting to use the same level of theory as other groups working on similar systems, in order to allow meaningful comparisons between calculated data. For instance, the field of d⁷-d⁸ metal complexes (Pd, Ni, Rh, Ir) simulated by DFT has been reviewed by the group of F. Schoenebeck.⁵⁴ The most popular methods for geometric optimization and energy calculation are reported on **Scheme 15-16**.



Scheme 15 - Most popular functionals (2013-2014) employed for the geometric optimization (left) and energy estimation (right) of transition metal complexes (Pd, Ni, Rh, and Ir).⁵⁴



Scheme 16 - Most popular basis sets for metal (Pd, Ni, Rh, and Ir) employed (2013-2014) for the geometric optimization (left) and energy estimation (right) of transition metal complexes.⁵⁴

⁵² R. J. Bartlett, M. Musial, *Rev. Mod. Phys.*, **2007**, 79, 291-352; I. Shavitt, R. J. Bartlett, *Many-Body Methods in Chemistry and Physics: MBPT and Coupled-Cluster Theory*, **2009**, Cambridge University Press. For tutorial review on CCSD see: T. D. Crawford, H. F. Schaefer, (ed. K. B. Lipkowitz, D. B. Boyd) *An Introduction to Coupled Cluster Theory for Computational Chemists*, In *Reviews of Computational Chemistry*, **2000**, VCH Publishers; R. J. Bartlett, J. F. Stanton, *Applications of Post-Hartree-Fock Methods: A Tutorial*, *ibid*.

⁵³ See CHAPTER III, section 2.5.

⁵⁴ T. Sperger, I. A. Sanhueza, I. Kalvet, F. Schoenebeck, *Chem. Rev.*, **2015**, 115, 17, 9532-9586.

3.7. Empirical dispersion corrections⁵⁵

The older, GGA and hybrid functionals (B3LYP, BP86, etc) are known to poorly reproduce the structure and energy effect due to dispersion forces. This is not so surprising as these forces emerge mainly from electronic correlation.

The most commonly used dispersion correction is the one implemented by the group of Grimme (D3).⁵⁶ Several damping functions can be used in combination.⁵⁵ We used this correction in combination with the Becket-Johnson (BJ)⁵⁷ damping function and the BP86 and B3LYP functionals for the calculations performed of triflate and triflimide salts (see CHAPTER III). On the contrary, the metaGGA Minnesota functionals (*vide supra*), for instance the M06 ones, used for the calculations performed on transmetalation (CHAPTER II), are known to correctly described the dispersion interactions (thanks to higher parameterization) and do not require the use of additional dispersion correction.⁵⁸

The D3-BJ correction added to the total Hamiltonian is:

$$E_{disp} = - \sum_n^{nuclei} \sum_{m < n} \sum_{p=6,8} s_p \frac{C_p^{n,m}}{(R_{n,m})^p} f_{damp,p}(R_{n,m})^{BJ}$$

With $C_p^{n,m}$ the p -order dispersion coefficient and s_p the scaling factor, the BJ damping factor ($f_{damp,p}(R_{n,m})^{BJ}$) is expressed as follows:

$$f_{damp,p}(R_{n,m})^{BJ} = \frac{s_p (R_{n,m})^p}{(R_{n,m})^p + (a_1 R_{n,m}^0 + a_2)^p}$$

With s_p , a_1 and a_2 adjustable parameters.

The group of Grimme has recently proposed a density-dependent dispersion correction (taking into account the charge change between the reference compound and the calculated one) named D4.⁵⁹ This correction is supposed to be much more accurate particularly in the case of metal based compounds but has a higher computational cost.

3.8. Modelization of solvent effects

Taking into account in a cost-efficient way the solvation effects using DFT is a real problem. The most accurate way is to implicitly add solvent molecules, this has though a very high computational cost. An alternative approach is to model the solvent as a polarizable dielectric continuum (PCM).⁶⁰

⁵⁵ For tutorial review on this subsection see: S. Grimme, *WIREs Comput. Mol. Sci.*, **2011**, *1*, 211–228.

⁵⁶ S. Grimme, J. Antony, S. Ehrlich, H. Krieg, *J. Chem. Phys.*, **2010**, *132*, 154104.

⁵⁷ S. Grimme, S. Ehrlich, L. Goerigk, *J. Comput. Chem.*, **2011**, *32*, 1456–1465.

⁵⁸ Y. Zhao, D. G. Truhlar, *J. Chem. Phys.*, **2006**, *125*, 194101.

⁵⁹ E. Caldeweyher, C. Bannwarth, S. Grimme, *J. Chem. Phys.*, **2017**, *147*, 034112.

⁶⁰ J. Tomasi, B. Mennucci, R. Cammi, *Chem. Rev.*, **2005**, *105*, 8, 2999-3094.

However, this approach is limited to the description of electrostatic effects: specific solvent effects such as chemical bond (hydrogen bond, donor or acceptor effect, etc) cannot be described as well as the entropic effects (*vide infra*) due to the solvent organization. Quantities such as solvation energy,⁶¹ redox electrochemical potential,⁶² rate of electron transfer,⁶³ association and dissociation energy⁶⁴ etc are not evaluated correctly using this model.

Another issue is that using a PCM increases the calculation time, particularly for the estimation of the vibration modes (the analytical calculation of vibration with a PCM is not possible, one needs to use a numerical resolution much more time-consuming). It is possible to perform the geometric optimization and frequencies calculation in vacuum and to add the electronic energy calculated with a PCM with a single point calculation (see CHAPTER III).

3.9. Calculation of thermodynamic parameters

The first information one wants to extract from a calculated reaction pathways are the enthalpies and free energies corresponding to each step. For each optimized structure, it is easy to obtain the standard enthalpies of formation starting from the separated atoms in gas phase. The evaluation of the free energy is more challenging.

To access the entropic contribution to the free energy, it is necessary to estimate the number of microstates (i.e. translational, rotational and vibrational states, excited electronic levels are usually non-accessible at classical temperatures) accessible for a molecule at a given temperature, entropy (S) is given (in gas phase) by:

$$S = R \ln(q) + RT \left(\frac{\partial \ln(q)}{\partial T} \right)_v$$

with T the temperature and R the gas constant. It is convenient to express the entropy as a function of the partition function (q) of the system:

$$q = \sum_i^{\mu\text{-states}} e^{-E_i}$$

Were E_i is the energy of the i microstate. The function partition can be decomposed as a product of the different contributions (translation, rotation, vibration):

$$q = q_{\text{trans}} q_{\text{rot}} q_{\text{vib}}$$

⁶¹ J. Zhang, H. Zhang, T. Wu, Q. Wang, D. van der Spoel, *J. Chem. Theory Comput.*, **2017**, *133*, 1034-1043

⁶² Y. Shimodaira, T. Miura, A. Kudo, H. Kobayashi, *J. Chem. Theory Comput.*, **2007**, *3*, 789-795; P. Jaque, A. V. Marenich, C. J. Cramer, D. G. Truhlar, *J. Phys. Chem. C*, **2007**, *111*, 15, 5783-5799; M. Uudsemaa, T. Tamm, *J. Phys. Chem. A*, **2003**, *107*, 46, 9997-10003.

⁶³ G. Jeanmairet, B. Rotenberg, M. Levesque, D. Borgis and M. Salanne, *Chem. Sci.*, **2019**, *10*, 2130-2143; K. M. Rosso, J. R. Rustad, *J. Phys. Chem. A*, **2000**, *104*, 29, 6718-6725.

⁶⁴ R. J. Deeth, L. I. Elding, *Inorg. Chem.*, **1996**, *35*, 17, 5019-5026; J. E. Park, Y. K. Kang, *Bull. Korean Chem. Soc.*, **2016**, *37*, 1057-1063.

that can be expressed as follows (using the classical approximations: rigid rotor for rotation and harmonic oscillator (*vide supra*) for vibration):

$$q_{trans} = \left(\frac{2\pi mk_b T}{h^2}\right)^{\frac{3}{2}} V; q_{rot} = \sqrt{\pi}/\sigma_r \left(\frac{T^{\frac{3}{2}}}{\sqrt{\theta_{r,x}\theta_{r,y}\theta_{r,z}}}\right); q_{vib} = \sum_k^{vibration} \frac{1}{1-e^{-\theta_{v,k}/T}}$$

with V the volume, σ_r the rotational symmetry numbers, $\theta_{r,i}$ the rotational temperatures, $\theta_{v,k}$ the vibrational temperatures associated to a vibration mode k (see section 3.2).

These formulae however are correct only under gas phase conditions (no intermolecular contribution, no solvent contribution, etc), thus leading to an overestimation of the entropic energies. Several corrections have been proposed such as taking only a fixed fraction of the calculated entropy.

3.10. Charge and bond analyses⁶⁵

It is of primordial importance for the theoretical chemist to translate the electronic density information in terms of familiar Lewis concepts (charge, bond etc). The simplest approach for this is the Mulliken charge calculation. Let us consider a polyelectronic wave function ($|\Phi(r_i)\rangle$) constituted of a single Slater determinant in which each mono-electronic ($\varphi_i(r_i)$) wave function can be developed on a set of atomic orbitals ($\vartheta_{i,j}$):

$$|\Phi(r_i)\rangle = |\varphi_i(r_i)\rangle$$

$$\varphi_i(r_i) = \sum_j c_{i,j} \vartheta_{i,j}$$

The number of electrons n is given by:

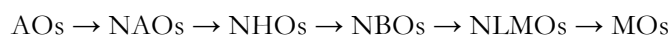
$$n = \sum_i^{e^-} \left(\sum_j c_{i,j}^2 + 2 \sum_{j<k} c_{i,j} c_{i,k} S_{i,j,k} \right)$$

In this expression $c_{i,j}^2$ corresponds to the electronic density located on the j atom, while $c_{i,j} c_{i,k} S_{i,j,k}$ is shared between atoms j and k . Mulliken hypothesized that this term can be equally attributed to both atoms. This hypothesis is of course counterintuitive with respect to electronegativity and actually leads to inconsistent results (basis-set dependent, etc). To solve the partition problem of shared electrons it is convenient to use another localized *orthogonal* basis-set.⁶⁶

Starting from a set of Atomic Orbitals (AOs), it is possible to construct several orthogonal sets of orbitals, from the more to the less localized: Natural Atomic Orbitals (NAO), Natural Hybrid Orbitals (NHO), *Natural Bonding Orbitals* (NBO), Natural Localized Molecular Orbitals (NLMO) sets and finally the molecular orbitals (MOs).

⁶⁵ For a tutorial review see : F. Weinhold and C. R. Landis, *Chem. Educ. Res. Pract.*, **2001**, 2, 2, 91-104.

⁶⁶ P. O. Löwdin, *J. Chem. Phys.*, **1950**, 18, 365-375.

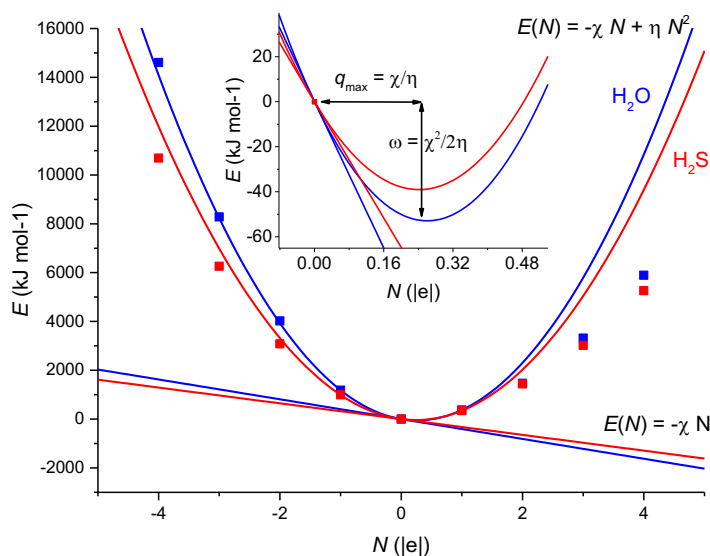


The NBO set of orthogonal orbitals is close to the Lewis description of a molecular system while the NAO set is localized on the atoms. In the Natural Population (charge) Analysis (NPA) the partial charges are obtained from the NAO set of orbitals.⁶⁷

3.11. Indicators of chemical reactivity: electronegativity, global and local hardness, Fukui functions and global electrophilicity index⁶⁸

The role of chemical reactivity indicators is to evaluate the impact of the approach of a nucleophile or of an electrophile on the energy of the system and on the spatial repartition of the electronic density.

Ideally, the approach of a nucleophile (respectively of an electrophile) can be mimicked by addition (respectively withdrawal) of electrons to the system. The chemical reactivity of molecular systems can thus be characterized by the plot of the electronic energy (at a given geometry) as a function of the total number of electrons in the system (**Scheme 17**).



Scheme 17 – Electronic energy E (kJ mol^{-1}) of H_2O (blue) and H_2S (red) as a function of the number of electrons added to the system (N , compared to the neutral compound), calculated at the PBE0/def2-SVP level.

The electronegativity (χ , $\text{kJ mol}^{-1} |e|^{-1}$) of the system is the trend of the compound to attract electrons thus it is proportionate to the first-derivate of this curve (energetic gain upon addition of electrons):

$$\chi = -\left(\frac{\partial E}{\partial N}\right)_v$$

⁶⁷ A. E. Reed, R. B. Weinstock, F. Weinhold, *J. Chem. Phys.*, **1985**, *83*, 735-746.

⁶⁸ H. Chermette, *J. Comput. Chem.*, **1999**, *20*, 129-154.

The global hardness (η , kJ mol⁻¹ |e|⁻²) of the system is the trend of the system to resist to a charge variation, thus it is proportionate with the curvature (second derivate) of the $E(N)$ plot i.e.:

$$\eta = \frac{1}{2} \left(\frac{\partial^2 E}{\partial N^2} \right)_v$$

Electronegativity and hardness are supposed to compensate each other at the minimal energy of the curve corresponding also to the highest authorized number of electrons (ΔN_{max}):

$$E(N) \approx -\chi N + \eta N^2$$

$$\Delta N_{max} = \chi/2\eta ; \omega \propto \Delta E_{max} = \frac{\chi^2}{4\eta}$$

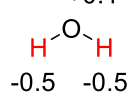
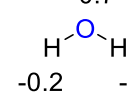
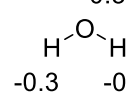
The energetic gain is called the global electrophilicity index (ω , kJ mol⁻¹) and quantifies the natural trend of a system to attract electrons (taking into account the hardness). For instance, the numerical values of these indicators are given in **Table 5** for H₂O and H₂S for comparison.

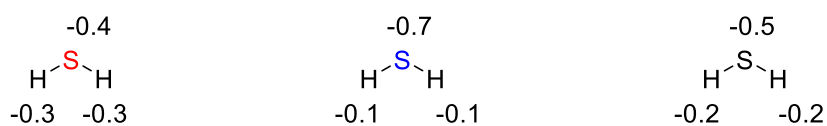
Table 5 – Electronegativity (χ , kJ mol⁻¹ |e|⁻¹), hardness (ω , kJ mol⁻¹ |e|⁻²), highest number of electrons (ΔN_{max} , |e|) and global electrophilicity index (ω , kJ mol⁻¹), calculated at the PBE0/def2-SVP level.

	χ	η	ΔN_{max}	ω
H ₂ O	406	779	0.26	52
H ₂ S	323	668	0.24	39

It is also interesting to study the local variation of electronic density upon addition (or withdrawal) of electron, the variation will give us information about the electrophilic (or nucleophilic) site of the molecular entities. The charge variations on an atom are called the Fukui functions (f), the most important local variation of the charge upon addition of an electron ($f^+(\vec{r})$) corresponds to the electrophilic site while the most important local variation upon subtraction of an electron ($f^-(\vec{r})$) corresponds to the nucleophilic sites. For instance, oxygen atom appears to be the nucleophilic site of water while hydrogens are electrophilic (**Table 6**).

Table 6 – Fukui functions of H₂O and H₂S (calculated from Mulliken charges, at the PBE0/def2-SVP level).

$f^+(\vec{r})$ = $\rho_{N+1}(\vec{r}) - \rho_N(\vec{r})$	$f^-(\vec{r})$ = $\rho_N(\vec{r}) - \rho_{N-1}(\vec{r})$	$f^0(\vec{r})$ = $\frac{\rho_{N+1}(\vec{r}) - \rho_{N-1}(\vec{r})}{2}$
Electrophilicity	Nucleophilicity	Interaction with radical
+0.1 	-0.7 	-0.3 



By extension of the ideas exposed above it is possible to define also a local softness (global softness is simply defined as the reciprocal of hardness, *ie*: $S = 1/\eta$) as the product of the “neutral” Fukui function with the global softness:

$$s = f^0(\vec{r})S$$

The local softness (s) is the softness of a single atom in a molecular entity. For instance, for H₂O and H₂S:



3.12. Conclusion

The experimental methods and theoretical tools introduced in this first chapter are applied in the case studies presented in CHAPTER II and III. The theoretic indicators of reactivity are particularly discussed in the second section of CHAPTER III, while all the other techniques are used in combination to solve several mechanisms. The mechanistic conclusions are used to solve the experimental issues encountered in practical synthesis.

CHAPTER II

Boron-to-Transition-Metals Transmetalation:

Mechanistic Studies

“Oui, j’ai été forcé d’amincir la chose et d’être mensonger, mais ce n’est pas un univers, c’est des millions, presque autant qu’il existe de prunelles et d’intelligences humaines qui s’éveillent tous les matins”

M. Proust, A la recherche du temps perdu (V)

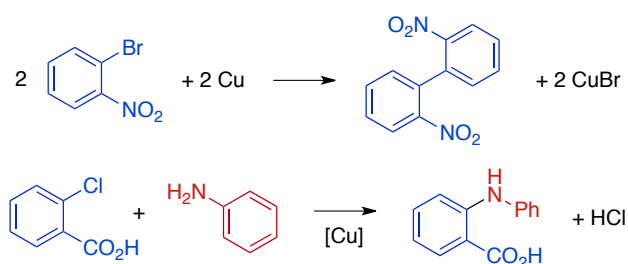
The work exposed in this chapter resulted in the following publication:

P. A. Payard, L. A. Perego,* I. Ciofini, L. Grimaud,*
*Taming Nickel-Catalyzed Suzuki-Miyaura Coupling: A Mechanistic Focus on Boron-to-Nickel
Transmetalation,*
ACS Catal., **2018**, 8 (6), 4812–4823

1. Context of the Study

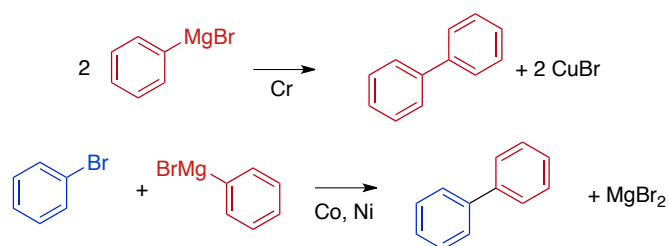
1.1. Transition-Metal Catalyzed Coupling Reactions

Coupling reactions involve a single (homocoupling) or two different (cross-coupling) starting materials that are reacted together to obtain a condensation product with the formation of a new covalent bond between the fragments. At the beginning of the last century, Ullmann and Goldberg reported the first examples of coupling reactions using copper as a catalyst (**Scheme 18**).⁶⁹ These reactions, however, raised only little interest due to the use of a stoichiometric amount of metal.



Scheme 18 – Copper-catalyzed Ullmann homocoupling of aryl bromide and copper-catalyzed amination.

The first observation of metal-*catalyzed* homocoupling reaction was made by Bennett and Turner in 1914: they serendipitously evidenced the decomposition of PhMgI in the presence of chromium(III) chloride (**Scheme 19**).⁷⁰ The first description of a metal-catalyzed *cross*-coupling (the reaction of an aryl halide with a Grignard derivative catalyzed by Co or Ni, later called the Corriu-Kumada coupling) was made by Kharasch in 1941 (**Scheme 19**).⁷¹



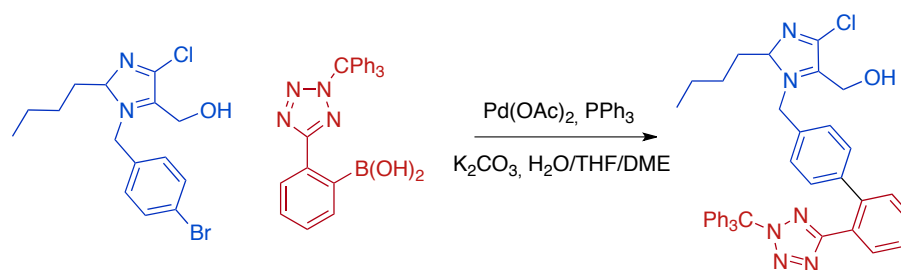
Scheme 19 – Early examples of transition-metal-catalyzed homo and cross-coupling reactions.

⁶⁹ F. Ullmann, J. Bielecki, *Ber. Dtsch. Chem. Ges.*, **1901**, *34*, 2174-2185; F. Ullmann, *Ber. Dtsch. Chem. Ges.*, **1903**, *36*, 2382-2384.; F. Ullmann, P. Sponagel, *Ber. Dtsch. Chem. Ges.*, **1905**, *38*, 2211-2212; I. Goldberg, *Ber. Dtsch. Chem. Ges.*, **1906**, *39*, 1691-1692.

⁷⁰ G. Bennett, E. Turner, *J. Chem. Soc., Trans.*, **1914**, 105, 1057-1062; H. Gilman, M. Lichtenwalter, *J. Am. Chem. Soc.*, **1939**, *6*, 14957-14959.

⁷¹ M. S. Kharasch, E. K. Fields, *J. Am. Chem. Soc.*, **1941**, *63*, 2316-232033; R. J. P. Corriu, J. P. Masse, *J. Chem. Soc., Chem. Commun.*, **1972**, 144a-144a; K. Tamao, K. Sumitani, M. Kumada, *J. Am. Chem. Soc.*, **1972**, *94*, 4374-4376.

The major breakthrough in the area was due to the development in the 70's of the Pd-catalyzed cross-coupling reactions. Heck-Mizoroki coupling using alkene in 1968-1973,⁷² Negishi coupling using an organozinc derivative in 1976-77,⁷³ and finally Suzuki-Miyaura coupling using boron derivatives in 1979⁷⁴ have led to a spectacular expansion of the field in the 80-90's. Various and efficient methodologies for the formation of C-C, C-O and C-N bonds have been settled.⁷⁵ Suzuki, Heck and Negishi were awarded with the Nobel Prize in 2010 for the development of Pd-catalyzed C-C bond formations,⁷⁶ these reactions have become staple in the organic chemist toolbox and are widely applied at the industrial scale especially for medicinal chemistry. In particular, the Suzuki-Miyaura cross-coupling has been applied to the industrial synthesis of the anti-hypertension drug Cozaar™ as early as in the 90's (Scheme 20).⁷⁷ It belongs in the top 10 of reactions used in the pharmaceutical industry.



Scheme 20 - Last step of the industrial synthesis of Lersatan (Cozaar™).

The palladium-catalyzed Suzuki-Miyaura (S-M) cross-coupling, involving an organoboron reagent and an organic halide (or pseudohalide), is one of the most widely used reactions for the formation of C-C bonds.⁷⁸ This transformation tolerates a broad range of experimental conditions, as it proceeds well with a large array of catalysts, bases, and solvents (Scheme 21).

⁷² T. Mizoroki, K. Mori, A. Ozaki, *Bull. Chem. Soc. Jpn.*, **1971**, *44*, 581; K. Mori, T. Mizoroki, A. Ozaki, *Bull. Chem. Soc. Jpn.*, **1973**, *46*, 1505-1508; R. F. Heck, *J. Am. Chem. Soc.*, **1968**, *90*, 5518-5526; R. F. Heck and J. P. Nolley, *J. Org. Chem.*, **1972**, *37*, 2320-2322.

⁷³ E. Negishi, S. Baba, *J. Chem. Soc., Chem. Commun.*, **1976**, 596b-597b; E. Negishi, A. O. King, N. Okukado, *J. Org. Chem.*, **1977**, *42*, 1821-1823; A. O. King, N. Okukado, E. Negishi, *J. Chem. Soc., Chem. Commun.*, **1977**, *19*, 683-684; J. F. Fauvarque, A. Jutand, *J. Organomet. Chem.*, **1977**, *132*, C17-C19.

⁷⁴ N. Miyaura, A. Suzuki, *J. Chem. Soc., Chem. Commun.*, **1979**, *19*, 866-867.

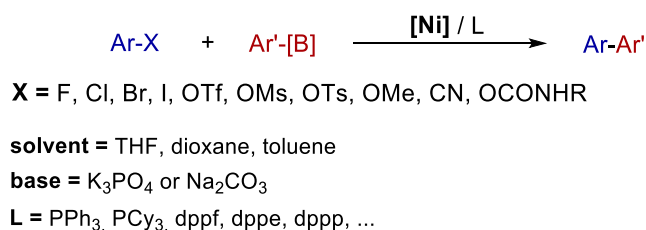
⁷⁵ Thomas Colacot, *New Trends in Cross-Coupling: Theory and Applications*, RSC publishing: Cambridge, UK, **2014**; Armin de Meijere, François Diederich, *Metal-Catalyzed Cross-Coupling Reactions*, Wiley-VCH, Verlag GmbH: Weinheim, Germany, **2004**.

⁷⁶ Thomas J. Colacot, *Platinum Metals Rev.*, **2011**, *55*, 84-90

⁷⁷ R. D. Larsen, A. O. King, C. Y. Chen, E. G. Corley, B. S. Foster, F. E. Roberts, C. Yang, D. R. Lieberman, R. A. Reamer, *J. Org. Chem.*, **1994**, *59*, 6391-6394.

⁷⁸ N. Miyaura, A. Suzuki, *Chem. Rev.*, **1995**, *95*, 2457-2483; E. Negishi, *Handbook of Organopalladium Chemistry for Organic Synthesis*; John Wiley & Sons, **2002**; A. Suzuki, *J. Organomet. Chem.*, **2002**, *653*, 83-90; N. Miyaura, In *Cross-Coupling Reactions: A Practical Guide*, Springer, **2002**; A. de Meijere, F. Diederich, *Metal-Catalyzed Cross-Coupling Reactions*, Wiley-VCH, **2004**; F. Bellina, A. Carpita, R. Rossi, *Synthesis*, **2004**, *2004*, 2419-2440; R. Martin, S. L. Buchwald, *Acc. Chem. Res.* **2008**, *41*, 1461-1473; H. Li, C. C. C. Johansson Seechurn, T. J. Colacot, *ACS Catalysis* **2012**, *2*, 1147-1164; C. C. C. Johansson Seechurn, M. O. Kitching, T. J. Colacot, V. Snieckus, *Angew. Chem. Int. Ed.* **2012**, *51*, 5062-5085; R. Rossi, F. Bellina, M. Lessi, C.

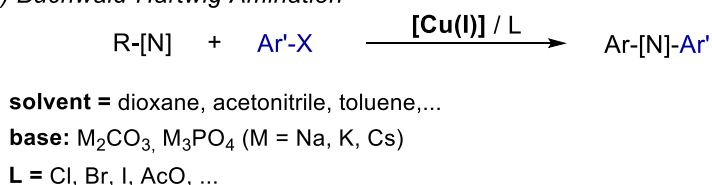
without the need of expensive ligands.⁹¹



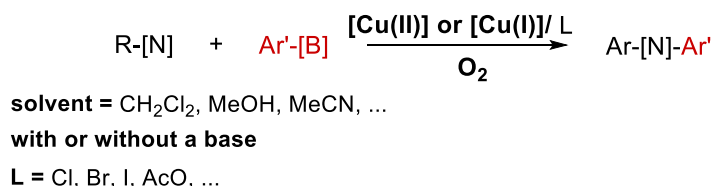
Scheme 22 - Nickel-Catalyzed Suzuki-Miyaura Cross-Coupling: Typical conditions

Despite these undeniable advantages, the nickel-catalyzed S-M coupling is still much less used in practical synthesis than the Pd-catalyzed version, probably due to its reputation of erratic performances. Indeed, Ni-catalyzed S-M reactions generally require high catalyst loading (3-10 mol%) and they are quite sensitive to the reaction conditions. The choice of the base/solvent combination is crucial:⁹² in most cases either THF, dioxane or toluene must be used in conjunction with scarcely soluble inorganic bases, such as K₃PO₄ or K₂CO₃. Conversely, alkali hydroxides and excessive amounts of water seem to deactivate nickel catalysts. To the best of our knowledge, the reasons for this behavior are still unknown.

a) *Buchwald-Hartwig Amination*



b) *Chan-Evans-Lam Amination*



Scheme 23 – Copper-Catalyzed Cross-Coupling Reactions

Another challenger of Pd for cross-coupling reaction is Cu: with large availability and low toxicity Cu may be of particular interest as a catalyst for cross-coupling reactions.⁹³ The first examples of Cu-catalyzed Suzuki Cross-coupling appeared in the literature in 2000 and 2006: Cu-based

⁹¹ S. Z. Tasker, E. A. Standley, T. F. Jamison, *Nature* **2014**, *509*, 299-309; S. Ge, J. F. Hartwig, *Angew. Chem. Int. Ed.*, **2012**, *51*, 12837-12841.

⁹² S. Ge, J. F. Hartwig, *Angew. Chem. Int. Ed.* **2012**, *51*, 12837-12841.

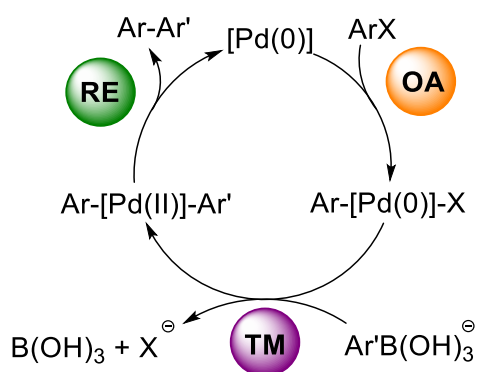
⁹³ C. Maaliki, E. Thiery, J. Thibonnet, *Eur. J. Org. Chem.*, **2017**, 209-228; Adiel Coca, *Boron Reagents in Synthesis*, **2016**, chapter 10, Oxford Univ Press; S. Thapa, B. Shrestha, S. K. Gurunga, R. Giri, *Org. Biomol. Chem.*, **2015**, *13*, 4816-4827.

clusters,⁹⁴ Cu^I(DABCO)⁹⁵ were proved to catalyze the coupling of a limited scope of aryl boronic acids with aryl halides. Liu and collaborator, using the catalytic system Cu^I/LiOtBu, extended the reaction scope to boronate ester with primary,⁹⁶ secondary, and tertiary halides and pseudo-halides.⁹⁷

It seems also that new selectivities and reactivities could be achieved through the use of Cu. For instance, a Cu-catalyzed sulfonylative Suzuki–Miyaura cross-coupling have been recently described, which was not accessible using Pd or Ni.⁹⁸ Finally, in 2014–2015 the activation of C–O and C–S bonds using Cu(OTf)₂ and Cu(OAc)₂ were also reported.⁹⁹

1.2. Generalities on the mechanism of the Suzuki–Miyaura cross-coupling reaction

The textbook mechanism for palladium-catalyzed S–M coupling (**Scheme 24**) includes three steps: oxidative addition (OA), transmetalation (TM) and reductive elimination (RE).¹⁰⁰



Scheme 24 – Textbook mechanism for the palladium-catalyzed S–M coupling.

Two alternative pathways have been proposed so far for the nickel-catalyzed S–M coupling (**Scheme 25**). A Ni(0)/Ni(II) mechanism involving OA first, followed by TM and RE, is generally put forward (**Scheme 25**, a), in analogy to what is usually claimed for the palladium catalyzed reaction.¹⁰¹

⁹⁴ M. B. Thathagar, J. Beckers, G. Rothenberg, *J. Am. Chem. Soc.*, **2002**, *124*, 11858–11859; M. Thathagar, J. Beckers, G. Rothenberg, *Adv. Synth. Catal.*, **2003**, *345*, 979–985.

⁹⁵ J.-H. Li, J.-L. Li, D.-P. Wang, S.-F. Pi, Y.-X. Xie, M.-B. Zhang, and X.-C. Hu, *J. Org. Chem.*, **2007**, *72*, 2053–2057

⁹⁶ C.-T. Yang, Z. Q. Zhang, Y.-C. Liu, L. Liu, *Angew. Chem. Int. Ed.*, **2011**, *50*, 3904–3907

⁹⁷ G.-Z. Wang, J. Jiang, X.-S. Bu, J.-J. Dai, J. Xu, Y. Fu, H.-J. Xu, *Org. Lett.* **2015**, *17*, 3682–3685.

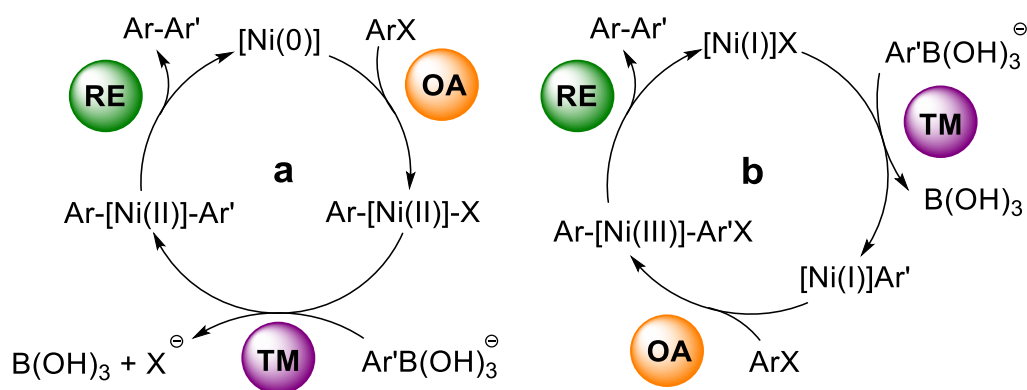
⁹⁸ Y. Chena, M. C. Willis, *Chem. Sci.*, **2017**, *8*, 3249–3253.

⁹⁹ H. S. P. Rao, A. V. B. Rao, *Eur. J. Org. Chem.* **2014**, 3646–3655; H. S. P. Rao, A. V. B. Rao, *J. Org. Chem.* **2015**, *80*, 1506–1516.

¹⁰⁰ D. V. Partyka, *Chem. Rev.*, **2011**, *111*, 1529–1595; A. J. J. Lennox, G. C. Lloyd-Jones, *Angew. Chem. Int. Ed.*, **2013**, *52*, 7362–7370.

¹⁰¹ S. Ge, J. F. Hartwig, *Angew. Chem. Int. Ed.*, **2012**, *51*, 12837–12841; S. Saito, S. Oh-tani, N. Miyaura, *J. Org. Chem.*, **1997**, *62*, 8024–8030; S. Saito, M. Sakai, N. Miyaura, *Tetrahedron Lett.*, **1996**, *37*, 2993–2996; A. H. Christian, P. Müller, S. Monfette, *Organometallics* **2014**, *33*, 2134–2137; J. Magano, S. Monfette, *ACS*

Nevertheless, Louie and co-workers¹⁰² have recently proposed a Ni(I)/Ni(III) cycle for N-heterocyclic carbene-ligated nickel(I) catalyst (**Scheme 25**, b). They showed that in this case TM occurs before OA. A computational study reported by Lin *et al.* also corroborates these findings.¹⁰² By contrast, a very recent study demonstrated that for S-M reactions performed using a bidentate phosphine-ligated Ni catalyst the formation of Ni(I) species is detrimental to the catalyst efficiency and the reaction proceeds *via* a Ni(0)/Ni(II) cycle.¹⁰³



Scheme 25 - Proposed mechanisms for the Ni-catalyzed S-M coupling, a. Ni(0)-Ni(II) cycle; b. Ni(I)-Ni(III) cycle.

For both Pd and Ni-catalyzed coupling the TM step is generally the rate determining one, thus it is of primordial interest to understand it perfectly.

1.3. The Palladium-to-Boron Transmetallation Step

The mechanism of Pd-to-B transmetallation has been investigated both experimentally¹⁰⁴ and theoretically.¹⁰⁵ The first mechanistic study focusing on the Pd-to-B transmetallation step was

Catal., **2015**, *5*, 3120-3123; E. A. Standley, S. J. Smith, P. Müller, T. F. Jamison, *Organometallics*, **2014**, *33*, 2012-2018.

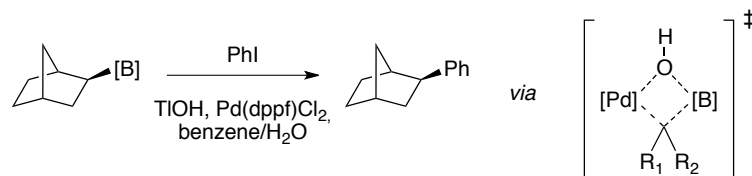
¹⁰² K. Zhang, M. Conda-Sheridan, S. R. Cooke, J. Louie, *Organometallics* **2011**, *30*, 2546-2552.

¹⁰³ M. Mohadjer Beromi, A. Nova, D. Balcells, A. M. Brasacchio, G. W. Brudvig, L. M. Guard, N. Hazari, D. J. Vinyard, *J. Am. Chem. Soc.* **2017**, *139*, 922-936.

¹⁰⁴ A. O. Aliprantis, J. W. Canary, *J. Am. Chem. Soc.* **1994**, *116*, 6985-6989; K. Matos, J. A. Soderquist, *J. Org. Chem.*, **1998**, *63*, 461-470; C. M. Nunes, A. L. Monteiro, *J. Brazilian Chem. Soc.*, **2007**, *18*, 1443-1447; C. Adamo, C. Amatore, I. Ciofini, A. Jutand, H. Lakmini, *J. Am. Chem. Soc.*, **2006**, *128*, 6829-6836; C. Sicre, A. A. C. Braga, F. Maseras, M. M. Cid, *Tetrahedron*, **2008**, *64*, 7437-7443; M. Butters, J. N. Harvey, J. Jover, A. J. J. Lennox, G. C. Lloyd-Jones, P. M. Murray, *Angew. Chem. Int. Ed.*, **2010**, *49*, 5156-5160; C. Amatore, A. Jutand, G. Le Duc, *Chem. Eur. J.*, **2011**, *17*, 2492-2503; B. P. Carrow, J. F. Hartwig, *J. Am. Chem. Soc.*, **2011**, *133*, 2116-2119; C. Amatore, A. Jutand, G. Le Duc, *Chem. Eur. J.*, **2012**, *18*, 6616-6625; C. Amatore, A. Jutand, G. Le Duc, *Angew. Chem.*, **2012**, *124*, 1408-1411; C. Amatore, A. Jutand, G. Le Duc, *Angew. Chem. Int. Ed.*, **2012**, *51*, 1379-1382; C. Amatore, G. Le Duc, A. Jutand, *Chem. Eur. J.*, **2013**, *19*, 10082-10093; J. W. B. Fyfe, E. Valverde, C. P. Seath, A. R. Kennedy, J. M. Redmond, N. A. Anderson, A. J. B. Watson, *Chem. Eur. J.*, **2015**, *21*, 8951-8964; A. A. Thomas, S. E. Denmark, *Science*, **2016**, *352*, 329-332; A. A. Thomas, H. Wang, A. Zahrt, S. E. Denmark, *J. Am. Chem. Soc.*, **2017**, *139*, 3805-3821; J. Kohlmann, T. Braun, R. Laubenstein, R. Herrmann, *Chem. Eur. J.*, **2017**, *23*, 12218-12232.

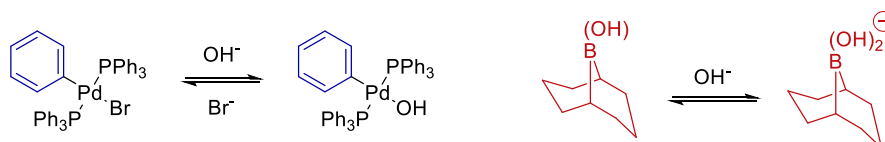
¹⁰⁵ K. W. Quasdorf, M. Riener, K. V. Petrova, N. K. Garg, *J. Am. Chem. Soc.*, **2009**, *131*, 17748-17749; L. J. Goossen, D. Koley, H. L. Hermann, W. Thiel, *J. Am. Chem. Soc.*, **2005**, *127*, 11102-11114; A. A. C. Braga, N. H. Morgon, G. Ujaque, F. Maseras, *J. Am. Chem. Soc.*, **2005**, *127*, 9298-9307; L. J. Goossen, D. Koley,

published by Matos and Soderquist in 1998.¹⁰⁶ They evidenced configuration retention in the transmetalation step (**Scheme 26**). This observation suggested that TM took place through a concerted mechanism involving a four-membered ring transition state (**Scheme 26**, inset).



Scheme 26 – Retention of configuration in Pd-to-B TM (ref. *J. Org. Chem.* **1998**, *63*, 461-470.)

They were also the first to tackle the problem of the role displayed by the base in the TM step. Indeed, it has long been noticed¹⁰⁷ that a base (M_2CO_3 , M_3PO_4 , MOH, MF, etc with $M = Na, K, Cs$)¹⁰⁸ was necessary for the TM to proceed. Matos and Soderquist evidenced the formation of Aryl-Pd intermediates featuring hydroxo ligands (**Scheme 27**). In the meantime, hydroxo are also involved in the equilibrium between boronic and boronate derivatives (**Scheme 27**).



Scheme 27 – Pre-transmetalation equilibria involving hydroxides (ref. *J. Org. Chem.* **1998**, *63*, 461-470.)

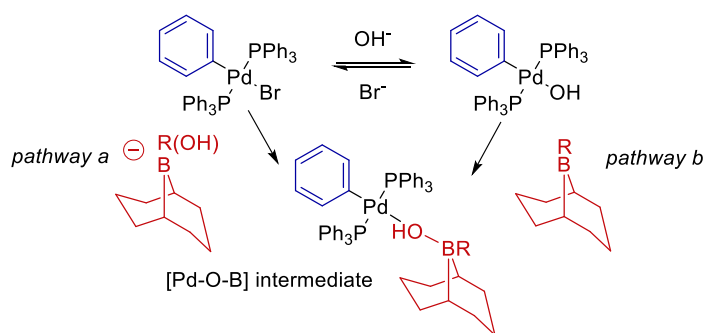
Based on these observations they proposed that the base could be necessary to access a crucial [Pd-O-B] intermediate (**Scheme 28**) either through the direct substitution of bromide with boronate (*pathway a*) or through the association of boronic acid on [Pd-OH] (*pathway b*).

H. L. Hermann, W. Thiel, *Organometallics*, **2006**, *25*, 54-67; A. A. C. Braga, G. Ujaque, F. Maseras, *Organometallics*, **2006**, *25*, 3647-3658; H. Lakmini, I. Ciofini, A. Jutand, C. Amatore, C. Adamo, *J. Phys. Chem. A*, **2008**, *112*, 12896-12903; Y.-L. Huang, C. -M. Weng, F.-E. Hong, *Chem. Eur. J.*, **2008**, *14*, 4426-4434; J. Jover, N. Fey, M. Purdie, G. C. Lloyd-Jones, J. N. Harvey, *J. Mol. Catal. A: Chem.*, **2010**, *324*, 39-47; M. García-Melchor, A. A. C. Braga, A. Lledós, G. Ujaque, F. Maseras, *Acc. Chem. Res.*, **2013**, *46*, 2626-2634; M. A. Ortuño, A. Lledós, F. Maseras, G. Ujaque, *ChemCatChem*, **2014**, *6*, 3132-3138; G. Audran, P. Brémond, S. R. A. Marque, D. Siri, M. Santelli, *Tetrahedron*, **2014**, *70*, 2272-2279.

¹⁰⁶ K. Matos, J. A. Soderquist, *J. Org. Chem.*, **1998**, *63*, 461-470.

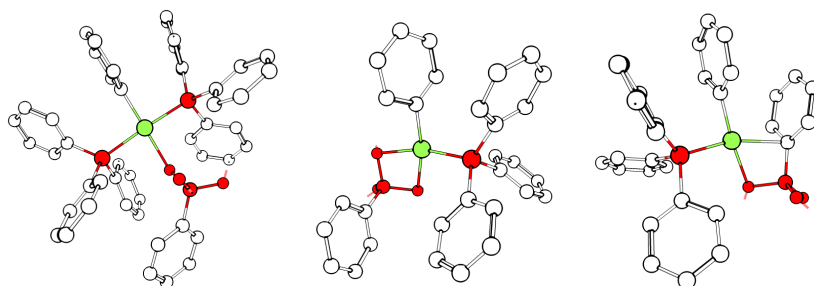
¹⁰⁷ N. Miyaura, T. Yanagi, A. Suzuki, *Synth. Commun.*, **1981**, *11*, 513-519.

¹⁰⁸ T. Watanabe, N. Miyaura, A. Suzuki, *Synlett*, **1992**, 207-210.



Scheme 28 – Formation of [Pd-O-B] intermediate (ref. *J. Org. Chem.*, **1998**, *63*, 461-470.)

This hypothesis was independently confirmed in 2005 by the teams of Maseras and Goossen using DFT calculations (**Scheme 29**).¹⁰⁹ Maseras and coll. compared the two pathways presented above using PH_3 as a phosphine but could not find any evidence any significant difference.¹¹⁰ The results obtained by Goossen *et al.* were consistent with the one obtained by Maseras but with a prior dissociation of one phosphine ligand from Aryl-Pd complex before TM (**Scheme 29**, b and c).¹¹¹ This result was later confirmed by DFT¹¹² and experiments⁴⁸ (see section II-2-3).



Scheme 29 – DFT-calculated structures of some critical intermediates for the TM reaction (Cartesian coordinates from *ChemCatChem* **2014**, *6*, 3132-3138, H omitted for clarity, B, O and P in red, Pd in green).

Later in 2011 Carrow *et al* proposed to differentiate experimentally between the two pathways (**Scheme 28**) using kinetics.¹¹³ They observed that aryl-Pd-OH complexes react rapidly with 10 equiv of PhB(OH)_2 while aryl-Pd-Br complexes react slowly with 10 equiv of PhB(OH)_3^- . However, this observation *does not* imply any differentiation between pathways since, the same year, Jutand and collaborators demonstrated that the *total* base concentration was the key parameter for the kinetic of transmetalation.¹¹⁴ The transmetalation process is deactivated at both low and high $\text{OH}/\text{PhB(OH)}_2$ ratios, the optimal ratio being found around 0.7 (**Figure 1**, note

¹⁰⁹ L. J. Goossen, D. Koley, H. L. Hermann, W. Thiel, *J. Am. Chem. Soc.*, **2005**, *127*, 11102-11114; A. A. C. Braga, N. H. Morgon, G. Ujaque, F. Maseras, *J. Am. Chem. Soc.*, **2005**, *127*, 9298-9307

¹¹⁰ A. A. C. Braga, N. H. Morgon, G. Ujaque, F. Maseras, *J. Am. Chem. Soc.*, **2005**, *127*, 9298-9307

¹¹¹ L. J. Goossen, D. Koley, H. L. Hermann, W. Thiel, *Organometallics*, **2006**, *25*, 54-67.

¹¹² A. A. C. Braga, G. Ujaque, F. Maseras, *Organometallics*, **2006**, *25*, 3647-3658; M. A. Ortuño, A. Lledós, F. Maseras, G. Ujaque, *ChemCatChem*, **2014**, *6*, 3132-3138.

¹¹³ B. P. Carrow, J. F. Hartwig, *J. Am. Chem. Soc.*, **2011**, *133*, 2116-2119

¹¹⁴ C. Amatore, A. Jutand, G. Le Duc, *Chem. Eur. J.*, **2011**, *17*, 2492-2503.

that the previous observation by Carrow *et al.* are thus included in this result). They also demonstrated a negative first order with respect to bromide anion which is in agreement with bromide dissociation being involved in the transmetalation process.

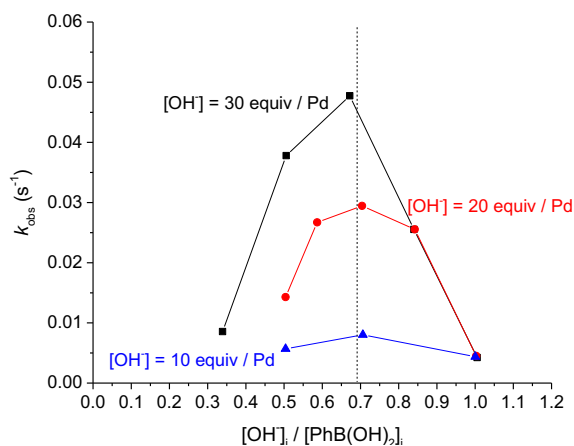
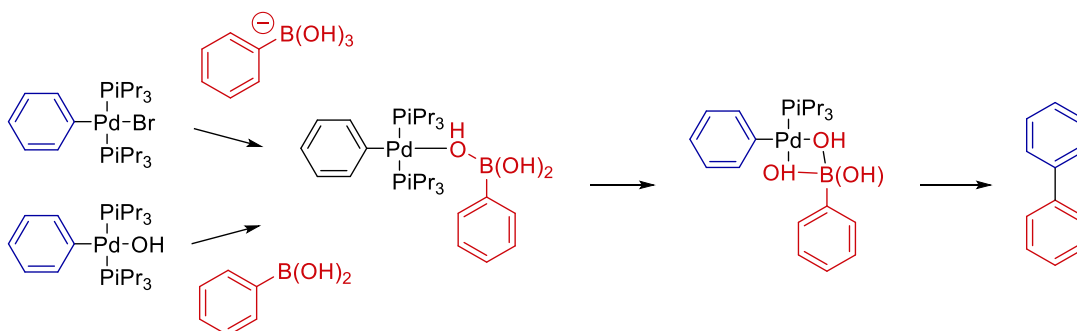


Figure 1 – Effect of the base concentration on the kinetic of TM and RE (*Chem. Eur. J.* **2011**, *17*, 2492).

Very recently, Denmark and collaborators¹¹⁵ have characterized the missing [Pd-O-B] intermediates using strongly hindered P(*i*Pr)₃ phosphine ligands and evaluated their reactivity (**Scheme 30**).



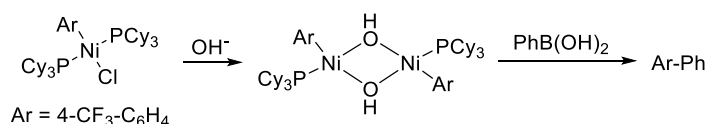
Scheme 30 – [Pd-O-B] intermediates for the TM process (ref. *Science*, **2016**, *352*, 329-332)

¹¹⁵ A. A. Thomas, S. E. Denmark, *Science*, **2016**, *352*, 329-332; A. A. Thomas, H. Wang, A. F. Zahrt, S. E. Denmark, *J. Am. Chem. Soc.*, **2017**, *139*, 3805-3821; A. A. Thomas, A. F. Zahrt, C. P. Delaney, S. E. Denmark, *J. Am. Chem. Soc.*, **2018**, *140*, 4401-4416.

2. Transmetalation from Boron to Nickel

2.1. Previous works

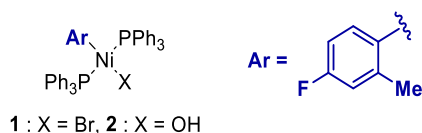
When the present work started in 2014,¹¹⁶ only a single publication by Monfette et al. had tackled the problem of transmetalation from B to Ni. They isolated dimeric hydroxide-bridged aryl-Ni complexes formed upon addition on OH⁻ on an aryl-Pd-Cl and, using the same erroneous reasoning as Carrow et al (vide supra), they proposed that the formation of such species could be the RDS of the whole catalytic cycle (**Scheme 31**).



Scheme 31 – Mechanistic proposal for the B to Ni TM as exposed by Monfette et al in *Organometallics*, **2014**, *33*, 9, 2134-2137.

2.2. Choice of the model reaction

To study the TM step, the aryl nickel complex *trans*-[ArNi(PPh₃)₂Br] (**1**, Ar = 4-F-2-Me-C₆H₄, **Scheme 32**) was selected, as it corresponds to a possible intermediate of the S-M reaction deriving from OA to Ni(0). *trans*-[ArNi(PPh₃)₂X] complexes (X = Cl, Br) very close in structure to **1** efficiently catalyze the S-M cross coupling of a variety of aromatic electrophiles with boronic acids.¹¹⁷ Triphenylphosphine (PPh₃) was chosen as a model ligand, as it is cheap, not very air sensitive and effective for the nickel-catalyzed S-M coupling proceeding at room temperature.¹¹⁸ 4-Fluoro-2-tolyl was selected as the organic moiety: the fluorine atom at the *para* position is a convenient probe for NMR studies (see **Table 7**, for the ¹⁹F and ³¹P chemical shift of complex **1** and its chlorinated analogue **1-Cl**)¹¹⁹ and the *ortho*-methyl substitution is known to impart greater stability to the complex.¹²⁰ Dioxane was selected as solvent for this study.



Scheme 32 - Structures of complex **1** and **2**.

¹¹⁶ A. H. Christian, P. Müller, S. Monfette, *Organometallics*, **2014**, *33*, 9, 2134-2137.

¹¹⁷ S. Ge, J. F. Hartwig, *Angew. Chem. Int. Ed.*, **2012**, *51*, 12837-12841; S. Saito, S. Oh-tani, N. Miyaura, *J. Org. Chem.*, **1997**, *62*, 8024-8030; S. Saito, M. Sakai, N. Miyaura, *Tetrahedron Lett.*, **1996**, *37*, 2993-2996; A. H. Christian, P. Müller, S. Monfette, *Organometallics*, **2014**, *33*, 2134-2137; J. Magano, S. Monfette, *ACS Catal.*, **2015**, *5*, 3120-3123; E. A. Standley, S. J. Smith, P. Müller, T. F. Jamison, *Organometallics*, **2014**, *33*, 2012-2018; X.-H. Fan, L.-M. Yang, *Eur. J. Org. Chem.*, **2011**, *2011*, 1467-1471.

¹¹⁸ S. Z. Tasker, E. A. Standley, T. F. Jamison, *Nature*, **2014**, *509*, 299-309; V. Percec, J.-Y. Bae, D. H. Hill, *J. Org. Chem.*, **1995**, *60*, 1060-1065; K. Inada, N. Miyaura, *Tetrahedron*, **2000**, *56*, 8657-8660.

¹¹⁹ W. R. Dolbier, *Guide to Fluorine NMR for Organic Chemists*, Wiley, **2009**.

¹²⁰ M. Hidai, T. Kashiwagi, T. Ikeuchi, Y. Uchida, *J. Organomet. Chem.*, **1971**, *30*, 279-282; J. Chatt, B. L. Shaw, *J. Chem. Soc.*, **1960**, 1718-1729.

Table 7 - NMR data of complexes **1** and **1-Cl**. Chemical shifts in ppm recorded in CD₂Cl₂.

	³¹ P{ ¹ H}	¹⁹ F{ ¹ H}
complex 1	20.9 (d, 3.4 Hz)	-127.7 (d, 3.4 Hz)
complex 1-Cl	21.8 (d, 2.9 Hz)	-127.8 (t, 2.9 Hz)

2.3. Formation of hydroxo-bridged dinuclear complexes

Since the presence of a base is essential for the S-M reaction, the interaction of complex **1** with hydroxide was investigated. Complex **1** was characterized by CV in dioxane at a steady gold disk electrode (**Figure 2**). All CVs were performed in the presence of 4 equiv of PPh₃ to stabilize electrogenerated Ni(0). Compound **1** was characterized by a main reduction peak (R₁, **Figure 2**) at $E = -1.7$ V versus saturated calomel electrode (SCE).

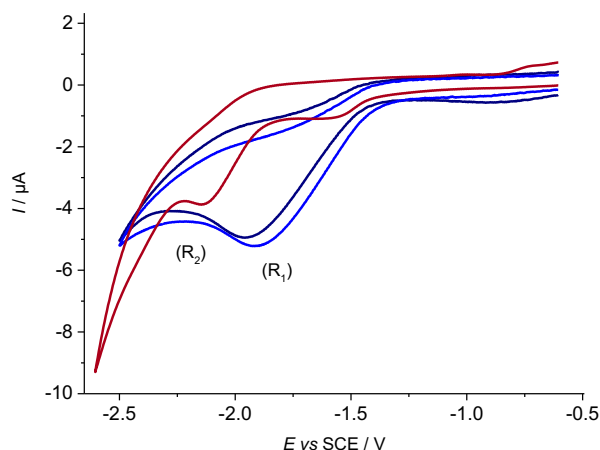


Figure 2 - Cyclic voltammetry performed towards reduction potentials at a steady gold disk electrode ($d = 1$ mm) in dioxane containing $n\text{Bu}_4\text{NBF}_4$ (0.3 M) at 20 °C, at a scan rate of 0.5 V s⁻¹. Dark blue: complex **1** (2 mM), PPh₃ (4 equiv); light blue: upon addition of PhB(OH)₂ (2 equiv); red: upon addition of TBAOH (1 equiv).

Tetrabutylammonium hydroxide (TBAOH) was first selected as a base to avoid solubility issues and specific cation effects. Upon addition of 1.0 equiv of TBAOH, the CV was significantly modified with a main reduction peak appearing at $E = -2.2$ V versus SCE (R₂, **Figure 2**) presumably due to the formation of aryl nickel hydroxo species.

To gain more insight into the structure of the formed species, a similar experiment was performed using ¹⁹F{¹H} and ³¹P{¹H} NMR. Complex **1** was characterized by a single resonance at 21.8 ppm in the ³¹P{¹H} NMR spectrum (**Figure 3**).

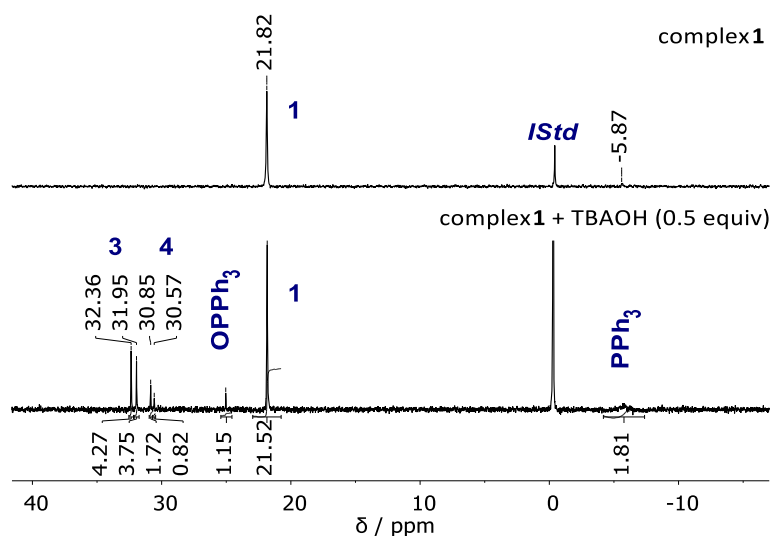


Figure 3 - Complex **1** (20 mM, dioxane, a coaxial insert containing a solution of H_3PO_4 in $[\text{D}_6]\text{DMSO}$ was used for locking and as an internal standard for integration) alone and in the presence of TBAOH (0.5 equiv), $^{31}\text{P}\{^1\text{H}\}$ NMR.

When TBAOH (0.5 equiv) was added, an approximately equal amount of free PPh_3 ($\delta = -5.9$ ppm) was immediately released and four new resonances were observed in the 30.5–32.5 ppm region (**Figure 3**). In the $^{19}\text{F}\{^1\text{H}\}$ NMR spectrum, complex **1** featured a broad singlet at -127.7 ppm (**Figure 4**).

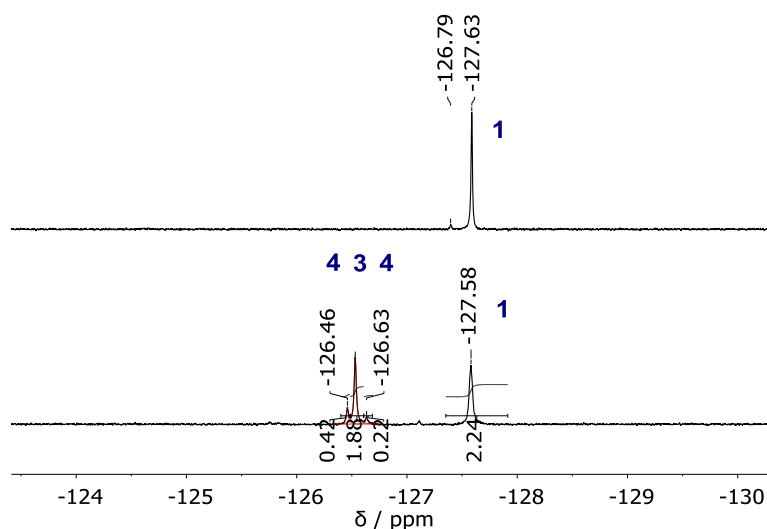


Figure 4 - Complex **1** (20 mM, dioxane, $[\text{D}_6]\text{DMSO}$ in a coaxial insert was used for locking) alone and in the presence of TBAOH (0.5 equiv), $^{19}\text{F}\{^1\text{H}\}$ NMR.

After addition of 0.5 equiv of TBAOH, a complex multiplet composed of at least three overlapping signals appeared around -126.6 ppm, accounting for about half of the total integration of the spectrum (**Figure 4**). Spectral deconvolution showed that this complex signal can be resolved into three resonances (**Table 8**). It is important to note that the same set of

$^{19}\text{F}\{^1\text{H}\}$ and $^{31}\text{P}\{^1\text{H}\}$ NMR was also observed (in the presence of water) with the bases classically used in catalytic couplings: K_2CO_3 and K_3PO_4 (Figure 5).

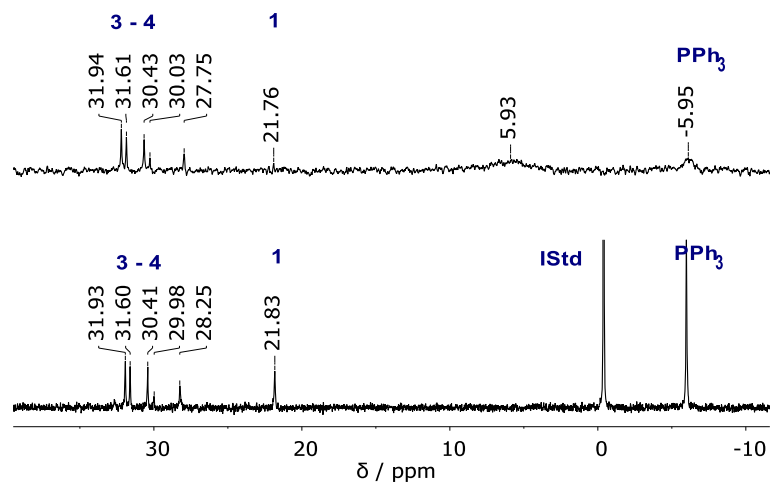


Figure 5 - Complex **1** (20 mM, dioxane/ H_2O (1 mL / 0.1 mL), a coaxial insert containing a solution of H_3PO_4 in $[\text{D}_6]\text{DMSO}$ was used for locking and as an internal standard for integration) and K_2CO_3 (13 equiv), $^{31}\text{P}\{^1\text{H}\}$ NMR.

Additionally, several broad singlets appeared in the region up-field of TMS in the ^1H NMR (Figure 6). These resonances are characteristic of protons of bridging OH^- ligands in square planar complexes.¹²¹

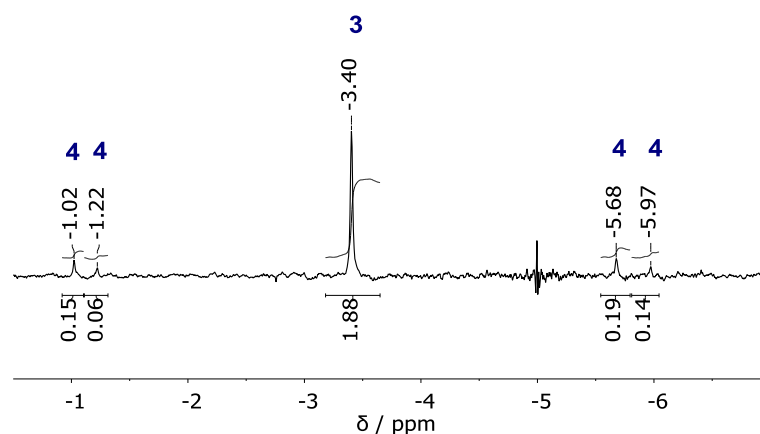
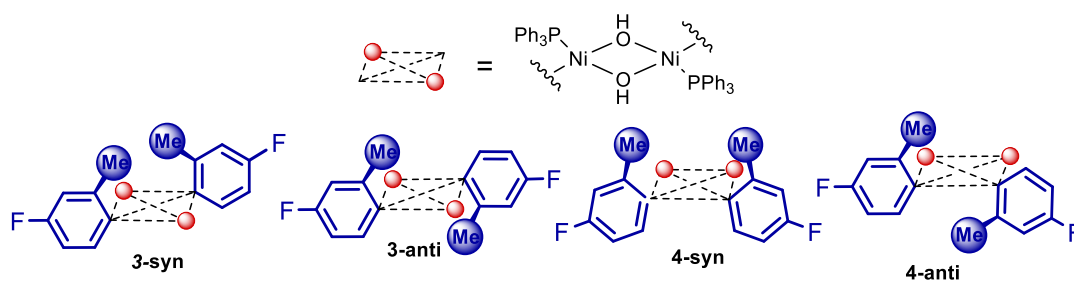


Figure 6 - Complex **1** (20 mM, dioxane, $[\text{D}_6]\text{DMSO}$ in a coaxial insert was used for locking) and TBAOH (0.5 equiv), ^1H NMR.

¹²¹ A. H. Christian, P. Müller, S. Monfette, *Organometallics*, **2014**, *33*, 2134-2137; V. V. Grushin, H. Alper, *Organometallics*, **1993**, *12*, 1890-1901; V. V. Grushin, C. Bensimon, H. Alper, *Organometallics*, **1995**, *14*, 3259-3263; V. V. Grushin, H. Alper, *Organometallics*, **1996**, *15*, 5242-5245.

These results are consistent with the formation of four isomeric hydroxo-bridged dinuclear complexes (**Table 8**).¹²² The phosphine ligand can be arranged in a *pseudo-trans* or in a *pseudo-cis* fashion around the dinuclear center and the *ortho*-methyl groups of Ar can be either *anti* or *syn* with respect to the Ni(μ -OH)₂Ni plane leading to species **3** et **4** (**Table 8**). The Ni(μ -OH)₂Ni moiety constitutes a slightly puckered four-membered ring (*vide infra* DFT optimized structures, **Scheme 33**) and the Ar moiety does not lie flat in the plane approximately described by this ring. In the case of the analogous complex *trans*-[(4-CF₃-C₆H₄)Ni(PPh₃)₂Cl], featuring no methyl group on Ar, only two peaks were observed in the ³¹P{¹H} NMR spectrum (δ = 32.0 (*cis*) and 34.0 (*trans*)), in agreement with what reported by Monfette and coll., for a similar complex featuring PCy₃ as a ligand.

Table 8 - NMR data of complexes **3** and **4**. Chemical shifts in ppm and relative integrations (in parentheses) are reported in dioxane (using [D₆]-DMSO in a coaxial insert).



	Complex 3 (<i>syn</i> and <i>anti</i>)		Complex 4 (<i>syn</i> and <i>anti</i>)	
³¹ P	32.4 (1)	32.0 (0.88)	30.9 (0.40)	30.6 (0.19)
¹⁹ F	-126.53 (1.88)		-126.46 (0.42)	-126.63 (0.22)
¹ H	-3.4 (1.88)		-1.0 (0.2)	-1.2 (0.1)
			-5.7 (0.2)	-6.0 (0.1)

To confirm the formation of dinuclear nickel complexes, a ³¹P{¹H} NMR diffusion ordered spectroscopy experiment (DOSY) was performed (**Figure 7**). All four peaks in the 30.5-32.5 ppm region are associated to species having the same diffusion rate, which is lower than that of the starting material **1**. Any attempt to isolate an OH-ligated aryl-nickel complex derived from **1** failed due to extensive decomposition.

¹²² A. H. Christian, P. Müller, S. Monfette, *Organometallics*, **2014**, *33*, 9, 2134-2137.

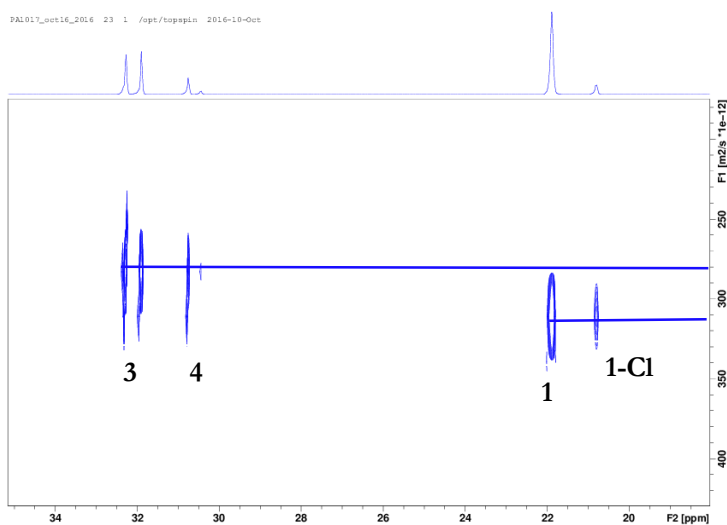
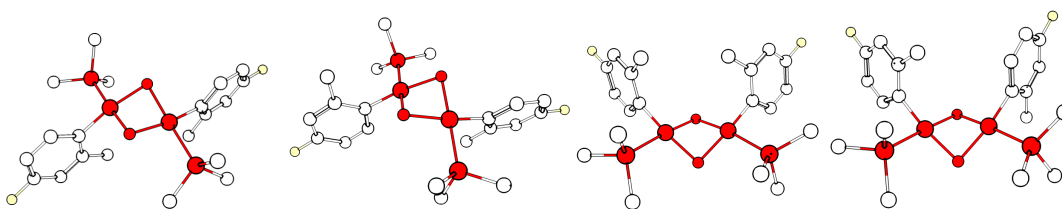


Figure 7 - Complex **1** (20 mM, dioxane, $[D_6]$ DMSO in a coaxial insert was used for locking) and TBAOH (0.5 equiv), $^{31}\text{P}\{^1\text{H}\}$ NMR DOSY.

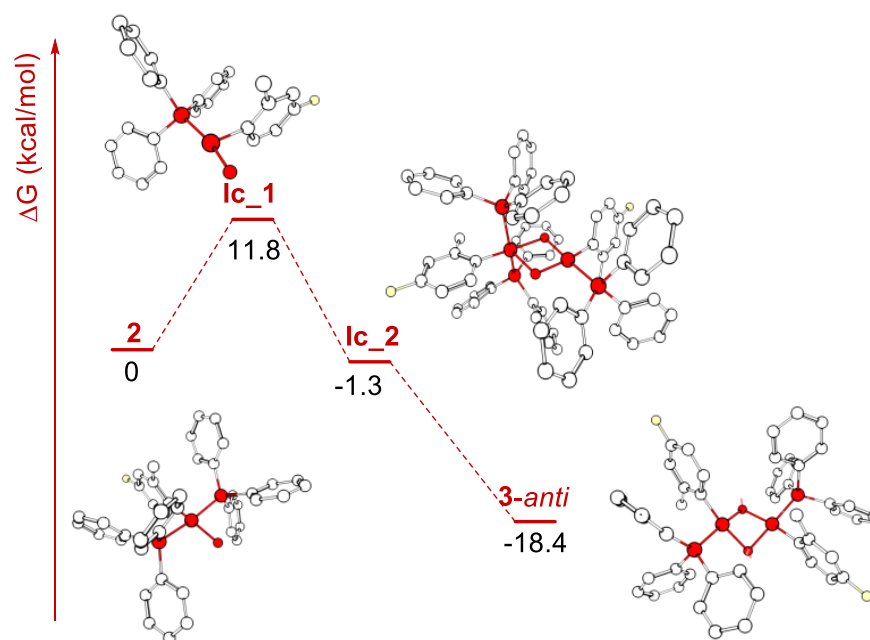
The relative stability of isomeric complexes **3** and **4** was evaluated by calculations performed at the DFT (Density Functional Theory) level (**Scheme 33**). Complex **3-anti** was found to be the most stable, with **3-syn** coming as a close second ($\Delta G = +0.4$ kcal mol $^{-1}$). The *pseudo-cis* species **4** were predicted to be less favorable to form, the *syn* isomer being slightly more stable ($\Delta G = +5.3$ kcal mol $^{-1}$ and $\Delta G = +6.4$ kcal mol $^{-1}$ for **4-syn** and **4-anti**, respectively).¹²³ The structures of intermediates potentially involved in the formation of the dinuclear species **3-4** were optimized by DFT calculation. A reasonable pathway involving the formation of a T-Shape Ni complex (**Ic_1**) reacting with Ni-OH complex **2** to give a dinuclear intermediate featuring a pentacoordinated Ni (**Ic_2**) was found accessible at ambient temperature (**Scheme 34**).



Scheme 33 – DFT-calculated structure of complexes **3-cis**, **3-trans**, **4-cis** and **4-trans**, hydrogen atoms are omitted and phenyl moieties are reduced to a single C atom for clarity. Ni, P, O and B atoms are colored in red, F atoms are colored in yellow. Computed relative Gibbs free energies (with respect to the most stable isomer) are reported.

¹²³ If the thermodynamic parameters computed at the DFT level were accurate, **4-syn** and **4-anti** should not have been observed by NMR. However, we can assume that the energy complexes **4** are overestimated due to the neglect of specific solvation effects, which are likely to be relevant for these OH-bridged species.

Addition of excess PPh₃ (up to 10 equiv) to a solution containing *in situ* generated **3** and **4** did not lead to the formation of mononuclear [ArNi(PPh₃)₂(OH)] (**2**) in any detectable amount by NMR spectroscopy, as already reported for related systems.¹²⁴ This behavior is in stark contrast with that of the analogous palladium complexes [ArPd(μ-OH)(PPh₃)₂], which are readily converted to mononuclear [ArPd(PPh₃)₂(OH)] in moderate to polar solvents in the presence of PPh₃.¹²⁵ To shed more light on this point, we resorted again to DFT calculations (**Scheme 35**).



Scheme 34 - Pathway for the formation of dinuclear species **3-4** as studied by DFT calculations. Computed relative Gibbs free energies are reported in kcal mol⁻¹.

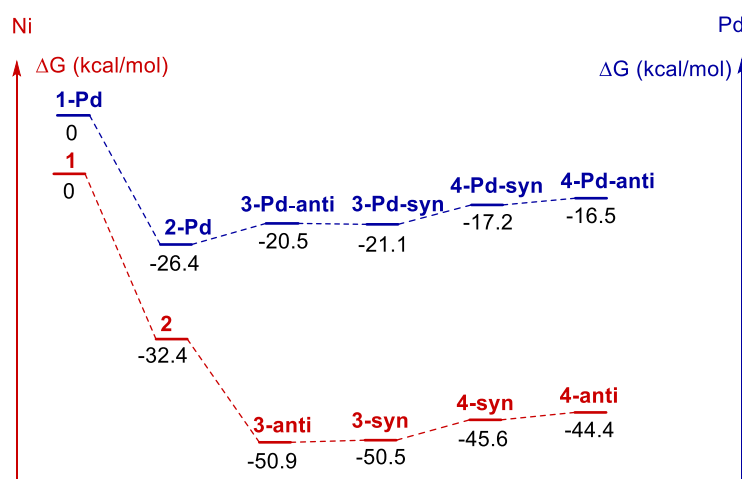
The formation of **2** from **1** and OH⁻ was found to be exergonic ($\Delta G = -32.4$ kcal mol⁻¹), as well as the reaction of two molecules of **2** to give **3-anti** ($\Delta G = -18.5$ kcal mol⁻¹). The picture is different for Pd: while the formation of *trans*-[ArPd(PPh₃)₂(OH)] (**2-Pd**) from *trans*-[ArPd(PPh₃)₂Br] (**1-Pd**) is favorable ($\Delta G = -26.4$ kcal mol⁻¹), the formation of dinuclear *anti,trans*-[ArPd(μ-OH)(PPh₃)₂] (**3-Pd-anti**) is slightly endergonic ($\Delta G = +5.9$ kcal mol⁻¹). Similar observations on the higher stability of hydroxo-bridged dimers for nickel than for palladium were also made by Grushin and coworkers.¹²⁶ This different behavior can be rationalized considering the higher oxophilicity and lower phosphine affinity of nickel.¹²⁷

¹²⁴ A. H. Christian, P. Müller, S. Monfette, *Organometallics*, **2014**, *33*, 2134-2137; D. D. VanderLende, K. A. Abboud, J. M. Boncella, *Inorg. Chem.*, **1995**, *34*, 5319-5326.

¹²⁵ C. Amatore, A. Jutand, G. Le Duc, *Chem. Eur. J.*, **2011**, *17*, 2492-2503; M. Hidai, T. Kashiwagi, T. Ikeuchi, Y. Uchida, *J. Organomet. Chem.*, **1971**, *30*, 279-282; J. Chatt, B. L. Shaw, *J. Chem. Soc.*, **1960**, *0*, 1718-1729.

¹²⁶ V. V. Grushin, C. Bensimon, H. Alper, *Organometallics*, **1995**, *14*, 3259-3263.

¹²⁷ V. V. Grushin, H. Alper, *Organometallics*, **1996**, *15*, 5242-5245; K. P. Kepp, *Inorg. Chem.*, **2016**, *55*, 9461-9470.



Scheme 35 - Gibbs free energy for the formation of hydroxide complexes **2** to **4**, comparison with the analogous species featuring a Pd instead of a Ni center (**2-Pd** to **4-Pd**).

2.4. Decomposition of the complex with excess base

Finally, the behavior of complex **1** in the presence of an excess of base was also investigated. Upon addition of 10 equiv of TBAOH to a solution of **1** (20 mM in dioxane), the signals observed in $^{31}\text{P}\{^1\text{H}\}$ were similar to those described above but the integration of a spectrum recorded under quantitative conditions demonstrated that more than 1 equiv of phosphine was released (**Figure 8**).

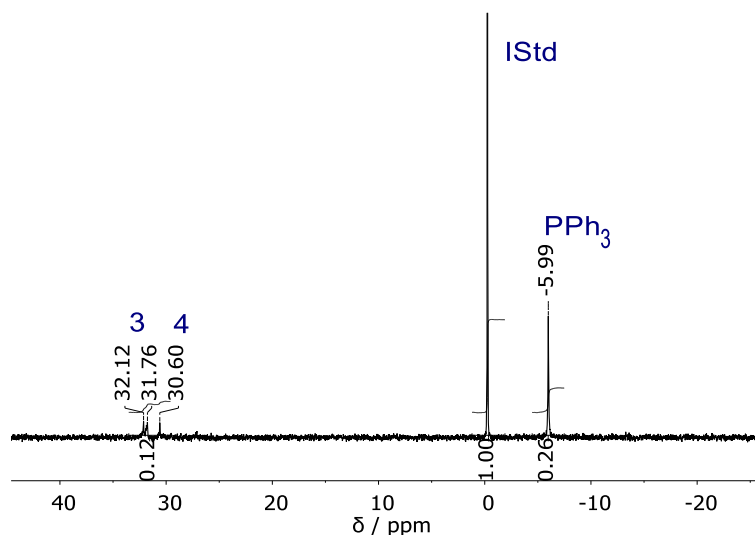


Figure 8 - Complex **1** (20 mM, dioxane, a coaxial insert containing a solution of H_3PO_4 in $[\text{D}_6]\text{DMSO}$ was used for locking and as an internal standard for integration), TBAOH (10 equiv), $^{31}\text{P}\{^1\text{H}\}$ NMR.

In parallel, in the $^{19}\text{F}\{^1\text{H}\}$ spectrum a new peak at -129.4 ppm appeared (**Figure 9**). These observations can be rationalized by assuming the formation of poly-hydroxo species (featuring no ligated PPh_3). These species are not stable at room temperature and they slowly decompose

to give 3-fluorotoluene¹²⁸ as well as the homocoupling product ArAr (**Figure 9**). The identity of these compounds was confirmed by comparison of the ¹⁹F NMR chemical shifts with authentic samples and by GC-MS.

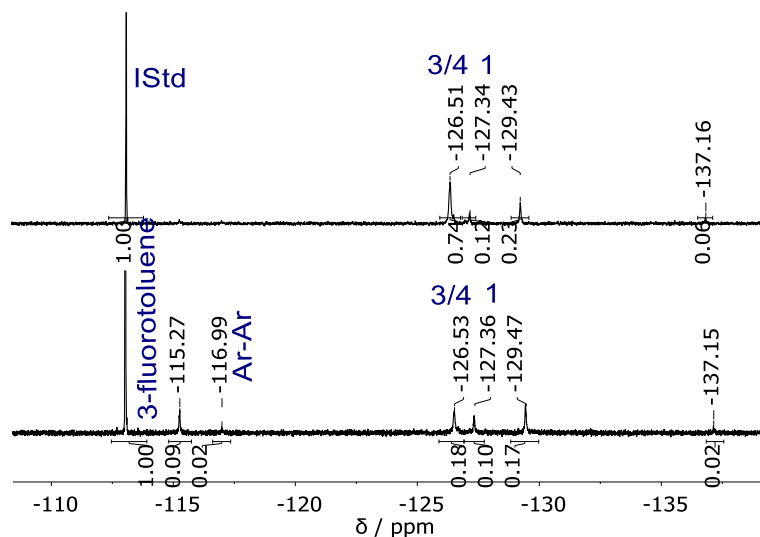


Figure 9 - Complex **1** (20 mM, dioxane, [D₆]DMSO in a coaxial insert was used for locking), TBAOH (10 equiv) ¹⁹F{¹H} NMR, fluorobenzene was used as an internal standard.

In summary, in the presence of hydroxide, complex **1** evolves towards a mixture of isomeric dinuclear species **3-4**. We anticipated that the different reactivity of these species could be responsible for the narrow range of experimental conditions tolerated by the nickel-catalyzed S-M reaction. Indeed, the nature of the base and solvent determines the effective concentration of OH⁻, and thus controls the equilibria involving aryl-nickel hydroxo species.

2.5. Interaction of PhB(OH)₃⁻ with complex **1**

As a comparatively strong Lewis acid, PhB(OH)₂ is quantitatively converted into PhB(OH)₃⁻ in the presence of a stoichiometric amount of TBAOH. The reaction between PhB(OH)₂ and the anionic boronate form PhB(OH)₃⁻ is known to be quantitatively displaced in favour of the latter in the presence of OH⁻ in water or in DMF.¹²⁹ The pK_a of PhB(OH)₂ in water is 8.9.¹³⁰ To the best of our knowledge, there was no data in dioxane. PhB(OH)₂ was characterized by a broad peak at 28.9 ppm in ¹¹B NMR. Upon addition of 1.0 equiv of TBAOH in water, a new broad peak appeared at 3.6 ppm corresponding to PhB(OH)₃⁻. Addition of more TBAOH did not affect the chemical shift, which is consistent with this reaction being quantitative.

Competition for hydroxide binding between PhB(OH)₂ and complex **1** was then investigated by CV (**Figure 10**, a). As stated above, an equimolar mixture of complex **1** and TBAOH in dioxane,

¹²⁸ The formation of 3-fluorotoluene may also take place in the presence of arylboronic acid as a significant side-reaction when the B-to-Ni is slow: *vide infra*.

¹²⁹ Amatore, C.; Jutand, A.; Le Duc, G. *Chem. Eur. J.* **2011**, *17*, 2492-2503.

¹³⁰ For an extended discussion on the acidity of boronic acids, see: D. G. Hall, in *Boronic Acids*, **2011**, Wiley, pp. 1-133.

in the presence of 2 equiv of added PPh_3 , is characterized by a reduction peak at $E = -2.2$ V vs SCE (R_2). When $\text{PhB}(\text{OH})_2$ (20 equiv) was added to the mixture, the reduction peak R_1 went back, suggesting that **1** is regenerated from **3-4** via a rapid equilibrium (Figure 10, a). After a few minutes at 45 °C, the solution turned red (characteristic color of PPh_3 -ligated $\text{Ni}(0)$), and two oxidation peaks Ox_1 and Ox_2 appeared at about -0.4 V and -0.2 V (Figure 10, b). The latter oxidation peaks could be attributed to PPh_3 -ligated $\text{Ni}(0)$, as confirmed by addition of an authentic sample of $[\text{Ni}(\text{cod})_2]$ ($\text{cod} = \text{cis,cis-cycloocta-1,5-diene}$) and PPh_3 .

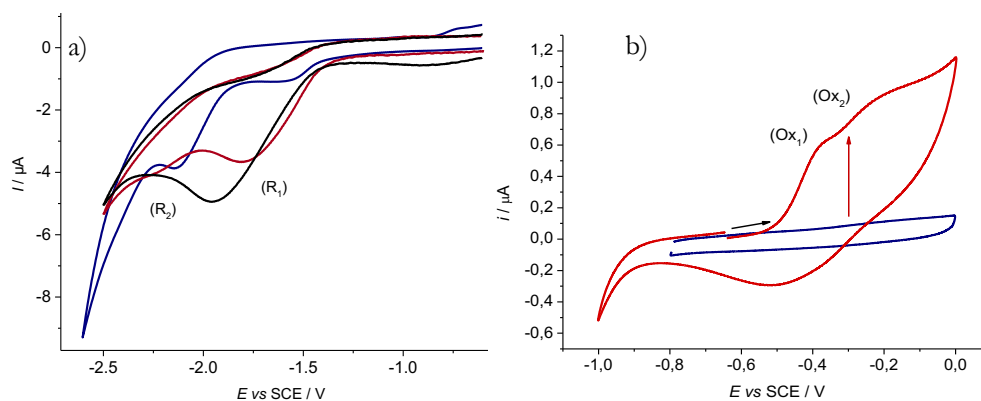


Figure 10 - CV at a steady gold disk electrode ($d = 1$ mm) in dioxane containing $n\text{Bu}_4\text{NBF}_4$ (0.3 M) at 20 °C, at a scan rate of 0.5 V s^{-1} . a) Performed towards reduction potentials, black: complex **1** (2 mM), PPh_3 (4 equiv); blue: upon addition of TBAOH (1 equiv); red: upon addition of $\text{PhB}(\text{OH})_2$ (2 equiv) and TBAOH (1 equiv). b) Performed towards oxidation potentials, blue: immediately after mixing complex **1** with $\text{PhB}(\text{OH})_2$ (10 equiv) and TBAOH (1 equiv); red: 5 min after addition.

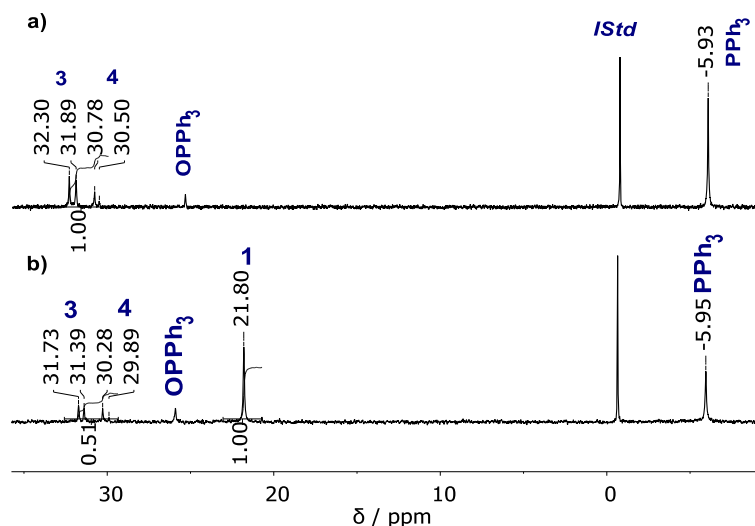
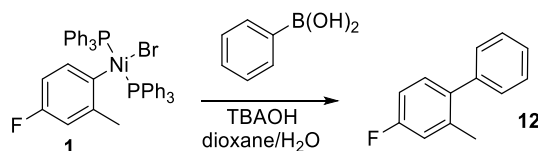


Figure 11 - Complex **1** (20 mM, dioxane, a solution of H_3PO_4 in $[\text{D}_6]\text{DMSO}$ in a coaxial insert was used a reference for integration), TBAOH (1 equiv), $^{31}\text{P}\{^1\text{H}\}$ NMR, a) alone; b) in the presence of $\text{PhB}(\text{OH})_2$ (10 equiv).

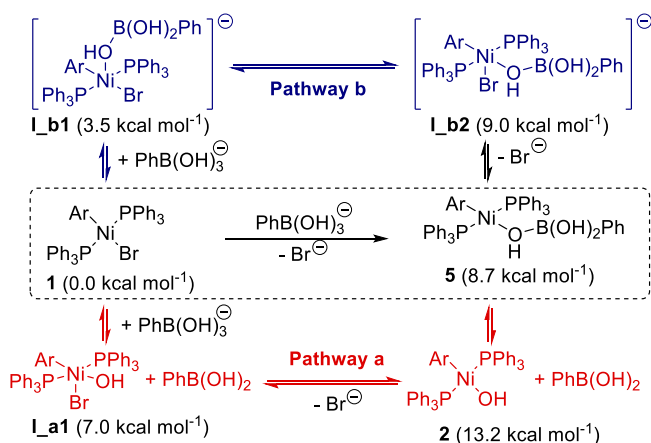
The same reaction was then monitored by $^{31}\text{P}\{^1\text{H}\}$ NMR spectroscopy. Upon addition of 10 equiv of $\text{PhB}(\text{OH})_2$ acid to an equimolar mixture of complex **1** and TBAOH, the intensity of the four signals associated to **3-4** decreased and the signal of **1** reappeared at 21.8 ppm (Figure 11).

This confirmed that the reaction of hydroxides with complex **1** to form dimeric complexes is rapidly reversed by addition of $\text{PhB}(\text{OH})_2$, due to the acidic properties of the latter. The solution quickly turned red and a new resonance appeared in the $^{19}\text{F}\{^1\text{H}\}$ NMR spectrum at -117.5 ppm, corresponding to the coupling product **12**, as confirmed by addition of an authentic sample (**Scheme 36**).



Scheme 36 - Reaction of complex **1** with $\text{PhB}(\text{OH})_2$ in the presence of TBAOH to form the biphenyl product **12**.

Formal replacement of Br^- ligand with $\text{PhB}(\text{OH})_3^-$ giving complex **5** can happen through two distinct pathways (**Scheme 37**): (a) by association of $\text{PhB}(\text{OH})_2$ with OH^- -ligated complex **2**; (b) by direct ligand substitution reaction of $\text{PhB}(\text{OH})_3^-$ on complex **1**. The energetics of these two pathways were studied at the DFT level. All these reactions were predicted to proceed easily at room temperature either via pentacoordinated, square-pyramidal intermediates or via direct substitution (**Scheme 37**).

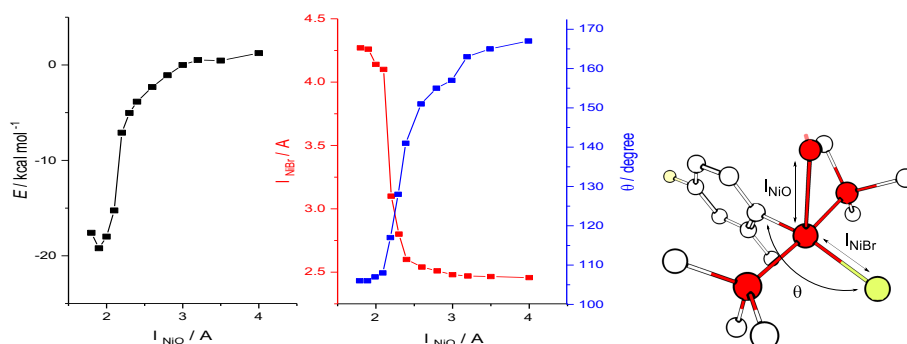


Scheme 37 - Possible pathways for the formal substitution of Br^- with $\text{PhB}(\text{OH})_3^-$ in complex **1**. Computed Gibbs free energies at the DFT level are reported in parentheses.

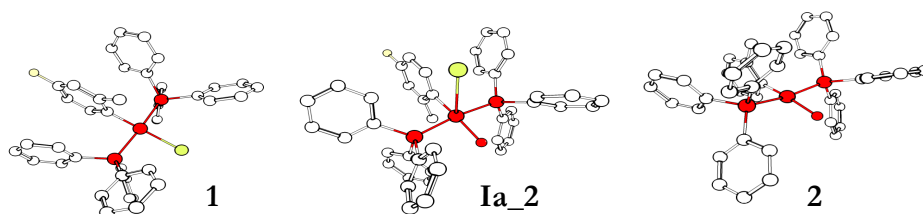
As it was not possible to localize the TS for the formation of complex **5** (*ie* bromide exchange with hydroxide or boronate ligand) the structure of complex **5** + L (with L = OH^- or $\text{PhB}(\text{OH})_3^-$) was optimized for different Ni-O bond lengths. The electronic energy obtained are plotted *vs* Ni-OH length on **Scheme 38** and **Scheme 40**. The Ni-Br bond length as well as the angle θ between the molecular plane and Ni-Br bond were also plotted as a function of the Ni-OH distance (**Scheme 38** and **Scheme 40**, insets), these two parameters have an evolution which is consistent with the one of Ni-OH: to the shortening of the Ni-O bond corresponds an elongation of the Ni-Br bond as well as a decrease of the θ angle.

In the case of the substitution of Br^- with hydroxide the process was found barrierless (regarding internal electronic energy) and the pentacoordinated product **Ia_c** can be obtained from direct

substitution (**Scheme 38** and **Scheme 39**). Ni-Br elongation and Br atom tilt are synchronous and happen around $l(\text{Ni-OH}) = 2.2 \text{ \AA}$.

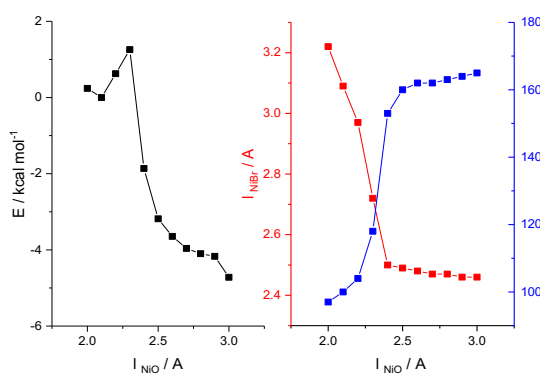


Scheme 38 - Energy scan for the formation of complex **5** via pathway (a)

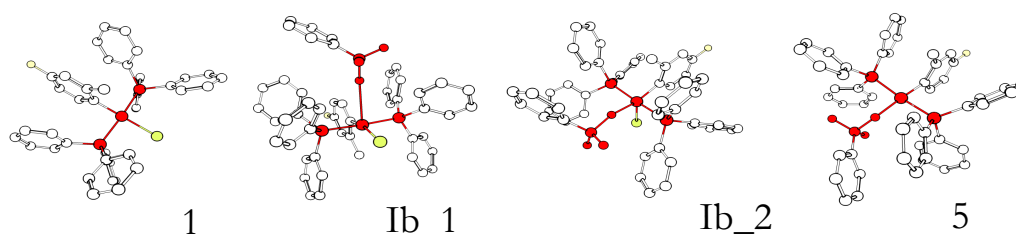


Scheme 39 - Structure of complexes **1-2** and of intermediate **Ia_2**, hydrogen atoms are omitted for clarity and Ni, P, O and B atoms are colored in red, Br and F atoms are colored in yellow.

In the case of the substitution of Br^- with $\text{PhB}(\text{OH})_3^-$ both pentacoordinated intermediates **Ib_1** and **Ib_2** (**Scheme 41**) are zero gradient points (which could be due to the size of $\text{PhB}(\text{OH})_3^-$ compared to OH^-). The electronic energy of activation for this process can be estimated around 5 kcal mol^{-1} . Similarly to the previous case of OH^- substitution, Ni-Br elongation and Br atom tilt are synchronous and happen around $l(\text{Ni-OH}) = 2.2 \text{ \AA}$ (**Scheme 40**).



Scheme 40 - Energy scan for the formation of complex **5** via pathway (b).



Scheme 41 - Structure of complexes **1-2** and of intermediate **Ia_2**, hydrogen atoms are omitted for clarity and Ni, P, O and B atoms are colored in red, Br and F atoms are colored in yellow.

2.6. Effect of the OH⁻/PhB(OH)₂ ratio on the kinetics of TM and RE

With this model system in hand –which reproduces under stoichiometric conditions the process relevant for the catalytic cycle– we studied in detail the kinetics of the TM reaction. A premixed solution of PhB(OH)₂ (10 equiv) and TBAOH (4 equiv) in dioxane was added to complex **1**. ¹⁹F{¹H} NMR analysis showed complete conversion of **1** into the coupling product **12** within 12 h. No intermediate product was observed, which is in agreement with RE being faster than TM.¹³¹ Under these conditions, integration of the peak at –117.5 ppm, corresponding to the coupling product **12** allowed to follow the kinetics of the reaction (**Figure 12**). Apparent first order with respect to complex **1** was obtained, suggesting that polynuclear species are likely not involved in the rate-determining TM step.

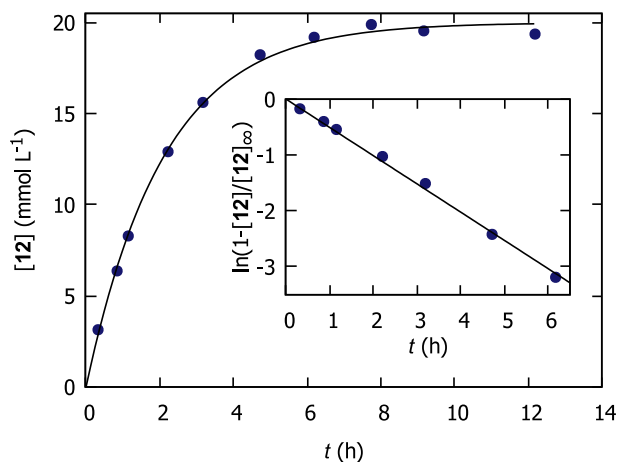


Figure 12 - Kinetics of the reaction of complex **1** (20 mM in dioxane) with PhB(OH)₂ (10 equiv) in the presence of TBAOH (4 equiv) at 20 °C, as followed by monitoring the formation of **12** by ¹⁹F{¹H} NMR. In the inset, selected data are represented using semi-logarithmic plot.

To better understand the role of the equilibria involving PhB(OH)₂ and dimeric species **3-4**, the influence of the [OH⁻]/[PhB(OH)₂] ratio was investigated. The pseudo first-order rate constant k_{app} was determined for different concentrations of added TBAOH, while keeping PhB(OH)₂ concentration constant (10 equiv, **Figure 13**, a). The concentration of added TBAOH has a

¹³¹ Z. Lu, A. Wilsily, G. C. Fu, *J. Am. Chem. Soc.* **2011**, *133*, 8154-8157; D. Zim, V. R. Lando, J. Dupont, A. L. Monteiro, *Org. Lett.* **2001**, *3*, 3049-3051.

strong influence on the observed rate: the reaction required 12 h to go to completion with 4 equiv of base, but less than 1 h using only 2 equiv. Similarly, k_{app} was measured for different amounts of added PhB(OH)_2 with a constant amount of TBAOH (2 equiv, **Figure 13**, b). The reaction is faster at high PhB(OH)_2 concentrations. In both cases, the reaction is more rapid for low TBAOH/ PhB(OH)_2 ratios.

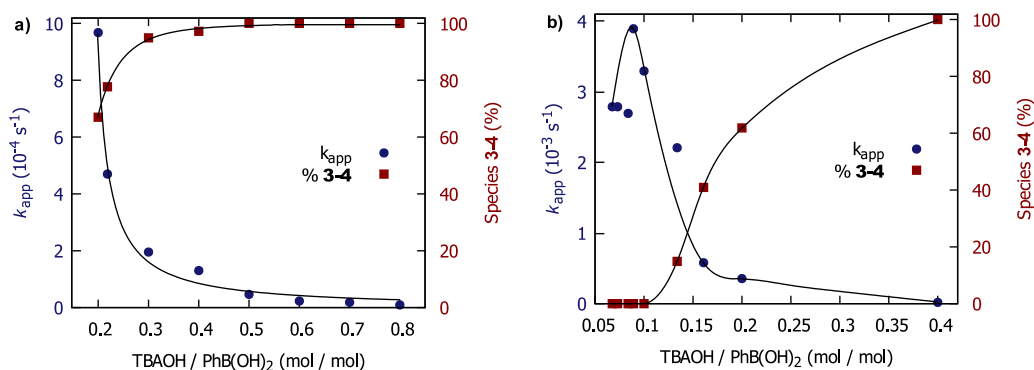


Figure 13 - a) Left scale: pseudo first-order rate constants (k_{app}) for the reaction of complex **1** (20 mM in dioxane) with PhB(OH)_2 (10 equiv) for various amounts of added TBAOH (1.5 M in water) at 20°C, as monitored by $^{19}\text{F}\{^1\text{H}\}$ NMR; b) Left scale: pseudo first-order rate constants (k_{app}) for the reaction of complex **1** (10 mM in dioxane) with various amounts of PhB(OH)_2 in the presence of 2 equiv of TBAOH (1.5 M in water) at 20°C as monitored by $^{19}\text{F}\{^1\text{H}\}$ NMR. Right scale: percentage of **1** converted to species **3-4** just after addition of all the reactants.

Thanks to $^{19}\text{F}\{^1\text{H}\}$ NMR analyses, it was possible to measure the fraction of complex **1** that had not been converted into **3-4** at the beginning of the reaction (**Figure 13**). The percentage of **3-4** and unconverted **1** were measured by $^{19}\text{F}\{^1\text{H}\}$ NMR at the beginning of the reaction soon after mixing the reactants. However, those values are supposed to vary as the reaction proceeds. Simulation of the percentage of those species as a function of the extent of the reaction shows that the variation is comparatively small up to approximately 80% conversion.¹³²

¹³² All through our studies on the Ni-catalyzed S-M reaction we have observed that the kinetics of the reaction of the formation of cross-coupling products via TM-RE involving ArNiL_2X and Ar'B(OH)_2 in the presence of OH^- followed a first order kinetic law. This observation is not easily explained since the concentrations of the species involved vary as the reaction proceeds (even if an excess of Ar'B(OH)_2 and OH^- is used), assuming the following the TM-RE reaction:



Moreover, the following equilibrium takes place:



The hydroxo-bridged dinuclear species so formed are not reactive, as explained in the main text. The thermodynamic constant K for the equilibrium (ii), presented above, has the expression that follows:

$$K = \frac{[\{\text{ArNiL}(\mu\text{-OH})\}_2][\text{L}]^2[\text{X}^-]^2}{[\text{ArNiL}_2\text{X}]^2[\text{OH}^-]^2}$$

Since X^- is released as the coupling reaction proceeds and the total concentration of aryl-nickel species present in solution varies as ArNiL_2X is consumed, the distribution of organonickel species between

A correlation is evident between the reaction rate and the concentration of **1**. While the reaction is slow when dimeric species **3-4** predominate, it is up to about 100 times faster when only complex **1** can be detected in solution. It thus appears that dimeric species **3-4** are resting states for the Ni catalyst. In the presence of more than 22 equiv of phenylboronic acid, however the reaction rate slightly decreased.

An analogous influence of the base/boronic acid ratio was reported for the TM involving $[(p\text{-NC-C}_6\text{H}_4)\text{PdBr}(\text{PPh}_3)_2]$ and $\text{PhB}(\text{OH})_2$. While the maximum rate was observed for a $\text{OH}^-/\text{PhB}(\text{OH})_2$ ratio of 0.7-0.8 for palladium, the optimal ratio is less than 0.1 for this Ni-based

$\{\text{ArNiL}(\mu\text{-OH})\}_2$ and ArNiL_2X should also vary. Let us define z as the molar fraction of unchanged ArNiL_2X and construct the equilibrium table that follows. Thus K has the following expression:

$$K = \frac{(1-z)C_{\text{Ni}}[C_{\text{P}} + (1-z)C_{\text{Ni}}]^2[C_{\text{X}} + (1-z)C_{\text{Ni}}]^2}{2(zC_{\text{Ni}})^2[\text{OH}^-]^2}$$

We will assume that $[\text{OH}^-]$ can be considered constant all through the reaction (i) due to the existence of the $\text{PhB}(\text{OH})_2/\text{PhB}(\text{OH})_3^-$ buffer system. As the TM-RE reaction (i) proceeds, the total concentration of arynickel species ($C_{\text{Ni}} = [\text{ArNiL}_2\text{X}] + [\{\text{ArNiL}(\mu\text{-OH})\}_2]$) and C_{X} vary in the experimental conditions. Defining s as the extent of the TM-ER reaction (i), the following equations hold:

$$C_{\text{Ni}} = (1-s) C_{\text{Ni},0} \text{ and } C_{\text{X}} = s C_{\text{Ni},0}$$

in which $C_{\text{Ni},0}$ is the C_{Ni} at the beginning of the reaction (i.e. the initial concentration of ArNiL_2X).

By substitution in the expression for K the following expression is obtained:

$$\frac{K[\text{OH}^-]^2}{C_{\text{Ni},0}^3} = \frac{(1-z)^3(1-s)[s + (1-z)(1-s)]^2}{2z^2}$$

This equation cannot be solved explicitly for $z(s)$, but a numerical solution can be found. It is convenient to introduce the adimensional constant parameter A :

$$A = \frac{K[\text{OH}^-]^2}{C_{\text{Ni},0}^3}$$

Since the value of A is unknown, the function $z(s)$ has been plotted for several different orders of magnitude ($10^{-4} < A < 10^2$), as reported in **Figure a**.

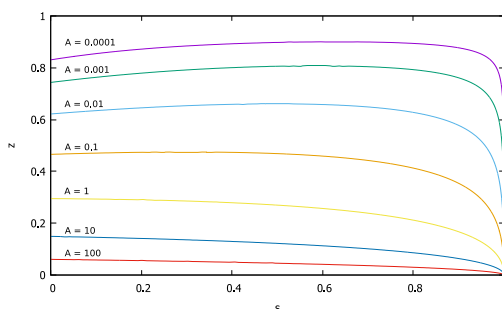


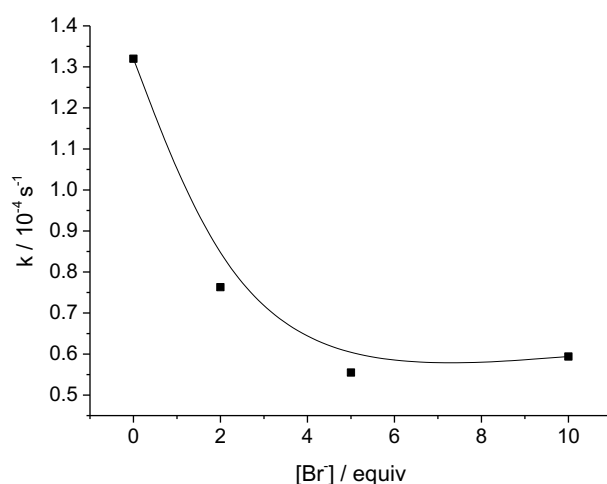
Figure a - Plots of the function $z(s)$ for different values of the parameter A .

The function $z(s)$ can be considered constant with a good approximation up to 80% conversion ($0 < s < 0.8$), which justifies that the observed kinetics are of apparent first-order and that the proportion of $\{\text{ArNiL}(\mu\text{-OH})\}_2$ and ArNiL_2X measured by NMR at the beginning of the reaction is representative of the composition of the mixture for most of the reaction time.

system. These results can explain the experimental observations concerning the greater sensitivity of nickel-catalyzed S-M couplings to the base and solvent combination. As stated before, only scarcely soluble inorganic bases in low-polarity solvents in the presence of controlled amounts of water enable the reaction to proceed efficiently. Under these conditions, a low concentration of available OH^- is indeed secured throughout the reaction. As a consequence the concentration of di-nuclear species **3-4** is kept low. All together these results indicate that dimeric species **3-4** are not directly involved in TM.

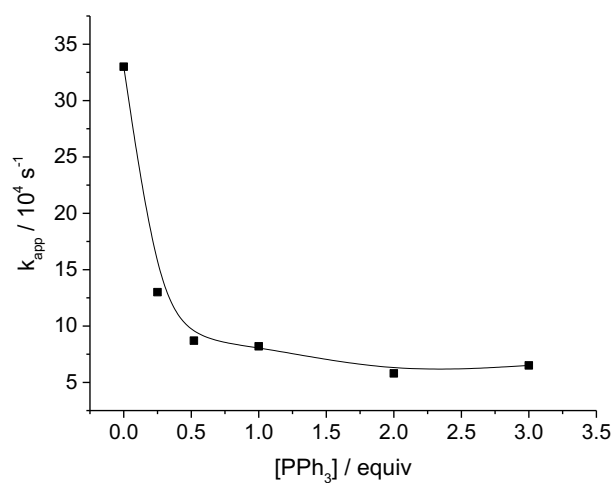
2.7. Influence of Br^- and PPh_3 on the rate of TM and RE

The influence of added bromide ions on the kinetics of the reaction of **1** with $\text{PhB}(\text{OH})_2$ was studied by addition of $n\text{Bu}_4\text{NBr}$ (TBAB). Excess of Br^- slowed the reaction down but no clear reaction order with respect to Br^- could be obtained by plotting k vs the concentration of added bromide (**Scheme 42**).



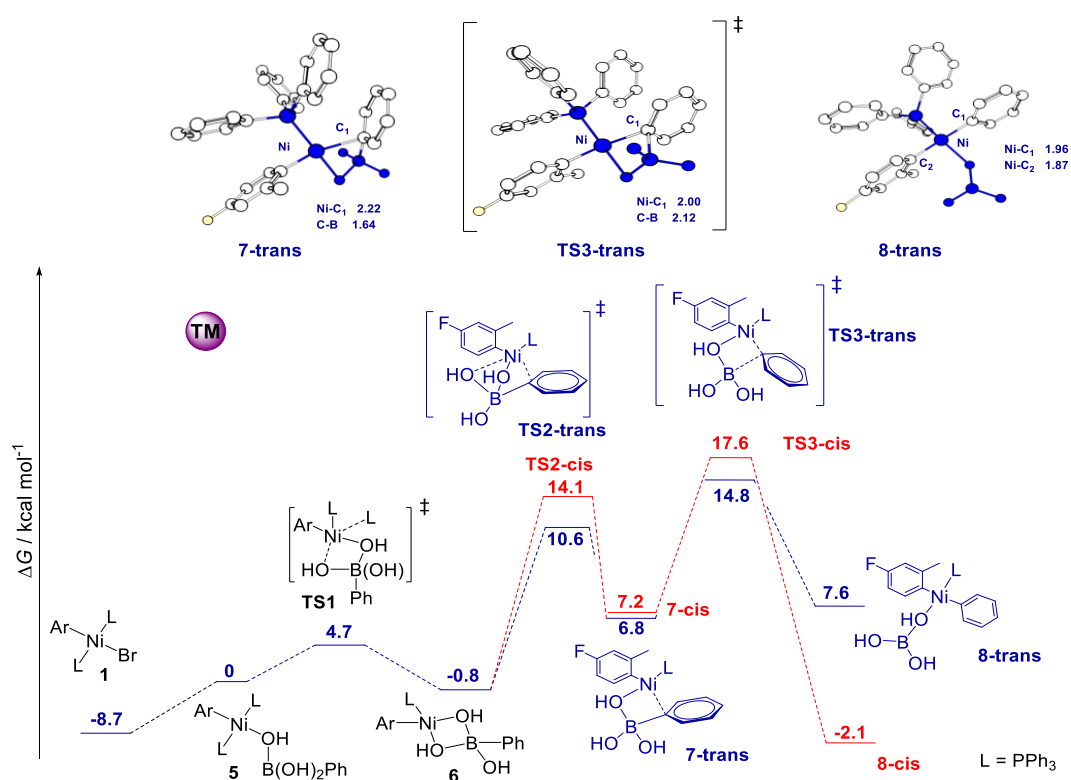
Scheme 42 - Pseudo first order rate constant (k) of the reaction of complex **1** (10 mM in dioxane) with phenylboronic acid (20 equiv) in the presence of 2 equiv of TBAOH (1.5 M in water) for various amounts of added TBABr monitored by $^{19}\text{F}\{^1\text{H}\}$ NMR at 20°C .

This observation suggests that expulsion of Br^- from the coordination sphere of the metal center is required for the TM reaction to proceed. Similarly, kinetic inhibition was observed when adding PPh_3 (**Scheme 43**), suggesting that dissociation of PPh_3 is required for the rate-determining TM event to take place.



Scheme 43 - Pseudo first order rate constant (k) of the reaction of complex **1** (10 mM in dioxane) with phenylboronic acid (20 equiv) in the presence of 2 equiv of TBAOH (1.5 M in water) for various amounts of added PPh₃ monitored by ¹⁹F NMR at 20°C.

2.8. Mechanism of the TM step



Scheme 44 - Pathway for TM process via the formation of T-shape complex **7-trans** (in blue) and **7-cis** (in red), as studied by DFT calculations. Computed relative Gibbs free energies are reported in kcal mol⁻¹. Selected bond lengths are reported in Å.

With all these data in hand, DFT calculations were performed to gain insight into the mechanism of TM and RE. Formal replacement of Br⁻ ligand in complex **1** by PhB(OH)₃⁻ yields complex **5** (**Scheme 44**). All these reactions were predicted to proceed easily at r.t. either via pentacoordinated, square-pyramidal intermediates or via direct substitution (*vide supra*).

The transition states for the whole process starting from complex **5** were located by DFT calculations (**Scheme 44**). The barrier for the TM reaction proceeding directly from the tetracoordinate intermediate **5** (TS-TM-(PPh₃)₂) was predicted to be by far inaccessible at room temperature ($\Delta G^\ddagger = 48.9$ kcal mol⁻¹). Consequently, we inferred that dissociation of one of the PPh₃ ligands should take place before TM. A similar monophosphine pathway for TM has been already proposed for the Pd-catalyzed S-M reaction.¹³³

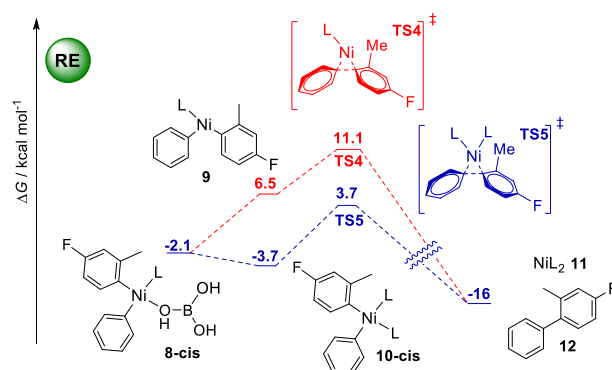
Phosphine dissociation from complex **5** to form **6** can be assisted by the coordinated boron species acting as a bidentate ligand. The intermediate **6** is a heterobimetallic Ni-B species featuring two bridging OH⁻ ligands (**Scheme 44**). The activation barrier for the formation of **6** was predicted to be only $\Delta G^\ddagger = +4.7$ kcal mol⁻¹. Decoordination from Ni of one of the bridging OH⁻ ligands can then take place, originating complexes **7-trans** and **7-cis**, in which an agostic-type interaction between the Ni center and the carbon atom linked to boron (**Scheme 44**) is established either *trans* or *cis* with respect to the Ar moiety. The formation of **7-trans** is predicted to be slightly more favorable than that of **7-cis** ($\Delta G^\ddagger = +11.4$ kcal mol⁻¹ and $+14.9$ kcal mol⁻¹, respectively), but **7-trans** and **7-cis** are approximately equally stable and their formation is endergonic with respect to **6** ($\Delta G = +7.6$ kcal mol⁻¹ and $+8.0$ kcal mol⁻¹ respectively). The C-Ni bond distance in **7-trans** is 2.22 Å, not very different from a C-Ni σ -bond (e.g. 1.96 Å in **8-trans**, *vide infra*): this interaction can be viewed as an important pre-activation for the TM step. The TM reaction can proceed starting from either **7-trans** or **7-cis**, the activation barrier being lower for the former than for the latter ($\Delta G^\ddagger = 8.0$ kcal mol⁻¹ and 10.4 kcal mol⁻¹ respectively). Interestingly, the TM product **8-trans** is significantly less stable than **8-cis** ($\Delta G = +0.8$ kcal mol⁻¹ and -9.3 kcal mol⁻¹ respectively).

To better understand these differences, the structure of the species involved was more closely examined and relevant geometric parameters are shown in **Scheme 44**. The transition state **TS3** has a reactant-like character: the C-B bond is elongated compared to **7-trans** (2.12 Å in **TS3-trans** vs. 1.64 Å in **7-trans**), but is still short compared to the product, in which there is no longer any significant interaction between those two centers. The relative stability of the **8-trans** and **8-cis** is in agreement with the *thermodynamic trans effect*, as it is unfavorable to arrange *trans* to each other the ligands having the strongest *trans* influence (i.e. the two aromatic residues).¹³⁴

¹³³ L. J. Goossen, D. Koley, H. L. Hermann, W. Thiel, *Organometallics*, **2006**, *25*, 54-67; M. A. Ortuño, A. Lledós, F. Maseras, G. Ujaque, *ChemCatChem*, **2014**, *6*, 3132-3138.

¹³⁴ R. G. Pearson, *Inorg. Chem.*, **1973**, *12*, 712-713; F. R. Hartley, *Chem. Soc. Rev.*, **1973**, *2*, 163-179.

2.9. Mechanism of the RE step



Scheme 45 - Pathways for RE step *via* the formation of T-shape complex **9** (in red) or the formation of complex **10-cis** (in blue) as studied by DFT calculations. Computed relative Gibbs free energies are reported in kcal mol⁻¹.

The product-forming RE step can proceed either through the T-shape mono-phosphine intermediate **9** or through the di-PPh₃-ligated intermediate **10-cis**. The bis-ligated pathway is favored with a transition state **TS5** lying at 3.7 *vs* 11.1 kcal mol⁻¹ for **TS4** (**Scheme 45**).¹³⁵ Nevertheless, both TS associated to the RE step are lower in energy than the TM transition state (**TS3**), which is consistent with the TM being rate-determining. As a final remark, the TM occurs from complex **6**, which is obtained via a series of equilibria involving the displacement of bromide from the coordination sphere of Ni and the decoordination of one phosphine ligand. These findings are consistent with the inhibitory effects of bromide and phosphine found experimentally by kinetic analyses.

In order to characterize the organometallic intermediate deriving from TM, the sterically hindered 2,6-dimethylphenylboronic acid (XylB(OH)₂) was employed instead of PhB(OH)₂ under experimental conditions analogous to those described previously. A mixture of 2,6-dimethylphenylboronic acid (20 equiv) and TBAOH (1 equiv) was added to a solution of complex **1** (10 mM in dioxane) and the reaction was monitored by multinuclear NMR spectroscopy (**Figure 14**).

Using this substrate, the formation of the coupling product (ArXyl) was quite slow and two new organometallic complexes were observed by ³¹P{¹H} and ¹⁹F{¹H} NMR at δ = 20.8 and -126.1 ppm and δ = 20.2 and -127.1 ppm respectively.¹³⁶

¹³⁵ This behaviour is in contrast to what was described in the case of Pd for which the TM proceed either from a T-shape intermediate (M. K. Loar, J. K. Stille, *J. Am. Chem. Soc.*, **1981**, *103*, 4174-4181) or via a pentacoordinated intermediate (C. Amatore, A. Jutand, G. Le Duc, *Chem. Eur. J.*, **2011**, *17*, 2492-2503) see also E. W. Abel, F. Gordon A. Stone, G. Wilkinson, R. J. Puddephatt, A. K. Smith, *Comprehensive Organometallic Chemistry II*, **1995**, Vol 9, p 62, Elsevier.

¹³⁶ The formation of 3-fluorotoluene was a significant side reaction under these conditions. Since the rate of appearance of this byproduct matched that of the formation of OPPh₃ (apparent rate constant $k_{app} = 1.7 \cdot 10^{-6} \text{ s}^{-1}$), we speculate that this apparent proto-demetalation is actually a redox process, which may be thought to take place stepwise, formally:

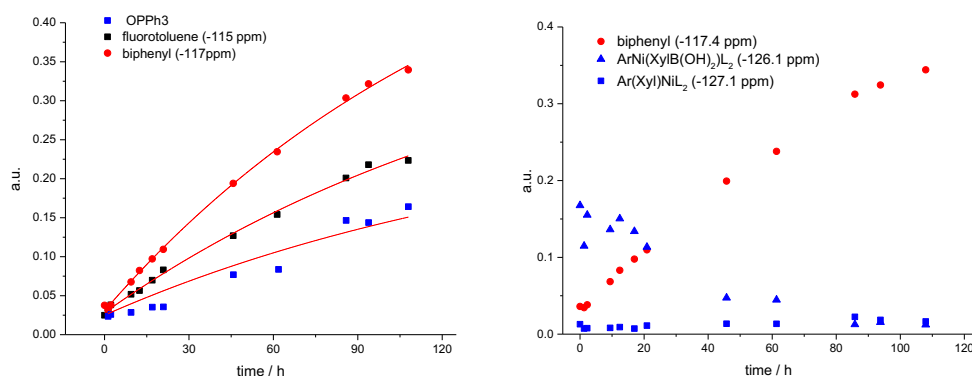


Figure 14 - Kinetic of the reaction of 2,6-dimethylphenyl boronic acid with complex **1** monitored by $^{31}\text{P}\{^1\text{H}\}$ and $^{19}\text{F}\{^1\text{H}\}$ NMR.

The complex at -126.1 ppm appeared rapidly and decreased as the reaction proceeded, in a pattern compatible with a quickly formed intermediate. In contrast, the complex at -127.1 ppm was only formed in small amounts with a maximal concentration reached at a later stage of the reaction. The first intermediate could reasonably be attributed to the associative complex $\text{ArNi}(\text{XylB}(\text{OH})_3)(\text{PPh}_3)_2$ (analogous to complex **5**) while the second could be the TM complex *trans*- $[\text{ArNi}(\text{Xyl})(\text{PPh}_3)_2]$.¹³⁷

To confirm this hypothesis, the transition states for TM and RE involving complex **1** and $\text{XylB}(\text{OH})_2$ were located by DFT calculations (Figure 7). The free energy gap between **TS3-trans** and **TS5** decreased from 11.1 kcal mol⁻¹ for $\text{PhB}(\text{OH})_2$ to 6.4 kcal mol⁻¹ for $\text{XylB}(\text{OH})_2$ (Figure 15), meaning that steric hindrance on the aryl moiety coming from the boronic acid hampers RE more than TM, in agreement with the fact that it was possible in this case to observe the intermediate TM product.

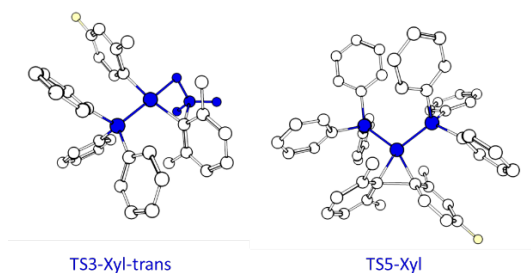
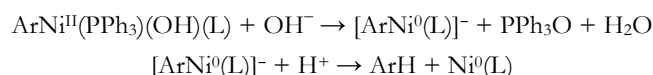


Figure 15 - Structures of the transition states for TM (left) and RE (right) for the reaction of **1** with $\text{XylB}(\text{OH})_2$ (Xyl = 2,6-(Me)₂C₆H₃).



¹³⁷ The $^{31}\text{P}\{^1\text{H}\}$ chemical shift between the *trans*- $[\text{ArNiAr}'(\text{PPh}_3)_2]$ and *trans*- $[\text{ArNiBr}(\text{PPh}_3)_2]$ (**1**) is similar to that observed in the case of analogous Pd complexes: e.g. for *trans*- $[(4\text{-NC-C}_6\text{H}_6)\text{PdBr}(\text{PPh}_3)_2]$ $\delta = 23.7$ ppm and for *trans*- $[\text{PhPd}(4\text{-NC-C}_6\text{H}_4)(\text{PPh}_3)_2]$ $\delta = 22.4$ ppm (see ref. 3d) so $\Delta\delta = -1.3$ ppm, to be compared with $\Delta\delta = -1.5$ ppm in our case.

2.10. Electronic Effects of TM

Electronic effects due to the substituents on both the electrophile and the organoboron derivatives are among the most important parameters that usually influence the outcome of S-M reactions. Moreover, for the construction of a non-symmetrical biaryl Ar-Ar', two pairs of electrophile/boron derivative partners are possible in principle (either ArB(OH)₂ and Ar'X or Ar'B(OH)₂ and ArX) and it is not obvious how to make the most appropriate choice without prior experiments. Since TM is the rate-determining step of the catalytic cycle, electronic effects due to the boronic acid partner are likely more important than those on the electrophile (except for substrates for which OA is actually rate-determining, such as chloroarenes).¹³⁸ Unfortunately, literature reports are not unanimous on this point. Positive, negative, or zero Hammett ρ values have been observed for various Pd-catalyzed S-M couplings.¹³⁹ Interestingly, for some Ni-catalyzed S-M reactions, electron-poor arylboronic acids react faster than electron-rich ones, which is counterintuitive if we consider that the organo-boron derivative is playing the role of a nucleophile in the TM step.¹⁴⁰ To assess the effect of substituents on the arylboronic acid, two Hammett plots were constructed using *para*-substituted boronic acids at two different initial boronic acid/TBAOH ratios (Figure 16). For a TBAOH / PhB(OH)₂ molar ratio of 0.4, the trend we found is in agreement with the literature:³⁵ electron-poor boronic acids react faster than electron-rich ones (Figure 16, a).

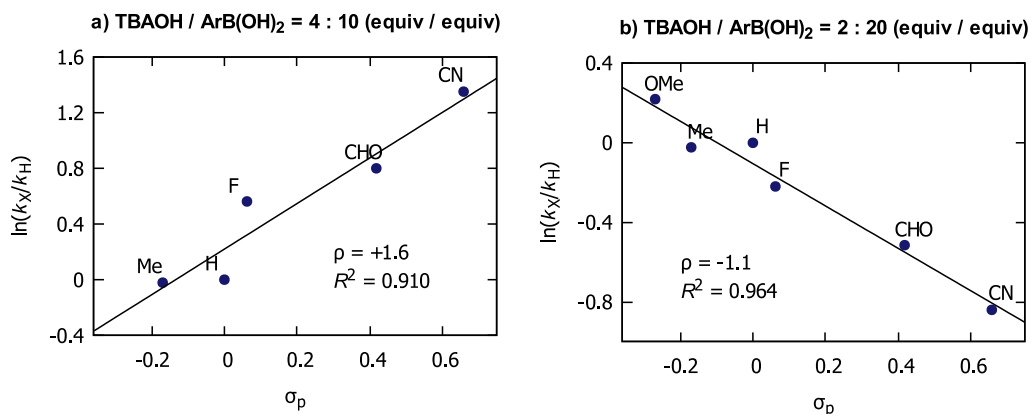


Figure 16 - Hammett correlations for the reaction of complex **1** at 20°C with: (a) aryl boronic (10 equiv) and TBAOH (4 equiv, concentration of **1**: 20 mM in dioxane); (b) aryl boronic (20 equiv) and TBAOH (2 equiv, concentration of **1**: 10 mM in dioxane).

To understand the electronic origin of this pattern, the activation barrier for TM was calculated at the DFT level for the same boronic acids. The results obtained were in complete disagreement with the experiment, with electron-rich boronic acids predicted to react faster than electron-poor ones (Figure 17).

¹³⁸ S. Saito, S. Oh-tani, N. Miyaura, *J. Org. Chem.*, **1997**, *62*, 8024-8030.

¹³⁹ A. J. J. Lennox, G. C. Lloyd-Jones, *Angew. Chem. Int. Ed.*, **2013**, *52*, 7362-7370.

¹⁴⁰ D. Zim, V. R. Lando, J. Dupont, A. L. Monteiro, *Org. Lett.*, **2001**, *3*, 3049-3051.

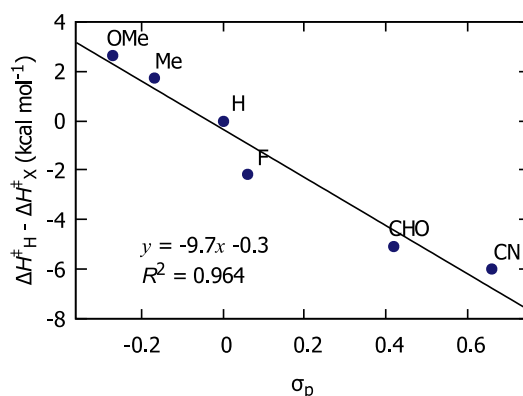


Figure 17 - Variation of the activation energy barrier (with respect to the case of PhB(OH)₂) of TM step for different *para*-substituted phenylboronic acids with complex **1**, as predicted by DFT calculations.

We expected that such effect could be due to the pre-equilibria involving species **3-4** and the boronic acid (**Scheme 33**). For this reason, we performed a second Hammett correlation at a lower TBAOH / PhB(OH)₂ ratio of 0.1. Under these conditions, electron-rich boronic acids actually reacted faster (**Figure 16, b**). The intrinsically higher reactivity of electron-rich boronic acids can be attributed to the positive variation of the partial charges located on the aromatic ring going from the free arylboronic acid to the transition state. Boronic acids have a nucleophile-like behaviour and the nickel centre acts as an electrophile. For instance, in the case of PhB(OH)₂ partial charge on nickel calculated by the NBO method¹⁴¹ decreases from +0.27 |e⁻| to +0.18 |e⁻| going from **7-trans** to **TS3-trans**. Simultaneously, the charge increases from -0.54 |e⁻| to -0.33 |e⁻| on PhB(OH)₃⁻ moiety.

This comparison highlights the strong role played by hydroxide in the nickel-catalyzed S-M coupling. At high base concentration, pre-equilibria dominate the kinetics: electron-poor boronic acids react faster than electron-rich ones, because they are more Lewis-acidic and thus the equilibria involving organonickel complexes are displaced away from unreactive hydroxo-bridged dimers **3-4**. At lower base concentration, however, the largely prevalent organonickel species is the mononuclear complex **1**. In this case, the observed electronic effects are directly correlated with the activation barriers for the TM.

Our findings clarify the ambiguity underlined by Lloyd-Jones and collaborators in their recent review of 2013 about the Pd-catalyzed S-M reaction:¹⁴² the authors suggested that since the S-M reaction features multiple steps involving the boron reagent, and that detailed studies of the electronic effects on each discrete step would have been necessary to explain the apparently contradictory observations regarding the influence of substituents on the rate of the overall reaction.

¹⁴¹ J. P. Foster, F. Weinhold, *J. Am. Chem. Soc.*, **1980**, *102*, 7211-7218; A. E. Reed, R. B. Weinstock, F. Weinhold, *J. Chem. Phys.*, **1985**, *83*, 735-746.

¹⁴² A. J. Lennox, G. Lloyd-Jones, *Angew. Chem. Int. Ed.*, **2013**, *52*, 7362-7370.

2.11. Effects of the counter-ion

As counter-cations introduced together with inorganic bases proved to be non-innocent in the Pd-catalyzed S-M coupling,¹⁴³ it was interesting to investigate whether analogous observations hold also for Ni catalysis. Moreover, these effects have been demonstrated for Pd in a strongly dissociating solvent (DMF). The less polar solvents commonly employed for nickel-catalyzed S-M couplings are expected to promote the formation of tighter ion pairs, thus enhancing the effect of cations.

First, the influence on the equilibria between **1** and μ -OH species **3-4** was studied by $^{19}\text{F}\{^1\text{H}\}$ NMR at a fixed $\text{OH}^-/\text{PhB}(\text{OH})_2$ molar ratio of 0.2 by varying the source of OH^- among TBAOH, NaOH, KOH and CsOH (**Figure 18**). In every case, the fraction of **1** converted to **3-4** was higher in the presence of alkali cations than for $n\text{Bu}_4\text{N}^+$, varying from 67% to 99.5% in the order $n\text{Bu}_4\text{N}^+ < \text{Na}^+ < \text{K}^+ < \text{Cs}^+$. In the presence of alkali cations, thus, unreactive species **3-4** are more favorable to form.

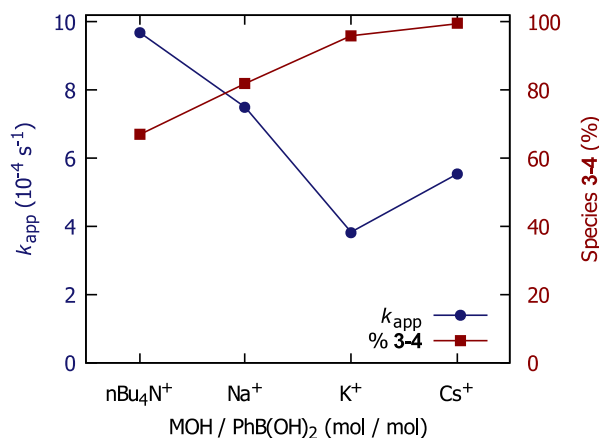


Figure 18 - Left scale: pseudo-first order rate constants for the reaction of complex **1** (20 mM in dioxane) with phenylboronic acid (10 equiv) at 20°C in the presence of TBAOH, NaOH, KOH or CsOH (2 equiv, all added as 1.5 M solution in water), as monitored by ^{19}F NMR spectroscopy. Right scale: percentage of **1** converted to species **3-4** just after mixing all the reactants.

The influence of these ions on reactivity was also evaluated. The apparent first-order rate constants for the TM-RE process obtained under the previously described conditions are also reported in **Figure 18**. As expected from the effect on the speciation of aryl-nickel complexes and in analogy to what observed for Pd,¹⁴² alkali cations slow the reaction down compared to $n\text{Bu}_4\text{N}^+$. The effect is the most important for K^+ , the reaction being approximately 2.5 times slower for KOH than for TBAOH under these conditions. No obvious relationship could be established between the previously described effect on the pre-equilibria involving **3-4** and the observed rate constants, since the latter varied in the order $\text{K}^+ < \text{Cs}^+ < \text{Na}^+ < n\text{Bu}_4\text{N}^+$.

¹⁴³ C. Amatore, A. Jutand, G. Le Duc, *Chem. Eur. J.*, **2012**, *18*, 6616-6625.

This complex picture may be justified by assuming that cations not only have an influence on the equilibria involving arylnickel species and OH^- , but they also interfere with the TM step by formation of ion pairs with the anion released during the reaction (Br^- in the case of **1**) or by association with the actual species that undergoes TM. These effects are expected to be very solvent-dependent. Moreover, in real-life catalytic couplings, solubility issues may also come into play and tune the available concentration of OH^- .

2.12. Effects of the nature of the halide and of the phosphine

As already stated in the introduction, a wide variety of electrophiles can be useful substrates for the nickel-catalyzed S-M reaction. In particular, readily available and cheap chloroarenes can be activated under mild conditions without using expensive ligands, which is a major advantage compared to palladium. In this perspective, we investigated whether substituting the Br^- ligand with Cl^- in the model complex **1** would have significant impact on reactivity. Complex *trans*- $[\text{ArNi}(\text{PPh}_3)_2\text{Cl}]$ (**1-Cl**, Ar = 4-F-2-Me- C_6H_4), which is representative of the product deriving from the OA of a chloroarene with $\text{Ni}(0)$, was thus prepared.¹⁴⁴

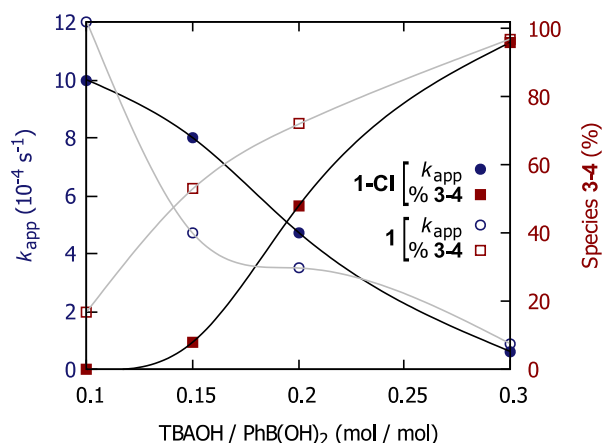
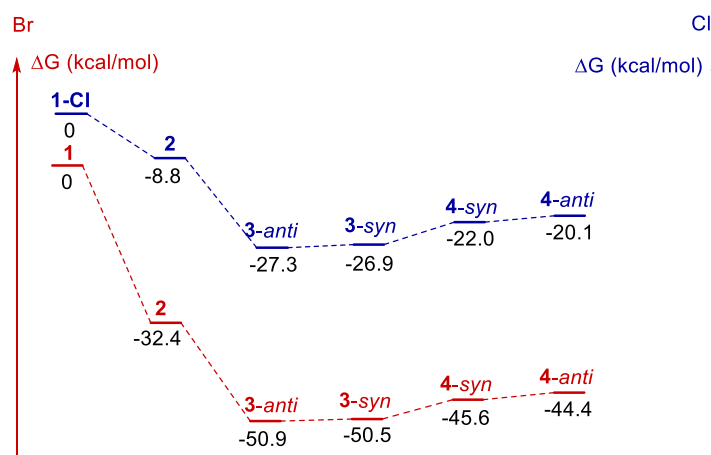


Figure 19 - Left scale: pseudo first order rate constant of the reaction of complex **1-Cl** and **1** (10 mM in dioxane) with $\text{PhB}(\text{OH})_2$ (20 equiv) in the presence of various amounts of added TBAOH (1.5 M in water) at 20°C monitored by $^{19}\text{F}\{^1\text{H}\}$ NMR. Right scale: percentage of complex **1-Cl** and **1** converted to species **3-4**, as assessed by $^{19}\text{F}\{^1\text{H}\}$ NMR.

First, the formation of species **3-4** in the presence of TBAOH and $\text{PhB}(\text{OH})_2$ was investigated (**Figure 19**) under experimental conditions similar to those described for complex **1**. **Figure 19** shows that in the case of complex **1-Cl** a smaller fraction of complex is converted to $\mu\text{-OH}$ species than for complex **1** at any TBAOH/ $\text{PhB}(\text{OH})_2$ ratio. This observation may be ascribed to the higher affinity of the Ni center for Cl^- than for Br^- . This hypothesis is supported by DFT calculations (**Scheme 46**).

¹⁴⁴ Complex **1-Cl** was obtained by halogen exchange: a solution of **1** in dichloromethane was treated with a saturated aqueous solution of NaCl. See the annexes for details.



Scheme 46 - Affinity toward hydroxide ligation, comparison between Cl⁻ and Br⁻ ligated nickel complexes.

A similar trend was found for analogous Pd complexes.¹⁴⁵ As a consequence, the formation of dinuclear species **3-4** not directly involved into the TM reaction is less important for catalytic reactions involving chloroarenes rather than bromoarenes. However, DFT calculations predict that the formation of intermediate **5** by the reaction with PhB(OH)₃⁻ is more endergonic starting from complex **1-Cl** (ΔG = 20.5 kcal mol⁻¹) rather than from complex **1** (ΔG = 8.7 kcal mol⁻¹), leading to a higher effective activation barrier for the TM process. The interplay of these two antagonistic effects (less favorable formation of inactive dinuclear species and more difficult coordination of PhB(OH)₃⁻) subtly tunes the relative reactivity of **1** and **1-Cl**.

The electron-rich, bulky PCy₃ is one of the most useful ligands for Ni-catalyzed S-M couplings.¹⁴⁶ We thus studied the B-to-Ni TM step involving the PCy₃-ligated complex *trans*-[ArNi(PCy₃)₂Cl] (**13**, Ar = 4-CF₃-C₆H₄), which has already been examined in a previous work.¹⁴⁷ Experiments were done under conditions analogous to that used for **1-Cl**, in order to make meaningful comparisons. Complex **13** in dioxane is characterized by a broad singlet at 12.6 ppm in ³¹P{¹H} NMR, upon addition of TBAOH (1 equiv) a single new peak appeared at 30.6 ppm corresponding to the *trans* dinuclear complex isolated by Monfette and co-workers. Differently from complex **1**, a significant amount of the starting complex **13** was still visible and excess TBAOH (1.5 equiv) was necessary to make it disappear completely. Interestingly, complex **13** exhibits thus lower affinity toward hydroxides compared to compounds **1** and **1-Cl**.

The kinetics of the reaction of complex **13** with PhB(OH)₂ were studied for various base/boronic acid ratios and a bell-shape curve having a maximum for a TBAOH/PhB(OH)₂ molar ratio around 0.4 was obtained (**Figure 20**). This maximum rate was lower than that found for PPh₃-ligated complexes. The deactivation effect of excess base on the kinetic of TM is less important in the case of complex **13** than in the case of complex **1** and **1-Cl**.

¹⁴⁵ C. Amatore, E. Carré, A. Jutand, *Acta Chem. Scand.*, **1998**, *52*, 100-106.

¹⁴⁶ B. M. Rosen, K. W. Quasdorf, D. A. Wilson, N. Zhang, A.-M. Resmerita, N. K. Garg, V. Percec, *Chem. Rev.*, **2011**, *111*, 1346-1416.

¹⁴⁷ A. H. Christian, P. Müller, S. Monfette, *Organometallics*, **2014**, *33*, 2134-2137.

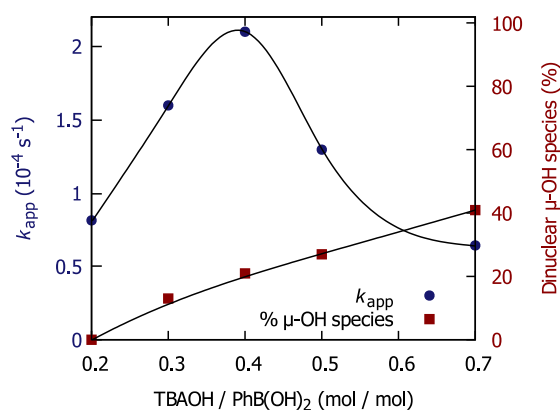
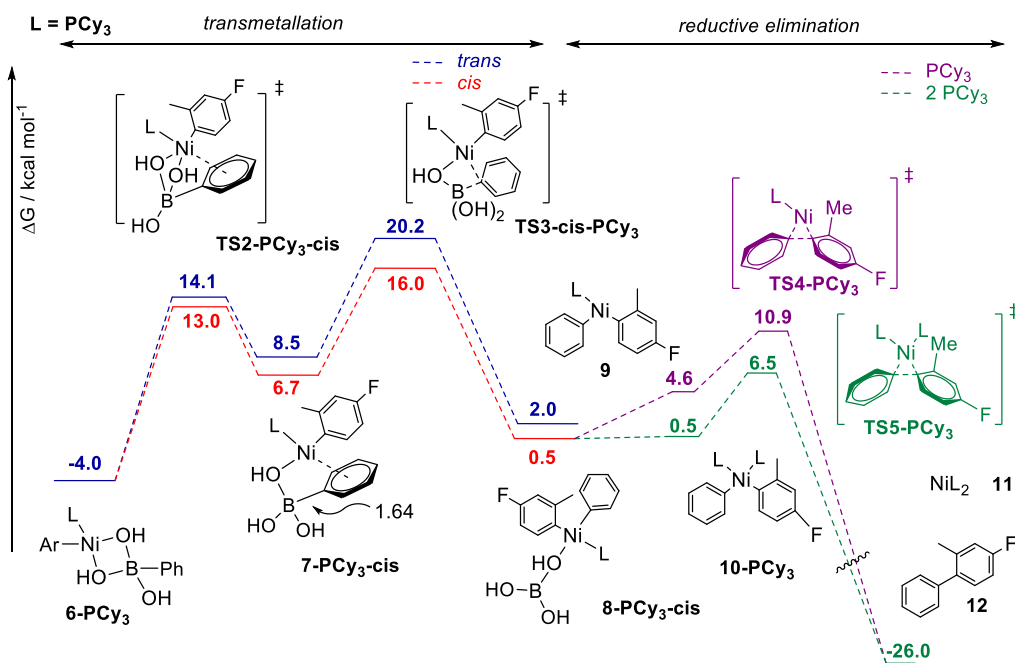


Figure 20 - Left scale: pseudo first order rate constant of the reaction of complex **13** (10 mM in dioxane) with phenylboronic acid (20 equiv) for various amounts of added TBAOH (1.5 M in water) at 20°C monitored by $^{19}\text{F}\{^1\text{H}\}$ NMR. Right scale: percentage of complex **13** converted to dinuclear species $\mu\text{-OH}$, as assessed by $^{19}\text{F}\{^1\text{H}\}$ NMR.

This is consistent with the lower affinity for OH^- of complex **13** evidenced by NMR spectroscopy. The behavior of the latter nickel complex is thus half-way between the more oxophilic nickel complex **1** (with an optimal TBAOH/ $\text{PhB}(\text{OH})_2$ ratio lower than 0.1) and their palladium-based analogues $[\text{ArPd}(\text{PPh}_3)_2\text{Br}]$ (with an optimal TBAOH/ $\text{PhB}(\text{OH})_2$ molar ratio around 0.8).¹⁴⁸

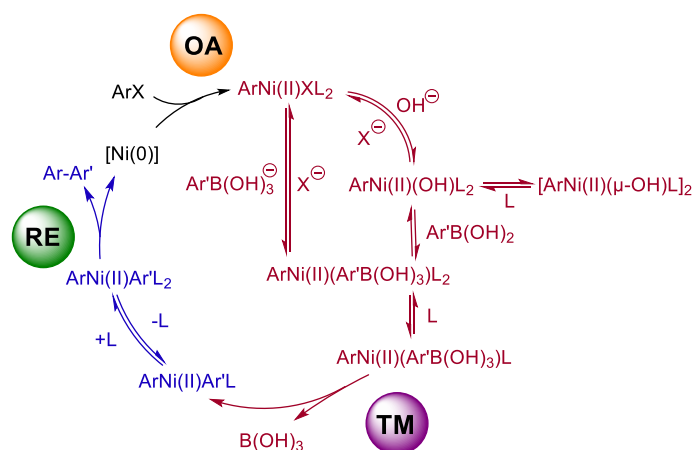


Scheme 47 - Pathway for TM process for PCy_3 , as studied by DFT calculations. Computed relative Gibbs free energies are reported in $\text{kcal}\cdot\text{mol}^{-1}$.

¹⁴⁸ Amatore, C.; Jutand, A.; Le Duc, G. *Chem. Eur. J.*, **2011**, *17*, 2492.

The effect of substituting PPh₃ with PCy₃ was also evaluated by studying the complete reaction pathway at the DFT level (**Scheme 47**). Both *cis* and *trans* TM transition state **TS3-PCy₃** were calculated and in contrast to the case of PPh₃, **TS3-PCy₃-cis** was found lower in energy than **TS3-PCy₃-trans** (16.0 *vs* 20.2 kcal mol⁻¹). This inversion is likely due to important steric hindrance in the *trans* TS between Ar moieties and the bulky PCy₃ ligand. Nevertheless, both the *cis* and *trans* activation barriers are higher than for the analogous PPh₃ case (**Scheme 44**), which is in agreement with the experimental reactivity trend. Based on electronic effects, it is possible to rationalize this lower reactivity. Indeed, as explained in the previous sections, the nickel center behaves as an electrophile, while the organoboron reagent plays the role of a nucleophile. With the electron-rich ligand PCy₃ the center is less electrophilic: the NBO partial charge on Ni is -0.60 |e⁻| in **TS3-PCy₃-trans** to be compared with -0.18 |e⁻| in **TS3-trans** (featuring PPh₃ as a ligand). Despite of an intrinsically lower reactivity towards the B-to-Ni TM reaction, the reduced sensitivity of PCy₃-ligated aryl-nickel species *vis-à-vis* the inhibition due to excessive [OH⁻] are likely key factors contributing to the efficiency and generality of PCy₃-based protocols for the Ni-catalyzed S-M reaction.

2.13. Conclusions



Scheme 48 - Revised catalytic cycle for the nickel-catalyzed Suzuki-Miyaura coupling.

The key steps of the S-M coupling reaction proceeding through arylnickel (II) complexes have been examined in detail. The interaction of a model complex **1** with OH⁻ has been studied, revealing that dinuclear μ -hydroxo-bridged complexes **3-4** are the main species formed, as already demonstrated for a related system (**Scheme 48**).¹⁴⁹

Nevertheless, kinetic analyses and theoretical studies showed that μ -hydroxo-bridged complexes **3-4** are not directly involved in transmetalation, but they rather act as a resting state for the catalyst. The relative affinity of the nickel and of the boron center for OH⁻ tunes the proportion of unchanged **1** and **3-4** actually present in solution under catalytic conditions. The boronic acid / OH⁻ couple thus acts as a buffer system and the ratio of these two species has a strong

¹⁴⁹ Christian, A. H.; Müller, P.; Monfette, S. *Organometallics*, **2014**, *33*, 2134.

influence on the rate of B-to-Ni transmetalation. The reaction, indeed, is slowed down by excessive amounts of OH⁻.

This effect, already observed for the Pd-catalyzed S-M coupling,¹⁵⁰ is exacerbated in the case of the Ni-catalyzed S-M reaction, since nickel has a greater affinity for OH⁻. This is most likely one of the reasons why Ni-catalyzed S-M protocols are rather little employed in practical synthesis: Ni-catalyzed S-M reactions are efficient under a narrower set of experimental conditions, and this range is substrate-dependent.¹⁵¹

A complex overall picture emerged, with the base playing multiple antagonistic roles. Capitalizing on the mechanistic information we collected, the following guidelines for the rational optimization of Ni-catalyzed Suzuki couplings can be given:

- a) the amount of available OH⁻ should be kept reasonably low at all time during the reaction, either by properly choosing an inorganic base/solvent couple and/or by slow addition; the amount of water in the solvent should also be controlled;
- b) the p*K*_a of boronic acids can span more than three orders of magnitude and it is of paramount importance for the reactivity, since not only it dictates the intrinsic reactivity towards B-to-Ni TM, but it also controls the proportion of inactive hydroxo-species formed in solution;¹⁵²
- c) PCy₃-ligated organonickel species are less prone to deactivation due to excessive [OH⁻], the optimization of the base/solvent combination may be less critical than for PPh₃ as a ligand.

Finally, based on this study we may give one additional warning: the nature of the leaving group of the electrophilic partner influences not only the OA step, but also the affinity of the resulting arylnickel(II) complex for OH⁻, thus experimental conditions for challenging substrates may not be transferable among different electrophile classes in an easily predictable way (e.g. bromoarenes give faster OA with Ni(0) than chloroarenes, but the resulting OA complex is more prone to the formation of inactive hydroxo-species).

¹⁵⁰ C. Amatore, A. Jutand, G. Le Duc, *Chem. Eur. J.*, **2011**, *17*, 2492-2503.

¹⁵¹ The nature of the base determines the concentration of available OH⁻, which is also limited by the solubility in the chosen solvent. This observation explains why only weak inorganic bases (such as carbonates and phosphates) that are scarcely soluble in low-polarity solvents, often together with a controlled amount of water, are useful for Ni-catalyzed S-M coupling.

¹⁵² For example, the p*K*_a = 9.7 for 2-tolylboronic acid in water and p*K*_a = 6.0 for 2-fluoro-5-nitrophenylboronic acid; see D. G. Hall, *Boronic Acids*, 2011, Wiley, pp. 1-133. for a complete survey on the acidity of boronic acids.

CHAPTER III

Lewis Acid and Redox Catalytic Properties of Triflate and Triflimide Salts

“Or donc, si je comprends bien, vous faites, et vous savez pourquoi vous faites, mais vous ne savez pas pourquoi vous savez que vous savez ce que vous faites ?”

U. Eco, Le nom de la Rose

The work exposed in this chapter resulted in three publications:

P.-A. Payard, Q. Gu, W. Guo, Q. Wang, J. Lai, M. Corbet, C. Michel, P. Sautet, L. Grimaud,
R. Wischert,* and M. Pera-Titus*

*Direct Amination of Alcohols Catalyzed by Aluminum Triflate:
an Experimental and Computational Study*
Chem. Eur. J., **2018**, *24*, 14146

P.-A. Payard,* C. Finidori, L. Guichard, D. Cartigny, M. Corbet, L. Khrouz, L. Bonneviot,
R. Wischert, L. Grimaud,* M. Pera-Titus*

*Rational Design of Lewis Superacids Leading to an Unprecedented Ti(III) Triflimide Catalyst for the
Direct Amination of Alcohols*
Manuscript in preparation

P.-A. Payard, Y.-T. Zheng, W. Zhou,* L. Khrouz, L. Bonneviot, C. Michel, R. Wischert,
L. Grimaud, M. Pera-Titus*

*Iron Triflate Salts as Precursor of Highly Active and Selective Catalyst for Solvent-Free
Oxidation of Cyclohexane*
Manuscript in preparation

1. Triflate and Triflimide Salts in Catalysis

1.1. Lewis Acidity: Definition and Quantification

Definition. The first *molecular* definition of acidity was proposed in 1884 by Arrhenius in his thesis: an acid was defined as a proton (H⁺) donor molecule and a base as a hydroxide (OH⁻) donor.¹⁵³ In 1923, Brønsted and Lowry independently suggested a more convenient definition of a base as a proton acceptor (avoiding the limitation to aqueous conditions).¹⁵⁴ The same year, Lewis offered a much more general definition: a Lewis acid (LA) is an *electron pair acceptor* entity and a Lewis base is an *electron pair donor*.¹⁵⁵ Note that, while Lewis base is always a Brønsted base, a Lewis acid may behave as a Brønsted acid only in the presence of water:



The main drawback of this definition is that the interaction between an electron vacancy and a doublet (Lewis base, LB) depends on a multiplicity of parameters such as the electrostatic interaction, covalent bonding and dispersion forces, which can show a non-trivial contribution depending on the LB. The Pearson Hard and Soft Acid and Base (HSAB) theory was developed to tackle this problem.¹⁵⁶ Hard acids are Lewis acids with an acceptor centre of low polarizability and soft acids are acceptor centres of high polarizability.¹⁵⁷ Thus, hard acids will combine preferentially with hard bases and soft acids with soft bases. Klopman¹⁵⁸ proposed to decompose the electronic energy of formation of the Lewis adduct into two mathematical terms (Eq below) the first one related to the electrostatic interactions and the second to the covalent part. Schematically, the first term corresponds to the hard-hard interaction and the second one to the soft-soft one.

$$\Delta E = \frac{q_a q_b}{\epsilon R_{ab}} + 2 \sum_{\text{occupied orbitals } m} \sum_{\text{unoccupied orbitals } n} \frac{(C_a^m C_b^n \beta_{mn})^2}{E_m - E_n}$$

It is interesting to compare the difference of this definition with other closely related concepts that will be used in the following sections. The definition of an oxidizing agent, i.e. an entity able to

¹⁵³ S. Arrhenius, *Recherches sur la conductivité galvanique des électrolytes*, **1884**, doctoral dissertation.

¹⁵⁴ J. Brønsted, *Recl. Trav. Chim. Pays-Bas.*, **1923**, *42*, 718-728; T. Lowry, *J. Chem. Technol. Biotechnol.*, **1923**, *42*, 43-47.

¹⁵⁵ G. N. Lewis, *Valence and the Structure of Atoms and Molecules*, The Chemical Catalog Co., **1923**, 141-142; G. N. Lewis, *J. Am. Chem. Soc.*, **1916**, *38*, 762-785; P. Muller, *Pure Appl. Chem.*, **1994**, *66*, 1077-1184, p1135; W. B. Jensen, *Chem. Rev.*, **1978**, *78*, 1-22.

¹⁵⁶ R. G. Pearson, *J. Am. Chem. Soc.*, **1963**, *85*, 3533-3539; S. Woodward, *Tetrahedron*, **2002**, *58*, 1017-1050; R. G. Pearson, *Acc. Chem. Res.*, **1993**, *26*, 250-255; R. G. Pearson, *J. Chem. Sci.*, **2005**, *117*, 369-377.

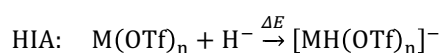
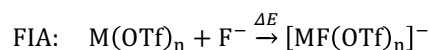
¹⁵⁷ P. Muller, *Pure Appl. Chem.*, **1994**, *66*, 1077-1184, p1120.

¹⁵⁸ R. F. Hudson and G. Klopman, *Tetrahedron Lett.*, **1967**, *12*, 1103-1108; R. F. Hudson and G. Klopman, *Theor. Chim. Acta*, **1967**, *8*, 165-168; G. Klopman, *J. Am. Chem. Soc.*, **1968**, *90*, 223-234.

accept the *transfer of one or several electrons*, seems very close to the one of Lewis acidity.¹⁵⁹ The nuance is that in the Lewis theory the electrons are supposed to be put in common to create the Lewis adduct (LA-LB) while in redox chemistry the transfer is supposed total. In a number of cases however the definitions overlap, particularly in the case of transition metals that behave both as redox center and Lewis acid. In this case, an increase of the Lewis acidity results in an increase of the electrochemical potential.¹⁶⁰ Another closely related concept is electronegativity, defined by Pauling as the ability of an atom to attract electrons to itself.¹⁶¹ The concept has been extended by Parr to any molecular entity.¹⁶² The difference with the Lewis definition is that Lewis acidity does not assess the extent of the electronic density transferred (the Lewis adduct may be covalent or ionic, for instance Na⁺ may form Lewis adducts but has only a poor electronegativity) but about the stability of the formed adduct. Finally, the electrophilicity, is related to the relative reactivity of an electrophilic reagent: this concept is quantified by the kinetics of a reaction while the Lewis acidity is, *a priori*, quantified by thermodynamic data.¹⁵⁶

Scale of Lewis acidity. A general controversy in the Catalysis community is how to establish a handy Lewis acidity scale.¹⁶³ Indeed, most often, the choice of a Lewis acid as catalyst encompasses a narrow selection of metal salts with few attempts for *rationale*. However, different methods have been proposed to assess the Lewis acidity.

The most extended method relies on experimental or calculated affinities, namely the enthalpy or Gibbs free energy of formation of the acid-base adduct. An intrinsic difficulty of this method is that the scale depends on the LB used. Indeed, the most used scale based on affinity, the Fluorine Ion Affinity (FIA),¹⁶⁴ quantifies rather the fluorophilicity than the Lewis acidity. Other scales have been proposed,¹⁶⁵ such as the Hydride Ion Affinity (HIA) for soft acids,¹⁶⁶ and the oxophilicity scale.¹⁶⁷ Although the result is doubtless a measurement of the Lewis acidity, the relationship between the reactivity and the stability of the Lewis acid-base adduct is not straightforward.



¹⁵⁹ P. Muller, *Pure Appl. Chem.*, **1994**, *66*, 1077-1184, p1148.

¹⁶⁰ D. B. Williams, M. E. Stoll, B. L. Scott, D. A. Costa, J. W. J. Oldham, *Chem. Commun.*, **2005**, 1438-1440; J. R. Cabrero-Antonino, A. Leyva-Pérez, A. Corma, *Chem. Eur. J.*, **2012**, *18*, 11107-11114.

¹⁶¹ *Pure Appl. Chem.* **1994**, *66*, 1077-1184, p1111.

¹⁶² R. G. Parr, R. G. Pearson, *J. Am. Chem. Soc.* **1983**, *105*, 7512-7516; R. G. Parr, W. Yang, *J. Am. Chem. Soc.*, **1984**, *106*, 4049-4050.

¹⁶³ L. Greb, *Chem. Eur. J.*, **2018**, *24*, 17881-17896; S. Antoniotti, V. Dalla, E. Duñach, *Angew. Chem. Int. Ed.*, **2010**, *49*, 7860-7888.

¹⁶⁴ J. C. Haartz, D. H. McDaniel, *J. Am. Chem. Soc.*, **1973**, *95*, 8562-8565.

¹⁶⁵ H. Böhrer, N. Trapp, D. Himmel, M. Schleep, I. Krossing, *Dalton Trans.*, **2015**, *44*, 7489-7499.

¹⁶⁶ K. B. Yatsimirskii, *Theor. Exp. Chem.*, **1981**, *17*, 75-79.

¹⁶⁷ K. P. Kepp, *Inorg. Chem.*, **2016**, *55*, 9461-9470.

A second method is based on the modification of a physical property (e.g. IR wave number, ^{31}P or ^1H NMR chemical shift) due to a change of electronic density of a LB probe (phosphine,¹⁶⁸ carbonyl,¹⁶⁹ amine,¹⁷⁰ RCN¹⁷¹) by transfer to the LA. The measured property should thus be correlated to theoretical indicators such as the *electronegativity* (χ) of a molecule as defined by Parr,¹⁷² or to the “global electrophilicity index” (GIE, ω).¹⁷³

Finally, a third method consists of measuring rate constants for LA-catalyzed model reactions.¹⁷⁴ In such a case, the rate constants are not directly correlated to the Lewis acidity, but rather to the *electrophilicity*.

1.2. Triflate and triflimide salts: history, preparation and characterisation

Lewis Superacids (LSA). The term superacid was first coined with regards to the Brønsted definition of an acid: a Brønsted superacid is more acidic than pure sulfuric acid.¹⁷⁵ By extension of this concept, several definitions of LSA have been proposed.¹⁷⁶ Dunach and co-workers¹⁷⁷ defined a LSA as a salt consisting of a metal cation and the conjugated base of a BSA, which is especially adapted to metal triflate $[\text{M}(\text{OTf})_n]$ ($\text{OTf} = \text{SO}_3\text{CF}_3$) and metal triflimide $[\text{M}(\text{NTf}_2)_n]$, $\text{NTf}_2 = \text{N}(\text{SO}_3\text{CF}_3)_2$, salts. In a recent review,¹² Greb proposed a more general definition of LSA

¹⁶⁸ U. Mayer, V. Gutmann, W. Gerger, *Monatsh. Chem.*, **1975**, *106*, 1235-1257; M. A. Beckett, G. C. Strickland, J. R. Holland, K. S. Varma, *Polymer*, **1996**, *37*, 4629-4631; G. J. P. Britovsek, J. Ugolotti, A. J. P. White, *Organometallics*, **2005**, *24*, 1685-1691; Y. Koito, K. Nakajima, H. Kobayashi, R. Hasegawa, M. Kitano, M. Hara, *Chem. Eur. J.*, **2014**, *20*, 8068-8075; A. R. Nödling, K. Mütter, V. H. G. Rohde, G. Hilt, M. Oestreich, *Organometallics*, **2014**, *33*, 302-308; H. Großekappenberg, M. Reißmann, M. Schmidtman, T. Müller, *Organometallics*, **2015**, *34*, 4952-4958.

¹⁶⁹ R. F. Childs, D. L. Mulholland, A. Nixon, *Can. J. Chem.*, **1982**, *60*, 809-812; R. F. Childs, D. L. Mulholland, A. Nixon, *Can. J. Chem.*, **1982**, *60*, 801-808.

¹⁷⁰ G. Hilt, F. Pünner, J. Möbus, V. Naseri, A. Bohn Martin, *Eur. J. Org. Chem.*, **2011**, *2011*, 5962-5966; G. Hilt, A. Nödling, *Eur. J. Org. Chem.*, **2011**, *2011*, 7071-7075.

¹⁷¹ I. R. Beattie, T. Gilson, *J. Chem. Soc.*, **1964**, 2292-2295; K. F. Purcell, R. S. Drago, *J. Am. Chem. Soc.*, **1966**, *88*, 919-924; B. Swanson, D. F. Shriver, *Inorg. Chem.*, **1970**, *9*, 1406-1416; D. F. Shriver, B. Swanson, *Inorg. Chem.*, **1971**, *10*, 1354-1365; D. M. Byler, D. F. Shriver, *Inorg. Chem.*, **1973**, *12*, 1412-1416; P. A. Chase, P. E. Romero, W. E. Piers, M. Parvez, B. O. Patrick, *Can. J. Chem.*, **2005**, *83*, 2098-2105; A. G. Pelmeshnikov, R. A. van Santen, J. Janchen, E. Meijer, *J. Phys. Chem.*, **1993**, *97*, 11071-11074.

¹⁷² R. G. Parr, R. G. Pearson, *J. Am. Chem. Soc.*, **1983**, *105*, 7512-7516; R. G. Parr, W. Yang, *J. Am. Chem. Soc.*, **1984**, *106*, 4049-4050.

¹⁷³ The definition of GIE, also proposed by Parr (see A. R. Jupp, T. C. Johnstone, D. W. Stephan, *Dalton Trans.*, **2018**, *47*, 7029-7035; R. G. Parr, L. v. Szentpály, S. Liu, *J. Am. Chem. Soc.*, **1999**, *121*, 1922-1924), and relying on the previous work of Maynard et al (A. T. Maynard, M. Huang, W. G. Rice, D. G. Covell, *Proc. Natl. Acad. Sci.*, **1998**, *95*, 11578).

¹⁷⁴ Y. Koito, K. Nakajima, H. Kobayashi, R. Hasegawa, M. Kitano, M. Hara, *Chem. Eur. J.*, **2014**, *20*, 8068-8075; G. A. Olah, S. Kobayashi, M. Tashiro, *J. Am. Chem. Soc.*, **1972**, *94*, 7448-7461; S. Kobayashi, S. Nagayama, T. Busujima, *J. Am. Chem. Soc.*, **1998**, *120*, 8287-8288; K. Yusuke, N. Kiyotaka, K. Hisayoshi, H. Ryota, K. Masaaki, H. Michikazu, *Chem. Eur. J.*, **2014**, *20*, 8068-8075.

¹⁷⁵ R. J. Gillespie, T. E. Peel, in *Adv. Phys. Org. Chem.*, **1971**, *9*, 1-24; F. Dickert, *Ber. Bunsenges. Phys. Chem.*, **1987**, *91*, 1073-1074.

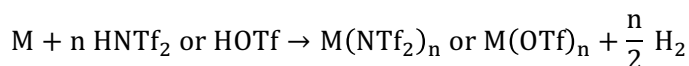
¹⁷⁶ L. Greb, *Chem. Eur. J.*, **2018**, *24*, 17881-17896.

¹⁷⁷ S. Antoniotti, V. Dalla, E. Duñach, *Angew. Chem. Int. Ed.*, **2010**, *49*, 7860-7888.

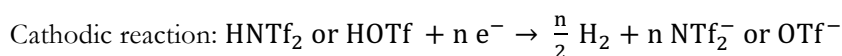
based on the comparison of the FIA (*vide supra*) of the salt with regards to SbF₅ or of the HIA (*vide supra*) toward B(C₆F₅)₃.

Preparation. Lewis super acids are highly hygroscopic compounds and thus difficult to synthesize under anhydrous form. These salts can be prepared by:¹⁷⁸

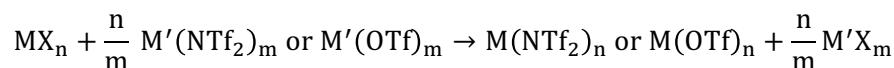
- Oxidation of the metal under acidic conditions:



This method works well for reductive metal,¹⁷⁹ but it can also be done by electrosynthesis:¹⁸⁰



- Salt metathesis:



Sulfate or nitrate metal salts may form the corresponding triflate or triflimide salts when treated with an excess of alkali metal triflate or triflimide,¹⁸¹ similarly metal halides can react with Ag(NTf₂).

- Ligand exchange:



Finally the last strategy involves the protonation of the X ligand (with X = CO₃²⁻,¹⁸² OiPr,¹⁸³ Ph,¹⁸⁴ OH,¹⁸⁵ etc).

¹⁷⁸ J.-F. Gal, C. Iacobucci, I. Monfardini, L. Massi, E. Duñach, S. Olivero, *J. Phys. Org. Chem.*, **2013**, 2687-2697; S. Antoniotti, V. Dalla, E. Duñach, *Angew. Chem. Int. Ed.*, **2010**, *49*, 7860-7888; B. A. Shainyan, L. L. Tolstikova, *Chem. Rev.*, **2013**, *11*, 31, 699-733.

¹⁷⁹ S. Antoniotti, E. Duñach, *Chem. Commun.*, **2008**, 993-995.

¹⁸⁰ I. Favier, E. Duñach, *Tetrahedron Lett.*, **2003**, *44*, 2031-2032.

¹⁸¹ A. Haas, C. Klare, P. Betz, J. Bruckmann, C. Kruger, Y. H. Tsay, F. Aubke, *Inorg. Chem.*, **1996**, *35*, 1918-1925.

¹⁸² A. Vij, Y. Y. Zheng, R. L. Kirchmeier, J. M. Shreeve, *Inorg. Chem.*, **1994**, *33*, 3281-3288; D. B. Baudry, A. Dormond, F. Duris, J. M. Bernard, J. R. Desmurs, *J. Fluorine Chem.*, **2003**, *121*, 233-238; K. Mikami, O. Kotera, Y. Motoyama, M. Tanaka, *Inorg. Chem. Commun.*, **1998**, *1*, 10-11; J. Nie, J. Xu, G. Zhou, *J. Chem. Res. Synop.*, **1999**, 446-447; L. Xue, C. W. Padgett, D. D. DesMarteau, W. T. Pennington, *Solid State Sci.*, **2002**, *4*, 1535-1545.

¹⁸³ K. Mikami, O. Kotera, Y. Motoyama, H. Sakaguchi, M. Maruta, *Synlett*, **1996**, 171-172.

¹⁸⁴ A. Picot, S. Repichet, C. Le Roux, J. Dubac, N. Roques, *J. Fluorine Chem.*, **2002**, *116*, 129-134.

¹⁸⁵ P. A. Grieco, S. T. Handy, *Tetrahedron Lett.*, **1997**, *38*, 2645-2648.

Characterization. The characterization of triflimide and triflate salts is non-trivial and only a few X ray diffraction structural data are available for these compounds. Li(OTf)¹⁸⁶ have been crystallized under anhydrous form as well as K, Cs,¹⁸⁷ Sr¹⁸⁸ and Zn¹⁸⁹ triflimides X ray structures are reported. Generally, these compounds are characterized only by elemental analysis and TGA.¹⁹⁰ Recently Duñach and coworkers have described a very interesting characterization of these salts using ESI-MS analysis in the presence of an ionizing agent (OPPh₃).¹⁹¹

The triflate anion in metal salts can potentially behave as a mono-, bi- or tridentate ligand.¹⁹² Similarly triflimides can be mono or polydentate ligands and may coordinate to a metal cation either via N or O atoms.¹⁹³ The structure of these compounds will be discussed more in detail in section 3.3.

1.3. Application of Triflate and Triflimides in Synthesis

LAs play a central role in synthetic chemistry for activating carbon-oxygen, carbon-nitrogen and carbon-carbon bonds.¹⁹⁴

Amination. Among the different methods for amine synthesis, the direct amination of alcohols (**Scheme 49**) constitutes an attractive transformation, since alcohols (including biomass-derived alcohols) are readily available, easy to handle and water is generated as sole byproduct.¹⁹⁵ Unlike traditional pre-activation methods which require transformation of the OH-group into leaving groups such as halides, carboxylates, phosphates or carbonates, this synthetic approach is consistent with the principles of green chemistry, both in terms of atom economy and waste prevention.¹⁹⁶

¹⁸⁶ R. Dinnebier, N. Sofina, M. Jansen, *Z. Anorg. Allg. Chem.*, **2004**, *630*, 1613-1616.

¹⁸⁷ L. Xue, C. W. Padgett, D. D. DesMarteau, W. T. Pennington, *Solid State Sci.*, **2002**, *4*, 1535-1545.

¹⁸⁸ L. Xue, D. D. DesMarteau, W. T. Pennington, *Solid State Sci.*, **2005**, *7*, 311-318,

¹⁸⁹ M. J. Earle, U. Hakala, B. J. McAuley, M. Nieuwenhuyzen, A. Ramania, K. R. Seddon, *Chem. Commun.*, **2004**, 1368-1369.

¹⁹⁰ D. B. Baudry, A. Dormond, F. Duris, J. M. Bernard, J. R. Desmurs, *J. Fluorine Chem.*, **2003**, *121*, 233-238.

¹⁹¹ J.-F. Gal, C. Iacobucci, I. Monfardini, L. Massi, E. Duñach, S. Olivero, *J. Am. Soc. Mass. Spectrom.*, **2012**, *23*, 2059-2062; G. Compain, L. Sikk, L. Massi, J. F. Gal, E. Duñach, *ChemPhysChem.*, **2017**, *18*, 683-691; C. Iacobucci, N. Jouini, L. Massi, S. Olivero, F. De Angelis, E. Duñach, J.-F. Gal, *ChemPlusChem.*, **2017**, *82*, 498-506; I. Monfardini, L. Massi, E. Duñach, S. Olivero, J.-F. Gal, *Chem. Commun.*, **2010**, *46*, 8472-8474.

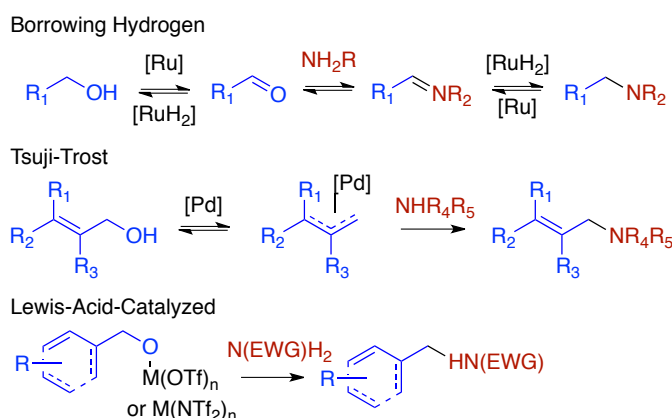
¹⁹² M. E. M. Hamidi, J.-L. Pascal, *Polyhedron* **1994**, *13*, 1787-1792; K. Boumizane, M. H. Herzog-Cance, D. J. Jones, J. L. Pascal, J. Potier, J. Roziere, *Polyhedron* **1991**, *10*, 2757-2769.

¹⁹³ D. B. Williams, M. E. Stoll, B. L. Scott, D. A. Costa, J. W. J. Oldham, *Chem. Commun.* **2005**, 1438-1440.

¹⁹⁴ H. A. Wittcoff, B. G. Reuben, J. S. Plotkin, *Industrial Organic Chemicals*, **2004** (2nd ed.), Wiley; S. A. Lawrence, *Amines: Synthesis Properties and Applications*, **2004**, Cambridge University Press; B. R. Brown, *The Organic Chemistry of Aliphatic Nitrogen Compounds*, **2004**, Cambridge University Press.

¹⁹⁵ E. Emer, R. Sinisi, M. G. Capdevila, D. Petruzzello, F. De Vincentiis, P. G. Cozzi, *Eur. J. Org. Chem.* **2011**, *2011*, 647-666; M. Pera-Titus, F. Shi, *ChemSusChem* **2014**, *7*, 720-722; S. Bähn, S. Imm, L. Neubert, M. Zhang, H. Neumann, M. Beller, *ChemCatChem* **2011**, *3*, 1853-1864; A. Baeza, C. Nájera, *Synthesis* **2014**, *46*, 25-34.

¹⁹⁶ B. Trost, *Science*, **1991**, *254*, 1471-1477.



Scheme 49 – Typical reaction conditions for the direct amination of alcohols.

During the last decades, three main strategies have emerged for the direct amination of alcohols: (i) the borrowing hydrogen methodology (BH₂) using either Ru or Ir complexes,¹⁹⁷ and more recently non-noble metal complexes based on Mn¹⁹⁸ or Fe,¹⁹⁹ (ii) Tsuji-Trost type reactions for allylic alcohols using Pd²⁰⁰ or Ni²⁰¹ complexes, and (iii) Lewis-acid catalysis based on a variety of salts and ligands.²⁰² The latter is attractive as it uses non-noble metal, inexpensive and low-toxic salts. Among the best performing catalysts, triflates and triflimides stand out. Metal triflates and triflimides, based on Ca,²⁰³ Al,²⁰⁴ In,²⁰⁵

¹⁹⁷ T. D. Nixon, M. K. Whittlesey, J. M. J. Williams, *Dalton Trans.*, **2009**, 753-762; G. Guillena, D. J. Ramón, M. Yus, *Chem. Rev.*, **2010**, *110*, 1611-1641; J. L. Klinkenberg, J. F. Hartwig, *Angew. Chem. Int. Ed.*, **2011**, *50*, 86-95; C. Gunanathan, D. Milstein, *Science*, **2013**, *341*, 1229712; Q. Yang, Q. Wang, Z. Yu, *Chem. Soc. Rev.*, **2015**, *44*, 2305-2329.

¹⁹⁸ J. Neumann, S. Elangovan, A. Spannenberg, K. Junge, M. Beller, *Chem. Eur. J.*, **2017**, *23*, 5410-5413.

¹⁹⁹ B. Emayavaramban, M. Roy, B. Sundararaju, *Chem. Eur. J.*, **2016**, *22*, 3952-3955.

²⁰⁰ H. Bricout, J.-F. Carpentier, A. Mortreux, *J. Mol. Cat. A: Chem.*, **1998**, *136*, 243-251; Y. Gumrukcu, B. de Bruin, J. N. H. Reek, *Catalysts*, **2015**, *5*, 349-365; S. Sawadjoon, P. J. R. Sjöberg, A. Orthaber, O. Matsson, J. S. M. Samec, *Chem. Eur. J.*, **2014**, *20*, 1520-1524; J. Muzart, *Eur. J. Org. Chem.*, **2007**, *2007*, 3077-3089.

²⁰¹ H. Bricout, J.-F. Carpentier, A. Mortreux, *J. Mol. Cat. A: Chem.*, **1998**, *136*, 243-251; H. Bricout, J.-F. Carpentier, A. Mortreux, *Tetrahedron*, **1998**, *54*, 1073-1084; Y. Kita, H. Sakaguchi, Y. Hoshimoto, D. Nakauchi, Y. Nakahara, J.-F. Carpentier, S. Ogoshi, K. Mashima, *Chem. Eur. J.*, **2015**, *21*, 14571-14578.

²⁰² E. Emer, R. Sinisi, M. G. Capdevila, D. Petruzzello, F. De Vincentiis, P. G. Cozzi, *Eur. J. Org. Chem.*, **2011**, *2011*, 647-666; A. Baeza, C. Nájera, *Synthesis*, **2014**, *46*, 25-34.

²⁰³ S. Haubenreisser, M. Niggemann, *Adv. Synth. Catal.*, **2011**, *353*, 469-474.

²⁰⁴ M. Gohain, C. Marais, B. C. B. Bezuidenhoudt, *Tetrahedron Lett.*, **2012**, *53*, 1048-1050; T. Ohshima, J. Ipposhi, Y. Nakahara, R. Shibuya, K. Mashima, *Adv. Synth. Catal.*, **2012**, *354*, 2447-2452.

²⁰⁵ J.-M. Yang, R. Jiang, L. Wu, X.-P. Xu, S.-Y. Wang, S.-J. Ji, *Tetrahedron*, **2013**, *69*, 7988-7994.

Yb,²⁰⁶ La,²² Hf,²² Bi,²⁰⁷ Cu,²⁰⁸ Ag,²⁰⁹ Hg,²¹⁰ and Au,²¹¹ including the parent triflic acid (HOTf),²¹² were found active for a broad range of acid-catalyzed reactions. In particular, Mashima and coworkers reported Al(OTf)₃ as a powerful catalyst for the amination of secondary allylic or benzylic alcohols.²⁰⁴ The reaction proceeded to completion and with high selectivity in nitromethane at mild temperature (25-50 °C) and short reaction times (from 5 min to 6 h, typically 10-30 min). However, as a major drawback, the reaction scope was limited to electron-poor amine derivatives, such as amides, sulfonamides, carbamates, and to activated alcohols (Scheme 49).²⁰⁴

With regard to the catalytic mechanism, there is general consensus that substitution of OH-groups with C-, S-, and O-nucleophiles proceeds *via* a S_N1-type mechanism, in the presence of hard Lewis or Brønsted acids.¹⁹⁵ Carbocation intermediates are generated by coordination of the alcohol to the acidic center, and subsequent formation of a [LA-OH] complex. Racemization of optically active alcohols,¹⁹⁵ and electronic and solvent effects support such a mechanism. Due to their polar nature, solvents typically used for S_N1-type reactions, such as dichloromethane, dioxane, nitromethane, and water, can stabilize ionic intermediates.

While a S_N1-type mechanism appears to be predominant for a large majority of metal triflates, key aspects of the Lewis acid-catalyzed amination of alcohols remain unclear. This lack of understanding can be certainly ascribed to the difficult access to the catalyst structure under working conditions. Likewise, few theoretical investigations of metal triflate-catalyzed reactions of alcohols²¹³ or ethers²¹⁴ exist. As a first step, Al(OTf)₃ was chosen as a model catalyst to find out the mechanism and species involved in LA-catalyzed amination and if possible extend the scope of this reaction to electron-rich amines.

²⁰⁶ W. Huang, Q.-S. Shen, J.-L. Wang, X.-G. Zhou, *Chin. J. Chem.*, **2008**, *26*, 729-735; W. Rao, X. Zhang, E. M. L. Sze, P. W. H. Chan, *J. Org. Chem.*, **2009**, *74*, 1740-1743; M. Noji, T. Ohno, K. Fujii, N. Futaba, H. Tajima, K. Ishii, *J. Org. Chem.*, **2003**, *68*, 9340-9347.

²⁰⁷ R. Jiang, C.-X. Yuan, X.-P. Xu, S.-J. Ji, *Appl. Organomet. Chem.*, **2012**, *26*, 62-66; H. Qin, N. Yamagiwa, S. Matsunaga, M. Shibasaki, *Angew. Chem. Int. Ed.*, **2007**, *46*, 409-413.

²⁰⁸ W. Rao, P. Kothandaraman, C. B. Koh, P. W. H. Chan, *Adv. Synth. Catal.*, **2010**, *352*, 2521-2530.

²⁰⁹ X. Giner, P. Trillo, C. Nájera, *J. Organomet. Chem.*, **2011**, *696*, 357-361; B. Sreedhar, P. Surendra Reddy, M. Amarnath Reddy, B. Neelima, R. Arundhathi, *Tetrahedron Lett.*, **2007**, *48*, 8174-8177.

²¹⁰ H. Yamamoto, E. Ho, I. Sasaki, M. Mitsutake, Y. Takagi, H. Imagawa, M. Nishizawa, *Eur. J. Org. Chem.*, **2011**, *2011*, 2417-2420.

²¹¹ V. Terrasson, S. Marque, M. Georgy, J.-M. Campagne, D. Prim, *Adv. Synth. Catal.*, **2006**, *348*, 2063-2067; H. Hikawa, H. Suzuki, Y. Yokoyama, I. Azumaya, *J. Org. Chem.*, **2013**, *78*, 6714-6720; T. Ohshima, Y. Nakahara, J. Ipposhi, Y. Miyamoto, K. Mashima, *Chem. Commun.*, **2011**, *47*, 8322-8324; B. Biannic, A. Aponick, *Eur. J. Org. Chem.*, **2011**, *2011*, 6605-6617; M. Georgy, V. Boucard, O. Debleds, C. D. Zotto, J.-M. Campagne, *Tetrahedron*, **2009**, *65*, 1758-1766.

²¹² P. Trillo, A. Baeza, C. Nájera, *Eur. J. Org. Chem.*, **2012**, *2012*, 2929-2934.

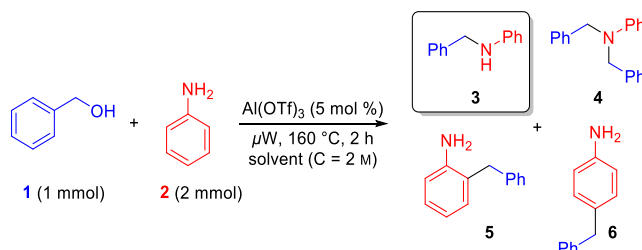
²¹³ L. Coulombel, M. Rajzmann, J.-M. Pons, S. Olivero, E. Duñach, *Chem. Eur. J.*, **2006**, *12*, 6356-6365; Z. Li, R. S. Assary, A. C. Atesin, L. A. Curtiss, T. J. Marks, *J. Am. Chem. Soc.*, **2013**, *136*, 104-107.

²¹⁴ Z. Li, R. S. Assary, A. C. Atesin, L. A. Curtiss, T. J. Marks, *J. Am. Chem. Soc.*, **2013**, *136*, 104-107; R. S. Assary, A. C. Atesin, Z. Li, L. A. Curtiss, T. J. Marks, *ACS Catal.*, **2013**, *3*, 1908-1914.

2. Mechanistic Study of a Model Reaction: Al(OTf)₃-Catalyzed Amination of Alcohol

2.1. Description of the Model Reaction and Solvent Effects

First, we investigated the catalytic properties of Al(OTf)₃ in nitromethane, a polar solvent typically used for metal triflate-catalyzed reactions.²¹⁵ For this purpose, a 1:2 mixture of benzyl alcohol (BnOH) and aniline was heated in the presence of a catalytic amount of Al(OTf)₃ (Scheme 50). Unlike the results reported by Mashima and coworkers obtained with electron-poor amine derivatives and secondary allylic this benzylic alcohols,²⁰⁵ our reaction required very harsh conditions. Indeed, even at 160 °C under microwave irradiation, the primary amination product *N*-phenylbenzylamine (**3**) was obtained with poor selectivity (Table 9, entry 1). Besides, the carbon balance turned out to be low, most likely due to the formation of oligomers. Lower temperatures did not lead to any product.



Scheme 50 - Main products obtained in the amination reaction of benzyl alcohol with aniline.

Table 9 - Conversion of BnOH (**1**), yields, and carbon balance (in %) in the reaction of benzyl alcohol with aniline in two different solvents, according to Scheme 2. Values obtained by GC analysis, using biphenyl as an internal standard.

Solvent	Conv.	Yield				Carbon balance
		3	4	5	6	
Nitromethane	63	26 (41) ^a	1.2	2.9	2.2	59
Toluene	41	37 (90) ^a	0.3	1.1	0.8	96

Unexpectedly, when the reaction was performed under the same conditions, but in toluene, a non-polar solvent, the expected product **3** was obtained with high selectivity (90%) and fair yield (Table 9, entry 2), and an almost quantitative carbon balance was achieved. Note that in both solvents only traces of the secondary amine **4** and Friedel-Craft products **5-6** were formed. Less byproduct was observed in toluene.

²¹⁵ T. Ohshima, J. Ipposhi, Y. Nakahara, R. Shibuya, K. Mashima, *Adv. Synth. Catal.*, **2012**, *354*, 2447-2452.

The markedly different reaction outcome for nitromethane and toluene suggests different mechanisms for benzyl alcohol amination with aniline. To better understand the different reactivity in both solvents and the need of much higher temperature, compared to electron-poor amines and activated secondary alcohols, a dedicated mechanistic study of the $\text{Al}(\text{OTf})_3$ -catalyzed amination reaction was undertaken in both nitromethane and toluene.

2.2. Nature of $\text{Al}(\text{OTf})_3$ in Nitromethane and Coordination of Benzyl Alcohol

The nature of $\text{Al}(\text{OTf})_3$ was first investigated in nitromethane by different analytical methods (CV, conductimetry, ^1H - and ^{13}C -NMR spectroscopy). CV allows the characterization of redox-active species by their oxidation and reduction potentials. With this technique, the reactivity can be assessed by considering that the reduction or oxidation currents are proportional to the concentration of electroactive species (see CHAPTER I for details). The CV of $\text{Al}(\text{OTf})_3$ dissolved in nitromethane (10 mM) exhibited two non-reversible reduction peaks (i.e. R_1 and R_2) centered at -0.55 V and -0.95 V *vs.* SCE, respectively (Figure 21a). An increase of the scan rate up to 2 Vs^{-1} modified the relative intensity between both peak currents (Figure 21b). Such a behavior can be typically ascribed to the existence of an equilibrium between two different species (ECr mechanism).

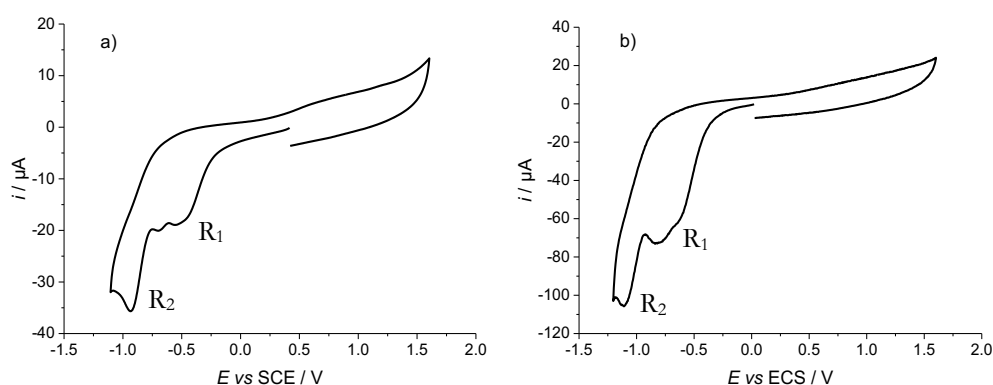


Figure 21 - Cyclic voltammetry (CV) toward reduction potentials performed at a steady carbon disk electrode ($d = 1\text{ mm}$) in nitromethane containing $0.3\text{ M } n\text{-Bu}_4\text{NBF}_4$ and $\text{Al}(\text{OTf})_3$ (10 mM) at $20\text{ }^\circ\text{C}$, a) at a scan rate of 0.5 V s^{-1} , b) at a scan rate of 2.0 V s^{-1} .

The addition of water increased the reduction peak current at R_1 at the expense of peak R_2 (Figure 22). The reduction peak R_1 could thus be attributed to water coordinated to $\text{Al}(\text{OTf})_3$, while peak R_2 could be attributed to nitromethane coordinated to $\text{Al}(\text{OTf})_3$.²¹⁶

²¹⁶ The presence of adventitious water in the experiment can be due either to the commercially available nitromethane (98.5% purity, kept on molecular sieves (3 \AA)) and to the hygroscopy of aluminum triflate (kept under vacuum on anhydrous P_2O_5).

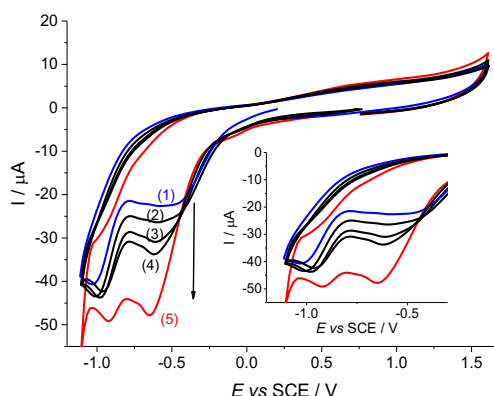


Figure 22 - CV recorded on a steady carbon disk electrode ($d = 1$ mm) in nitromethane containing 0.3 M n -Bu₄NBF₄ and Al(OTf)₃ (10 mM) at 20 °C with a scan rate of 0.5 V s⁻¹ (1) without added water, 2) with 5 μL of added water, 3) with 25 μL of added water, 4) with 50 μL of added water, and 5) with 100 μL of added water.

A similar reduction pattern for nitromethane was observed in the presence of various Lewis acids such as LiNTf₂, LiBF₄ and AlCl₃ (**Figure 23**).

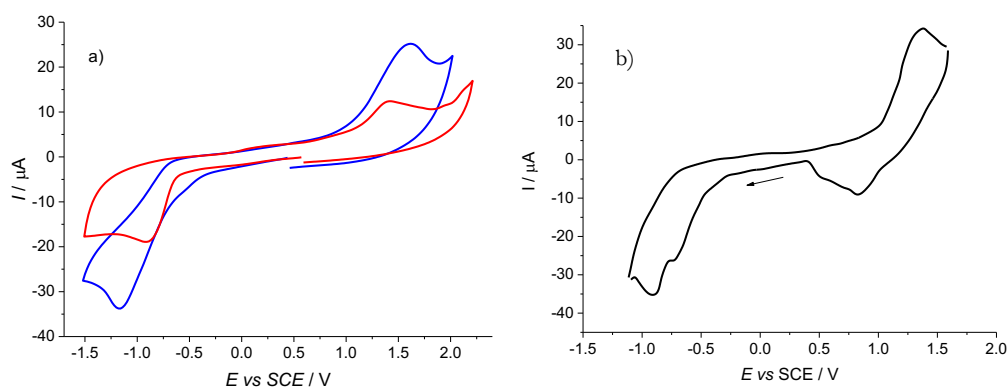


Figure 23 - CV recorded on a steady carbon disk electrode ($d = 1$ mm) at 20 °C with a scan rate of 0.5 V s⁻¹ in nitromethane containing: a) LiBF₄ (0.3 M) (blue), LiNTf₂ (0.3 M) (red); b) AlCl₃ (10 mM) and n Bu₄NBF₄ (0.3 M).

To assess any potential triflate dissociation, a series of conductivity measurements was performed in nitromethane at different Al(OTf)₃ concentrations. The conductivity of the parent solution was found to be very low and a plot of the conductivity *vs.* Al(OTf)₃ concentration is characteristic of poorly dissociated electrolytes (**Figure 24**, ▲). This observation is consistent with published reports establishing a weak dissociation of metal triflate salts in low-coordinating solvents such as nitromethane.²¹⁷

²¹⁷ J.-F. Gal, C. Iacobucci, I. Monfardini, L. Massi, E. Duñach, S. Olivero, *J. Am. Soc. Mass. Spectrom.*, **2012**, *23*, 2059-2062; G. Compain, L. Sikk, L. Massi, J. F. Gal, E. Duñach, *Chemphyschem*, **2017**, *18*, 683-691; C. Iacobucci, N. Jouini, L. Massi, S. Olivero, F. De Angelis, E. Duñach, J.-F. Gal, *ChemPlusChem*, **2017**, *82*, 498-506; I. Monfardini, L. Massi, E. Duñach, S. Olivero, J.-F. Gal, *Chem. Commun.*, **2010**, *46*, 8472-8474.

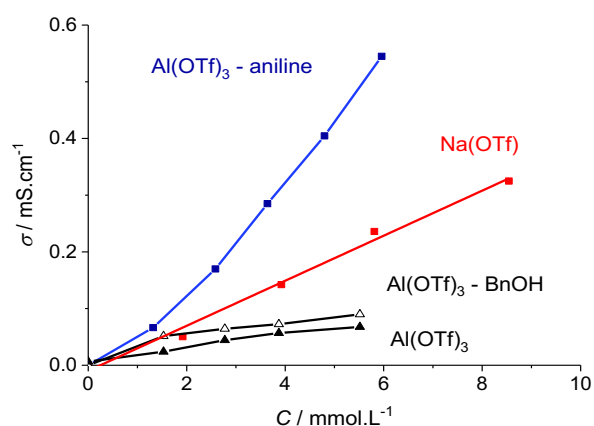


Figure 24 - Conductivity of $\text{Al}(\text{OTf})_3$ in nitromethane (\blacktriangle), with excess BnOH (100 mM, Δ) and with excess aniline (100 mM, blue \blacksquare) as a function of the $\text{Al}(\text{OTf})_3$ concentration. For comparison, the conductivity of NaOTf in nitromethane (red \blacksquare) is also plotted.

Additional CV experiments were conducted to investigate the coordination of BnOH to Al(III). The reduction peak R_2 decreased significantly upon BnOH addition (**Figure 25b, c**), whereas the current intensity increased at a reduction potential similar to R_1 . This observation is likely due to the appearance of a new peak (R_3), which can be attributed to BnOH coordinated to $\text{Al}(\text{OTf})_3$. This complex is expected to behave similarly to that formed with water (reduced at R_1), which could explain the similar reduction potentials. These results underline the high affinity of BnOH for Al(III), being able to displace nitromethane under conditions similar to those of the catalytic reaction. However, by analogy with water, coordination of BnOH does not result in the dissociation of the triflate ions, as apparent from the plot of conductivity *vs.* $\text{Al}(\text{OTf})_3$ concentration in the presence of excess BnOH (100 mM) (see **Figure 24**, Δ).

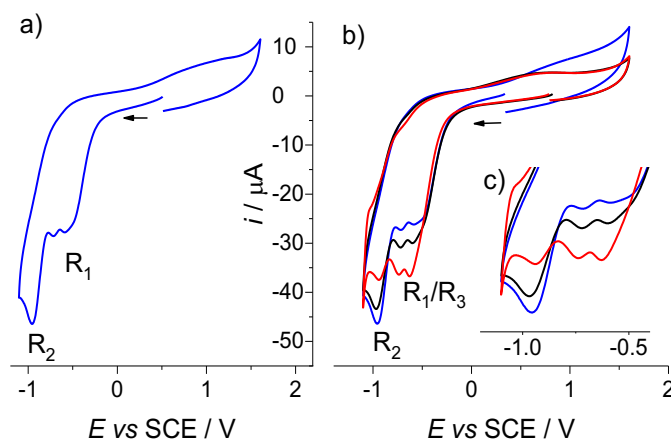


Figure 25 - CV towards reduction potentials recorded on a steady *glassy carbon* disk electrode ($d = 1$ mm) in nitromethane containing $n\text{-Bu}_4\text{NBF}_4$ (300 mM) at 20 °C with a scan rate of 0.5 V s⁻¹. a) $\text{Al}(\text{OTf})_3$ (10 mM); b) $\text{Al}(\text{OTf})_3$ upon addition of increasing amounts of BnOH (0 [in blue], 11 [in black] and 50 equiv [in red]), and c) inserted image of b).

To gain more insight into the nature of the possible reaction intermediates, the complexes formed between BnOH and $\text{Al}(\text{OTf})_3$ were analyzed by ^1H - and ^{13}C -NMR. In the presence of 10 equiv of $\text{Al}(\text{OTf})_3$, the singlet at 4.63 ppm accounting for the two benzylic protons of BnOH was shifted to 4.64 ppm (**Figure 26a**). Comparable shifts were observed by ^{13}C -NMR, with all signals being shifted by about 0.5 ppm (**Figure 26b,c**). Even if tiny, this shift is consistent with the coordination of BnOH to $\text{Al}(\text{III})$ and corresponds to a rapid equilibrium with respect to the NMR timescale.²¹⁸

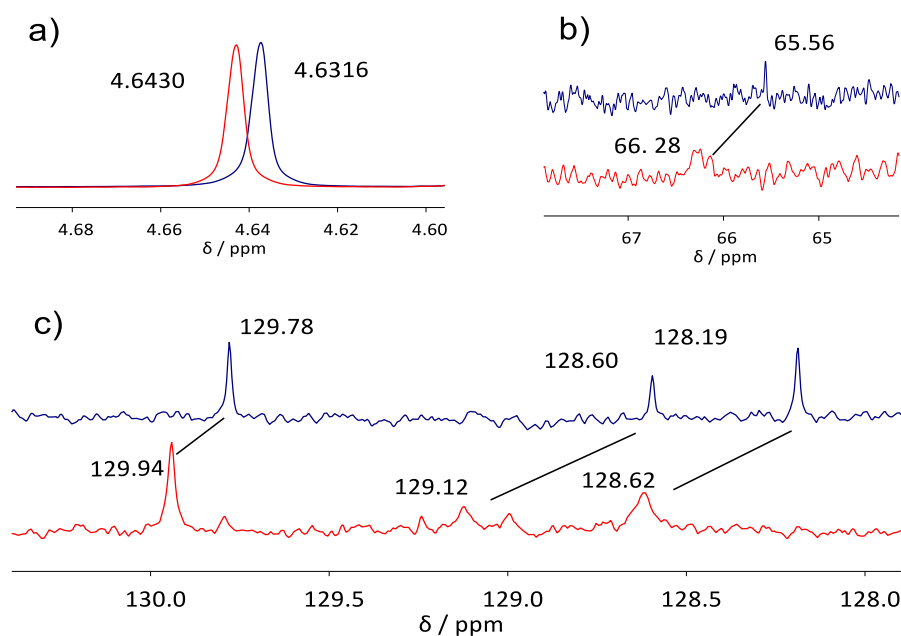


Figure 26 - a) ^1H -NMR chemical shifts [ppm vs TMS], and b) and c) ^{13}C -NMR spectra [ppm vs TMS] of BnOH (20 mM in *t*-MeNO₂) alone (red) and in the presence of 10 equiv of $\text{Al}(\text{OTf})_3$ (blue).

2.3. Deactivation of $\text{Al}(\text{OTf})_3$ by aniline in nitromethane

Upon addition up to 1.5 equiv of aniline to a solution of $\text{Al}(\text{OTf})_3$, no free aniline was present, as evidenced by the absence of its characteristic oxidation peak at +1.0 V *vs.* SCE in the CV plot (**Figure 27a**). CV towards negative potentials exhibited a new reduction peak at -0.7 V *vs.* SCE (R_4), together with a markedly lower intensity of the reduction peak at -0.95 V (R_2) (**Figure 27b**). This observation is consistent with the formation of a complex between $\text{Al}(\text{III})$ and aniline.

²¹⁸ Comparable shifts due to the formation of alcohol- $\text{Al}(\text{OTf})_3$ complexes were observed by Duñach and collaborators in the mechanistic study of the hydroalkoxylation of unactivated olefins, see L. Coulombel, M. Rajzmann, J.-M. Pons, S. Olivero, E. Duñach, *Chem. Eur. J.*, **2006**, *12*, 6356-6365.

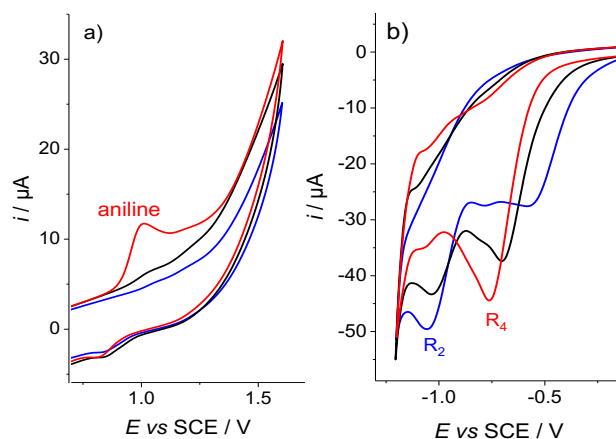


Figure 27 - CV recorded on a steady carbon disk electrode ($d = 1$ mm) in nitromethane containing n -Bu₄NBF₄ (300 mM) at 20 °C and at a scan rate of 0.5 V s⁻¹. a) oxidation of Al(OTf)₃ (10 mM) with 1.5 equiv of aniline [blue], 1.6 equiv of aniline [black] and 1.8 equiv of aniline [red]; b) reduction of Al(OTf)₃ (10 mM) without aniline [blue], with 1 equiv of aniline [black] and 3 equiv of aniline [red].

Upon addition of 3 equiv of aniline (**Figure 27b**), the reduction peak at -1.0 V *vs.* SCE almost vanished. Moreover, the conductivity measured for Al(OTf)₃ with an aniline excess (100 mM) exhibited higher values than for a solution of sodium triflate, together with a linear-shaped curve that is consistent with the formation of ionic species (**Figure 24 ■**). *p*-Fluoroaniline was used as ¹⁹F-NMR probe to study the complexation of aniline to Al(III).

In the presence of 1 equiv of Al(OTf)₃, the ¹⁹F-NMR signal shifted from -127 ppm to -110 ppm (fluorobenzene was used as an internal standard at -112 ppm). This shift confirms the coordination of aniline to Al(III), thus allowing the determination of the stoichiometry of the complex using the Job plot method (**Figure 28**).²¹⁹ The point-shaped plot obtained is indicative

²¹⁹ Job plot (also called method of continuous variation) is an efficient way to access the stoichiometry (it is generally poorly efficient for the estimation of association constants) of a metal-ligand complex. In order to obtain a Job plot, one just need to have access to any measurable property proportionate to the concentration of the complex formed.

In the case of a rapid exchange compared to NMR timescale, between two species the observed chemical shift is:

$$\delta = \delta_1 x_1 + \delta_2 (1 - x_1)$$

with δ_1 the chemical shift of the free ligand, δ_2 the chemical shift of the ligand in the complex and x the molar fraction of the free ligand. The chemical shift variation

$$\Delta\delta = \delta - \delta_1 = (\delta_1 + \delta_2)(1 - x_1)$$

is thus proportionate to the molar fraction of the complex $x_2 = 1 - x_1$.

The Job plot is obtained by plotting value (in our case, $\Delta\delta$) proportionate to the concentration of the complex as a function of the introduced molar fraction of the ligand (or metal) for a *fixed* total concentration of both species. A bell-shaped curve is thus obtained with a maximum obtained for a molar ratio corresponding to the formed complex stoichiometry.

For more details about Job plots see: E. J. Olson, P. Bühlmann, *J. Org. Chem.*, **2011**, *76*, 8406-8412; E. J. Olson, P. Bühlmann, *J. Org. Chem.*, **2014**, *79*, 830; J. S. Renny, L. L. Tomasevich, E. H. Tallmadge, D. B. Collum, *Angew. Chem. Int. Ed.*, **2013**, *52*, 11998-12013, for a critic of the method see: F. Ulatowski, K.

of a large constant with a maximum observed at 0.6 corresponding to a 3:2 complex. The latter result is consistent with the CV curves, as free aniline was evidenced beyond 1.5 equiv of aniline with respect to $\text{Al}(\text{OTf})_3$.

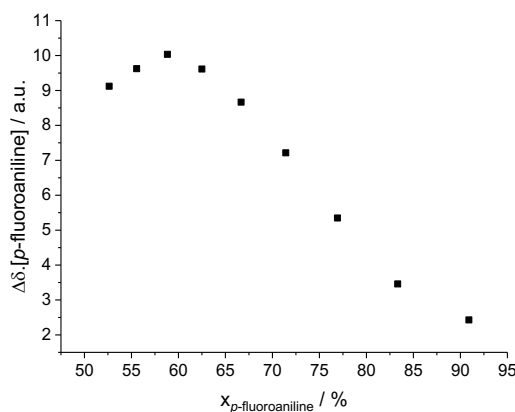


Figure 28 - Job plot of *p*-fluoroaniline with $\text{Al}(\text{OTf})_3$ obtained from $^{19}\text{F}\{^1\text{H}\}$ NMR data at a total concentration of 20 mM in nitromethane ($[\text{D}_6]$ DMSO in a coaxial insert was used for locking and fluorobenzene was used as a reference).

To further rationalize the potential competition between BnOH and aniline, CV and NMR experiments were conducted in the presence of excess BnOH. All these tests confirm that aniline was able to displace BnOH from Al(III) (**Figure 29**).

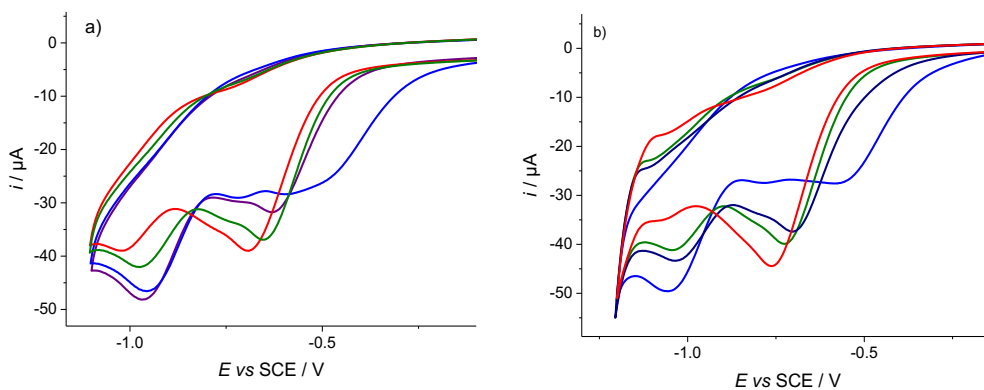


Figure 29 - a) Reduction of $\text{Al}(\text{OTf})_3$ (10 mM) without (light blue) aniline and with 1 equiv of aniline (dark blue); 2 equiv of aniline (green); 3 equiv of aniline (red), b) reduction of $\text{Al}(\text{OTf})_3$ (10 mM) in the presence of 3 equiv of BnOH without (light blue) aniline and with 1 equiv of aniline (dark blue); 2 equiv of aniline (green); 3 equiv of aniline (red).

Moreover, when 1-phenylethanol was reacted with electron-poor *p*-tolylsulfonamide (2 equiv) at room temperature in the presence of 10%mol $\text{Al}(\text{OTf})_3$ and aniline (2 equiv), no amination product was observed after several hours. Conversely, when the same reaction was performed

under the very same conditions as in ref.²²⁰ but in the absence of aniline, the amination product was obtained (**Figure 30**). The kinetics of the amination reaction was monitored using ^1H NMR spectroscopy: (*R*)-1-phenylethanol in the presence of 10 mol% of $\text{Al}(\text{OTf})_3$ and *p*-tolylsulfonamide (2 equiv) quickly gave a mixture of the ether and the amination product (**Figure 30**). The resulting mixture evolved further and after one day, the amination product was the major one. This behavior is consistent with both products being formed competitively with a good final selectivity in favor of the secondary sulfonamide. When the same kinetic experiment was performed in the presence of aniline, neither the ether product nor the amination product was observed. This observation clearly evidences that aniline deactivate the catalyst.

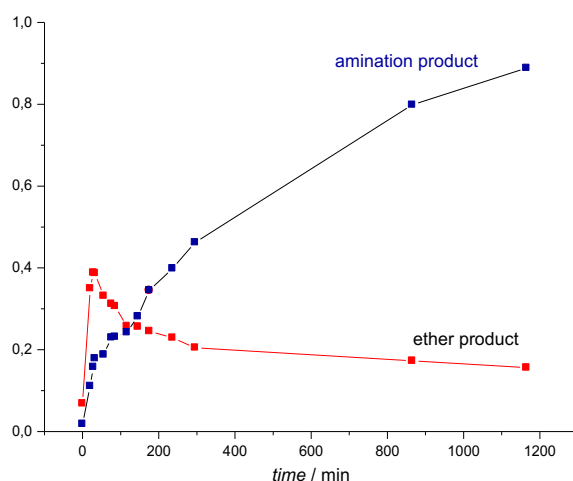


Figure 30 - Kinetics of the amination reaction monitored by ^1H NMR, (*R*)-1-phenylethanol (0.1 M in d_3 - MeNO_2) and *p*-tolylsulfonamide (2 equiv) catalyzed by $\text{Al}(\text{OTf})_3$ (10 mol%) in d_3 - MeNO_2 recorded at 25 °C.

Overall, we can conclude that, in nitromethane, $\text{Al}(\text{OTf})_3$ is deactivated by the formation of cationic complexes featuring aniline as ligand (**Scheme 51**). Hence, BnOH is not expected to coordinate to $\text{Al}(\text{III})$, which is consistent with the low reactivity observed under reaction conditions (*vide supra*).

2.4. Competition between BnOH and aniline for Al in toluene

Next, we studied the coordination of BnOH and aniline to $\text{Al}(\text{OTf})_3$ in toluene. $\text{Al}(\text{OTf})_3$ alone proved to be insoluble in toluene. However, upon addition of 2 equiv of aniline, a single reduction plateau at $E_{1/2} = -0.5$ V *vs.* SCE (R_5) was observed by CV, using a stationary method on an ultramicroelectrode (see **CHAPTER I**). Likewise, $\text{Al}(\text{OTf})_3$ with 10 equiv of BnOH exhibited a single reduction plateau at $E_{1/2} = -1.0$ V *vs.* SCE (R_6) (**Figure 31**). When 20 equiv of aniline were added to a solution of $\text{Al}(\text{OTf})_3$ (10 mM) and 10 equiv of BnOH , two reduction plateaux associated with BnOH - and aniline-ligated $\text{Al}(\text{III})$, respectively, were observed. Still, the equilibrium was in favor of the BnOH complex and up to 80 equiv of aniline were necessary to

²²⁰ T. Ohshima, J. Ipposhi, Y. Nakahara, R. Shibuya, K. Mashima, *Adv. Synth. Catal.*, **2012**, *354*, 2447-2452.

fully shift the equilibrium towards coordinated aniline (**Figure 31**). Note, that this situation contrasts with the BnOH and aniline coordination pattern in nitromethane (*vide supra*).

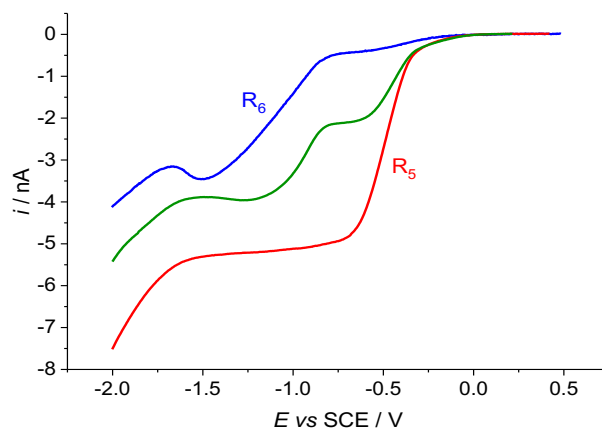
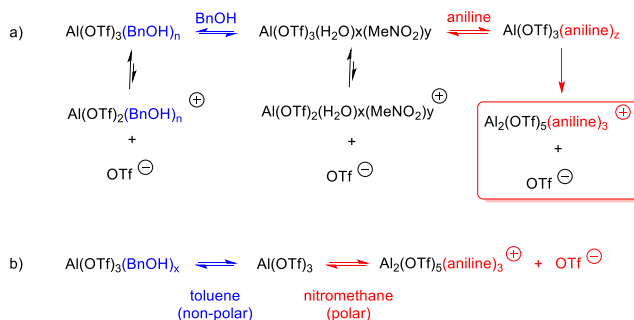


Figure 31 - CV recorded on a steady gold ultramicroelectrode ($d = 25 \mu\text{m}$) in toluene containing $n\text{-hex}_4\text{NBF}_4$ (60 mM) at 20°C with a scan rate of 0.01 V s^{-1} . From top to bottom: complexation of $\text{Al}(\text{OTf})_3$ (10 mM) with 10 equiv of BnOH (blue), 10 equiv of BnOH and 30 equiv of aniline (green), and 10 equiv of BnOH and 80 equiv of aniline (red).

The competition between BnOH and aniline was further confirmed by ^{19}F -NMR spectroscopy, using *p*-fluoroaniline. In the presence of 5 equiv of *p*-fluoroaniline, $\text{Al}(\text{OTf})_3$ was not soluble in toluene and this situation persisted even up to 40 equiv of *p*-fluoroaniline. From the integration of the *p*-fluoroaniline signal, it appeared that 1 equiv of *p*-fluoroaniline was coordinated to a non-soluble $\text{Al}(\text{III})$ -complex. In contrast, in the presence of excess BnOH (30 equiv), $\text{Al}(\text{OTf})_3$ (2 mM) was completely soluble in toluene, as evidenced by the integration of the signal at -78 ppm for ligated triflates. This behavior does not exclude, however, a competition between BnOH and *p*-fluoroaniline under catalytic conditions. Indeed, when both BnOH and *p*-fluoroaniline were in excess with respect to $\text{Al}(\text{OTf})_3$, the *p*-fluoroaniline signal in ^{19}F NMR shifted from -127 ppm to -121 ppm , proving that a significant quantity of *p*-fluoroaniline was ligated to $\text{Al}(\text{III})$.



Scheme 51 - a) Deactivation of $\text{Al}(\text{OTf})_3$ in the presence of aniline in nitro-methane by the formation of ionic complexes, b) simplified coordination pattern of $\text{Al}(\text{OTf})_3$ complexes in toluene and nitromethane under catalytic conditions.

Overall, the above results point out that the nature of $\text{Al}(\text{OTf})_3$ under catalytic conditions depends to an important extent on the polarity of the solvent. While polar solvents such as

nitromethane favor its dissociation and accordingly the coordination with electron-rich ligands such as aniline, no charged species are formed in the presence of non-polar solvents such as toluene (**Scheme 51**). In this view, it is reasonable to expect a different catalytic mechanism as a function of the solvent. In particular, a S_N1 -type mechanism seems very unlikely in toluene.

2.5. Validation of the DFT methodology

Calculations of this sub-section (2.5), except nbo analysis, have been performed by Dr R. Wischert

To validate the experimental findings and provide mechanistic insight, we performed a DFT study, focusing on the surprisingly selective amination reaction in toluene. In the absence of experimental binding (free) energies, accurate theoretical estimates for the electronic part of the binding energy can be obtained from high-level quantum-chemical methods, such as CCSD(T) (see **CHAPTER I**). Benchmark calculations were performed for the electronic binding energies, $\Delta E_{\text{bind}}(\text{ref})$, of the molecules in the reaction medium for two systems with different size: AlF_3 (**Table 10**) and $\text{Al}(\text{OTf})_3$ (**Table 11**).

Table 10 - Binding of different molecule present in the reaction medium to AlF_3 . Difference in binding energy (ΔE_{bind} , kJ mol^{-1}) compared to the reference value $E_{\text{bind}}(\text{ref})$ obtained at the CCSD(T)-F12*/cc-pVDZ-F12 level.

$E_{\text{bind}}(\text{ref})^a$	ΔE_{bind}^b		
CCSD(T)- F12* cc-pVDZ-F12	B2PLYP- D3(BJ) def2-QZVP	B3LYP- D3(BJ) def2-TZVP	B3LYP def2-TZVP
-147.1	-3.1	-4.0	+17.6
-154.0	-0.9	-0.5	+17.1
-159.4	+1.2	-0.1	+27.2
(-171.9) ^c	0.0	-1.3	+34.0
-130.3	+0.6	-2.2	+5.8
-173.5	+0.6	-1.8	+8.7
-110.5	+2.5	+2.4	+14.1

a) single-point calculations on structures optimized at the TPSS-D3(BJ)/def2-TZVP level, $E_{\text{bind}}(\text{ref}) = \Sigma E(\text{products}) - \Sigma E(\text{reactants})$; b) single-point calculations on structures optimized at the BP86-D3(BJ)/def2-SV(P) level, $\Delta E_{\text{bind}} = E_{\text{bind}} - E_{\text{bind}}(\text{ref})$; c) CCSD(T) calculation not feasible. B2PLYP-D3(BJ) value used as reference value.

Table 11 - Binding of different molecule present in the reaction medium to $\text{Al}(\text{OTf})_3$. Difference in binding energy (ΔE_{bind} , kJ mol^{-1}) compared to the reference value $E_{\text{bind}}(\text{ref})$ obtained at the B2PLYP-D3(BJ)/def2-QZVP//TPSS-D3(BJ)/def2-TZVP level.

	$E_{\text{bind}}(\text{ref})^{\text{a}}$	$\Delta E_{\text{bind}}^{\text{b}}$
	B2PLYP-D3(BJ) def2-QZVP	B3LYP-D3(BJ) def2-TZVP
Benzyl Alcohol	-122.0	-4.5
N-butanol	-111.8	-1.7
Aniline	-117.8	-2.4
N-Phenylbenzylamine	-126.7	-1.7
Water	-104.4	-5.5
Ammonia	-131.9	-4.2
Nitromethane	-60.7	-1.3

a) single-point calculations on structures optimized at the TPSS-D3(BJ)/def2-TZVP level, $E_{\text{bind}}(\text{ref}) = \Sigma E(\text{products}) - \Sigma E(\text{reactants})$; b) single-point calculations on structures optimized at the BP86-D3(BJ)/def2-SV(P) level, $\Delta E_{\text{bind}} = E_{\text{bind}} - E_{\text{bind}}(\text{ref})$.

AlF_3 was chosen as a small model system for CCSD calculations. The CCSD(T)-F12* method²²¹ is a more economical way to approach the basis set limit. For computational efficiency the rather small double-zeta cc-pVDZ-F12 basis set was used, but the error in the binding energies of water and ammonia was found to be acceptable (0.5 and 0.3 kJ mol^{-1} , respectively), compared to the triple-zeta cc-pVTZ-F12 basis set generally recommended for this method.²²¹ In all CCSD calculations 5 occupied shells were frozen for Al and additionally 1 occupied shell for each first row heavy atom (e.g., 8 frozen orbitals for AlF_3). In cases when CCSD(T) was not applicable (N-phenylbenzylamine and all calculations with Al triflate), the reference values were obtained with a dispersion-corrected double-hybrid functional, B2PLYP-D3(BJ), and the large def2-QZVP basis set. All structures for the benchmark calculations were optimized at the TPSS-D3(BJ)/def2-TZVP level, as recommended by others.²²² From **Table 10** (binding to AlF_3), we note the excellent agreement between CCSD(T) and the double hybrid method, with deviations (ΔE_{bind}) of less than 3 kJ mol^{-1} , thus validating the use of the latter as reference for calculations

²²¹ C. Hättig, D. P. Tew, A. Köhn, *J. Phys. Chem.*, **2010**, *132*, 231102; D. P. Tew, W. Klopper, C. Neiss, C. Hättig, *Phys. Chem. Chem. Phys.*, **2007**, *9*, 1921-1930; R. A. Bachorz, F. A. Bischoff, A. Glöß, C. Hättig, S. Höfener, W. Klopper, D. P. Tew, *J. Comput. Chem.*, **2011**, *32*, 2492-2513.

²²² J. Antony, R. Sure, S. Grimme, *Chem. Commun.*, **2015**, *51*, 1764-1774.

which are not feasible with CCSD(T). Noteworthy, for both AlF_3 and $\text{Al}(\text{OTf})_3$, results of similar quality can be obtained with the B3LYP-D3(BJ)/def2-TZVP//BP86-D3(BJ)/def2-SV(P) method chosen for the present work. Note, that it is very important to include the dispersion corrections as omitting them leads to large differences with the reference values (up to 34 kJ mol⁻¹, see column 4 in **Table 10**). The excellent performance of the B3LYP-D3(BJ)/def2-TZVP//BP86-D3(BJ)/def2-SV(P) method is replicated with $\text{Al}(\text{OTf})_3$ (**Table 11**), thus lending further confidence to the chosen DFT method.

2.6. Determination of the structure of the catalyst by DFT calculations

$\text{Al}(\text{OTf})_3$ can coordinate up to three molecules, assuming monodentate coordination of the triflate anions (as opposed to the bidentate κ^2 -coordination in free $\text{Al}(\text{OTf})_3$, **Figure 32a**).

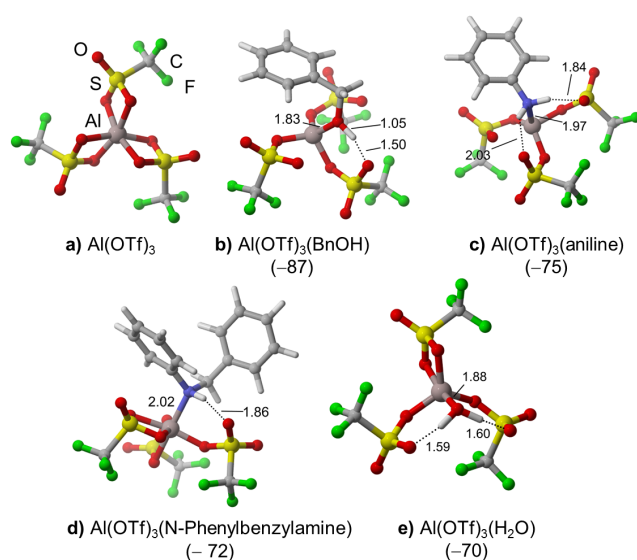


Figure 32 - Optimized structures of free $\text{Al}(\text{OTf})_3$ (a), after coordination of reactants (b-c) and products (d-e), and calculated binding free energies (G_{bind} at 25 °C in toluene, kJ mol⁻¹, indicated in brackets).

The binding free energy (G_{bind}) of n ligands L to $\text{Al}(\text{OTf})_3$ is defined as the free energy associated with the formation of a $[\text{Al}(\text{OTf})_3\text{L}_n]$ complex from $\text{Al}(\text{OTf})_3$ and n ligands L. At 25 °C in toluene this binding is strongest for BnOH ($G_{\text{bind}} = -87$ kJ mol⁻¹), followed by aniline ($G_{\text{bind}} = 75$ kJ mol⁻¹) and the reaction products, N-phenylbenzylamine ($G_{\text{bind}} = -72$ kJ mol⁻¹) and water ($G_{\text{bind}} = -70$ kJ mol⁻¹) (**Figure 32b-e** and **Table 12**, entries 1-4). These values agree well with the experimentally observed stronger binding of BnOH compared to aniline (*vide supra*). Note, that alcoholysis of $\text{Al}(\text{OTf})_3$ by BnOH leading to the formation of $\text{Al}(\text{OTf})_2(\text{BnO})$ and HOTf was found to be much less favorable than binding of BnOH to Al(III) ($\Delta G = +32$ vs $G_{\text{bind}} = -87$ kJ mol⁻¹).

Table 12 - Calculated binding free energies (G_{bind} , kJ mol⁻¹) at 25 and 160 °C of 1-3 equiv. of BnOH, aniline or water to Al(OTf)₃ in toluene solvent.

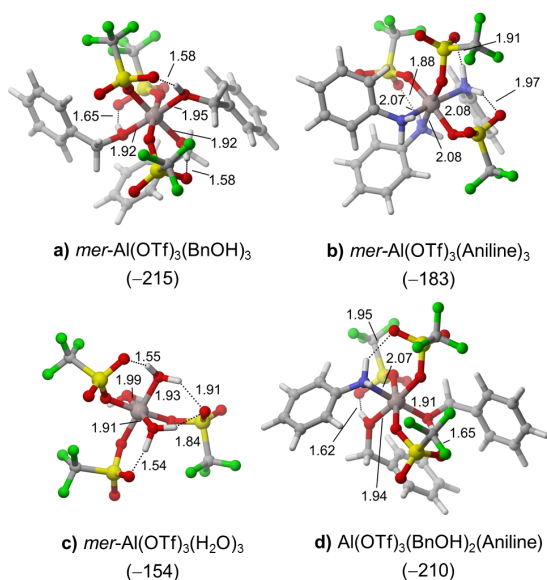
Entry		G_{bind} (25 °C)	G_{bind} (160 °C)
1	1 BnOH	-87	-75
2	1 Aniline	-75	-61
3	1 N-Phenylbenzylamine	-72	-54
4	1 H ₂ O	-70	-60
5	2 BnOH	-145	-104
6	2 Aniline	-122	-85
7	2 H ₂ O	-111	-79
8	3 BnOH <i>mer</i>	-215	-159
9	2 BnOH, 1 Aniline	-210	-155
10	2 Aniline, 1 BnOH	-196	-138
11	1 BnOH, 1 Aniline, 1 H ₂ O	-195	-142
12	2 BnOH, 1 H ₂ O	-194	-144
13	2 Aniline, 1 H ₂ O	-189	-138
14	3 Aniline <i>mer</i>	-183	-126
15	3 BnOH <i>fac</i>	-183	-125
16	2 H ₂ O, 1 BnOH	-173	-127
17	2 H ₂ O, 1 Aniline	-172	-123
18	3 H ₂ O <i>mer</i>	-154	-111
19	3 H ₂ O <i>fac</i>	-139	-96
20	3 Aniline <i>fac</i>	-131	-73

The high affinity of BnOH for Al(III) can be rationalized *a priori* by the high oxophilicity of Al(III),^[28] but it is possible to analyze more in detail the nature of the interaction by NBO charge analysis (**Table 13**): Both Al-O and Al-N bonds result mainly from ionic interactions between the strongly charged atoms (Interestingly, the coordination of a single molecule (BnOH or aniline) leads to a higher charge separation (for BnOH: from +1.92 to +2.17 on the Al(III) and from -0.71 to -0.87 on the O atom). For aniline coordination, charge separation is significantly smaller with a lower polarization on Al(III) (+0.14 *vs.* +0.25 for BnOH). Also, the Al-O bond is much shorter than the Al-N bond, leading to a stronger coulombic interaction for the O atom. All these observations are consistent with a hard acid / hard base interaction, favoring O-coordination.

Table 13 - Selected NBO partial charges estimated by NBO,^[29] and Al-O/N bond lengths (d) for Al(OTf)₃, Al(OTf)₃(BnOH) and Al(OTf)₃(aniline). Changes, compared to free Al(OTf)₃, BnOH and aniline, are indicated in brackets.

	Al(OTf) ₃	Al(OTf) ₃ (BnOH)	Al(OTf) ₃ (aniline)	BnOH	aniline
charge on Al	1.92	2.17 (+0.25)	2.06 (+0.14)		
charge O/N		-0.87 (-0.16)	-0.96 (-0.19)	-0.71	-0.79
d(Al-O/N) (Å)		1.83	1.97		
q ₁ q ₂ /d		-1.0316	-1.0039		

A second interaction likely contribute to the difference between BnOH and aniline. The coordination of the reactant and product molecules leads to decooordination of one or several O atoms of the initially κ^2 -coordinated triflate anions from the Al(III) center. These O atoms can now participate in stabilizing H-bonds with protons from the molecules coordinated to Al(III) (**Figure 32**). The strongest H-bonds are formed with O-bound molecules, i.e. BnOH (1 bond with $d(\text{O}_{\text{OTf}}\text{-H}) = 1.50 \text{ \AA}$) and water (2 bonds with $d(\text{O}_{\text{OTf}}\text{-H}) = 1.59\text{-}1.60 \text{ \AA}$), while much weaker bonds are formed with the N-containing aniline and *N*-phenyl benzylamine ($d(\text{O}_{\text{OTf}}\text{-H}) = 1.84\text{-}2.03 \text{ \AA}$). The energetic gain of binding a second BnOH molecule to Al(OTf)₃(BnOH) is smaller (-58 kJ mol^{-1} , see **Table 12**, entry 5) than for the first molecule, probably because the Lewis acidity of Al(III) is reduced by the already bound BnOH. Note that for the other molecules, the relative binding strengths (i.e. BnOH > aniline > H₂O) are preserved (**Table 12**, entries 6-7).

**Figure 33** - Selected optimized structures of complexes of Al(OTf)₃ with 3 molecules of BnOH, aniline, or water; and calculated binding free energies (G_{bind} at 25 °C in toluene, kJ mol^{-1} , indicated in brackets) defined relative to separate Al(OTf)₃ and ligand molecules.

The binding of a 3rd BnOH molecule on Al(III) results in a strong stabilization by -70 kJ mol^{-1} *vs.* Al(OTf)₃(BnOH)₂, probably because a very stable octahedral structure is formed ($G_{\text{bind}} = -215 \text{ kJ mol}^{-1}$, **Figure 33a** and **Table 12**, entry 8). Note that when only one type of

molecule is coordinated, both *fac* and *mer* isomers can be formed with either all triflate ions and ligands grouped on opposite sides of the octahedron (*fac*), or occupying the octahedral planes (*mer*). *mer*-Arrangement was found more stable than *fac*-coordination by 32, 51 and 14 kJ mol⁻¹ for BnOH, aniline and water, respectively, most likely because steric and electrostatic repulsion between the coordinated molecules and the triflate anions is minimized (**Table 12**). The higher binding strength of BnOH, compared to aniline and water is conserved for the binding of 3 molecules ($G_{\text{bind}} = -215$ vs. -183 kJ mol⁻¹ and -154 kJ mol⁻¹, respectively, see **Figure 33a-c**). We also calculated all possible mixed combinations with *n* BnOH / *l* aniline and *m* water molecules ($n + l + m = \text{max. } 3$, see **Table 12**). This analysis confirms that *mer*-Al(OTf)₃(BnOH)₃ is indeed the most stable structure in toluene, thus corroborating the experimental findings, which clearly indicated preferential binding of BnOH in toluene. BnOH is present in all most mixed stable configurations (see for example **Figure 33d** and **Table 12**, entries 8-12) and all combinations without BnOH are significantly less stable. Unlike the monoligated complexes, the partial charge on Al(III) decreased and the Al-O/N bond length increased (**Table 14**), both factors being consistent with a decreasing binding energy per ligand (**Figure 34a**).

Table 14 - Selected partial charges estimated by NBO, and bond lengths for Al(OTf)₃(BnOH), Al(OTf)₃(BnOH)₂ and Al(OTf)₃(BnOH)₃. Changes, compared to Al(OTf)₃(BnOH) are indicated in brackets.

Entry	Complex	Charge Al	Al-O bond (Å)
1	Al(OTf) ₃ (BnOH)	2.17	1.83
2	Al(OTf) ₃ (BnOH) ₂	2.16 (-0.01)	1.91 (+0.08)
3	Al(OTf) ₃ (BnOH) ₃	2.09 (-0.08)	1.95 (+0.12)

The binding free energies were in addition computed at 160 °C (**Table 12, Figure 34b**). At this temperature, binding to Al(OTf)₃ is much less favorable. Low-coordinated and potentially more reactive metastable complexes such as Al(OTf)₃(BnOH)₂ and Al(OTf)₃(BnOH) are thus accessible under reaction conditions, but unlikely at 25 °C, at which CV and conductometry tests were performed. In what follows, Al(OTf)₃(BnOH)₃ is the most stable structure in toluene, i.e. the *resting* state of the catalyst, while less stable structures will be called *reactive* states.

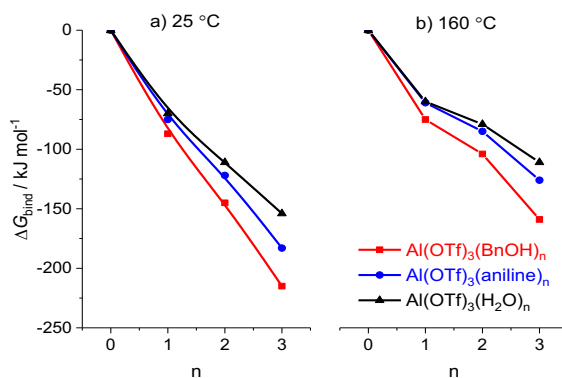


Figure 34 - Binding free energy (ΔG_{bind} , kJ mol⁻¹) of 1-3 BnOH, aniline or water molecules to Al(OTf)₃ at 160 °C and 25 °C in toluene.

2.7. Amination Mechanism

In polar solvents, a S_N1 -type mechanism can be proposed for the direct amination reaction of BnOH. Indeed, dissociation of $\text{Al}(\text{OTf})_3(\text{BnOH})_3$ into $[\text{Al}(\text{OTf})_3(\text{BnOH})_2(\text{OH})]^-$ and a benzyl cation is feasible in nitromethane, albeit associated with a sizeable barrier ($\Delta G = +97 \text{ kJ mol}^{-1}$). Combined with the energetic cost to displace the strongly bound aniline from the Al(III) center (*vide supra*), this explains why much harsher conditions are necessary than for the more reactive secondary alcohols, and less basic and thus less coordinating amine derivatives used by Mashima.²²³ The formation of cationic species is very likely responsible for side reactions and in turn for the low selectivity. In contrast, in toluene, where a S_N1 mechanism is impossible ($\Delta G = +272 \text{ kJ mol}^{-1}$), one can more reasonably assume a S_N2 -type mechanism, in which aniline attacks the C-atom of BnOH coordinated to Al(III), thus avoiding the formation of ionic species.

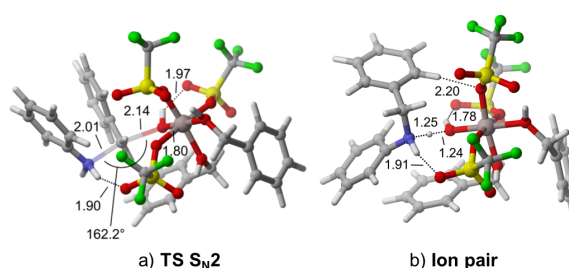


Figure 35 - Transition state (TS S_N2) and ion-pair occurring in the reaction of aniline with $\text{Al}(\text{OTf})_3(\text{BnOH})_3$ in toluene; selected distances are indicated in Å.

Starting from $\text{Al}(\text{OTf})_3(\text{BnOH})_3$, three different C-O bonds can be broken. Since the structures of the transition states are similar, we only report the most favorable case (**Figure 35a** and **Figure 36**, $\Delta G^\ddagger = 117 \text{ kJ mol}^{-1}$; attack on the other two benzylic carbon atoms is slightly less favorable by 3 and 13 kJ mol^{-1}). The transition state features trigonal-bipyramidal coordination and sp^2 -hybridization of carbon, as expected for a S_N2 reaction. The O-C-N angle formed between the breaking C-O and the forming C-N bond is close to linear (162°). Note, that a triflate ligand stabilizes the transition state by forming a H-bond with one of the protons of aniline. The product of an intrinsic reaction coordinate (IRC) run starting from the transition state converges to a stable structure in which protonated *N*-phenyl benzylamine is bound to $[\text{Al}(\text{OTf})_3(\text{BnOH})_2(\text{OH})]^-$ (**Figure 35a** and **Figure 36**, $\Delta G = -21 \text{ kJ mol}^{-1}$). This structure can be interpreted either as an ion-pair, or as an acid-base adduct in which the basic N of the amine product interacts with the proton of the water molecule, which, in turn, is acidified by its coordination to Al(III). Proton transfer and decoordination of *N*-phenylbenzylamine leads to $\text{Al}(\text{OTf})_3(\text{BnOH})_2(\text{H}_2\text{O})$ ($\Delta G = -1 \text{ kJ mol}^{-1}$), and release of water to $\text{Al}(\text{OTf})_3(\text{BnOH})_2$. Unlike the most stable isomer found for coordination of 2 BnOH (**Table 12**, entry 5), the resulting structure is five-coordinate and therefore less stable ($\Delta G = +70 \text{ kJ mol}^{-1}$). Finally, BnOH coordination leads back to $\text{Al}(\text{OTf})_3(\text{BnOH})_3$ ($\Delta G = -18 \text{ kJ mol}^{-1}$), the resting state of the catalyst.

²²³ T. Ohshima, J. Ipposhi, Y. Nakahara, R. Shibuya, K. Mashima, *Adv. Synth. Catal.* **2012**, *354*, 2447-2452

In addition to $\text{Al}(\text{OTf})_3(\text{BnOH})_3$, the resting state of the catalyst (i.e. the most stable situation), we studied *reactive* states of the catalyst, i.e. less stable structures in which one or several BnOH have been exchanged by either aniline or water. The height of the intrinsic barrier ($\Delta G_{\text{intr}}^\ddagger$) provides a measure of the reactivity of each reactive state, while the total barrier ($\Delta G_{\text{tot}}^\ddagger$) compares the reactivity with that of $\text{Al}(\text{OTf})_3(\text{BnOH})_3$ (**Table 15**). For both $\text{Al}(\text{OTf})_3(\text{BnOH})_2(\text{X})$ and $\text{Al}(\text{OTf})_3(\text{BnOH})(\text{X})_2$ with $\text{X} = \text{H}_2\text{O}$ or aniline, the structures of the transition state and ion-pairs (**Figure 37**) are very similar to those found for $\text{Al}(\text{OTf})_3(\text{BnOH})_3$.

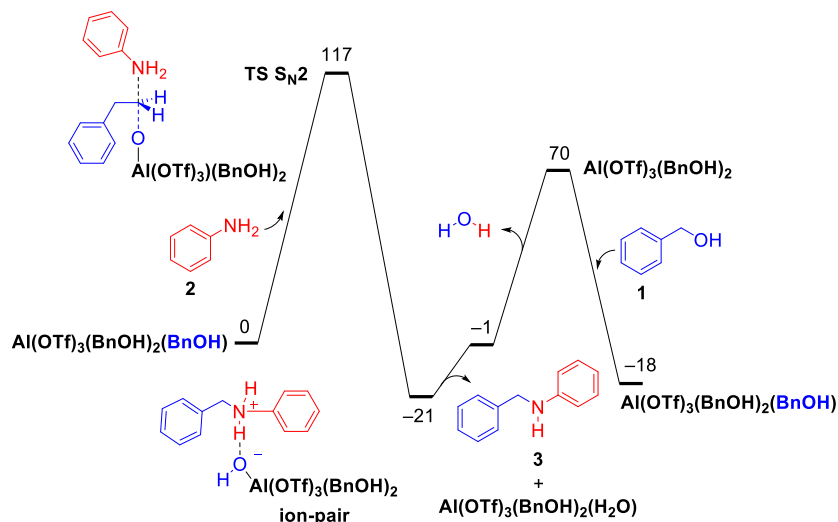


Figure 36 - Calculated free energy profile for the direct amination of benzyl alcohol with aniline to *N*-phenylbenzylamine and water in toluene. Free energies (ΔG at 160 °C, kJ mol^{-1}) are defined relative to separate $\text{Al}(\text{OTf})_3(\text{BnOH})_3$ and aniline.

As a result, the intrinsic barriers are similar (**Table 15**, entries 2-5) ($\Delta G_{\text{intr}}^\ddagger = 117 \text{ kJ mol}^{-1}$, **Table 15**, entry 1), while in the case of $\text{Al}(\text{OTf})_3(\text{BnOH})_2(\text{H}_2\text{O})$ the barrier is even lower ($\Delta G_{\text{intr}}^\ddagger = +108 \text{ kJ mol}^{-1}$, **Table 15**, entry 3). This means that for coordination of 3 ligands to Al(III), the nature of the ligands has no significant effect on the reactivity of coordinated BnOH. However, given the lower stability of the reactive states compared to $\text{Al}(\text{OTf})_3(\text{BnOH})_3$, the cost for ligand exchange has to be accounted for. Indeed, when only 1 BnOH is exchanged for aniline or water, the effect is small, ($\Delta G_{\text{tot}}^\ddagger = 121\text{-}123 \text{ kJ mol}^{-1}$, **Table 15**, entries 2-3), but when 2 ligands are exchanged, the reaction becomes significantly more difficult ($\Delta G_{\text{tot}}^\ddagger = 140\text{-}151 \text{ kJ mol}^{-1}$, **Table 15**, entries 4-5).

Table 15 - Calculated intrinsic free energy barrier with respect to the reactive state ($\Delta G_{\text{intr}}^{\ddagger}$) and aniline, total free energy barrier ($\Delta G_{\text{tot}}^{\ddagger}$) with respect to the resting state $\text{Al}(\text{OTf})_3(\text{BnOH})_3$ and aniline, and partial charge on the Al atom calculated by NBO (difference *vs.* $\text{Al}(\text{OTf})_3(\text{BnOH})_3$ in brackets); free energies in toluene at 160 °C (kJ mol^{-1}).

Entry	Reactive state	$\Delta G_{\text{intr}}^{\ddagger}$	$\Delta G_{\text{tot}}^{\ddagger}$	Charge on Al
1	$\text{Al}(\text{OTf})_3(\text{BnOH})_3$	117	117	2.09
2	$\text{Al}(\text{OTf})_3(\text{BnOH})_2(\text{Aniline})$	117	121	2.06 (-0.03)
3	$\text{Al}(\text{OTf})_3(\text{BnOH})_2(\text{H}_2\text{O})$	108	123	2.03 (-0.06)
4	$\text{Al}(\text{OTf})_3(\text{BnOH})(\text{Aniline})_2$	119	140	2.05 (-0.04)
5	$\text{Al}(\text{OTf})_3(\text{BnOH})(\text{H}_2\text{O})_2$	119	151	2.01 (-0.08)
6	$\text{Al}(\text{OTf})_3(\text{BnOH})$	71	155	2.17 (+0.08)

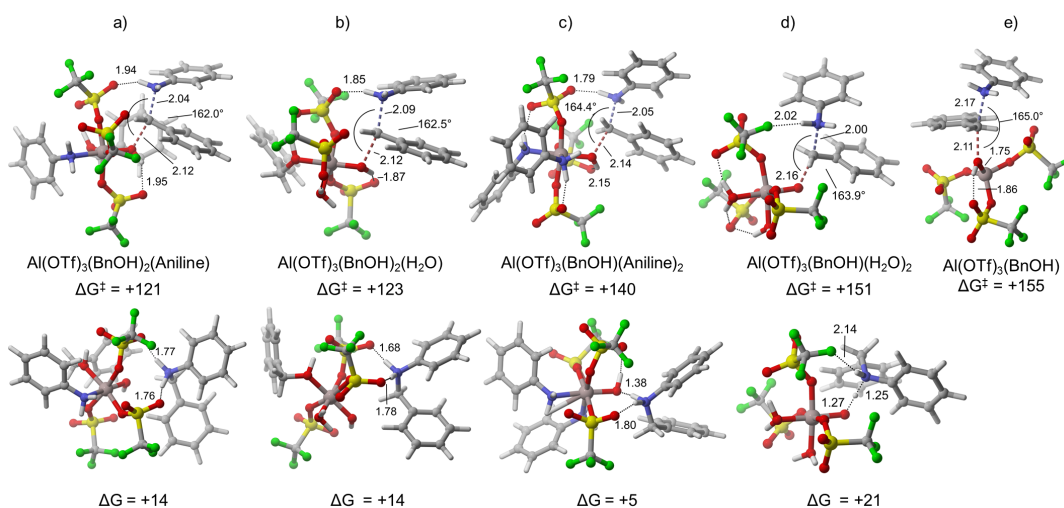


Figure 37 - Optimized structures for the $\text{S}_{\text{N}}2$ -type transition state in the reaction of aniline with different "reactive states" of $\text{Al}(\text{OTf})_3$, and corresponding product-catalyst ion pairs; free energies at 160 °C (kJ mol^{-1}) relative to the "resting state" $\text{Al}(\text{OTf})_3(\text{BnOH})_3$; selected distances are indicated in Å.

Finally, we also studied the reactivity of the low-coordinated complex $\text{Al}(\text{OTf})_3(\text{BnOH})$. Not surprisingly, the energy barrier for the $\text{S}_{\text{N}}2$ reaction is very low ($\Delta G_{\text{intr}}^{\ddagger} = 71 \text{ kJ mol}^{-1}$, **Figure 37e**), most likely because of its higher Lewis acidity, as apparent from the higher partial charge on Al(III) compared to coordination by 3 ligands (**Table 15**, last column). However, as already mentioned, starting from $\text{Al}(\text{OTf})_3(\text{BnOH})_3$, the formation of $\text{Al}(\text{OTf})_3(\text{BnOH})_2$ and $\text{Al}(\text{OTf})_3(\text{BnOH})$ by successive losses of BnOH is associated with an energetic cost of 55 and 29 kJ mol^{-1} , respectively (**Table 12**, entries 1, 5, and 8). Overall, cost the energetic cost to generate $\text{Al}(\text{OTf})_3(\text{BnOH})$ outweighs its higher reactivity, leading to an overall barrier of $\Delta G_{\text{tot}}^{\ddagger} = 155 \text{ kJ mol}^{-1}$ (**Table 15**, entry 6), which is significantly higher than that for the fully coordinated resting state of the catalyst, or other reactive states. To summarize, the high selectivity in the direct amination of primary benzyl alcohol by aniline in toluene solvent can be rationalized by an $\text{S}_{\text{N}}2$

mechanism. To our knowledge, such pathway has not been proposed before for OH-substitution reactions mediated by metal triflates. We also propose that, instead of 1 active species, several active species can play a role, generated by exchange of coordinated BnOH with water or aniline, thus underlining the robustness (ability to work under very different concentrations of reactants and products) of metal triflates.

2.8. Conclusions

These preliminary results on Al(OTf)₃-catalyzed direct amination of activated secondary alcohols with electron-poor and electron-rich amines, on the model reaction of benzyl alcohol and aniline allowed us to provide detailed insight into the structure of the catalyst and the mechanism of the reaction, which were found to strongly depend on the type of solvent (polar vs. non-polar). Competition between aniline and benzyl alcohol was evidenced both by NMR spectroscopy and cyclic voltammetry, and proved to be critical to explain how the solvent tunes the reactivity. The strong affinity of aniline for Al(III) in nitromethane solvent, which can be attributed to the formation of ionic species, is responsible for catalyst deactivation and very low selectivity. Under such conditions, a S_N1-type mechanism is active. In contrast, in toluene, the reaction is very selective, leading to almost exclusive formation of the desired *N*-phenylbenzylamine even at high temperature allowing an extension of the scope to more electron rich amines.

The next step was naturally to try to improve the yield of the model reaction by screening the various commercially available metal triflate and triflimide salts. The results of these trials are presented in the next section of this chapter.

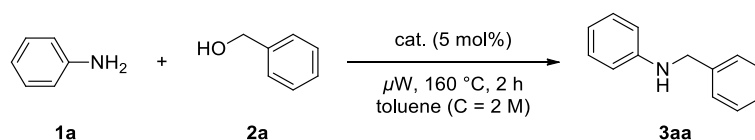
3. Rational Design of Lewis Acids for the Direct Amination of Alcohols

3.1. Experimental Trends for Amination within a series of Lewis Acids

The experimental part of this sub-section (3.1.) has been performed by Celine Finidori under the supervision of Dr Damien Cartigny.

A series of non-noble $M(\text{OTf})_n$ and $M(\text{NTf}_2)_n$ salts were screened on the model amination reaction between benzyl alcohol (**1a**) and aniline (**2a**) in toluene targeting the formation of *N*-benzylaniline (**3aa**) (Table 16 and Table 17). Several general trends emerged from these results. As a rule, triflimides gave better results than triflates, matching the literature.²²⁴ Both alkaline and alkaline-earth metals displayed very low activity. Likewise, late transition metals were not efficient. On the contrary, high yields were obtained using early transition metals, *p*-block metals and lanthanides. Noteworthy, this behavior differs from that reported by Kobayashi and co-workers for Mukaiyama reaction in wet THF.²²⁵

Table 16 - Triflate salts screening.



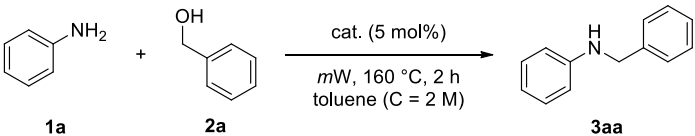
Entry	Catalyst	Yield (%) ^[a]
1	-	< 1
2	Cs(OTf) ₂	< 1
3	Zn(OTf) ₂	< 1
4	Cu(OTf) ₂	< 1
5	Ca(OTf) ₂	< 1
6	Y(OTf) ₃	6
7	Sc(OTf) ₃	6
8	La(OTf) ₃	6
9	Ti(OTf) ₄	9
10	Al(OTf) ₃	17
11	Fe(OTf) ₃	39
12	Bi(OTf) ₃	49

[a] Determined by ¹H NMR

²²⁴ S. Antoniotti, V. Dalla, E. Duñach, *Angew. Chem. Int. Ed.* **2010**, *49*, 7860-7888.

²²⁵ (b) S. Kobayashi, S. Nagayama, T. Busujima, *J. Am. Chem. Soc.* **1998**, *120*, 8287-8288; (c) K. Yusuke, N. Kiyotaka, K. Hisayoshi, H. Ryota, K. Masaaki, H. Michikazu, *Chem. Eur. J.* **2014**, *20*, 8068-8075.

Table 17 - Triflimidate salts screening.

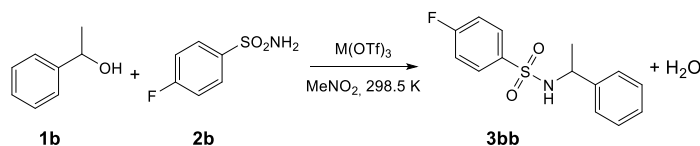


Entry	Catalyst	Yield (%)	Entry	Catalyst	Yield (%)
1	-	< 1	18	Fe(NTf ₂) ₃	32
2	HNTf ₂	< 1	19	Y(NTf ₂) ₃	37
3	Ba(NTf ₂) ₂	0	20	In(NTf ₂) ₃	37
4	Cd(NTf ₂) ₂	0	21	La(NTf ₂) ₃	46
5	Sr(NTf ₂) ₂	0	22	Ga(NTf ₂) ₃	48
6	Ni(NTf ₂) ₂	0	23	Cr(NTf ₂) ₃	49
7	K(NTf ₂)	< 1	24	Sc(NTf ₂) ₃	51
8	Cu(NTf ₂) ₂	< 1	25	Bi(NTf ₂) ₃	51
9	Ca(NTf ₂) ₂	< 1	26	Al(NTf ₂) ₃	52
10	Li(NTf ₂)	< 1	27	Ho(NTf ₂) ₃	58
11	Cs(NTf ₂)	< 1	28	Sm(NTf ₂) ₃	59
12	Mg(NTf ₂) ₂	5	29	Gd(NTf ₂) ₃	67
13	Ir(NTf ₂) ₃	7	30	Sb(NTf ₂) ₃	72
14	Zn(NTf ₂) ₂	9	31	Nd(NTf ₂) ₃	73
15	Co(NTf ₂) ₂	11	33	Pr(NTf ₂) ₃	80
16	Mn(NTf ₂) ₂	25	34	Eu(NTf ₂) ₃	87
17	Ce(NTf ₂) ₃	29	35	Yb(NTf ₂) ₃	88

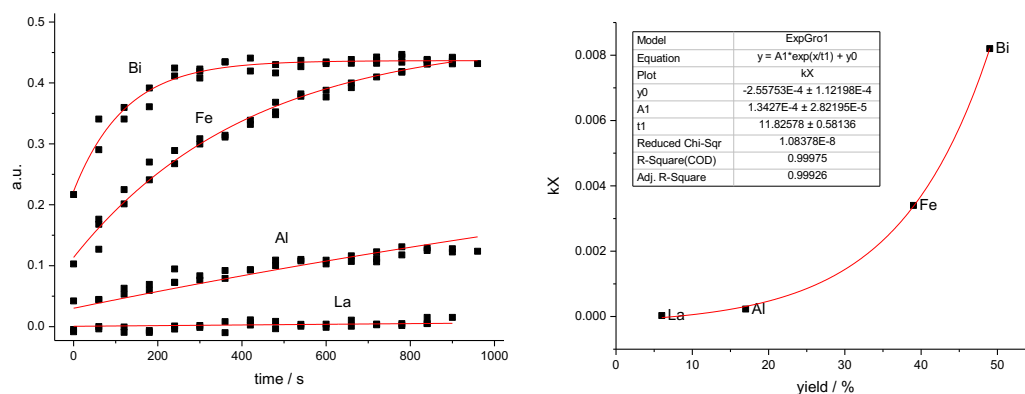
[a] Determined by ¹H NMR.

3.2. Experimental Descriptors of Lewis Acidity

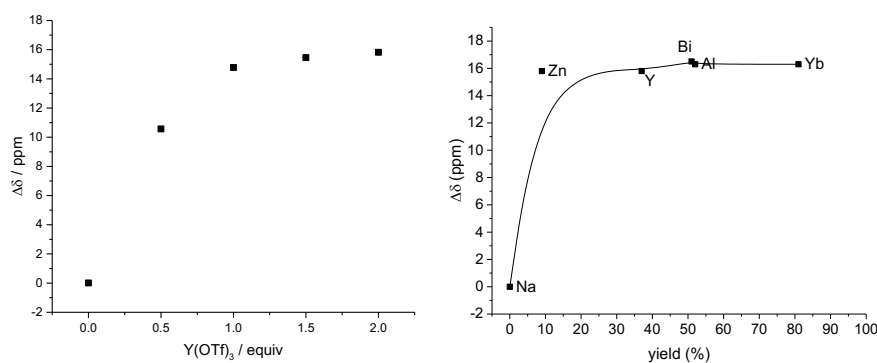
We were curious to figure out if the above trends were general for other LSA-catalyzed reactions. To this aim, we chose another amination reaction using electron-poor nitrogen derivatives in a polar and non-coordinating solvent (**Figure 38**).²²⁶ The kinetics of formation of the amination product **3bb** was monitored by ¹⁹F NMR. The first order rate constant was measured using several M(OTf)_n salts (M = La²⁺, Al³⁺, Fe³⁺, Bi³⁺). The reactivity order for both amination reactions was similar: Bi³⁺ > Fe³⁺ > Al³⁺ > La²⁺ (**Figure 39**). Note that the rate constants suffer from uncontrolled hydration, which can vary for the different salts. In all cases, the ether resulting from self-condensation was observed as by-product (**see below, section 2.3**).



²²⁶ T. Ohshima, J. Ipposhi, Y. Nakahara, R. Shibuya, K. Mashima, *Adv. Syn. Cat.* **2012**, *354*, 2447-2452.

Figure 38 - Amination of phenylethanol **1b** and *p*-fluorophenyl sulfonamide **2b**.**Figure 39** – **Left:** Kinetics of the amination reaction 2 (**1b** + **2b** = **3bb**), in the presence of $M(\text{OTf})_3$ (5 mol%) monitored by ^{19}F NMR (fluorobenzene was used as an internal standard), initial concentration: **1b**, 0.1 M; **2b** 0.2 M in nitromethane at 298.5 K. **Right:** Correlation between the yield obtained for the reaction 1 (**1a** + **2a** = **3aa**) and the first order rate constant (k_x) obtained for the reaction 2 (**2a** + **2b** = **3bb**).

We first investigated the method described by Beckett and Childs to estimate the Lewis acidity and achieve proper correlation with the catalytic results.²²⁷ This method relies on the chemical shift variation associated to the formation of a Lewis adduct to assess the electron withdrawing ability of a LA. Heteronuclear ^{19}F and ^{31}P NMR were implemented, as they are much more sensitive than ^1H NMR and do not require deuterated solvents. *p*-Fluoroaniline and triphenylphosphine oxide both exhibited very large chemical shifts with a LA excess to form mainly a 1:1 Lewis adduct (**Figure 40-Left**).²²⁸

**Figure 40** – **Left:** Variation of the chemical shift of *p*-fluoroaniline (10 mM) in nitromethane upon addition of a 0.1 M solution of $Y(\text{OTf})_3$ in nitromethane ($\Delta\delta = ^{19}\text{F}$ NMR chemical shift of *p*-fluoroaniline in the presence of n equiv of $Y(\text{OTf})_3$ – chemical shift of free *p*-fluoroaniline). **Right:** Plot of the maximal chemical shift variation ($\Delta\delta$) of *p*-fluoroaniline in the presence of $M(\text{OTf})_3$ versus the yield obtained in reaction 1 (**1a** + **2a** = **3aa**).

²²⁷ G. J. P. Britovsek, J. Ugoletti, A. J. P. White, *Organometallics* **2005**, *24*, 1685-1691; R. F. Childs, D. L. Mulholland, A. Nixon, *Can. J. Chem.* **1982**, *60*, 809-812; c) R. F. Childs, D. L. Mulholland, A. Nixon, *Can. J. Chem.* **1982**, *60*, 801-808.

²²⁸ G. Hilt, F. Pünner, J. Möbus, V. Naseri, A. Bohn Martin, *Eur. J. Org. Chem.* **2011**, *2011*, 5962-5966; G. Hilt, A. Nödling, *Eur. J. Org. Chem.* **2011**, *2011*, 7071-7075.

However, the chemical shift variation measured for different $M(\text{OTf})_n$ salts did not correlate with the reactivity order (**Figure 40-Right**), matching an earlier study.²²⁹ 2-Cyclohexen-1-one was then tested as ^1H and ^{13}C NMR probe. Under LA excess, so as to form mainly a 1:1 Lewis adduct, an up-field shift of all resonances was observed (**Figure 41**), which can be attributed to electron-withdrawing effects.²³⁰

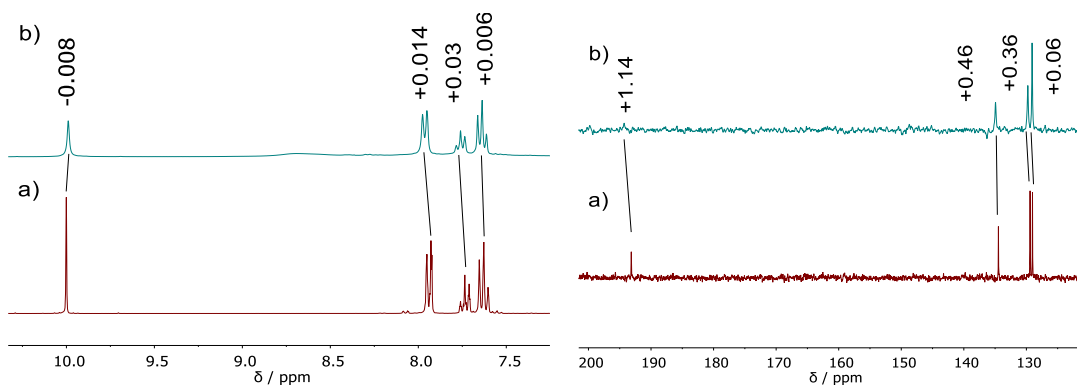


Figure 41 - ^1H and ^{13}C NMR spectra of benzaldehyde (0.09 M) in MeNO_2-d_3 , alone (a) and in the presence of excess $\text{Al}(\text{OTf})_3$, (b) (CH_3NO_2 was used as an internal reference for chemical shift calibration).

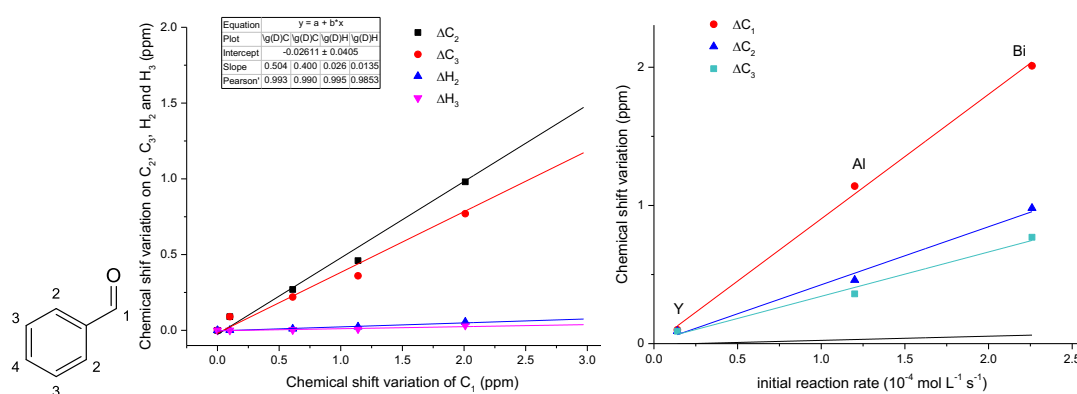


Figure 42 - **Left:** Linear correlation between the chemical shift variation of ^1H ($\Delta\delta_{\text{H}}$) and ^{13}C ($\Delta\delta_{\text{C}}$) nuclei; **Right:** Correlation between ^{13}C chemical shift variation in the presence of $M(\text{OTf})_3$ and the initial rate of the amination 2 ($1\mathbf{b} + 2\mathbf{b} = 3\mathbf{bb}$).

It was indeed possible to correlate the variation of the chemical shift with the reactivity (**Figure 42**). Nevertheless, this method is not really convenient: it requires expensive deuterated nitromethane and even in this solvent, the solubility of $M(\text{OTf})_n$ or $M(\text{NTf}_2)_n$ salts is very low. Moreover, the hydration level is once again difficult to evaluate. To circumvent these limitations, we turned our attention into theoretical descriptors.

²²⁹ These observations are consistent with the results reported in H. Böhrer, N. Trapp, D. Himmel, M. Schleep, I. Krossing, *Dalton Trans.* **2015**, 44, 7489-7499. These results are not surprising, as the ^{31}P NMR chemical shift cannot be easily correlated to electronic effects, see also J. Tong, S. Liu, S. Zhang, S. Z. Li, *Spectrochim. Acta A: Mol. Biomol. Spec.* **2007**, 67, 837-846.

²³⁰ R. F. Childs, D. L. Mulholland, A. Nixon, *Can. J. Chem.* **1982**, 60, 801-808.

3.3. Structures of metal triflate and triflimides salts

The 3D structures of a large series of M^{n+} , $M(OTf)_n$ and $M(NTf_2)_n$ salts were optimized at the BP86-BJ/def2-SVP level, while the electronic energy was calculated at the B3LYP/def2-TZVP level using the method previously reported for $Al(OTf)_3$ (see section 2.5). At this level of theory, triflates were found to be bidentate ligands in all the calculated structures with two oxygen atoms coordinated to the metal cation (**Figure 43-47**)

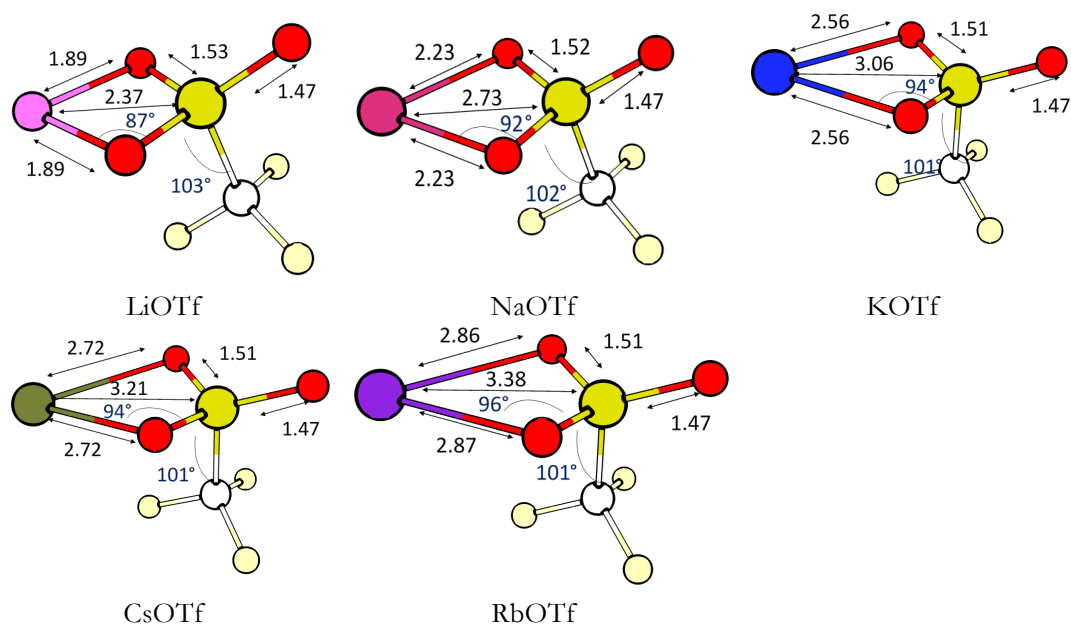


Figure 43 - Structure of alkali metal triflates.

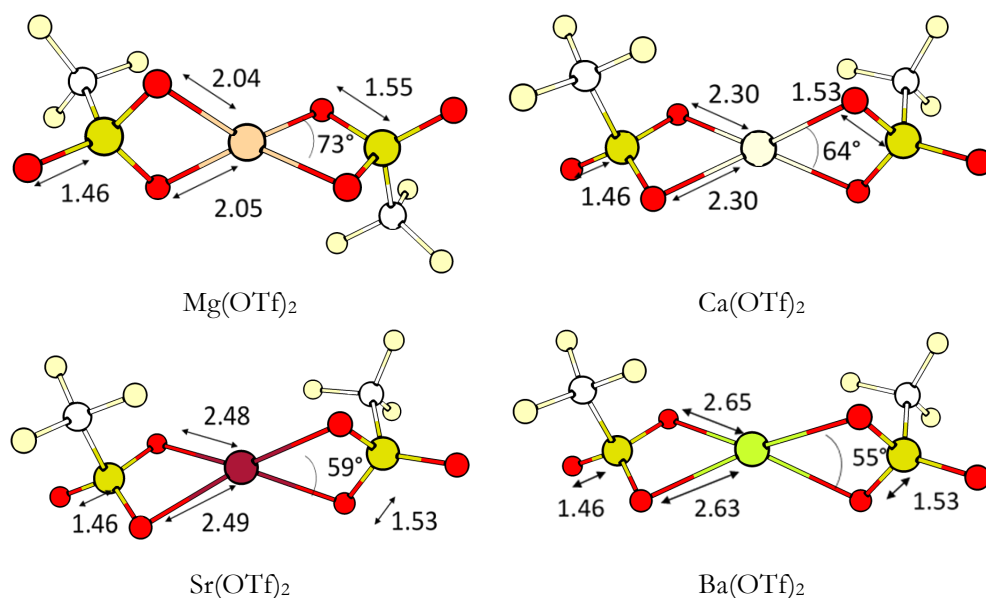


Figure 44 - Structure of alkali earth metal triflates.

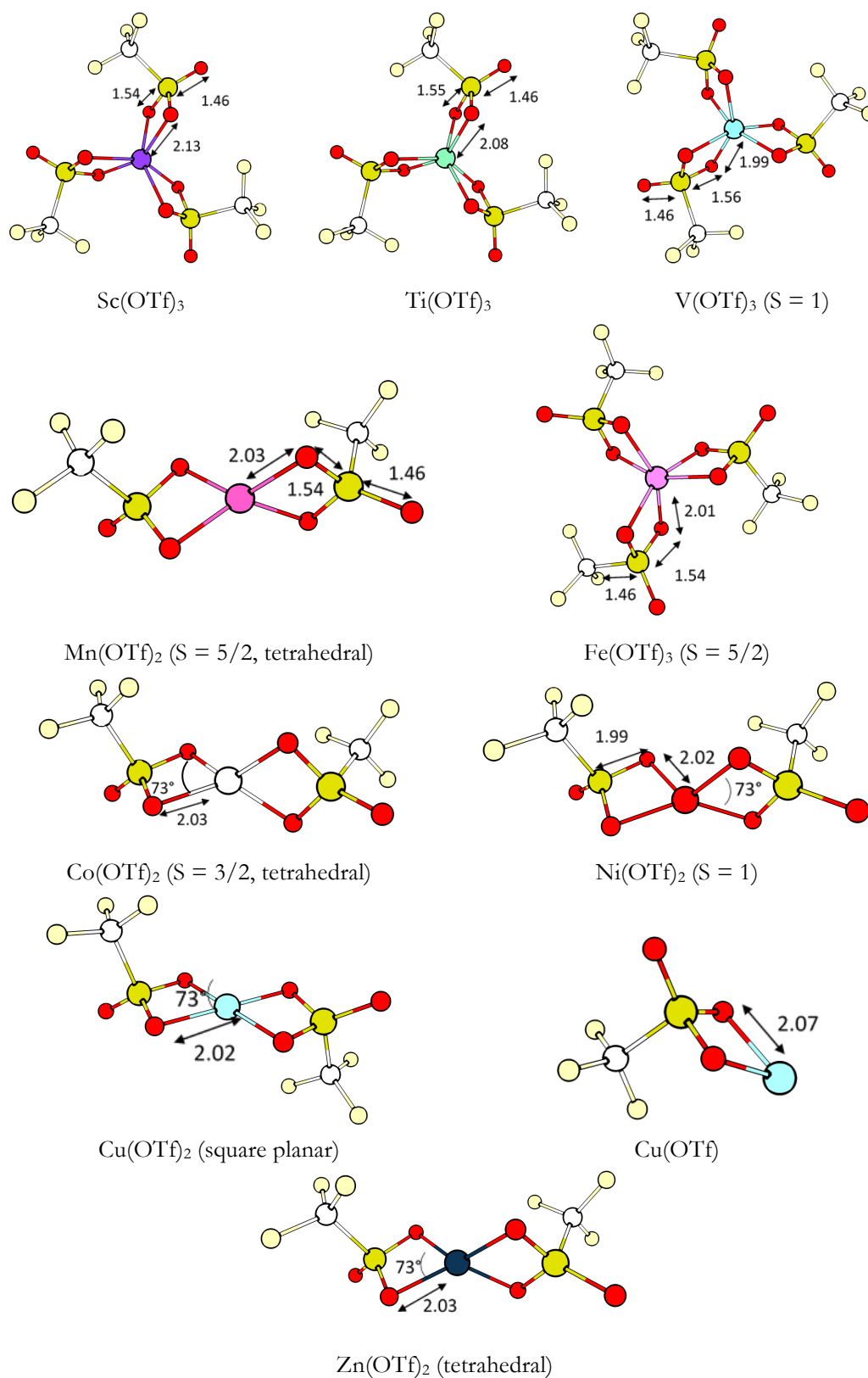


Figure 45 – Structures of Transition Metal Triflates.

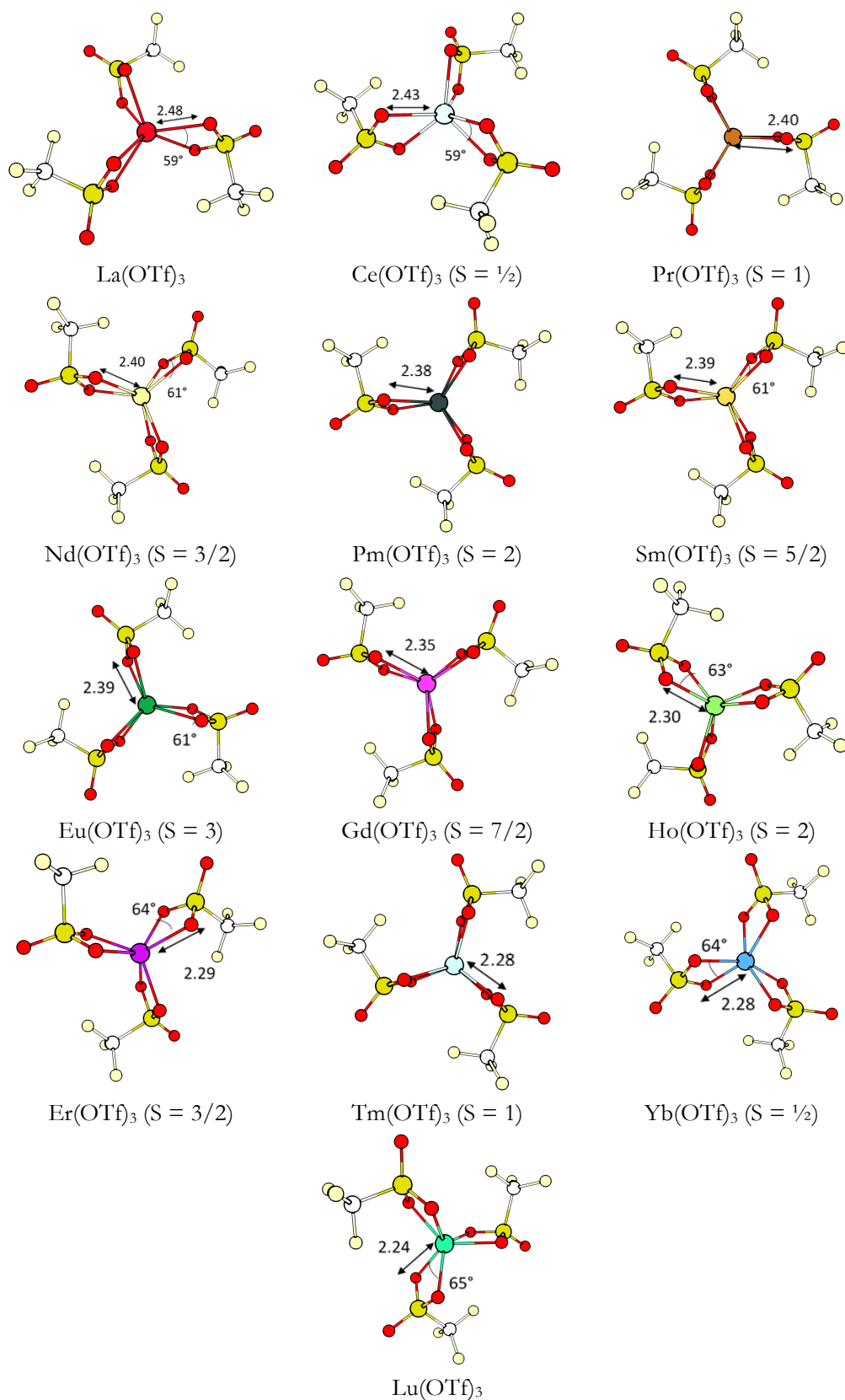


Figure 46 – Structures of Lanthanide Triflates.

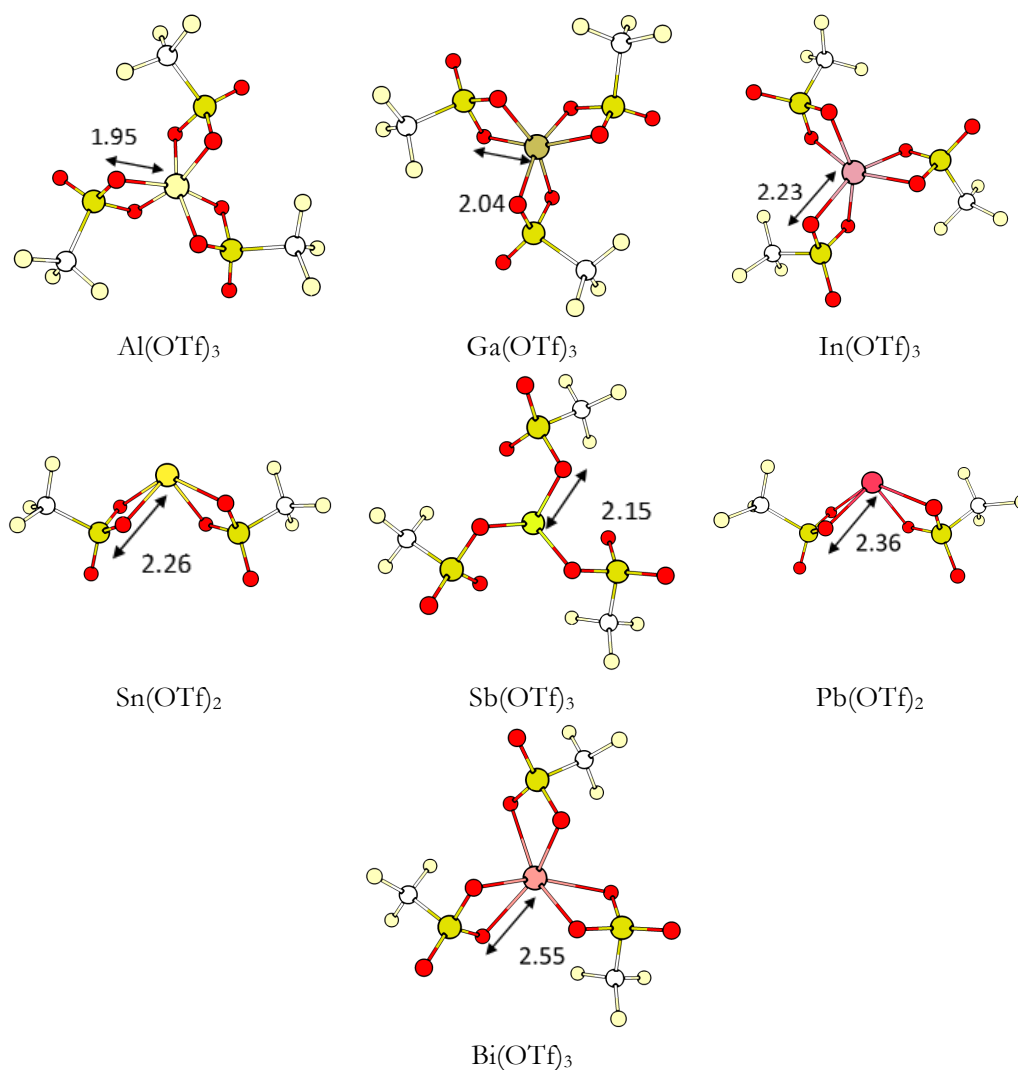


Figure 47 – Structures of post-transition metal triflates.

The case of triflimides is more challenging: triflimide anion can coordinate to a metal cation either via N or O atoms. O-bonding is generally favored for hard metals: alkali metals,²³¹ Zn,²³² La,²³³ Eu/Yb,²³⁴ or even U.²³⁵

²³¹ L. Xue, C. W. Padgett, D. D. DesMarteau, W. T. Pennington, *Solid State Sci.* **2002**, *4*, 1535-1545.

²³² M. J. Earle, U. Hakala, B. J. McAuley, M. Nieuwenhuyzen, A. Ramani, K. R. Seddon, *Chem. Commun.* **2004**, 1368-1369.

²³³ D. B. Baudry, A. Dormond, F. Duris, J. M. Bernard, J. R. Desmurs, *J. Fluorine Chem.* **2003**, *121*, 233-238.

²³⁴ M. Kawamura, S. Shimada, *Inorg. Chim. Acta* **2007**, *360*, 2162-2168.

²³⁵ S. M. Cornet, I. May, M. P. Redmond, A. J. Selvage, C. A. Sharrad, O. Rosnel, *Polyhedron* **2009**, *28*, 363-369.

In contrast, for soft metals, N-coordination was reported, especially for Cu²³⁶ Au²³⁷ (single N-coordination) Ru²³⁸ (O-N pincer coordination), and even FeCp²³⁹ (single N-coordination). Our observations from the optimized structures are consistent with experimentally reported trends.²⁴⁰ As a matter of fact, alkali triflimides are always coordinated by two O atoms, whereas for end-of-column elements (K, Rb, Cs), the interaction with the central N atom increases (**Figure 48**).

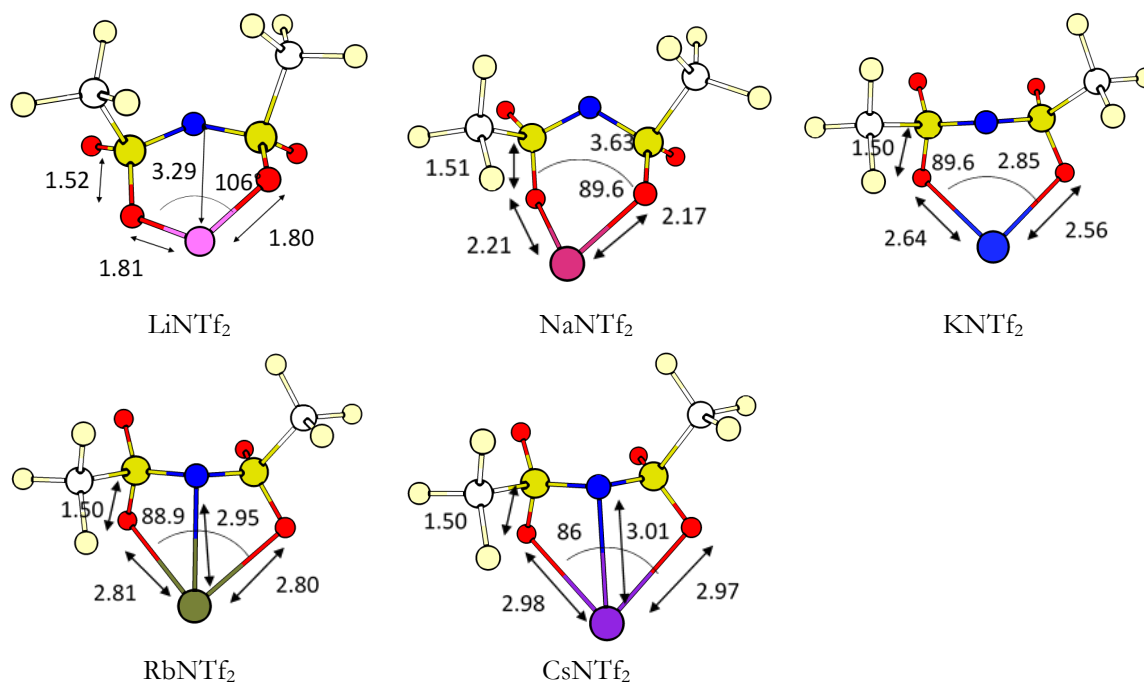


Figure 48 – Structures of alkali metal triflimides.

A similar pattern is observed for alkali earth triflimides: Mg(NTf₂)₂ exhibits a perfect tetrahedral conformation, while salts based on Sr and Ba are distorted due to an additional interaction with N atoms (**Figure 49**). Early transition metal (Ti, V, Mn, Fe) triflimides adopt a conformation with bidentate O-bonded ligands resulting in a regular octahedral or tetrahedral geometry (**Figure 50**). On the contrary, late transition metal salts (Co, Ni, Cu, Zn) feature bidentate N- and O-bonding ligands (**Figure 50**). Coordination by two O atoms is generally favored for salts featuring three triflimide ligands due to steric effects, namely based on Al, In, Ga and lanthanides (**Figure 51-52**).

²³⁶ O. G. Polyakov, S. M. Ivanova, C. M. Gaudinski, S. M. Miller, O. P. Anderson, S. H. Strauss, *Organometallics* **1999**, *18*, 3769-3771.

²³⁷ (a) N. Mézailles, L. Ricard, F. Gagosz, *Org. Lett.* **2005**, *7*, 4133-4136; (b) L. Ricard, F. Gagosz, *Organometallics* **2007**, *26*, 4704-4707.

²³⁸ D. B. Williams, M. E. Stoll, B. L. Scott, D. A. Costa, J. W. J. Oldham, *Chem. Commun.* **2005**, 1438-1440.

²³⁹ L. Coulombel, M. Rajzmann, J.-M. Pons, S. Olivero, E. Duñach, *Chem. Eur. J.* **2006**, *12*, 6356-6365.

²⁴⁰ With the exception of highly fluorophilic metals (Ca, La), a significant interaction with fluorine atoms was obtained (Figure S12 and S16).

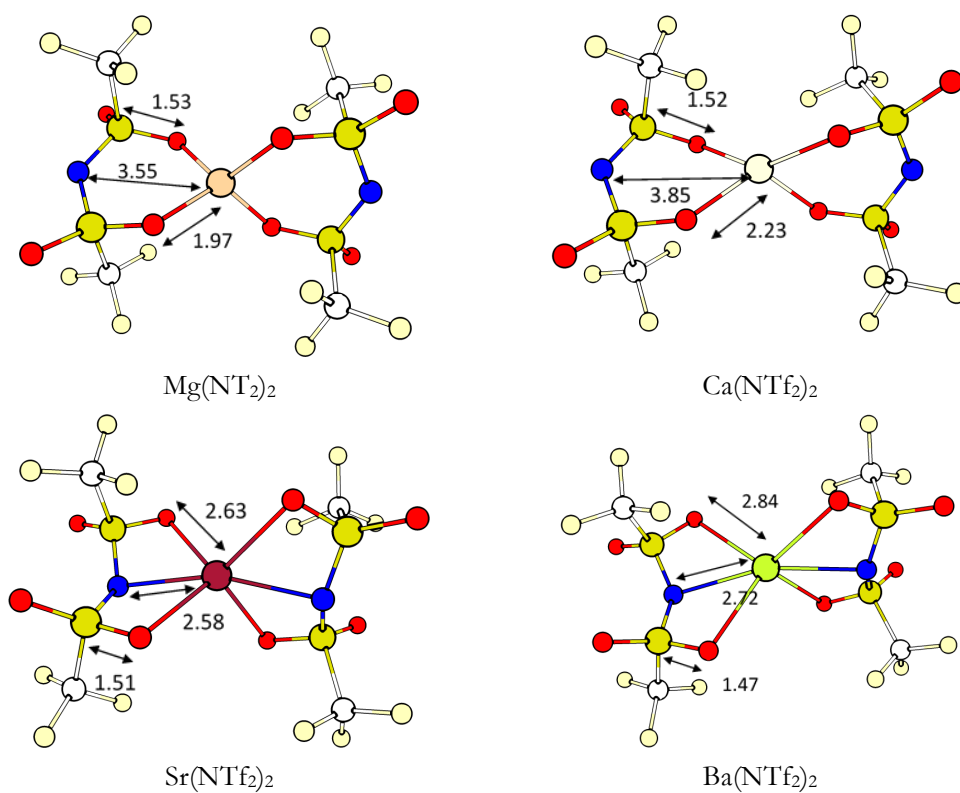


Figure 49 - Structure of alkaline earth metal triflimides.

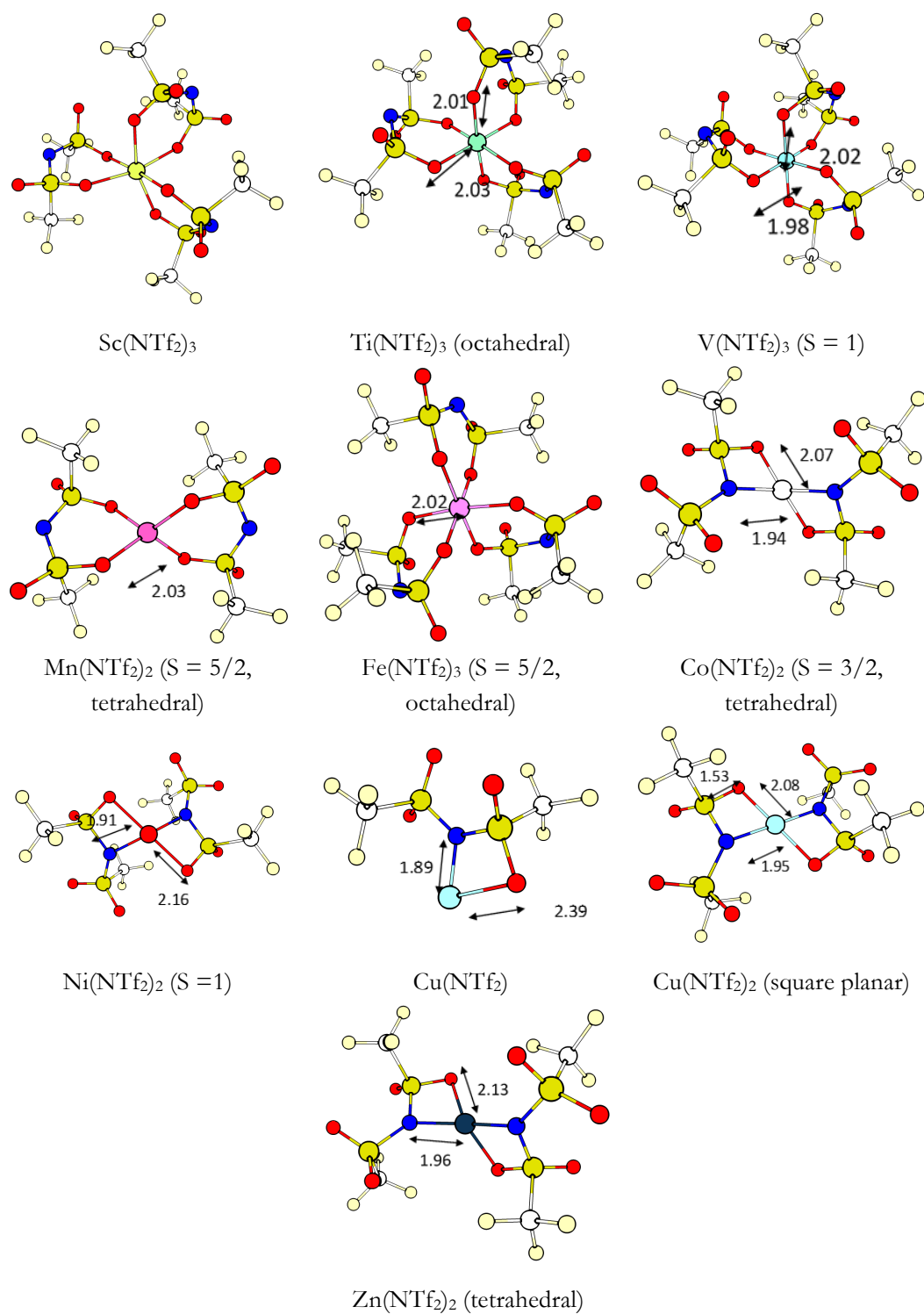


Figure 50 – Structure of early-transition-metal triflimides.

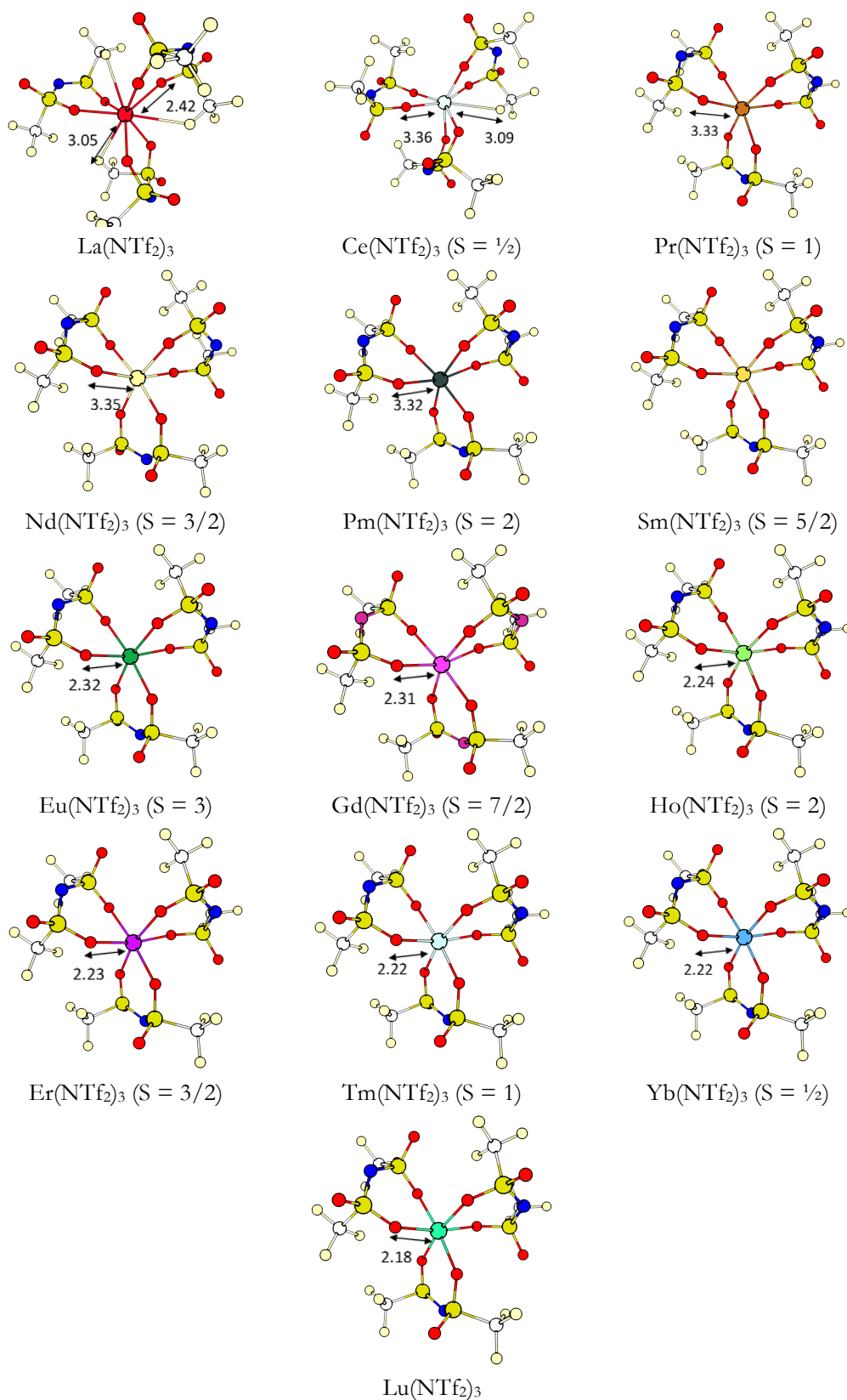


Figure 51 - Structure of lanthanide metal triflimides.

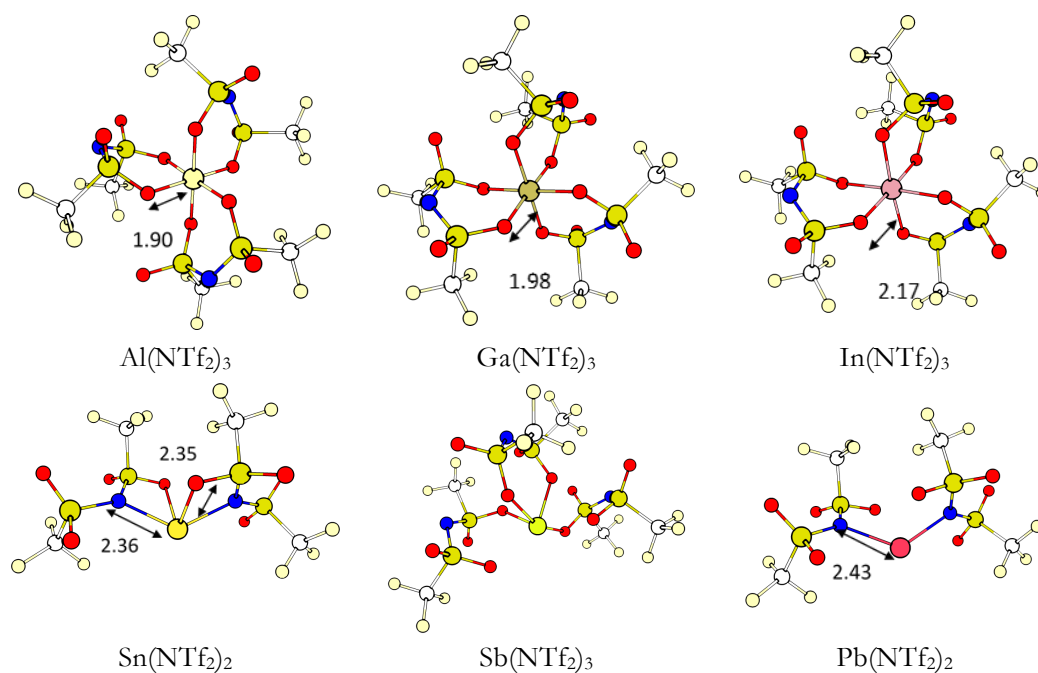


Figure 52 - Structure of post-transition metal triflimides.

Case study of $\text{Ti}(\text{NTf}_2)_3$ conformations. Triflimide ligands can be linked around titanium either via a N/O pincer or via a O/O pincer. In the case of the O/O coordination a 6-membered ring is formed (Figure 53) while in the case of the N/O coordinated ligand it is a tighter 4-membered ring (Figure 53b). Thus, four structures can theoretically be obtained. The four structures were optimized (Figure 53c-e) and the Gibbs energy of formation was calculated using hexaoxygen coordinated structure as a reference. Replacing a Ti-O bond with a Ti-N bond costs around 15 kJ/mol for each triflimide (Table 18).

Table 18 - Enthalpy of formation ($\Delta H_{[\text{L}]\text{A}]\text{L}}$, kJ mol⁻¹) and Gibbs energy of formation ($\Delta G_{[\text{L}]\text{A}]\text{L}$, kJ mol⁻¹) of O-O-bonded $\text{Ti}(\text{NTf}_2)_3$.^a

Ti-N bond	Enthalpy of formation	Free energy
0	0	0
1	+18.6	+14.5
2	+23.4	+21.6
3	+44.9	+54.0

^a Calculated at the BP-BJ/def2-SVP level

Further charge and structure analyses were done in order to understand the origin of this preference. NBO analysis of the triflimide anion showed that the charge on N and O atoms are very close (0.9 for O vs 1.1 for N). And the C-O and C-N bond lengths were found very close at 200 pm in these structures and thus the electrostatic interactions (the hard bonding) should be of the same order of magnitude. However, the coordination of N atom, instead of O atom, creates a strong distortion of the structure compared to the quasi-octahedral complex O-O bonded Ti (Figure 53h-k). This deformation is due to the formation of the 4-membered ring Ti-O-S-N and seems to be mainly responsible of the energetic gap observed.

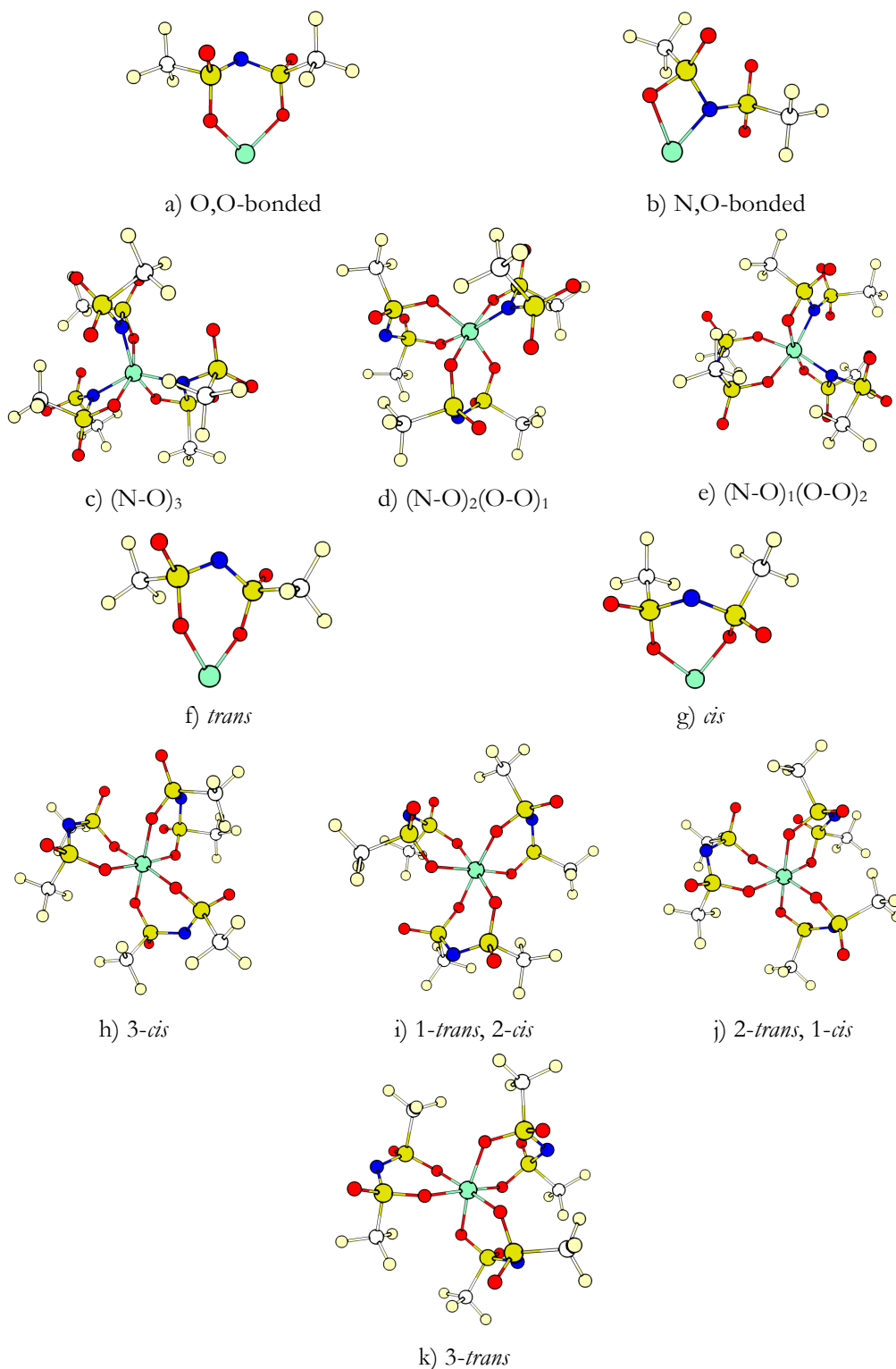


Figure 53 - a-b) Ti(NTf₂) moiety with O-bonded (left) and N- and O-bonded triflimide ligand (right). c-e) Ti(NTf₂)₃ with one, two or three N,O-bonded triflimide f-g) *trans* and *cis* conformation of the Ti(NTf₂) moiety. h-k) Ti(NTf₂)₃ with O,O-bonded triflimide, with no, one, two and three triflimide in the *trans* conformation.

Table 19 - Enthalpy of formation ($\Delta_f H_{[L]_n-L}$, kJ mol⁻¹) and Gibbs energy of formation ($\Delta_f G_{[L]_n-L}$, kJ mol⁻¹) of O-O-bonded Ti(NTf₂)₃.^a

Number of <i>trans</i> -triflimide	Enthalpy of formation	Free energy
0	0	0
1	-2.9	-3.0
2	+2.1	-0.8
3	-0.8	+0.5

^a Calculated at the BP-BJ/def2-SVP level

The triflimide ligand can *a priori* adopts two distinct conformations: the CF₃ moieties may be either *cis* or *trans* with respect with the (TiOSNSO) cycle, thus leading to four isomers of O-O-bonded Ti(NTf₂)₃ (**Figure 53h-k**). The structure with two ligands in the *cis* conformation and one in the *trans* conformation was the most stable ($\Delta G = -3$ kJ mol⁻¹) but the others are accessible at room temperature (**Table 19**).

3.4. Theoretical Descriptors of Lewis Acidity

With these structures in hand, several descriptors that could *a priori* correlate with the Lewis acidity were calculated for M^{n+} , $M(OTf)_n$ and $M(NTf_2)_n$. The affinity scale based on the binding energy of $[LA-OPH_3]$ adducts was first investigated (**Table 20-22**). The affinity scale is defined as the binding enthalpy ($\Delta_f H_{[LA]-L}$) or free energy ($\Delta_f G_{[LA]-L}$) of L to [LA] to form the Lewis adduct $[LA]-L$ (with [LA] a Lewis acid, M^{n+} , $M(OTf)_n$ or $M(NTf_2)_n$ and L a Lewis base (OPH_3):

$$\Delta_f H_{[LA]-L} = H_{[LA]-L} - (H_{[LA]} + H_L)$$

$$\Delta_f G_{[LA]-L} = G_{[LA]-L} - (G_{[LA]} + G_L)$$

Table 20 - Binding enthalpy ($\Delta_f H_{[LA]-L}$, kJ mol⁻¹) and free energy ($\Delta_f G_{[LA]-L}$, kJ mol⁻¹) of OPH_3 to M^{n+} .

Cation	$\Delta_f H_{[LA]-L}$	$\Delta_f G_{[LA]-L}$	Triflate salt	$\Delta_f H_{[LA]-L}$	$\Delta_f G_{[LA]-L}$
Ag⁺	-198.05	-211.43	Lu³⁺	-947.61	-958.86
Al³⁺	-1398.29	-1408.55	Mg²⁺	-566.31	-568.89
Au⁺	-246.20	-259.41	Mn²⁺	-580.45	-587.79
Au³⁺	- ^[a]	- ^[a]	Na⁺	-172.40	-175.85
Ba²⁺	-329.57	-340.90	Nd³⁺	-1911.42	-1929.36
Bi³⁺	-1026.79	-1042.42	Ni²⁺	-848.72	-860.86
Ca²⁺	-432.18	-437.18	Pb²⁺	-455.19	-468.65
Cd²⁺	-544.00	-556.25	Pd²⁺	-672.53	-686.08
Ce³⁺	-827.85	-839.92	Pm³⁺	-891.20	-903.35
Co²⁺	-657.31	-667.38	Pt²⁺	-743.72	-758.97
Cs⁺	-104.07	-120.24	Rb⁺	-578.41	-592.13
Cu⁺	-253.20	-263.41	Sb³⁺	-838.64	-852.36
Cu²⁺	-774.25	-790.89	Sc³⁺	-1202.19	-1210.47
Dy³⁺	-791.05	-804.19	Sm³⁺	-897.43	-918.57
Er³⁺	-936.20	-952.29	Sn²⁺	-513.89	-524.69
Eu³⁺	-965.96	-990.43	Sr²⁺	-367.14	-376.10
Fe³⁺	-1583.72	-1599.79	Tb³⁺	- ^[b]	- ^[b]
Ga³⁺	-1518.67	-1540.01	Ti³⁺	-1394.60	-1404.29
Gd³⁺	-1109.70	-1127.47	Tm³⁺	-947.88	-967.08
Ho³⁺	-908.52	-931.21	V³⁺	-1474.05	-1485.71
In³⁺	-1229.69	-1253.52	Yb³⁺	-955.52	-980.72
Ir³⁺	-1420.46	-1445.20	Y³⁺	-906.41	-915.81
K⁺	-128.46	-138.67	Zn²⁺	-667.15	-676.82
La³⁺	-748.65	-759.93	Zr³⁺	-914.05	-924.44
Li⁺	-232.93	-232.06			

^[a] Structure optimization did not converge due to O abstraction.

^[b] Self-consistent field step did not converge using BP/def2-SVP.

Table 21 - Binding enthalpy ($\Delta_f H_{[LA]-L}$ kJ mol⁻¹) and free energy ($\Delta_f G_{[LA]-L}$ kJ mol⁻¹) of OPH₃ to M(OTf)_n.

Triflate salt	$\Delta_f H_{[LA]-L}$	$\Delta_f G_{[LA]-L}$	Triflate salt	$\Delta_f H_{[LA]-L}$	$\Delta_f G_{[LA]-L}$
Ag(OTf)	-117.48	-64.18	Lu(OTf)₃	-144.01	-79.81
Al(OTf)₃	-122.07	-74.17	Mg(OTf)₂	-155.75	-101.88
Au(OTf)	-174.42	-126.41	Mn(OTf)₂	-133.41	-86.88
Au(OTf)₃	-204.37	-135.33	Na(OTf)	-112.37	-61.27
Ba(OTf)₂	-125.67	-73.68	Nd(OTf)₃	-138.11	-76.02
Bi(OTf)₃	-124.00	-63.33	Ni(OTf)₂	-139.63	-78.42
Ca(OTf)₂	-146.62	-92.65	Pb(OTf)₂	-122.18	-65.81
Cd(OTf)₂	-130.62	-77.54	Pd(OTf)₂	-96.67	-37.85
Ce(OTf)₃	-138.47	-76.74	Pm(OTf)₃	-135.59	-70.35
Co(OTf)₂	-134.54	-79.14	Pt(OTf)₂	-101.80	-52.95
Cs(OTf)	-96.23	-37.02	Rb(OTf)	-88.82	-40.54
Cu(OTf)	-156.56	-102.41	Sb(OTf)₃	-101.91	-44.73
Cu(OTf)₂	-111.87	-56.19	Sc(OTf)₃	-122.08	-50.40
Dy(OTf)₃	- ^[a]	- ^[a]	Sm(OTf)₃	-144.23	-80.41
Er(OTf)₃	-140.66	-74.47	Sn(OTf)₂	-119.05	-62.96
Fe(OTf)₃	-100.51	-35.14	Sr(OTf)₂	-137.05	-86.12
Ga(OTf)₃	-116.42	-63.82	Tb(OTf)₃	- ^[a]	- ^[a]
Gd(OTf)₃	-137.20	-74.97	Ti(OTf)₃	-86.44	-31.99
Ho(OTf)₃	-148.28	-84.48	Tm(OTf)₃	-142.21	-79.79
In(OTf)₃	-120.54	-60.21	V(OTf)₃	-80.94	-20.86
Ir(OTf)₃	-125.11	-63.44	Yb(OTf)₃	-147.57	-91.09
K(OTf)	-94.24	-42.90	Y(OTf)₃	-144.71	-83.82
La(OTf)₃	-146.11	-95.89	Zn(OTf)₂	-142.83	-89.83
Li(OTf)	-129.42	-77.59	Zr(OTf)₃	-99.31	-51.03

^[a] Self-consistent field step did not converge using BP/def2-SVP.

Table 22 - Binding enthalpy ($\Delta_f H_{[M(NTf_2)_n]-OPH_3}$ kJ mol⁻¹) and free energy ($\Delta_f G_{[M(NTf_2)_n]-OPH_3}$ kJ mol⁻¹) of OPH₃ to M(NTf₂)_n.

Triflimide salt	$\Delta_f H_{[LA]-L}$	$\Delta_f G_{[LA]-L}$	Triflimide salt	$\Delta_f H_{[LA]-L}$	$\Delta_f G_{[LA]-L}$
Ag(NTf₂)₃	-131.44	-76.67	Lu(NTf₂)₃	-137.45	-72.57
Al(NTf₂)₃	-93.80	-34.10	Mg(NTf₂)₂	-108.72	-49.37
Au(NTf₂)	-175.69	-119.83	Mn(NTf₂)₂	-102.38	-39.84
Au(NTf₂)₃	-83.50	-25.05	Na(NTf₂)	-100.78	-48.74
Ba(NTf₂)₂	-128.60	-60.84	Nd(NTf₂)₃	-144.26	-81.60
Bi(NTf₂)₃	-99.90	-37.18	Ni(NTf₂)₂	-166.50	-104.45
Ca(NTf₂)₂	-109.06	-50.69	Pb(NTf₂)₂	-144.73	-75.88
Cd(NTf₂)₂	-114.08	-50.19	Pd(NTf₂)₃	-73.62	-6.99
Ce(NTf₂)₃	-150.55	-87.72	Pm(NTf₂)₃	-149.53	-82.20
Co(NTf₂)₂	-157.33	-99.37	Pt(NTf₂)₂	-69.73	-1.11
Cs(NTf₂)	-87.64	-39.06	Rb(NTf₂)	-93.07	-45.84
Cu(NTf₂)	-178.94	-125.43	Sb(NTf₂)₃	-105.27	-42.23
Cu(NTf₂)₂	-144.45	-84.41	Sc(NTf₂)₃	-92.85	-26.89
Dy(NTf₂)₃	- ^[a]	- ^[a]	Sm(NTf₂)₃	-139.72	-77.98
Er(NTf₂)₃	-141.41	-75.72	Sn(NTf₂)₂	-140.55	-76.40
Eu(NTf₂)₃	-141.85	-78.85	Sr(NTf₂)₂	-167.57	-107.80
Fe(NTf₂)₃	-89.21	-36.16	Tb(NTf₂)₃	- ^[a]	- ^[a]
Ga(NTf₂)₃	-91.95	-32.21	Ti(NTf₂)₃	-101.24	-34.98
Gd(NTf₂)₃	-148.40	-87.30	Tm(NTf₂)₃	-132.73	-67.28
Ho(NTf₂)₃	-141.17	-77.87	V(NTf₂)₃	-105.11	-42.21
In(NTf₂)₃	-93.63	-34.99	Yb(NTf₂)₃	-143.02	-82.89
Ir(NTf₂)₃	-104.52	-51.10	Y(NTf₂)₃	-147.01	-80.06
K(NTf₂)	-97.87	-47.69	Zn(NTf₂)₃	-148.68	-91.40
La(NTf₂)₃	-145.26	-82.53	Zr(NTf₂)₃	-73.95	-4.97
Li(NTf₂)	-109.31	-61.78			

^[a] Structure optimization did not converge due to O abstraction.

Entropic effects are always of the same order of magnitude in these systems and thus similar trends were obtained for enthalpy and free energy (**Figure 54**). No correlation was found between the binding energy of OPH₃ to the bare Mⁿ⁺ cations and the binding energy of OPH₃ to M(OTf)_n or M(NTf₂)₃ (**Figure 55a-b**), probably due to an overestimation of charge effects on the naked cation. When comparing the binding energy of OPH₃ to M(OTf)_n and M(NTf₂)_n, a rough trend was found, with triflate salts generally featuring higher affinity / binding energies (**Figure 55c**).

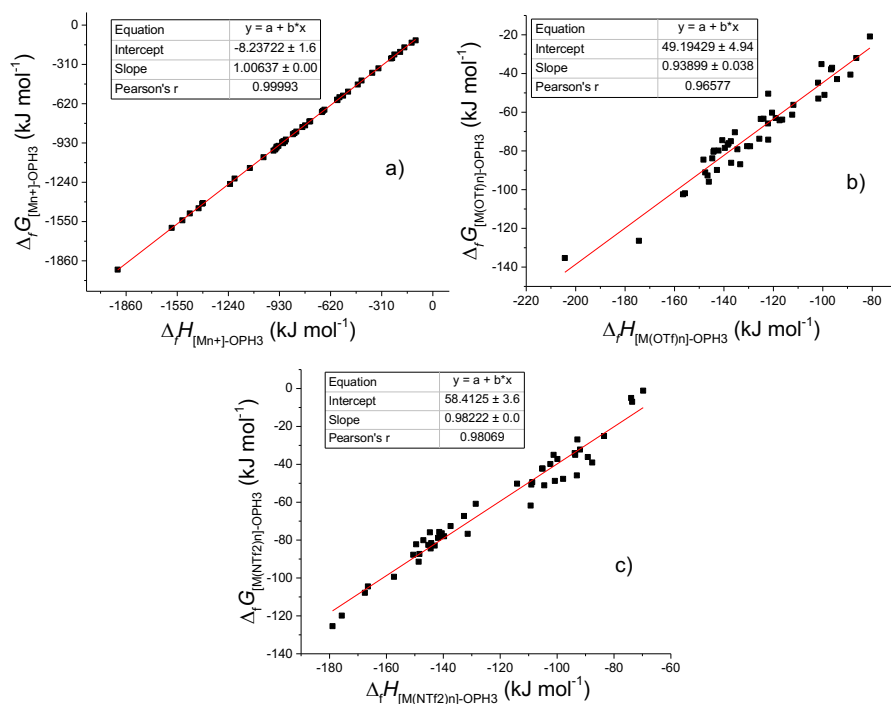


Figure 54 Correlation between the binding enthalpy ($\Delta H_{[LA]_n-L}$) and binding free energy ($\Delta G_{[LA]_n-L}$) of OPH_3 a) to M^{n+} ; b) to $M(OTf)_n$ c) to $M(NTf_2)_n$.

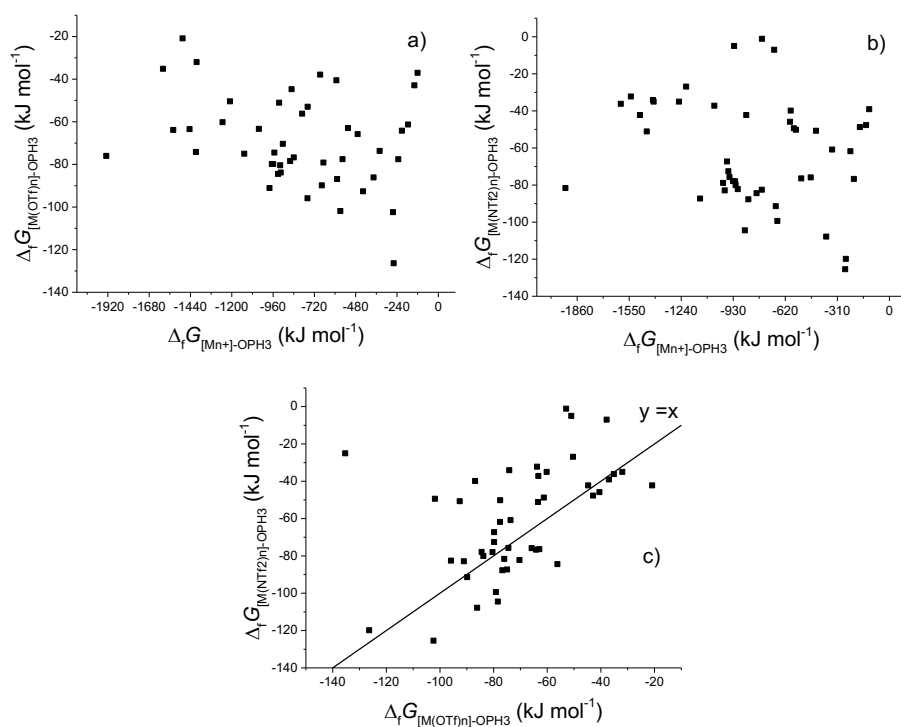


Figure 55 - Correlation between a) the binding free energy ($\Delta G_{[M(OTf)_n]OPH_3}$) of OPH_3 to $M(OTf)_n$ with the binding free energy ($\Delta G_{[Mn+]OPH_3}$) of OPH_3 to M^{n+} ; b) the binding free energy ($\Delta G_{[M(NTf_2)_n]OPH_3}$) of OPH_3 to $M(NTf_2)_n$ with the binding free energy ($\Delta G_{[Mn+]OPH_3}$) of OPH_3 to the complex M^{n+} ; c) the binding free energy ($\Delta G_{[M(NTf_2)_n]OPH_3}$) of OPH_3 to $M(NTf_2)_n$ with the binding free energy ($\Delta G_{[M(OTf)_n]OPH_3}$) of OPH_3 to $M(OTf)_n$.

Overall, this affinity scale proved meaningless with respect to the catalytic properties of the different salts. This is clearly evidenced by plotting the yield of **3aa** against the affinity, showing no correlation (**Figure 56**). For instance, $\text{Al}(\text{OTf})_3$ and $\text{Fe}(\text{OTf})_3$, two powerful catalysts for LA-assisted mechanisms, have a lower affinity value than that of inactive NaOTf .

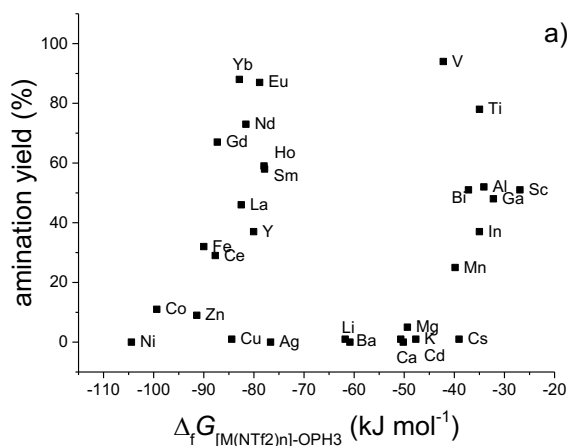


Figure 56 - Correlation between the yield of the amination reaction catalyzed by $\text{M}(\text{NTf}_2)_3$ (**1a** + **2a** = **3aa**) and the binding free energy of OPH_3 to $\text{M}(\text{NTf}_2)_3$ ($\Delta G_{[\text{LA}]\text{-L}}$, kJ mol^{-1}).

Alternatively, the Parr electronegativity and global electrophilicity index are potential descriptors of the reactivity, as they are supposed to describe the ability of a LA to withdraw electronic density from the LB. The Electronic Affinity (EA) is defined as:

$$EA = E_{[\text{LA}]} - E_{[\text{LA}]^-}$$

With E the electronic energy so the expression can be rewritten as follows:

$$EA = E(N) - E(N + 1)$$

With N the number of electrons of the system. Similarly, the Ionization Energy (IE) is:

$$IE = E_{[\text{LA}]^+} - E_{[\text{LA}]} = E(N - 1) - E(N)$$

The Electronegativity (χ) is defined as:²⁴¹

$$\chi = -\left(\frac{\partial E}{\partial N}\right)_v$$

With v the nucleus field (i.e. we consider the change of energy corresponding to the variation of the number of electrons at a fixed geometry). Since we can only consider integer variation of N , electronegativity may be assimilated to:

$$\chi \approx -\frac{1}{2} [E(N + 1) - E(N - 1)] \text{ i.e. } \chi \approx \frac{1}{2}(EA + IE)$$

²⁴¹ (a) R. G. Parr, R. G. Pearson, *J. Am. Chem. Soc.* **1983**, *105*, 7512-7516; (b) R. G. Parr, W. Yang, *J. Am. Chem. Soc.* **1984**, *106*, 4049-4050.

Table 23 - Electronic affinity (EA, kJ mol⁻¹), ionization energy (IE, kJ mol⁻¹) and electronegativity (χ , kJ mol⁻¹ e⁻¹) of M(OTf)_n.

	EA	IE	χ		AE	IE	χ
Al(OTf)₃	-56.59	1118.74	531.08	Lu(OTf)₃	7.98	1092.50	550.24
Ag(OTf)	180.38	969.83	575.11	Mg(OTf)₂	-2.57	1104.41	550.92
Au(OTf)	263.73	1002.74	633.24	Mn(OTf)₂	93.97	1012.57	553.27
Au(OTf)₃	426.88	1050.84	738.86	Na(OTf)	69.53	989.48	529.50
Ba(OTf)₂	48.19	1025.66	536.92	Nd(OTf)₃	157.64	1071.76	614.70
Bi(OTf)₃	154.22	1088.22	621.22	Ni(OTf)₂	220.51	1078.89	649.70
Ca(OTf)₂	28.68	1074.65	551.66	Pb(OTf)₂	99.46	1049.89	574.67
Cd(OTf)₂	132.90	1067.97	600.43	Pd(OTf)₂	268.09	1021.12	644.60
Ce(OTf)₃	62.23	966.74	514.48	Pm(OTf)₃	157.77	1077.46	617.61
Co(OTf)₂	186.40	1032.96	609.68	Pt(OTf)₂	174.94	961.33	568.14
Cs(OTf)	45.23	925.33	485.28	Rb(NTf₂)₃	54.44	935.56	495.00
Cu(OTf)	130.87	947,20	539,03	Sb(OTf)₃	79.33	1082.90	581.11
Cu(OTf)₂	299.23	1122,91	711,07	Sc(OTf)₃	84.28	1106.85	595.56
Dy(OTf)₃	-[a]	-[a]	-[a]	Sm(OTf)₃	263.90	1076.12	670.01
Er(OTf)₃	103.51	1089.77	596.64	Sn(OTf)₂	77.00	1057.45	567.23
Eu(OTf)₃	356.35	1072.44	714.40	Sr(OTf)₂	39.53	1046.64	543.08
Fe(OTf)₃	395.26	1072.50	733.88	Tb(OTf)₃	-[a]	-[a]	-[a]
Ga(OTf)₃	25.01	1104.05	564.53	Ti(OTf)₃	136.73	837.53	487.13
Gd(OTf)₃	224.36	1078.86	651.61	Tm(OTf)₃	201.43	1113.93	657.68
Ho(OTf)₃	132.20	1096.52	614.36	V(OTf)₃	232.48	926.49	579.48
In(OTf)₃	153.65	1089.79	621.72	Yb(OTf)₃	281.69	1084.57	683.13
Ir(OTf)₃	158.63	946.88	552.75	Y(OTf)₃	34.62	1085.65	560.14
K(OTf)	48.56	950.39	499.47	Zn(OTf)₂	31.71	1095.49	563.60
La(OTf)₃	71.84	1063.04	567.44	Zr(OTf)₃	42.30	666.48	354.39
Li(OTf)	25.22	1058.30	541.76				

^[a] Self-consistent field step did not converge using BP/def2-SVP.

The chemical hardness (η) can be defined as,

$$\eta = \frac{1}{2} \left(\frac{\partial^2 E}{\partial N^2} \right)_v = \frac{1}{2} \left(\frac{\partial \chi}{\partial N} \right)_v$$

With same approximations as precedent it can be expressed as:

$$\eta \approx \frac{1}{2} [(E(N+1) - E(N)) - (E(N) - E(N-1))]$$

$$\eta \approx \frac{1}{2} (IE - EA)$$

The reciprocal of hardness is the softness (S):

$$S = 1/\eta$$

Table 24 - Electronic affinity (EA, kJ mol⁻¹), ionization energy (IE, kJ mol⁻¹) and electronegativity (χ , kJ mol⁻¹) of M(NTf₂)_n

	AE	IE	χ		AE	IE	χ
Al(NTf₂)₃	11.30	1029.28	520.29	Lu(NTf₂)₃	19.54	1022.74	521.14
Ag(NTf₂)₂	202.38	989.92	596.15	Mg(NTf₂)₂	5.52	1061.83	533.67
Au(NTf₂)₂	260.17	1007.71	633.94	Mn(NTf₂)₂	71.34	1154.12	612.73
Au(NTf₂)₃	410.20	1031.38	720.79	Na(NTf₂)₂	59.56	970.93	515.25
Ba(NTf₂)₂	23.26	993.65	508.45	Nd(NTf₂)₃	157.01	1018.11	587.56
Bi(NTf₂)₃	174.42	988.72	581.57	Ni(NTf₂)₂	329.76	1053.31	691.54
Ca(NTf₂)₂	13.75	1032.17	522.96	Pb(NTf₂)₂	156.73	1001.12	578.92
Cd(NTf₂)₂	132.12	1057.86	594.99	Pd(NTf₂)₂	298.44	974.87	636.65
Ce(NTf₂)₃	52.99	942.81	497.90	Pm(NTf₂)₃	166.69	1019.46	593.07
Co(NTf₂)₂	251.09	1018.89	634.99	Pt(NTf₂)₂	207.29	920.83	564.06
Cu(NTf₂)₂	161.10	969.93	565.51	Rb(NTf₂)₂	49.79	928.64	489.22
Cu(NTf₂)₃	358.32	1055.93	707.12	Sb(NTf₂)₃	157.45	977.80	567.62
Cs(NTf₂)₂	43.35	922.76	483.05	Sc(NTf₂)₃	47.61	1128.95	588.28
Dy(NTf₂)₃	- ^[a]	- ^[a]	- ^[a]	Sm(NTf₂)₃	263.44	1021.69	642.57
Er(NTf₂)₃	113.47	1017.18	565.33	Sn(NTf₂)₂	135.02	984.06	559.54
Eu(NTf₂)₃	342.91	1025.82	684.37	Sr(NTf₂)₂	11.16	992.30	501.73
Fe(NTf₂)₃	422.21	1024.80	723.51	Tb(NTf₂)₃	- ^[a]	- ^[a]	- ^[a]
Ga(NTf₂)₃	53.85	1029.38	541.61	Ti(NTf₂)₃	186.63	801.18	493.91
Gd(NTf₂)₃	221.06	1027.28	624.17	Tm(NTf₂)₃	198.34	1017.92	608.13
Ho(NTf₂)₃	131.06	1027.24	579.15	V(NTf₂)₃	202.82	1018.70	610.76
In(NTf₂)₃	157.22	1027.01	592.12	Yb(NTf₂)₃	288.19	1016.28	652.24
Ir(NTf₂)₃	163.74	905.59	534.66	Y(NTf₂)₃	35.16	1018.04	526.60
K(NTf₂)₂	43.35	932.62	487.98	Zn(NTf₂)₂	52.14	1061.44	556.79
La(NTf₂)₃	45.36	1024.16	534.76	Zr(NTf₂)₃	60.97	615.73	338.35
Li(NTf₂)₂	16.47	1024.01	520.24				

^[a] Self-consistent field step did not converge using BP/def2-SVP.

At the second order the electronic energy of the system can thus be estimated to:

$$\Delta E \approx -\chi \cdot \Delta N + \eta \cdot \Delta N^2$$

The maximal density transferable is obtained for:

$$\frac{\Delta E_{max}}{\Delta N_{max}} = 0$$

The combination of the two previous equations resulted in:

$$\Delta N_{max} = \chi/\eta$$

And thus, at the first order, the “global electrophilicity index” (ω) is:

$$\omega = \Delta E_{max} = \frac{\chi^2}{2\eta}$$

Table 25 - Hardness (η , $\text{kJ mol}^{-1} \text{e}^{-2}$) and global electrophilicity index (ω , kJ mol^{-1}) of $\text{M}(\text{OTf})_n$

	η	ω		η	ω
Al(OTf)₃	587.66	239.97	Lu(OTf)₃	542.26	279.17
Ag(OTf)	394.72	418.96	Mg(OTf)₂	553.49	274.18
Au(OTf)	369.51	542.60	Mn(OTf)₂	459.30	333.24
Au(OTf)₃	311.98	874.93	Na(OTf)	459.97	304.77
Ba(OTf)₂	488.73	294.93	Nd(OTf)₃	457.06	413.35
Bi(OTf)₃	467.00	413.18	Ni(OTf)₂	429.19	491.76
Ca(OTf)₂	522.98	290.96	Pb(OTf)₂	475.22	347.47
Cd(OTf)₂	467.53	385.56	Pd(OTf)₂	376.52	551.79
Ce(OTf)₃	452.25	292.64	Pm(OTf)₃	459.84	414.76
Co(OTf)₂	423.28	439.08	Pt(OTf)₂	393.19	410.46
Cs(OTf)	440.05	267.58	Rb(OTf)	440.56	278.09
Cu(OTf)	408.17	355.93	Sb(OTf)₃	501.79	336.49
Cu(OTf)₂	411.84	613.86	Sc(OTf)₃	511.28	346.87
Dy(OTf)₃	-[a]	-[a]	Sm(OTf)₃	406.11	552.70
Er(OTf)₃	493.13	360.94	Sn(OTf)₂	490.22	328.16
Eu(OTf)₃	358.05	712.71	Sr(OTf)₂	503.56	292.86
Fe(OTf)₃	338.62	795.25	Tb(OTf)₃	-[a]	-[a]
Ga(OTf)₃	539.52	295.35	Ti(OTf)₃	350.40	338.61
Gd(OTf)₃	427.25	496.89	Tm(OTf)₃	456.25	474.02
Ho(OTf)₃	482.16	391.41	V(OTf)₃	347.01	483.86
In(OTf)₃	468.07	412.91	Yb(OTf)₃	401.44	581.24
Ir(OTf)₃	394.12	387.61	Y(OTf)₃	525.51	298.52
K(OTf)	450.92	276.63	Zn(OTf)₂	531.89	298.60
La(OTf)₃	495.60	324.85	Zr(OTf)₃	312.09	201.21
Li(OTf)	516.54	284.10			

[a] Self-consistent field step did not converge using BP/def2-SVP.

It is interesting to note that in agreement with what was qualitatively expected triflate salts are generally harder than triflimide ones (**Figure 57**, left).

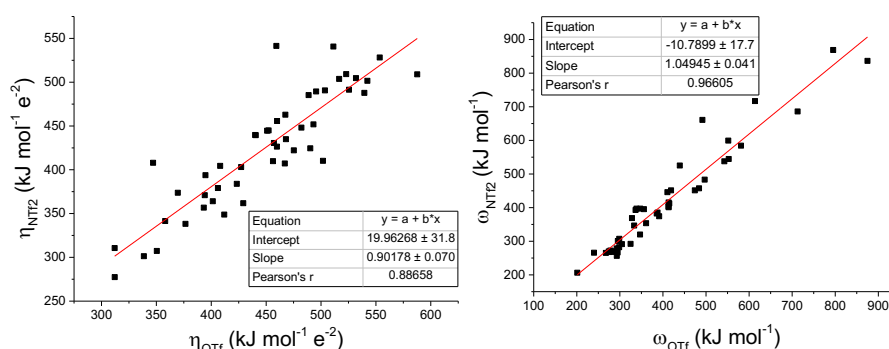


Figure 57 - Right: Correlation between the hardness (η) of the $\text{M}(\text{OTf})_n$ the hardness of the $\text{M}(\text{NTf}_2)_n$; **Left:** Correlation between the global electrophilicity index (ω) of the $\text{M}(\text{OTf})_n$ the global electrophilicity index of the $\text{M}(\text{NTf}_2)_n$.

Table 26 - Hardness (η , kJ mol⁻¹ e⁻²) and global electrophilicity index (ω , kJ mol⁻¹) of M(NTf₂)_n.

	η	ω		η	ω
Al(NTf ₂) ₃	508.99	265.92	Lu(NTf ₂) ₃	501.60	270.72
Ag(NTf ₂)	393.77	451.27	Mg(NTf ₂) ₂	528.16	269.62
Au(NTf ₂)	373.77	537.60	Mn(NTf ₂) ₂	541.39	346.74
Au(NTf ₂) ₃	310.59	836.38	Na(NTf ₂)	455.69	291.29
Ba(NTf ₂) ₂	485.20	266.41	Nd(NTf ₂) ₃	430.55	400.92
Bi(NTf ₂) ₃	407.15	415.35	Ni(NTf ₂) ₂	361.78	660.93
Ca(NTf ₂) ₂	509.21	268.54	Pb(NTf ₂) ₂	422.19	396.92
Cd(NTf ₂) ₂	462.87	382.41	Pd(NTf ₂) ₂	338.21	599.21
Ce(NTf ₂) ₃	444.91	278.60	Pm(NTf ₂) ₃	426.38	412.47
Co(NTf ₂) ₂	383.90	525.15	Pt(NTf ₂) ₂	356.77	445.89
Cs(NTf ₂)	439.70	265.34	Rb(NTf ₂)	439.43	272.33
Cu(NTf ₂)	404.42	395.39	Sb(NTf ₂) ₃	410.18	392.75
Cu(NTf ₂) ₂	348.81	716.76	Sc(NTf ₂) ₃	540.67	320.04
Dy(NTf ₂) ₃	-[a]	-[a]	Sm(NTf ₂) ₃	379.13	544.53
Er(NTf ₂) ₃	451.85	353.65	Sn(NTf ₂) ₂	424.52	368.76
Eu(NTf ₂) ₃	341.45	685.83	Sr(NTf ₂) ₂	490.57	256.57
Fe(NTf ₂) ₃	301.30	868.69	Tb(NTf ₂) ₃	-[a]	-[a]
Ga(NTf ₂) ₃	487.76	300.70	Ti(NTf ₂) ₃	307.27	396.95
Gd(NTf ₂) ₃	403.11	483.23	Tm(NTf ₂) ₃	409.79	451.24
Ho(NTf ₂) ₃	448.09	374.27	V(NTf ₂) ₃	407.94	457.21
In(NTf ₂) ₃	434.90	403.09	Yb(NTf ₂) ₃	364.05	584.28
Ir(NTf ₂) ₃	370.93	385.34	Y(NTf ₂) ₃	491.44	282.13
K(NTf ₂)	444.63	267.78	Zn(NTf ₂) ₂	504.65	307.16
La(NTf ₂) ₃	489.40	292.16	Zr(NTf ₂) ₃	277.38	206.36
Li(NTf ₂)	503.77	268.63			

[a] Self-consistent field step did not converge using BP/def2-SVP.

However, any attempt to correlate both descriptors with the yield of **3aa** failed (**Figure 58**), even if the GIE reproduced more or less the experimental trend.

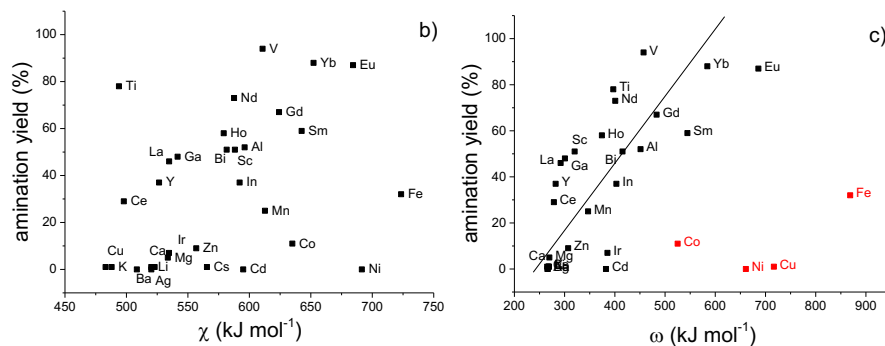


Figure 58 – a) Correlation between the Paar Electronegativity (χ) of the $M(\text{NTf}_2)_n$ and the yield of the amination reaction ($\mathbf{1a} + \mathbf{2a} = \mathbf{3aa}$) catalyzed by $M(\text{NTf}_2)_n$. b) Correlation between the global electrophilicity index (ω) of the $M(\text{NTf}_2)_n$ and the yield of the amination reaction ($\mathbf{1a} + \mathbf{2a} = \mathbf{3aa}$) catalyzed by $M(\text{NTf}_2)_n$.

3.5. Fukui functions and local hardness

The Fukui function is defined as, $f(\vec{r}) = \left(\frac{\partial \rho(\vec{r})}{\partial N}\right)_v$

As for χ and η one should approximate in the case of integer number of electrons:

$$\begin{aligned} f^+(\vec{r}) &= \rho_{N+1}(\vec{r}) - \rho_N(\vec{r}) \\ f^-(\vec{r}) &= \rho_N(\vec{r}) - \rho_{N-1}(\vec{r}) \\ f^0(\vec{r}) &= \frac{f^+(\vec{r}) - f^-(\vec{r})}{2} = \frac{\rho_{N+1}(\vec{r}) - \rho_{N-1}(\vec{r})}{2} \end{aligned}$$

The most pertinent function in our case should be the f^+ function, associated to the electrophilic behaviour. The local softness can be defined (by analogy between N and Q) as:

$$s(\vec{r}) = \left(\frac{\partial \rho}{\partial \chi}\right)_v s(\vec{r}) = \left(\frac{\partial \rho}{\partial N}\right)_v \cdot \left(\frac{\partial N}{\partial \chi}\right)_v s(\vec{r}) = f(\vec{r}) \cdot S$$

Table 27 - Fukui functions (f^+ , f and f^0 , |e|), global (S , $10^{-3} \text{ e}^2 \text{ mol kJ}^{-1}$) and local softness (s_M , $\text{e}^2 \text{ mol kJ}^{-1}$) of $M(\text{OTf})_n$.

	f^+	f	f^0	S	s_M	f^+	f	f^0	S	s_M	
Al(OTf)₃	-0.08	0.02	-0.03	1.70	-0.05	Lu(OTf)₃	-0.71	0.00	-0.36	1.84	-0.43
Ag(OTf)	-0.92	-0.20	-0.56	2.53	-1.41	Mg(OTf)₂	-0.78	-0.15	-0.47	1.81	-0.65
Au(OTf)	-0.80	-0.38	-0.59	2.71	-1.60	Mn(OTf)₂	-0.97	-0.02	-0.50	2.18	-1.01
Au(OTf)₃	-0.21	-0.03	-0.12	3.21	-0.39	Na(OTf)	-0.61	-0.06	-0.34	2.17	-1.07
Ba(OTf)₂	-0.90	-0.02	-0.46	2.05	-0.94	Nd(NTf)₃	-0.64	-0.03	-0.33	2.19	-0.73
Bi(OTf)₃	-0.60	-0.02	-0.31	2.14	-0.67	Ni(OTf)₂	-0.61	-0.06	-0.34	2.33	-0.78
Ca(OTf)₂	-0.83	-0.02	-0.43	1.91	-0.81	Pb(OTf)₂	-0.80	-0.06	-0.43	2.10	-0.91
Cd(OTf)₂	-0.77	-0.04	-0.41	2.14	-0.86	Pd(OTf)₂	-0.37	-0.34	-0.35	2.66	-0.94
Ce(OTf)₃	-0.65	-0.20	-0.43	2.21	-0.94	Pm(OTf)₃	-0.65	-0.03	-0.34	2.17	-0.74
Co(OTf)₂	-0.67	-0.25	-0.46	2.36	-1.09	Pt(OTf)₂	-0.38	-0.42	-0.40	2.54	-1.03
Cs(OTf)	-0.99	-0.02	-0.50	2.27	-1.15	Rb(OTf)	-0.99	-0.02	-0.50	2.27	-1.14
Cu(OTf)	-0.89	-0.37	-0.63	2.45	-1.55	Sb(OTf)₃	-0.60	-0.09	-0.34	1.99	-0.68
Cu(OTf)₂	-0.51	-0.05	-0.28	2.43	-0.68	Sc(OTf)₃	-0.52	0.01	-0.25	1.96	-0.49
Dy(OTf)₃	-[a]	-[a]	-[a]	-[a]	-[a]	Sm(OTf)₃	-0.65	-0.02	-0.33	2.46	-0.82
Er(OTf)₃	-0.70	-0.01	-0.36	2.03	-0.72	Sn(OTf)₂	-0.77	-0.30	-0.53	2.04	-1.09
Eu(OTf)₃	-0.67	0.00	-0.34	2.79	-0.93	Sr(OTf)₂	-0.87	-0.02	-0.44	1.99	-0.88
Fe(OTf)₃	-0.37	0.05	-0.16	2.95	-0.48	Tb(OTf)₃	-[a]	-[a]	-[a]	-[a]	-[a]
Ga(OTf)₃	-0.41	0.02	-0.20	1.85	-0.36	Ti(OTf)₃	-0.40	-0.26	-0.33	2.85	-0.94
Gd(OTf)₃	-0.53	-0.01	-0.27	2.34	-0.63	Tm(OTf)₃	-0.71	-0.01	-0.36	2.19	-0.79
Ho(OTf)₃	-0.70	0.00	-0.35	2.07	-0.72	V(OTf)₃	-0.37	-0.08	-0.23	2.88	-0.64
In(OTf)₃	-0.58	0.01	-0.29	2.14	-0.61	Yb(OTf)₃	-0.71	-0.01	-0.36	2.49	-0.89
Ir(OTf)₃	-0.27	-0.29	-0.28	2.54	-0.72	Y(OTf)₃	-0.58	0.00	-0.29	1.90	-0.55

K(OTf)	-0.97	-0.02	-0.50	2.22	-1.10	Zn(OTf)₂	-0.68	-0.02	-0.35	1.88	-0.66
La(OTf)₃	-0.94	-0.02	-0.48	2.02	-0.76	Zr(NTf₂)₃	-0.39	-0.53	-0.46	3.61	-1.66
Li(OTf)	-0.46	0.00	-0.23	1.94	-0.93						

^[a] Self-consistent field step did not converge using BP/def2-SVP.

Table 28 - Fukui functions (f^+ , f and f^0 , |e|), softness (S , 10^{-3} e² mol kJ⁻¹) and local softness (s_M , e² mol kJ⁻¹) of M(NTf₂)_n.

	f^+	f	f^0	S	s_M	f^+	f	f^0	S	s_M	
Al(NTf₂)₃	-0.01	0.01	0.00	1.96	0.00	Lu(NTf₂)₃	-0.19	0.00	-0.09	1.99	-0.19
Ag(NTf₂)	-0.89	-0.21	-0.55	2.54	-1.39	Mg(NTf₂)₂	-0.32	0.00	-0.16	1.89	-0.30
Au(NTf₂)	-0.76	-0.39	-0.57	2.68	-1.53	Mn(NTf₂)₂	-0.60	-0.10	-0.35	1.85	-0.65
Au(NTf₂)₃	-0.20	-0.05	-0.13	3.22	-0.40	Na(NTf₂)	-0.95	-0.01	-0.48	2.19	-1.06
Ba(NTf₂)₂	-0.78	-0.01	-0.40	2.06	-0.82	Nd(NTf₂)₃	-0.59	-0.01	-0.30	2.32	-0.70
Bi(NTf₂)₃	-0.58	-0.02	-0.30	2.46	-0.74	Ni(NTf₂)₂	-0.62	-0.08	-0.35	2.76	-0.96
Ca(NTf₂)₂	-0.49	0.00	-0.25	1.96	-0.49	Pb(NTf₂)₂	-0.77	-0.11	-0.44	2.37	-1.05
Cd(NTf₂)₂	-0.68	-0.05	-0.37	2.16	-0.80	Pd(NTf₂)₂	-0.33	-0.26	-0.29	2.96	-0.87
Ce(NTf₂)₃	-0.41	-0.22	-0.32	2.25	-0.71	Pm(NTf₂)₃	-0.64	-0.01	-0.32	2.35	-0.76
Co(NTf₂)₂	-0.64	-0.28	-0.46	2.60	-1.19	Pt(NTf₂)₂	-0.34	-0.35	-0.35	2.80	-0.97
Cs(NTf₂)	-0.98	-0.36	-0.61	2.47	-1.51	Rb(NTf₂)	-0.98	-0.01	-0.50	2.28	-1.13
Cu(NTf₂)	-0.86	-0.01	-0.26	2.87	-0.73	Sb(NTf₂)₃	-0.53	-0.08	-0.30	2.44	-0.73
Cu(NTf₂)₂	-0.50	-0.01	-0.50	2.27	-1.13	Sc(NTf₂)₃	-0.36	-0.20	-0.28	1.85	-0.52
Dy(NTf₂)₃	- ^[a]	Sm(NTf₂)₃	-0.64	-0.01	-0.32	2.64	-0.86				
Er(NTf₂)₃	-0.68	0.00	-0.34	2.21	-0.76	Sn(NTf₂)₂	-0.71	-0.24	-0.48	2.36	-1.12
Eu(NTf₂)₃	-0.66	-0.02	-0.34	2.93	-1.00	Sr(NTf₂)₂	-0.48	0.00	-0.24	2.04	-0.49
Fe(NTf₂)₃	-0.36	0.01	-0.18	3.32	-0.58	Ti(NTf₂)₃	-0.45	-0.19	-0.32	3.25	-1.04
Ga(NTf₂)₃	-0.31	0.01	-0.15	2.05	-0.31	Tm(NTf₂)₃	-0.68	0.00	-0.34	2.44	-0.34
Gd(NTf₂)₃	- ^[a]	V(NTf₂)₃	-0.43	0.01	-0.21	2.45	-0.51				
Ho(NTf₂)₃	-0.67	-0.01	-0.34	2.23	-0.75	Yb(NTf₂)₃	-0.70	0.00	-0.35	2.75	-0.96
In(NTf₂)₃	-0.49	0.01	-0.24	2.30	-0.56	Y(NTf₂)₃	-0.31	0.00	-0.16	2.03	-0.32
Ir(NTf₂)₃	-0.27	-0.27	-0.27	2.70	-0.72	Zn(NTf₂)₂	-0.53	-0.01	-0.27	1.98	-0.54
K(NTf₂)	-0.96	-0.01	-0.49	2.25	-1.10	Zr(NTf₂)₃	-0.39	-0.53	-0.46	3.61	-1.66
La(NTf₂)₃	-0.45	0.00	-0.23	2.04	-0.47						
Li(NTf₂)	-0.91	-0.01	-0.46	1.99	-0.91						

^[a] Self-consistent field step did not converge using BP/def2-SVP.

3.6. “In silico Child’s method”

The poor predictive behavior of the different descriptors presented above contrast with the promising correlations obtained using the experimental Beckett-Childs method (*vide supra*). In this view, we developed an *in silico* analogous method using OPH₃ as molecular probe to describe the electron withdrawing ability of LAs. The charge variation on the OPH₃ moiety upon formation of a 1:1 Lewis adduct with Mⁿ⁺, M(OTf)_n and M(NTf₂)_n was calculated using NBO analysis (Table 29-31).²⁴²

Table 29 - NBO charge variation on OPH₃ due to its coordination of Mⁿ⁺

cation	Charge on OPH ₃	Charge on MeSH	Charge on MeOH	cation	Charge on OPH ₃	Charge on MeSH	Charge on MeOH
Ag ⁺	0.054	0.236	0.06	Lu ³⁺	0.306	_[a]	_[a]
Al ³⁺	0.339	_[a]	_[a]	Mg ²⁺	0.0427	0.332	0.052
Au ⁺	0.189	0.445	0.167	Mn ²⁺	0.221	0.411	_[a]
Au ³⁺	_[a]	_[a]	_[a]	Na ⁺	0.006	0.041	0.007
Ba ²⁺	0.044	0.087	0.038	Nd ³⁺	0.473	_[a]	_[a]
Bi ³⁺	0.404	0.801	0.369	Ni ²⁺	0.397	0.713	0.448
Ca ²⁺	0.071	0.134	0.060	Pb ²⁺	0.128	0.334	0.116
Cd ²⁺	0.220	0.616	0.259	Pd ²⁺	0.690	1.017	0.731
Ce ³⁺	0.328	_[a]	0.250	Pm ³⁺	0.356	_[a]	_[a]
Co ²⁺	0.310	0.617	0.340	Pr ³⁺	0.352	_[a]	_[a]
Cs ⁺	0.003	0.013	0.005	Pt ²⁺	0.627	0.978	0.647
Cu ⁺	0.060	0.239	0.064	Rb ⁺	0.003	0.015	0.004
Cu ²⁺	0.592	0.922	0.734	Sb ³⁺	0.441	_[a]	_[a]
Dy ³⁺	0.415	_[a]	_[a]	Sc ³⁺	0.561	_[a]	_[a]
Er ³⁺	0.304	_[a]	_[a]	Sm ³⁺	0.523	_[a]	_[a]
Eu ³⁺	0.921	_[a]	_[a]	Sn ²⁺	0.143	_[a]	_[a]
Fe ³⁺	0.938	_[a]	_[a]	Sr ²⁺	0.045	_[a]	_[a]
Ga ³⁺	0.924	_[a]	_[a]	Ti ³⁺	0.755	_[a]	_[a]
Gd ³⁺	0.480	_[a]	_[a]	Tm ³⁺	0.417	_[a]	_[a]
Ho ³⁺	0.309	_[a]	_[a]	V ³⁺	0.934	_[a]	_[a]
In ³⁺	0.967	_[a]	_[a]	Yb ³⁺	0.631	_[a]	_[a]
Ir ³⁺	1.071	_[a]	1.1	Y ³⁺	0.318	_[a]	_[a]
K ⁺	0.004	0.018	0.006	Zn ²⁺	0.175	0.626	0.209
La ³⁺	0.231	_[a]	_[a]	Zr ³⁺	0.417	_[a]	_[a]
Li ⁺	0.012	0.050	0.011				

[a] structure optimization did not converge either due to S or O abstraction or distance between OPH₃ and Mⁿ⁺ divergence.

²⁴² (a) J. P. Foster, F. Weinhold, *J. Am. Chem. Soc.* **1980**, *102*, 7211-7218; (b) A. E. Reed, L. A. Curtiss, F. Weinhold, *Chem. Rev.* **1988**, *88*, 899-926.

OPH₃ was chosen as it is a convenient molecular probe (small size, etc), but the choice is not critical. Indeed, partial charge transfer from MeOH and MeSH were also calculated (Table 29) and proved consistent (Figure 59).

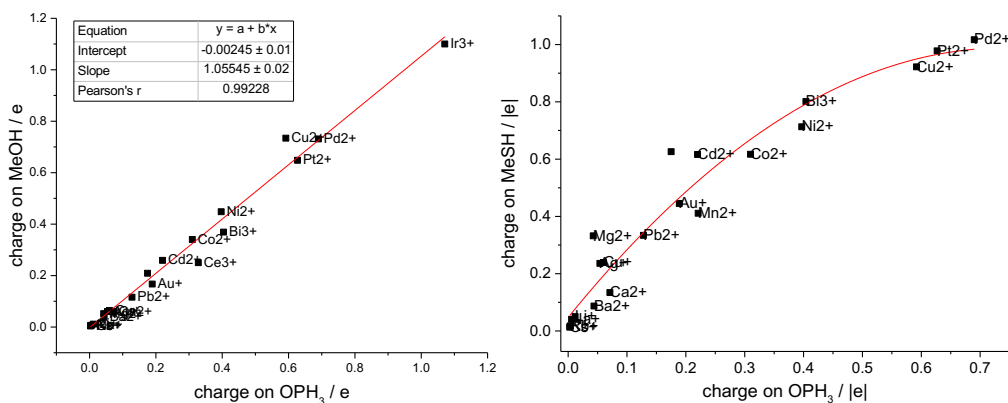


Figure 59 - Right: Correlation between the partial charge on OPH₃ linked with Mⁿ⁺ and the partial charge on MeOH linked on Mⁿ⁺. **Left:** Correlation between the partial charge on OPH₃ linked with Mⁿ⁺ and the partial charge on MeSH linked on Mⁿ⁺.

Table 30 - nbo charge variation on OPH₃ due to its coordination of M(OTf)_n.

Triflate salt	Charge on OPH ₃	Triflate salt	Charge on OPH ₃	Triflate salt	Charge on OPH ₃
Ag(OTf)	0.047	Ga(OTf) ₃	0.138	Pt(OTf) ₂	0.214
Al(OTf) ₃	0.135	Gd(OTf) ₃	0.137	Rb(OTf)	-0.015
Au(OTf)	0.139	Ho(OTf) ₃	0.129	Sb(OTf) ₃	0.105
Au(OTf) ₃	0.253	In(OTf) ₃	0.140	Sc(OTf) ₃	0.198
Ba(OTf) ₂	-0.005	Ir(OTf) ₃	0.228	Sm(OTf) ₃	0.134
Bi(OTf) ₃	0.093	K(OTf)	-0.009	Sn(OTf) ₂	0.108
Ca(OTf) ₂	0.011	La(OTf) ₃	0.089	Sr(OTf) ₂	0.001
Cd(OTf) ₂	0.032	Li(OTf)	0.006	Tb(OTf) ₃	- ^[a]
Ce(OTf) ₃	0.139	Lu(OTf) ₃	0.115	Ti(OTf) ₃	0.195
Co(OTf) ₂	0.084	Mg(OTf) ₂	0.017	Tm(OTf) ₃	0.126
Cs(OTf)	-0.009	Mn(OTf) ₂	0.072	V(OTf) ₃	0.199
Cu(OTf)	0.061	Na(OTf)	-0.004	Yb(OTf) ₃	0.122
Cu(OTf) ₂	0.091	Nd(OTf) ₃	0.136	Y(OTf) ₃	0.102
Dy(OTf) ₃	- ^[a]	Ni(OTf) ₂	0.082	Zn(OTf) ₂	0.035
Er(OTf) ₃	0.127	Pb(OTf) ₂	0.096	Zr(OTf) ₃	0.138
Eu(OTf) ₃	0.075	Pd(OTf) ₂	0.199		
Fe(OTf) ₃	0.169	Pm(OTf) ₃	0.131		

^[a] Self-consistent field step did not converge using BP/def2-SVP.

Table 31 - nbo charge variation on OPH₃ due to its coordination of M(NTf₂)_n

Triflimide salt	Charge on OPH ₃	Triflimide salt	Charge on OPH ₃	Triflimide salt	Charge on OPH ₃
Ag(NTf ₂) ₃	0.070	Ga(NTf ₂) ₃	0.143	Pt(NTf ₂) ₂	0.247
Al(NTf ₂) ₃	0.139	Gd(NTf ₂) ₃	0.153	Rb(NTf ₂)	-0.008
Au(NTf ₂)	0.137	Ho(NTf ₂) ₃	0.139	Sb(NTf ₂) ₃	0.157
Au(NTf ₂) ₃	0.234	In(NTf ₂) ₃	0.134	Sc(NTf ₂) ₃	0.197
Ba(NTf ₂) ₂	-0.001	Ir(NTf ₂) ₃	0.316	Sm(NTf ₂) ₃	0.137
Bi(NTf ₂) ₃	0.137	K(NTf ₂)	-0.006	Sn(NTf ₂) ₂	0.082
Ca(NTf ₂) ₂	0.015	La(NTf ₂) ₃	0.086	Sr(NTf ₂) ₂	0.005
Cd(NTf ₂) ₂	0.041	Li(NTf ₂)	0.015	Tb(NTf ₂) ₃	- ^[a]
Ce(NTf ₂) ₃	0.153	Lu(NTf ₂) ₃	0.125	Ti(NTf ₂) ₃	0.268
Co(NTf ₂) ₂	0.104	Mg(NTf ₂) ₂	0.023	Tm(NTf ₂) ₃	0.136
Cs(NTf ₂)	-0.008	Mn(NTf ₂) ₂	0.079	V(NTf ₂) ₃	0.285
Cu(NTf ₂)	0.073	Na(NTf ₂)	0.000	Yb(NTf ₂) ₃	0.153
Cu(NTf ₂) ₂	0.118	Nd(NTf ₂) ₃	0.148	Y(NTf ₂) ₃	0.105
Dy(NTf ₂) ₃	- ^[a]	Ni(NTf ₂) ₂	0.091	Zn(NTf ₂) ₃	0.042
Er(NTf ₂) ₃	0.135	Pb(NTf ₂) ₃	0.071	Zr(NTf ₂) ₃	0.215
Eu(NTf ₂) ₃	0.140	Pd(NTf ₂) ₃	0.233		
Fe(NTf ₂) ₃	0.204	Pm(NTf ₂) ₃	0.147		

^[a] Self-consistent field step did not converge using BP/def2-SVP.

To our delight, a good prediction level was achieved between the yield of **3aa** and the charge variation for triflimide salts (**Figure 60**). Overall, the electron withdrawal from OPH₃ was higher for triflimide salts, than for triflate ones, which correlates with their higher catalytic activity. Among the triflimide salts, transition metal ones followed a consistent trend, but displayed lower activity (**Figure 60**, red line). This may be due to higher poisoning of these salts (*vide infra*), as they also exhibit higher affinity for OPH₃. Besides, the behavior of some lanthanide salts (Nd, Eu, Yb) is not well reproduced, maybe due to the difficulty to model lanthanides by DFT.

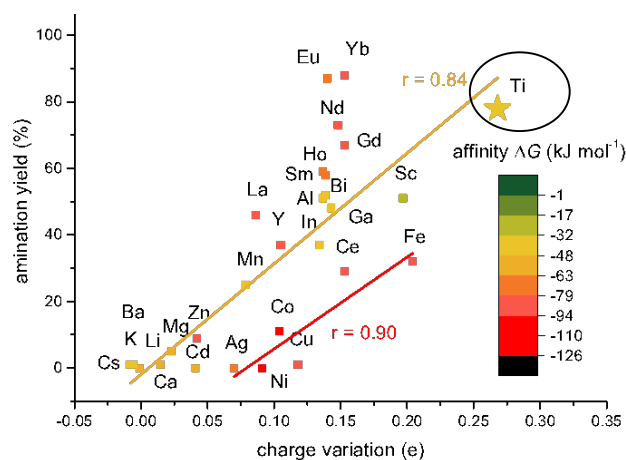


Figure 60 - Correlation between the partial charge on OPH₃ in the complex M(NTf₂)_n-OPH₃ and the yield of the amination reaction 1 (**1a** + **2a** = **3aa**).

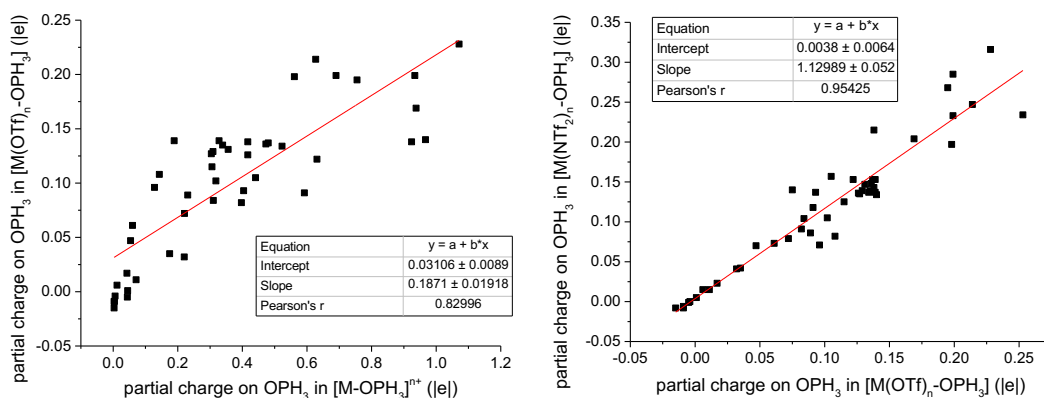


Figure 61 - Left: Correlation between the partial charge on OPH_3 linked with M^{n+} and the partial charge on OPH_3 linked with $\text{M}(\text{OTf})_n$; **Right:** Correlation between the partial charge on OPH_3 linked with $\text{M}(\text{OTf})_n$ and the partial charge on OPH_3 linked with $\text{M}(\text{NTf}_2)_n$.

Finally, it may be interesting to question the link between the charge variation of OPH_3 upon coordination and the global electrophilicity index as both scales reproduce the experimental trend. Both indicators are related to the maximal charge transferable (χ / η) or the energetic gain ($\omega = \chi^2 / 2\eta$) associated to this transfer (*vide supra* definition in CHAPTER I). However, the maximal charge transfer estimated by both approaches yields very different results (**Figure 62**). These differences are probably due to the strong approximations considered in the calculation of global electrophilicity index: no geometric relaxation (fixed potential) and transfer of one electron. This could explain the better correlation obtained using our approach.

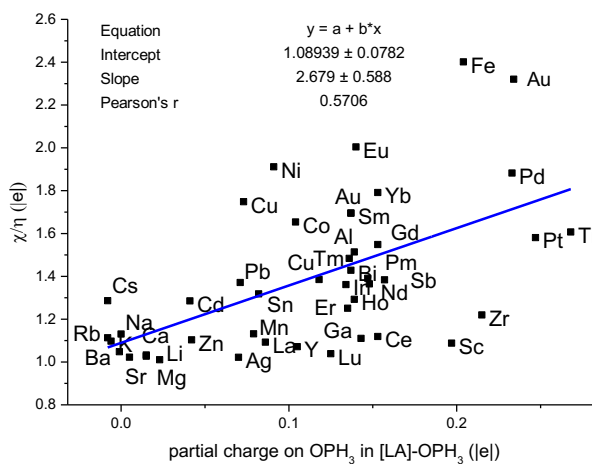


Figure 62 - Correlation between the maximal charge transfer (χ/η) and the partial charge on OPH_3 ligated to $\text{M}(\text{NTf}_2)_n$.

Interestingly, among the different triflimide salts, a high catalytic activity was predicted for Ti triflimide (**Figure 60**). This prediction prompted us to try out the synthesis of this salt, which has never been described.

3.7. Synthesis and Characterization of Titanium Triflimide

To our knowledge, there is only one unsuccessful report concerning the synthesis of $\text{Ti}(\text{OTf})_4$.²⁴³ The main shortcoming of Ti(IV) salt synthesis relies on their propensity to form titanium oxides in the presence of water.³¹

We attempted to perform the synthesis of $\text{Ti}(\text{NTf}_2)_n$ by addition of excess triflimide acid (HNTf_2) on Ti metal in water. A pale pink solution was obtained after two days at reflux. Water and excess triflimide acid were removed under vacuum to give a pink solid **4**.²⁴⁴

This color was unexpected for a Ti(IV) salt and to understand its origin, a complete set of analyses of **4** was performed. Back titration of **4** using a reducing agent²⁴⁵ showed the presence of 7.4 wt% Ti. The F mass fraction was estimated to 33 wt% by ^{19}F NMR using an internal standard, corresponding to 2 NTf_2^- per Ti. This result is compatible with the formation of a partially hydrolyzed $\text{Ti}(\text{NTf}_2)_n$ salt. The average molecular weight was measured using TGA analysis.²⁴⁶ Assuming that the final decomposition product of **4** at around 120 °C is TiO_2 , the

²⁴³ H. M. el Mustapha, J.-L. Pascal, *J. Fluorine Chem.* **1991**, *55*, 63-78.

²⁴⁴ **Procedure for the synthesis of 4.** Trifluoromethanesulfonimide (82.5%) 136.3 g (0.4 mol) was dissolved in water (200 mL), and titanium powder (Alpha Aesar (150 mesh) was added (4.79 g, 0.1 mol) to the stirring solution. The reaction mixture was stirred 2 days at reflux condition. After cooling and filtration (around 1.6 g of Ti(0) was recovered) the resulting red solution was concentrated using rotary evaporator. The remaining solution was further dry using oil pump equipped with a liquid nitrogen trap at 100 °C for 4 days in order to eliminate excess water and Trifluoromethanesulfonimide (HNTf_2 sublimates under vacuum at about 60 °C, see J. Sun (2010). Triflimide. In *Encyclopedia of Reagents for Organic Synthesis*. Note than one must not heat over 100 °C to avoid the decomposition of the salt according to the reaction: $[\text{Ti}(\text{H}_2\text{O})(\text{NTf}_2)] \rightarrow [\text{Ti}(\text{OH})] + \text{HNTf}_2$, see TGA analysis section). At last get 34 g pale pink solid of target product. Yield 29 %.

²⁴⁵ **Procedure for the titration of Ti in a sample of 4.** 0.2311 g were added in a 500 mL Erlenmeyer flask and diluted with 5 mL of water until a milky and homogeneous solution was obtained. 30 mL of concentrated (98 wt%) sulfuric acid were then added and the solution turn transparent. After addition of 12 g of ammonium sulfate and heating the solution was cool down using 120 mL of water and 40 mL of concentrated. All the titanium was then reduced using an excess of aluminum turning (3 g, dihydrogen degassing was directed toward a saturated aqueous sodium hydrogencarbonate solution in a gas washing bottle). After complete dissolution of aluminum a pale pink solution was obtained and titrated using a 0.01 M solution of iron(III) nitrate using KSCN as an indicator. The titration has been reproduced two times by two different operators.

The mass fraction of Ti in the sample is directly given by:

$$x_{\text{Ti}} = \frac{C_{\text{Fe}} \cdot V_{\text{eq}} \cdot M_{\text{Ti}}}{m_{\text{tot}}}$$

With $C_{\text{Fe}} = 0.01$ M the concentration of the iron solution, V_{eq} volume of titrant used, M_{Ti} the molecular weight of titanium and m_{tot} the total mass of the sample.

²⁴⁶ D. B. Baudry, A. Dormond, F. Duris, J. M. Bernard, J. R. Desmurs, *J. Fluorine Chem.* **2003**, *121*, 233-238.

molecular weight of **4** is 842 g/mol (**Figure 63**), with 5.7 wt% of absorbed water (2.5 equiv, desorbing around 90 °C).

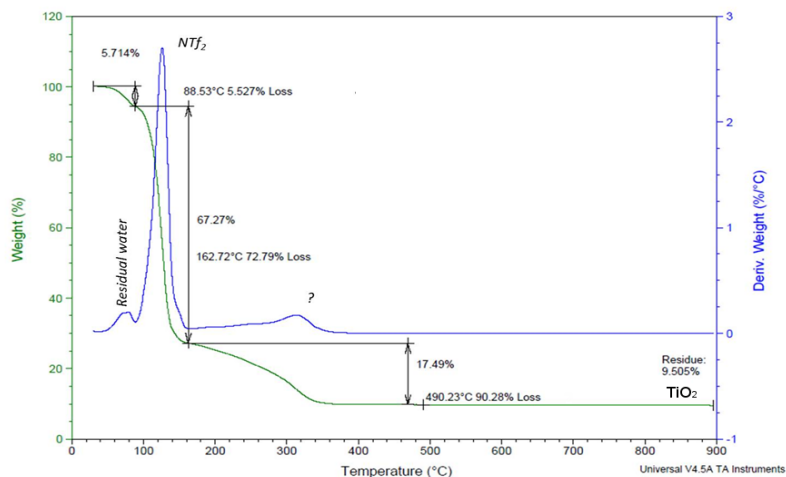


Figure 63 - Thermogravimetric analysis (TGA) of the **4** under Air Flow.

However, none of the above analyses allowed us to explain the origin of the pink color of this salt. Surprisingly, when performing back titration of **4** in the absence of a reducing agent, 20% of Ti(III) was detected.²⁴⁷ The presence of Ti(III) was rather unexpected due to the experimental conditions used (water, air and prolonged heating). This observation was further confirmed by Electron Paramagnetic Resonance (EPR). In THF, the EPR spectrum of **4** featured the typical symmetrical pattern for a Ti-center single radical without Jahn-Teller effect ($g_{iso} = 1.960$) (**Figure 64**). The well-defined hyperfine structure can be ascribed to the coupling ($a_{iso} = 18$ G) with the nuclear spin of ^{46}Ti and ^{49}Ti isotopes.

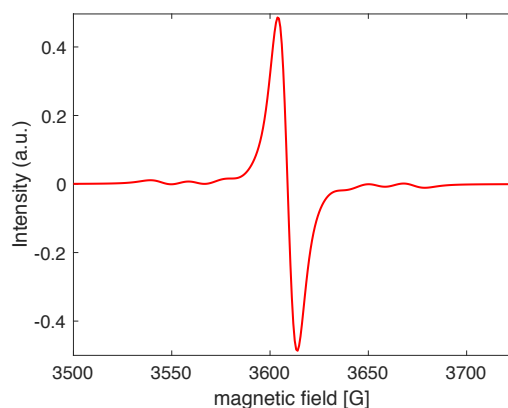


Figure 64 - EPR spectra of **4** in THF ($g_{iso} = 1.96$, $a_{iso} = 18$ G).

²⁴⁷ Procedure for the titration of Ti(III) in a sample of **4**. The procedure was similar to the one described above except that no reducing agent (aluminium) was added.

EPR was also performed on solid **4** at 110 K and 20 K under liquid He. At 110 K, the signal exhibited a large single resonance corresponding to a faintly distorted Ti(III) center $g = [1.972 \ 1.925 \ 1.870]$ with no hyperfine coupling. At 20 K, **4** displayed a low field transition at $g = 3.85$, which is characteristic of small spin-spin dipolar interaction between two neighboring Ti(III) centers (**Figure 65**).²⁴⁸ Dimeric structures were reported for triflimide-based Ti(IV) complexes, most often with alkoxy groups as bridging ligands (e.g. $\text{Ti}_2(\text{NTf}_2)_2(\text{O}^i\text{Pr})_6$).²⁴⁹ Triflimide anions can also behave as bridging ligands, especially for alkali metals.²⁵⁰

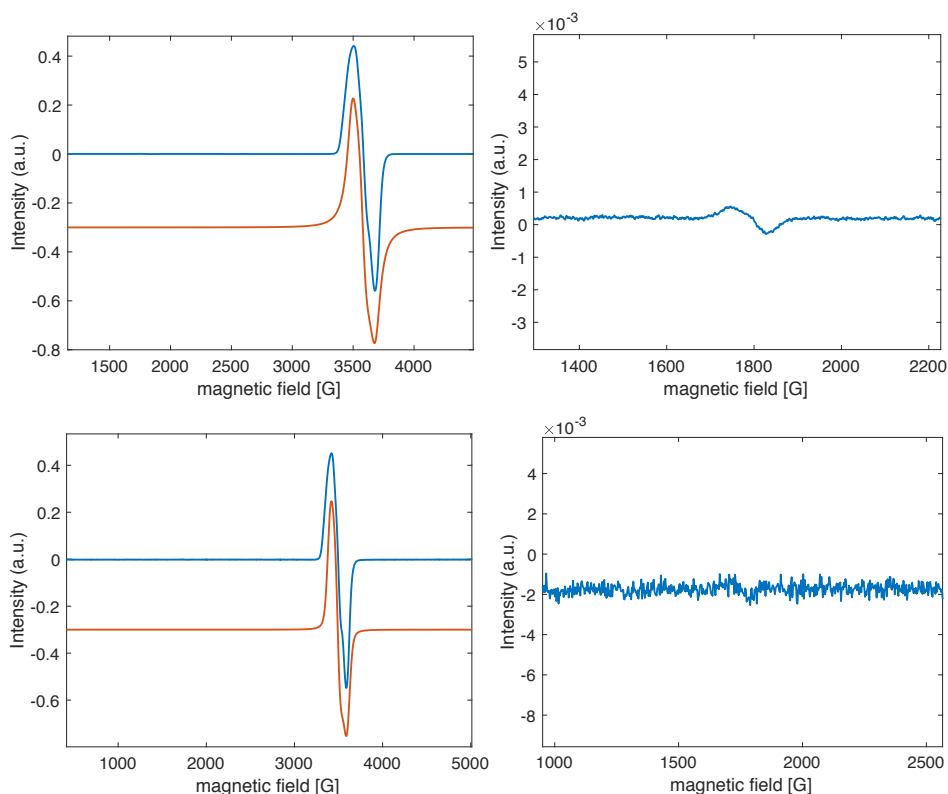


Figure 65 - EPR spectra of solid **4**, **top**: at 20 K ($g = [1.972 \ 1.925 \ 1.870]$); **bottom**: at 20 K ($g = [1.972 \ 1.925 \ 1.870]$), **right**: zoom on the low field signal ($\times 1000$).

It was not possible to use the mass spectrometry method developed by the group of Duñach²⁵¹ to evidence Ti(III) complexes, as Ti(III) is not stable in nitromethane (the absence of Ti(III) when the complex is in solution in nitromethane was demonstrated by EPR spectroscopy). However, several complexes between Ti(IV) and triflimides were found by mass (**Figure 66**).

²⁴⁸ A. Faucitano, A. Buttafava, F. Martinotti, *Radiat. Phys. Chem.*, **1995**, *45*, 31-36.

²⁴⁹ A. L. Johnson, M. G. Davidson, M. D. Jones, M. D. Lunn, *Inorg. Chem. Acta*, **2010**, *363*, 2209-2214.

²⁵⁰ L. Xue, C. W. Padgett, D. D. DesMarteau, W. T. Pennington, *Solid State Sci.*, **2002**, *4*, 1535-1545.

²⁵¹ J.-F. Gal, C. Iacobucci, I. Monfardini, L. Massi, E. Duñach, S. Olivero, *J. Am. Soc. Mass. Spectrom.*, **2012**, *23*, 2059-2062; G. Compain, L. Sikk, L. Massi, J. F. Gal, E. Duñach, *ChemPhysChem.*, **2017**, *18*, 683-691; C. Iacobucci, N. Jouini, L. Massi, S. Olivero, F. De Angelis, E. Duñach, J.-F. Gal, *ChemPlusChem.*, **2017**, *82*, 498-506; I. Monfardini, L. Massi, E. Duñach, S. Olivero, J.-F. Gal, *Chem. Commun.*, **2010**, *46*, 8472-8474.

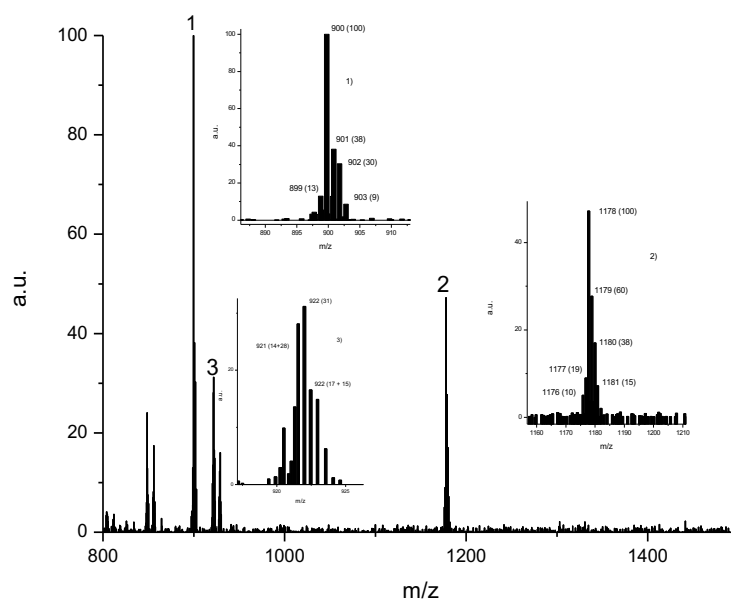


Figure 66 - ESI-MS spectrum (direct injection, no fragmentation) of **4** and TPPO in nitromethane.

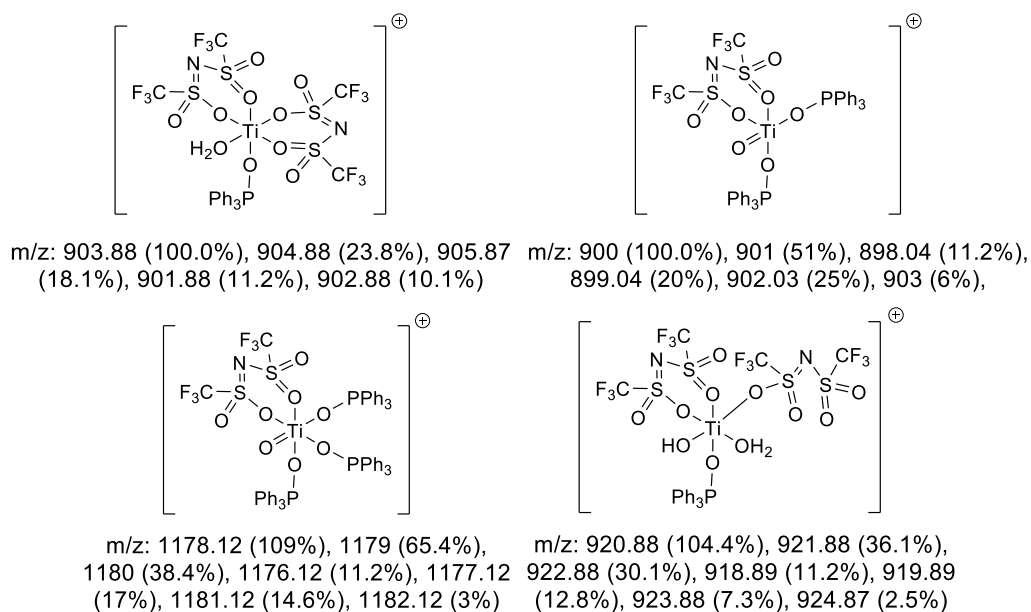


Figure 67 – Ti-triflimide complexes potentially observed by ESI-MS.

On the basis of elemental analysis, ESI-MS and EPR data, we may thus tentatively assign the following molecular formula to **4**: $\text{Ti}^{\text{III}}_{0.2}\text{Ti}^{\text{IV}}_{0.8}(\text{NTf}_2)_2(\text{O})_x(\text{OH})_y(\text{H}_2\text{O})_z, 2.5 \text{ H}_2\text{O}$.

To rationalize the unexpected stabilization of Ti(III) by triflimide ligands, electrochemical analysis was performed (**Figure 68**). Ti(III) chloride in HCl (15 wt%) exhibited a single non-reversible oxidation peak at +0.75 V *vs* SCE (i.e. 1.0 V *vs* SHE).²⁵²

The absence of reversibility can be explained by the formation of TiO₂.²⁵³ Ti(III) present in **4** displayed in water a single non-reversible oxidation peak at +1.41 V *vs* SCE (around +1.6 V *vs* SHE). This large shift (+0.65 V) can only be explained if triflimide anions remain coordinated to Ti(III),²⁵⁴ suggesting a strong stabilization of this oxidation state by the ligands. With a poor ligand such as triflimide, the oxidation of Ti(III) to Ti(IV) appeared highly unfavorable. The capacity of triflate and triflimide ligands to stabilize low oxidation valences has been reported earlier for FeX₃²⁵⁵ and TiCp₂X²⁵⁶ complexes, and it can be exploited to access unstable low oxidation states of metals.

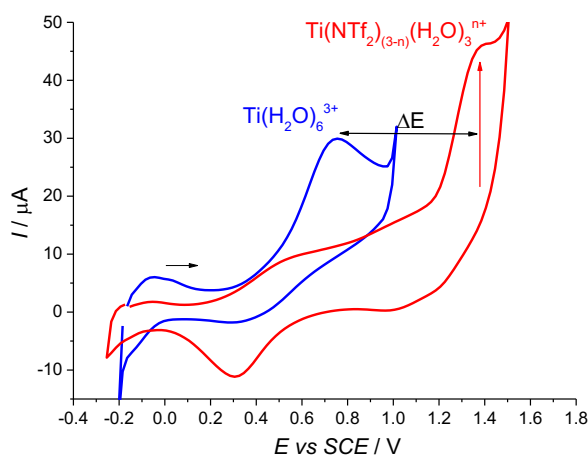


Figure 68 - CV towards oxidation potentials recorded on a steady glassy carbon disk electrode ($d = 1$ mm) in water at 20 °C with a scan rate of 0.5 V s⁻¹. TiCl₃ in aqueous HCl (15 wt%) in blue and **4** (in red).

²⁵² G. Casalbore, P. G. d. Marco, G. Giro, M. Mastragostino, *J. Electroanal. Chem. Interfacial Electrochem.*, **1980**, *111*, 369-375.

²⁵³ The reduction Ti(IV) could not be observed. G. M. Habashy, *Z. Anorg. Allg. Chem.*, **1960**, *306*, 312-316; J. D. Ellis, G. A. K. Thompson, A. G. Sykes, *Inorg. Chem.*, **1976**, *15*, 3172-3174.

²⁵⁴ Triflimide seems to remain in the coordination sphere of Ti(III). This results was further confirmed by EPR spectroscopy, the spectrum of **4** in water proved different of the one of TiCl₃ in water (see the SI). "TiCl₃" in concentrated HCl is hexahydrated (in the form Ti(H₂O)₆³⁺), see S. Maurelli, S. Livraghi, M. Chiesa, E. Giamello, S. Van Doorslaer, C. Di Valentin, G. Pacchioni, *Inorg. Chem.*, **2011**, *50*, 2385-2394.

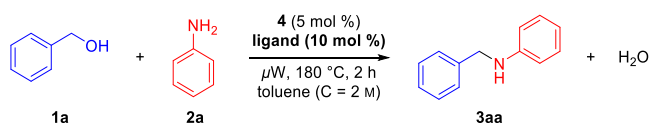
²⁵⁵ J. R. Cabrero-Antonino, A. Leyva-Pérez, A. Corma, *Chem. Eur. J.*, **2012**, *18*, 11107-11114.

²⁵⁶ D. B. Williams, M. E. Stoll, B. L. Scott, D. A. Costa, J. W. J. Oldham, *Chem. Commun.*, **2005**, 1438-1440.

3.8. Catalytic Activity of **4**

Complex **4** was then tested for the direct amination of benzyl alcohol with aniline. The desired product **3aa** was obtained with 78% yield and good selectivity, matching the prediction (**Figure 60**). Given this promising result, the effect of additives and ligands on the catalytic performance of **4** was further investigated.²⁵⁷

Table 32 - Ligand Effect on Catalytic Performance of **4**^a



entry	ligand	yield of 3aa (%) ^b
1	none	69
2	2,2'-bipyridine (1 equiv)	61
3	2,2'-bipyridine (2 equiv)	93
4	2,2'-bipyridine (3 equiv)	57
5	Phenanthroline	93
6	4,4'-dibromo-2,2'-bipyridine	78
7	6,6'-dibromo-2,2'-dipyridyl	79
8	4,4'-dimethyl-2,2'-dipyridyl	93
9	4,4'-di-tert-butyl-2,2'-dipyridyl	91
10	2,2'-bipyridine (bpy)	96 ^c
11	Terpyridine (tpy)	97 ^c

^aGeneral reaction conditions: **1a** (1 mmol) and **2a** (2 mmol, 2 equiv) were sequentially added at room temperature to a solution of **4** (0.05 mmol, 0.05 equiv) and the ligand (0.1 mmol, 0.1 equiv) in toluene (0.5 mL) in a microwave vial equipped with a magnetic stirrer. The vial was then capped and heated under microwave irradiation at 180 °C for 2 h. ^bDetermined by ¹H NMR using 2,4,6-trimethoxybenzene as internal standard. ^cUsing 7.5 mol% of **4**, at 160 °C, 1 h heating.

The addition of 2,2'-bipyridine (bpy) as ligand increased the yield of **3aa** up to 93% (**Table 32**). The optimal amount of ligand was 2 equiv, while further excess deactivated the catalyst (**Table 32**, entries 1-4). Different bipyridines were assessed under the same conditions, giving either

²⁵⁷ Catalytic amounts of Brønsted superacids such as triflic (HOTf) or triflimidic (HNTf₂) acids did not induce the formation of **3aa**, and their use as additive in the reaction turn out to be detrimental to the catalytic activity of **4**. However, the addition of the sterically hindered tertiary diamine Proton Sponge® (1,8-bis(dimethylamino)naphthalene) under otherwise identical conditions, did not affect significantly the reaction, thus ruling out a “hidden proton” catalytic pathway, see representative examples: A. Dzudza, T. J. Marks, *Chem. Eur. J.* **2010**, *16*, 3403-3422; T. T. Dang, F. Boeck, L. Hintermann, *J. Org. Chem.* **2011**, *76*, 9353-9361; R. K. Schmidt, K. Müther, C. Mück-Lichtenfeld, S. Grimme, M. Oestreich, *J. Am. Chem. Soc.* **2012**, *134*, 4421-4428.

similar or poorer results (Table 32, entries 5-9).²⁵⁸ Increasing the catalyst loading from 5 mol% to 7.5 mol% allowed to reduce both the temperature and the reaction time (Table 32, entries 10-11). However, beyond 10 mol%, the yield of **3aa**.

The scope of the most active catalytic system – **4**/bpy – was next assessed (Table 33-34). First, electronic effects on aniline derivatives were investigated. Electron-rich anilines proved to be less reactive than electron-poor anilines due to catalyst deactivation (Figure 69). Higher temperatures (or longer reaction times) were required for these substrates.

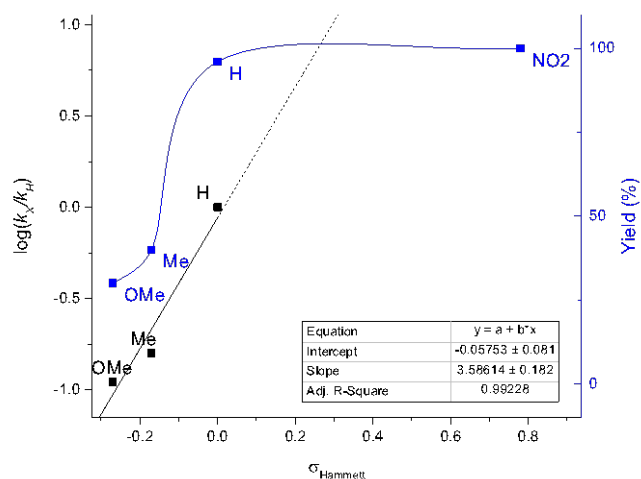
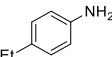
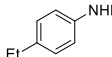
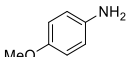
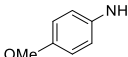
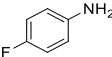
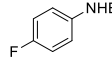
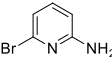
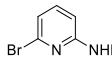


Figure 69 - Yield of the amination reaction of *p*-X-aniline (with X = H, Me, OMe and NO₂) catalyzed by **4** (5 mol%) after 2h of heating versus the Hammett constant of the substituent X. The k_x constant was roughly estimated using the formula $k_x = -\ln(1-\eta/100)/t$ (with η the yield of the reaction and t the reaction time).

Primary anilines **2c–2g** bearing electron-donating (Table 33, entries 2-4) or electron-withdrawing groups (Table 33, entries 5-6) reacted to give the corresponding secondary amines **3ac–3ag** selectively in excellent yield. 6-Amino-2-bromopyridine **2h** could be benzylated, but longer reaction times were required to allow isolation of product **3ah** in good yield (Table 33, entry 7). Owing to higher steric effects, secondary benzyl amines such as tetrahydroisoquinoline **2i** and dibenzyl amine **2j** were more reluctant to undergo benzylation with **1a**, demanding higher catalyst/ligand loading and longer reaction times (Table 33, entries 8 and 9). Finally, the reaction of dodecylamine **2k** with **1a** only afforded moderate yield due to a significant drop of the selectivity (Table 33, entry 10).

²⁵⁸ At this point, it is worth mentioning that the experiments performed under thermal heating in mesitylene led to much lower performance, even after prolonged times.

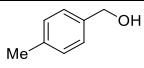
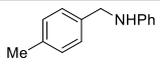
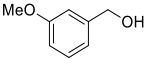
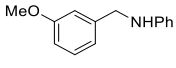
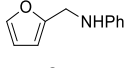
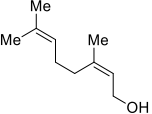
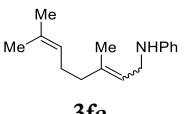
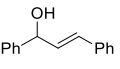
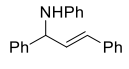
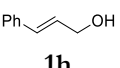
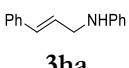
Table 33 - Table 3. Scope the Direct Amination of Alcohols Using the 4/ligand System^a

$\text{R}^1\text{-OH} + \text{R}^2\text{-N(H)-R}^3 \xrightarrow[\text{toluene (C = 2 M)}]{\text{4 (7.5 mol \%)} \text{ bpy or tpy (10 mol \%)} \text{ } \mu\text{W, 160 }^\circ\text{C}}$		$\text{R}^1\text{-N(H)-R}^3 + \text{H}_2\text{O}$		
1	2	3		
entry	alcohol (1)	amine (2)	product (3)	yield (%) ^b
1	BnOH 1a	 3a	 3aa	96 / 76 ^c (100)
2	BnOH 1a	 2c	 3ac	96
3	BnOH 1a	 2d	 3ad	20 ^c (100)
4	BnOH 1a	 2e	 3ae	60 ^c (100)
5	BnOH 1a	 2f	 3af	98
6	BnOH 1a	 2g	 3ag	75 ^d
7	BnOH 1a	 2h	 3ah	86 ^e
8	BnOH 1a	 2i	 3ai	91 ^f
9	BnOH 1a	 2j	 3aj	96 ^f
10	BnOH 1a	 2k	 3ak	36 ^g

^aReaction conditions: **1** (1 mmol) and **2** (2 mmol, 2 equiv) were sequentially added at room temperature to a solution of **4** (0.075 mmol, 0.075 equiv) and the ligand (0.15 mmol, 0.2 equiv) in toluene (0.5 mL) in a microwave vial equipped with a magnetic stirrer. The vial was then capped and heated under microwave irradiation at 160 °C for 1 h). ^bIsolated yield (yield determined by ¹H NMR using 2,4,6-trimethoxy-benzene as internal standard). ^c 4.5 mol%, 180 °C, 2 h; ^d 140 °C, 8 h; ^e 160 °C, 8 h; ^f 180 °C, 12 h; ^g 190 °C, 8 h.

Next, we assessed the reactivity of different alcohols (**Table 34**). Benzyl alcohols bearing electron-donating groups either at the *p*- (**1c**) or at the *m*-position (**1d**) reacted smoothly with aniline (**2a**) affording the corresponding secondary amines **3ca** and **3da** in good yields (**Table 34**, entries 1 and 2). Interestingly, biomass-derived furfuryl alcohol (**1e**) proved to be an excellent substrate for the reaction, and the desired furfuryl aniline (**3ea**) was obtained in 98% yield using lower heating conditions (**Table 34**, entry 3). The reactivity of allyl alcohols toward amination was then assessed (**Table 34**, entries 4-6). Even at low temperature, the thermodynamically favored *C*-alkylated product was formed together with the kinetic *N*-alkylated product.^[65] For instance, the reaction of nerol (**1f**) with aniline (**2a**) at 80 °C delivered a *ca.* 2:1 mixture of *C*- and *N*-alkylated isomers in good overall yield (**Table 34**, entry 4). The isolation of the latter product revealed partial isomerization of the original (*Z*) double bond. Likewise, the reaction of **1g** and **1h** with **2a** led to a mixture of isomers (**Table 34**, entries 5-6).

Table 34 - Scope the Direct Amination of Alcohols Using the **4**/tpy System^a

$ \begin{array}{c} \text{R}^1\text{-OH} \quad + \quad \begin{array}{c} \text{H} \\ \\ \text{R}^2\text{N-R}^3 \end{array} \\ \mathbf{1} \quad \quad \quad \mathbf{2} \end{array} \xrightarrow[\text{toluene (C = 2 M)}]{\begin{array}{c} \mathbf{4} \text{ (7.5 mol \%)} \\ \text{tpy (10 mol \%)} \\ \mu\text{W, } 160 \text{ }^\circ\text{C} \end{array}} \begin{array}{c} \begin{array}{c} \text{R}^1 \\ \\ \text{R}^2\text{N-R}^3 \end{array} \\ \mathbf{3} \end{array} + \text{H}_2\text{O} $				
entry	alcohol (1)	amine (2)	product (3)	yield (%) ^b
1	 1c	PhNH ₂ 2a	 3ca	61
2	 1d	PhNH ₂ 2a	 3da	93 ^c
3	 1e	PhNH ₂ 2a	 3ea	98 ^d
4	 1f	PhNH ₂ 2a	 3fa	81 ^e (<i>N</i> -/ <i>C</i> - = 67:33)
5	 1g	PhNH ₂ 2a	 3ga	99 ^f (<i>N</i> -/ <i>C</i> - = 80:20)
6	 1h	PhNH ₂ 2a	 3ha	98 ^f (<i>N</i> -/ <i>C</i> - = 36:64)

^a Reaction conditions as in **Table 23**; ^b Isolated yield (yield determined by ¹H NMR using 2,4,6-trimethoxy-benzene as an internal standard). ^c **4** 5 mol%, 180 °C, 2 h; ^d 100 °C, 2 h; ^e 80 °C, 16 h; ^f 120 °C, 0.5 h; ^g 100 °C, 1 h, 14% of **4ja**; ^h 140 °C, 4 h; 220 °C, 16 h.

3.9. Mechanistic Insights

On the guidance of the promising catalytic performance of Ti triflimide, we decided to investigate in detail the catalytic mechanism. Based on our previous study on Al triflate (section 2) and complementary experiments, a S_N-type mechanism was proposed. For each catalytic system, the crude reaction mixtures were carefully examined: plausible imine intermediates were never identified, thus providing evidence for an S_N-type rather than a “borrowing hydrogen” mechanism. An additional crossover experiment using an equimolar mixture of *m*-methylbenzyl alcohol (**1i**) and deuterated benzyl alcohol (**1a'**) led to neither deuterium incorporation into product **3ia** nor the loss of deuterium in **3a'a** as observed by ¹H NMR and HRMS. To go further into our mechanistic investigations and to discriminate between S_N1 and S_N2 mechanisms, (*R*)-1-phenylethanol (**1b'**) was reacted with **2a** and racemic **3b'a** was isolated, which advocates for a carbocationic intermediate (or *in situ* isomerization).

We intend to answer two main questions: i) what is the oxidation state of the catalyst during the reaction, and ii) what is the role played by the ligand. Ti(IV) halides (TiCl₄ and TiBr₄) are inactive for the amination reaction of benzyl alcohol with aniline. On the contrary Ti(III) halides catalyzed this reaction. TiBr₄/Zn, generating *in-situ* TiBr₃, and TiCl₃(THF)₃ gave product **3aa** with 20% and 15% yield respectively, at 160 °C after 1 h (with TiCl₃(THF)₃/bpy 39% yield was obtained). At first sight, the higher activity of Ti(III) could be attributed to lower hydrolysis than Ti(IV). Besides, other results highlight the role played by the triflimide anion. For instance, a mixture of TiCl₄ and LiNTf₂ (or AgNTf₂) is catalytically active, as well as Cp₂Ti(NTf₂)₂. Moreover, the reaction works similarly both under Ar and under air, and EPR monitoring of the initial reaction mixture (**4**/bpy in the presence of BnOH and aniline) reveals the absence of residual Ti(III) after addition of aniline (*vide infra*).

EPR Study. **4** was not soluble in toluene and the EPR spectrum was similar to that measured on the solid salt. DFT estimation of the *g*-tensor of Ti(NTf₂)₃ was compatible with the experimental spectra (**Table 35**).²⁵⁹

Table 35 - DFT-predicted *g*-tensor of some Ti(III)-complexes resulting from the coordination of BnOH, aniline and bpy.

Species	<i>g</i>		
Ti(NTf ₂) ₃ (5) ^a	1.920	1.944	1.976
<i>mer</i> -Ti(NTf ₂) ₃ (BnOH) ₃ (6)	1.924	1.945	1.995
<i>fac</i> -Ti(NTf ₂) ₃ (BnOH) ₃ (7)	1.942	1.951	1.997
<i>fac</i> -Ti(NTf ₂) ₃ (H ₂ O) ₃ (8)	1.923	1.942	2.000
Ti(NTf ₂) ₂ (BnO)(BnOH) ₂ (9)	1.961	1.973	1.979

²⁵⁹ Structures and free energy corrections (*G*_{gas} at T = 25 °C and P = 1 bar) were calculated at the (DFT) BP86-D3(BJ)/def2-SVP level. The EPR *g*-tensor of radical species was calculated on optimized structures at the PBE0/def2-TZVP level using ORCA's default settings for the gauge origin (center of electronic charge), see CHAPTER I.

Ti(NTf ₂) ₂ (BnO) (10)	1.958	1.975	1.985
<i>mer</i> -Ti(NTf ₂) ₃ (aniline) ₃ (11)	1.933	1.953	1.981
<i>fac</i> -Ti(NTf ₂) ₃ (aniline) ₃ (12)	1.932	1.947	1.984
[Ti(NTf ₂) ₂ (aniline) ₂] ⁺ (13)	1.921	1.946	1.988
[Ti(NTf ₂) ₂ (aniline) ₄] ⁺ (14)	1.954	1.956	1.974
[Ti(aniline) ₄] ³⁺ (15)	1.929	1.978	1.997
[Ti(aniline) ₆] ³⁺ (16)	1.930	1.962	1.989
[Ti(bpy) ₂] ³⁺ (17)	1.874	1.980	1.998
[Ti(bpy) ₃] ³⁺ (18)	1.878	1.936	1.997
[Ti(bpy) ₂ (BnOH) ₂] ³⁺ (19)	1.972	1.974	1.998
[Ti(bpy) ₂ (BnO)(BnOH)] ²⁺ (20)	1.973	1.982	1.991

^b Note that **4** is a mixture Ti(III) and Ti(IV), we chose to model Ti(III) part by Ti(NTf₂)₃, noted **5**.

When BnOH (20 equiv) was added, a homogenous, air-stable and purple solution was obtained. The EPR spectrum revealed the formation of at least two complexes. The main species featured a characteristic signal of an octahedral Ti(III) complex distorted by Jahn-Teller effect ($g = [1.992\ 1.901\ 1.901]$), a second symmetrical signal was observed at $g = [1.963\ 1.950\ 1.935]$ (**Figure 70**).

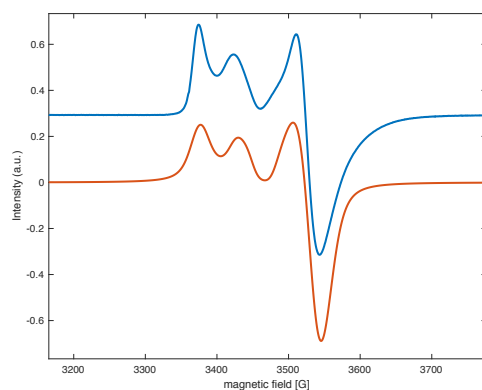


Figure 70 - Experimental (blue) and simulated (orange) EPR spectra of **4** in toluene, in the presence of BnOH (20 equiv) ($g = [1.963\ 1.95\ 1.935]$, 20%, $g = [1.992\ 1.901\ 1.901]$, 80%).

The main signal could be attributed to Ti(NTf₂)₃(BnOH)₃ (**6-7**) as inferred from the DFT calculations (**Table 35**). Ti(NTf₂)₃(H₂O)₃ should also have a similar EPR signature. On the contrary, a Ti(III) complex featuring an alcoxy ligand, i.e. Ti(NTf₂)₂(BnO)(BnOH)₂ (**9**) or Ti(NTf₂)₂(BnO) (**10**) is predicted to show a very fine EPR signal, which is in agreement with reported experimental and simulated data on the TiCl₃/MeOH system.²⁶⁰ Based on our DFT

²⁶⁰ S. Maurelli, E. Morra, S. Van Doorslaer, V. Busicod, M. Chiesa, *Phys. Chem. Chem. Phys.* **2014**, *16*, 19625-19633.

calculations, we propose a *fac*-Ti(NTf₂)₃(BnOH)₃ complex as the main species together with partial formation of Ti(NTf₂)₂(BnO)(BnOH)₂ (9) (Figure 71-72). These complexes could behave as active species for the reaction.

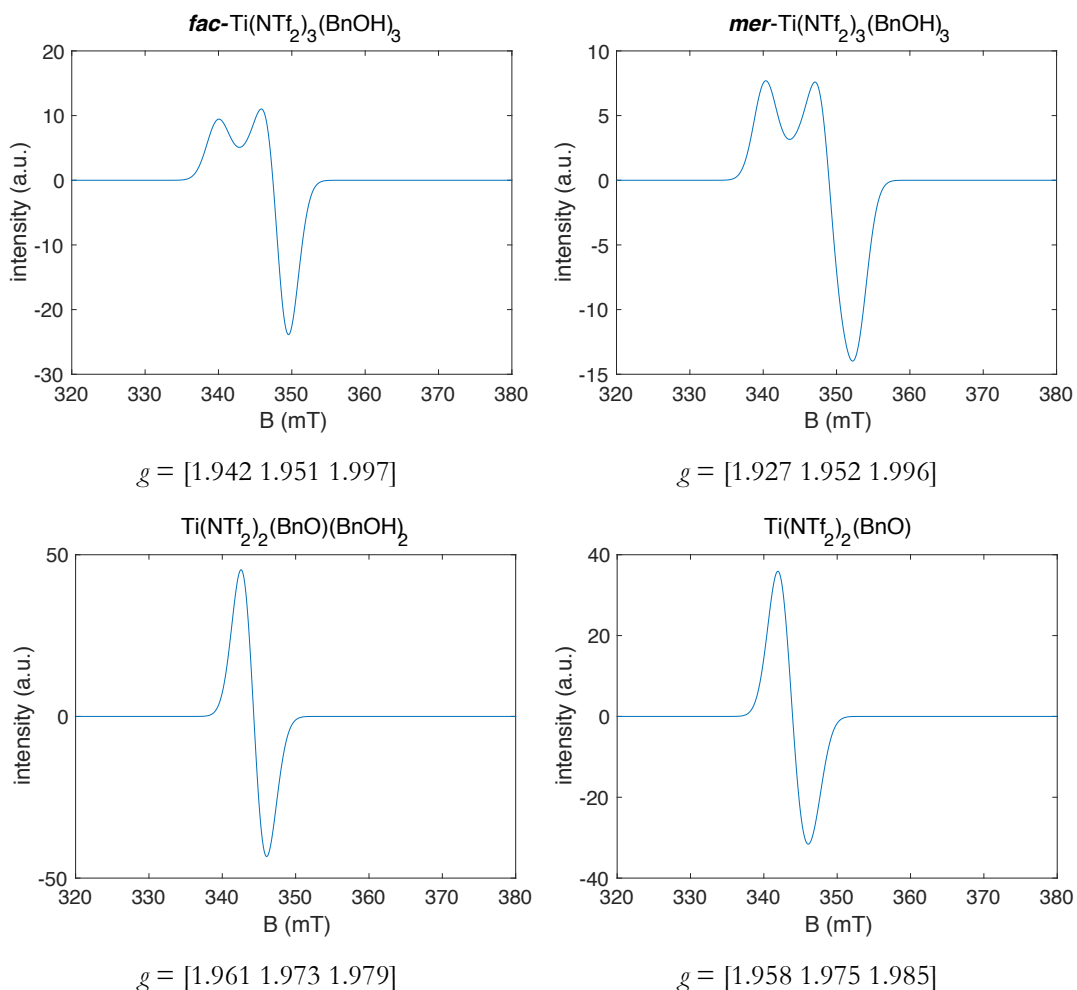


Figure 71 - DFT-predicted EPR spectra of Ti(III) triflimide species generated upon coordination of BnOH.

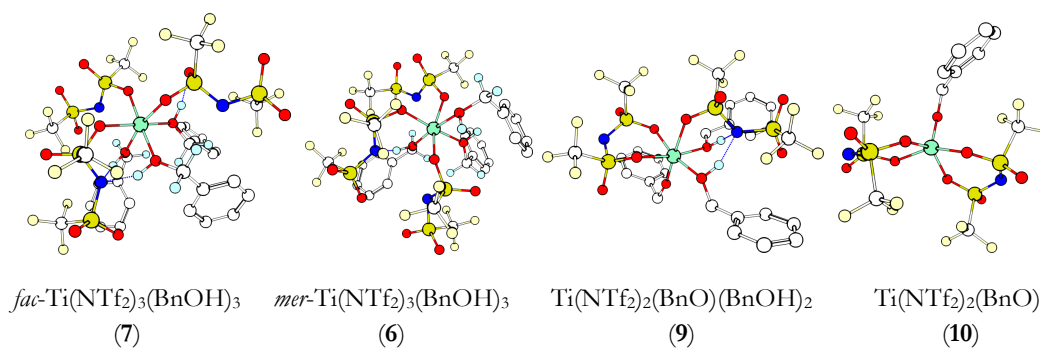


Figure 72 - DFT-predicted 3D structures of Ti(III) triflimide species generated upon coordination of BnOH.

Upon addition of aniline on **4**, a dark blue precipitate was formed that quickly discolored, most likely due to oxidation by oxygen traces, yielding a yellowish solid. The corresponding EPR spectrum of the blue precipitate displayed a sharp resonance $g = [1.966\ 1.940\ 1.903]$ (**Figure 73**), while the mixture becomes EPR silent when turning yellowish.

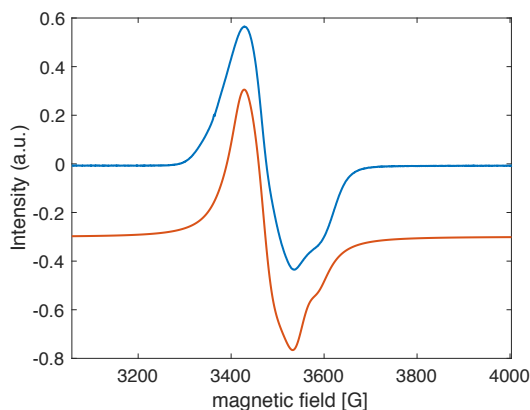


Figure 73 - Experimental (blue) and simulated (orange) EPR spectra of **4** in toluene, in the presence of aniline (10%, $g = 1.990\ 1.880\ 1.880$; 90%, $g = 1.966\ 1.940\ 1.903$).

The formation of a solid upon addition of aniline indicates that an ionic salt is formed through triflimide displacement by aniline. This result was confirmed by addition of aniline on $\text{TiCl}_3(\text{THF})_3$, showing a very similar spectrum which confirms that both chlorides and triflimides are displaced by aniline. When the experiment was repeated in water, a similar signal was obtained for the dark-blue soluble complex. A similar species was also obtained in the presence of BnOH which confirms the poisoning role of aniline (**Figure 74**). The formed species are prone to be oxidized, probably due to the electron-donation ability of aniline.

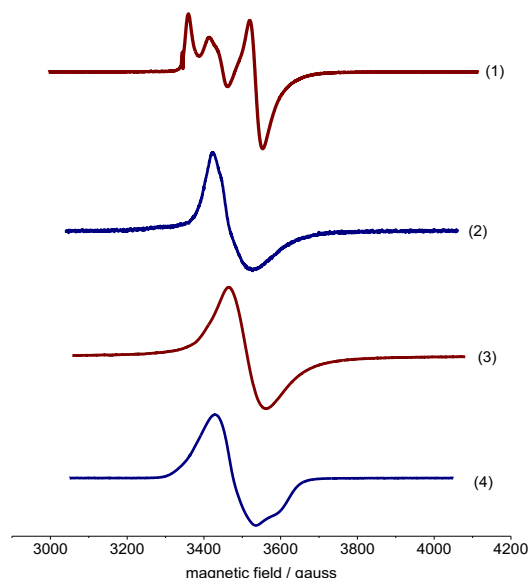


Figure 74 – EPR spectra of **4** in the presence of 1) BnOH (40 equiv) in toluene; aniline (10 equiv) 2) in toluene, 3) in water; 4) with BnOH (40 equiv) and aniline in toluene.

Indeed $\text{Ti}(\text{NTf}_2)_3(\text{aniline})_3$ (**11-12**) should have an EPR signature close to that of $\text{Ti}(\text{NTf}_2)_3(\text{BnOH})_3$ (**Table 35, Figure 75**). Also $[\text{Ti}(\text{NTf}_2)_2(\text{aniline})_2]^+$ and $[\text{Ti}(\text{NTf}_2)_2(\text{aniline})_4]^+$ (**13-14**) are expected to feature similar Jahn-Teller splitted spectra. Both $\text{Ti}(\text{aniline})_4^{3+}$ and $\text{Ti}(\text{aniline})_6^{3+}$ (**15-16**) were optimized and $\text{Ti}(\text{aniline})_6^{3+}$ displayed a compatible isotropic g -tensors (**Table 35**).

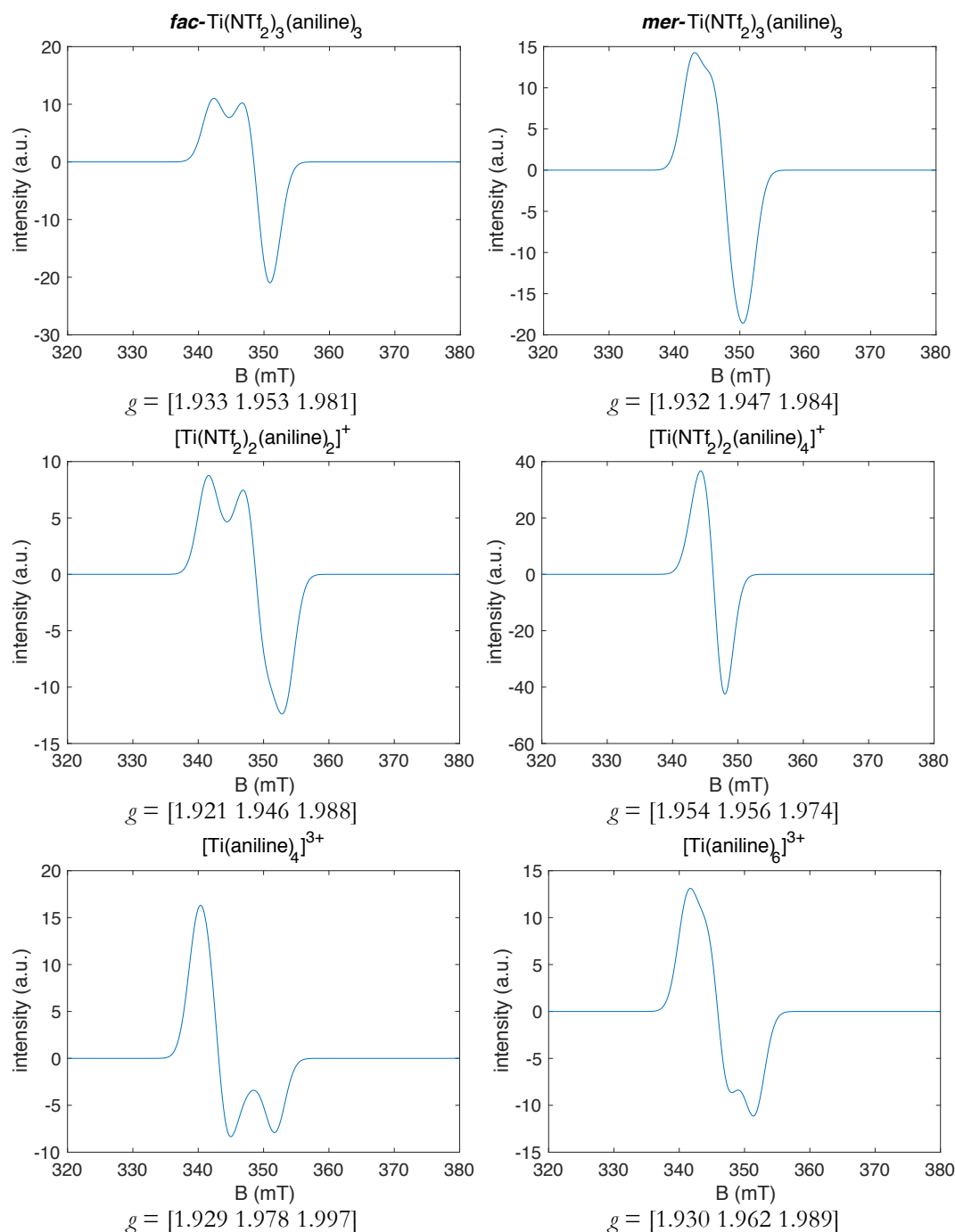


Figure 75 - DFT-predicted EPR spectra of Ti(III) triflimide species generated upon coordination of aniline.

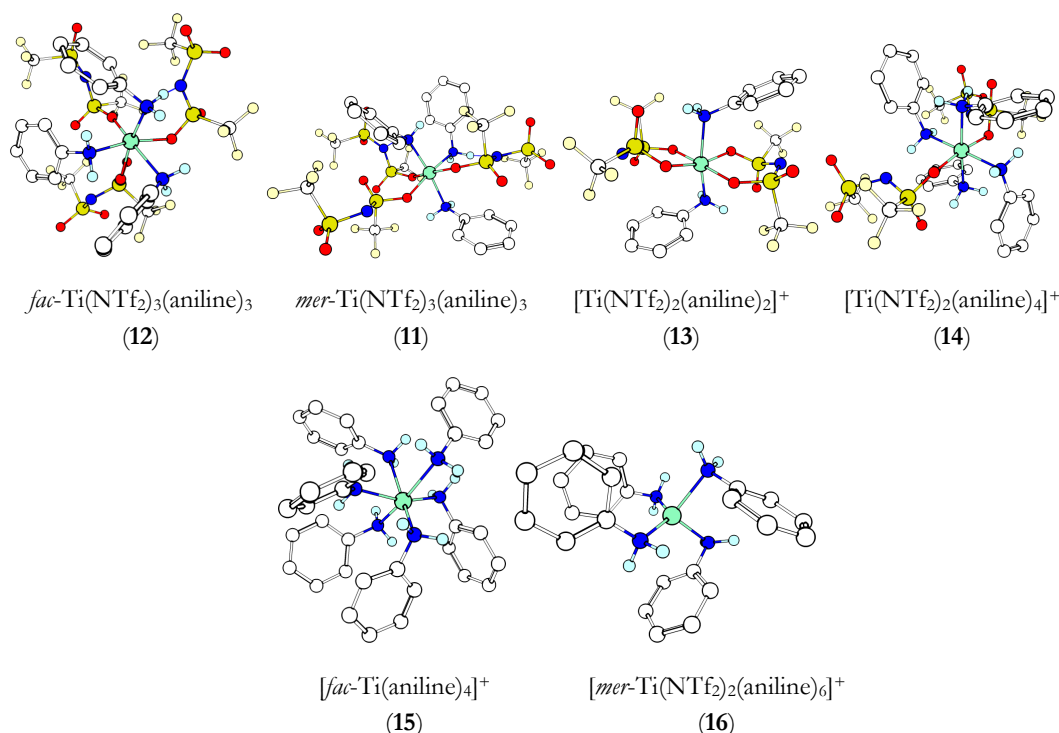


Figure 76 - DFT-predicted structures of Ti(III) triflimide species generated upon coordination of aniline.

To gain insight into the structure of the **4** in the presence of bpy, the $\text{TiCl}_3(\text{THF})_3/\text{bpy}$ system was first studied. Upon addition of bpy (2 equiv) on $\text{TiCl}_3(\text{THF})_3$ in toluene a blue salt precipitated (**Figure 77**). Two species were identified by EPR featuring low g components 84%, $g = [1.973 \ 1.901 \ 1.785]$; 16%, $g = [1.945 \ 1.940 \ 1.825]$. $\text{Ti}(\text{bpy})_3^{3+}$ (**18**) and $\text{Ti}(\text{bpy})_2^{3+}$ (**17**) were predicted to have expanded g -tensors ($\Delta g = 0.12$ and 0.17 , respectively, **Table 35**, **Figure 78**). Thus, the high field part of the signal ($g = 1.8$, **Figure 77**) could be attributed to such unsaturated Ti(III) species.

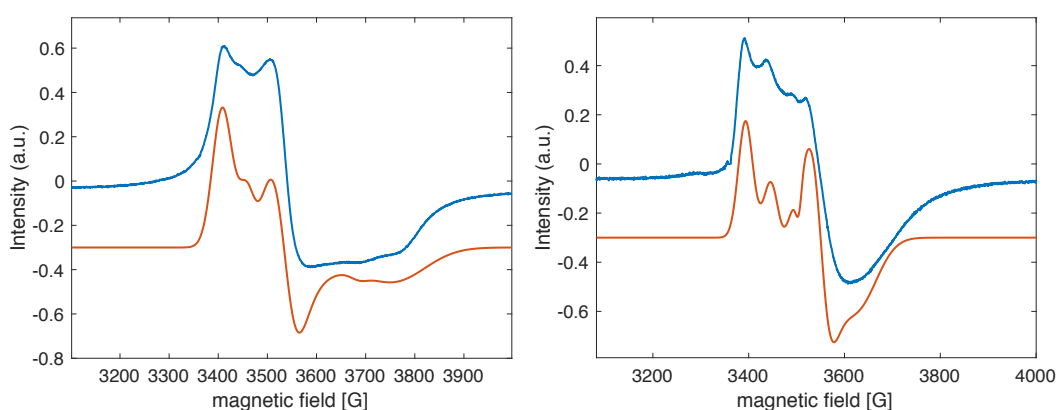


Figure 77 - Experimental (blue) and simulated (orange) EPR spectra of $\text{TiCl}_3(\text{THF})_3$ in toluene, **Left**: in the presence of 2 equiv of bpy (84%, $g = [1.973 \ 1.901 \ 1.785]$; 16%, $g = [1.945 \ 1.94 \ 1.825]$); **Right**: bpy (2 equiv) and BnOH (20 equiv) (75%, $g = [1.982 \ 1.893 \ 1.85]$, 25%, $g = [1.955 \ 1.943 \ 1.92]$).

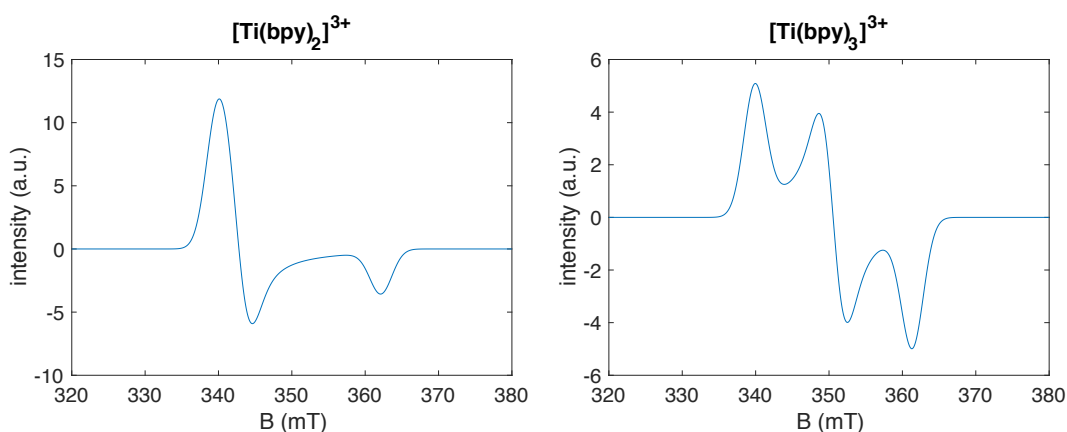


Figure 78 - DFT-predicted EPR spectra of cationic Ti(III) triflimide species generated upon coordination of bpy.

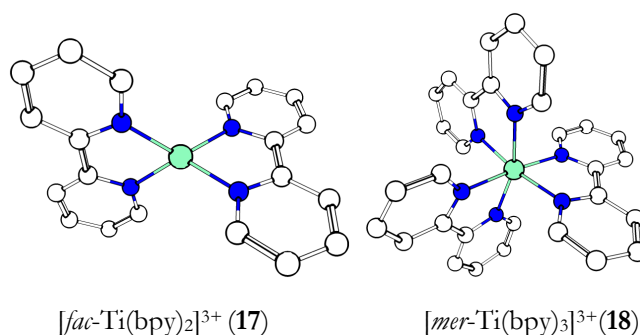


Figure 79 - DFT-predicted 3D structures of cationic Ti(III) triflimide species generated upon coordination of bpy.

This hypothesis was confirmed by addition of BnOH, showing the disappearance of the signal at $g = 1.8$ (**Figure 77**). We postulated that $[\text{Ti}(\text{bpy})_2(\text{BnOH})_2]^{3+}$ (**18**) was formed: a much more symmetrical signal was indeed foreseen for this compound (**Table 35**, **Figure 80**).

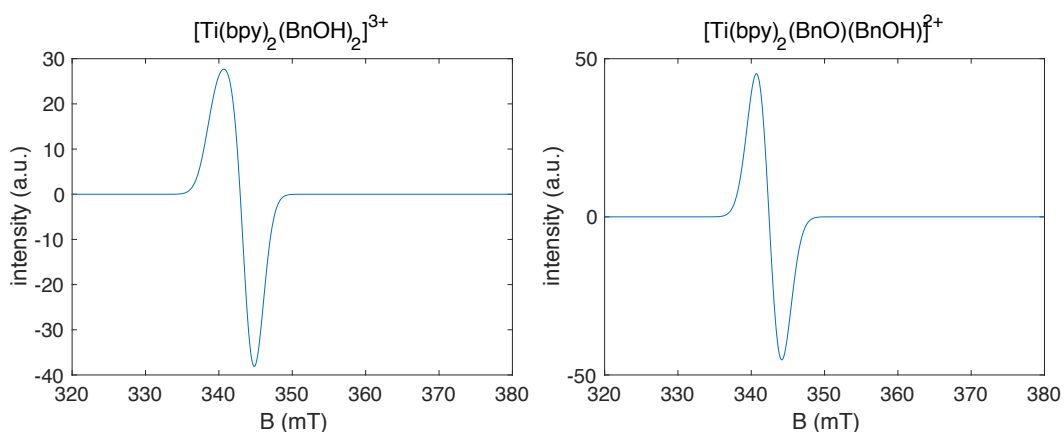


Figure 80 - DFT-predicted EPR spectra of $[\text{Ti}(\text{bpy})_2(\text{BnOH})_2]^{3+}$.

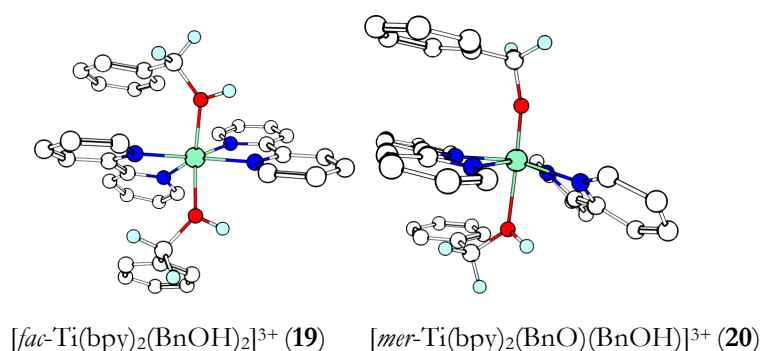


Figure 81 - DFT-predicted 3D structures of cationic Ti(III) triflimide species generated upon coordination of bpy and BnOH.

To mimic the experimental conditions, a solution of **4** in the presence of BnOH (20 equiv, for solubilization) was prepared and increasing amounts of bpy were added on it (**Figure 82**). A blue complex precipitated.

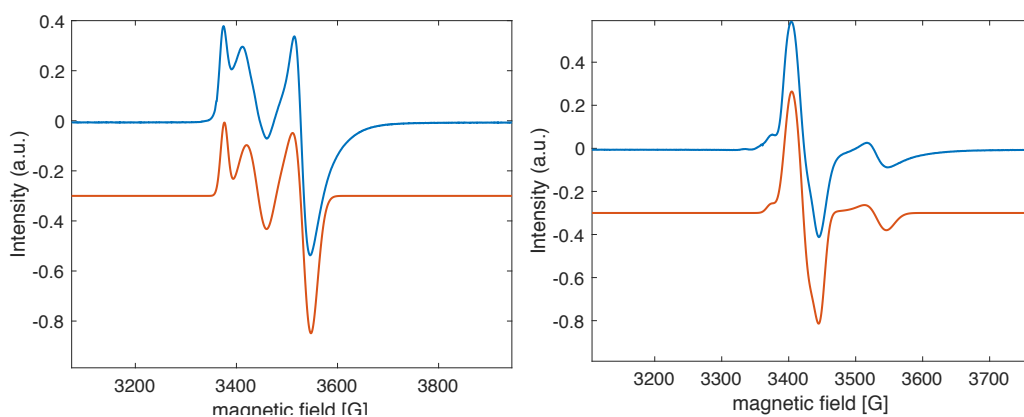


Figure 82 - Experimental (blue) and simulated (orange) EPR spectra of **4** in toluene, in the presence of BnOH (20 equiv), **Left**: with bpy (2 equiv; 70%, $g = 1.9925$ 1.901 1.901, 30%, $g = 1.97$ 1.955 1.942); **Right**: with bpy (4 equiv, 10%, $g = 1.9935$ 1.901 1.901, 90%, $g = 1.9778$ 1.966 1.9515).

This complex was characterized by a sharp signal at $g = [1.978$ 1.966 1.952] (**Figure 82**), which cannot be attributed to $\text{Ti}(\text{bpy})_3^{3+}$ (**18**). On the contrary, the formation of $[\text{Ti}(\text{bpy})_2(\text{BnOH})_2]^{3+}$ (**19**) or $[\text{Ti}(\text{bpy})_2(\text{BnO})(\text{BnOH})]^{2+}$ (**20**) would be compatible with the data. We propose that this **19** or **20** is an active species for amination. Bipyridine could thus help: i) improve the catalyst solubility, ii) avoid catalyst deactivation by aniline (and or hydrolysis), and iii) form a more active cationic species (**19-20**).

The main conclusions of our EPR study are reported on **Figure 83**. In the presence of BnOH, Ti(III) triflimide forms a mixture of $mer\text{-Ti}(\text{NTf}_2)_3(\text{BnOH})_3$ (**6**) and partially deprotonated $\text{Ti}(\text{NTf}_2)_2(\text{BnO})(\text{BnOH})_2$ (**9**). Aniline can also coordinate and is able to displace triflimides from Ti(III) to form inactive ion-pair, likely, $[\text{Ti}(\text{aniline})_6]^{3+}$, 3 NTf_2^- (**16**). Finally, bpy is also able to displace triflimides from Ti(III), but in the presence of excess of BnOH, mixed species such as $[\text{Ti}(\text{bpy})_2(\text{BnOH})_2]^{3+}$ (**19**) are formed and they seem to be highly active catalysts for amination.

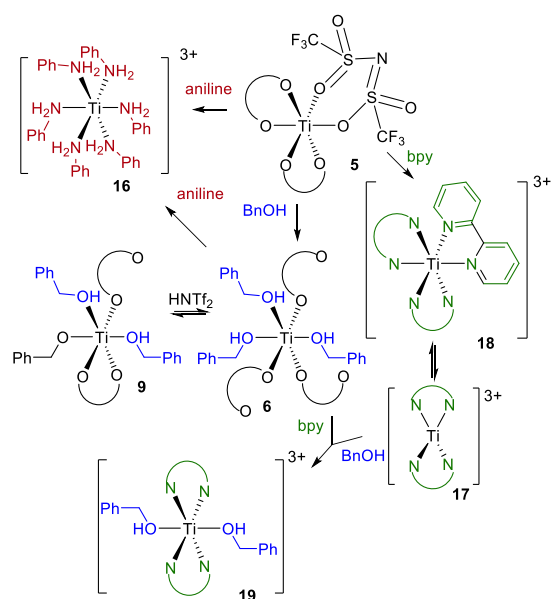


Figure 83 - Most likely formed Ti(III)-complexes resulting from the coordination of BnOH, aniline and bpy.

3.10. Conclusions

In summary, we developed an “*in silico* Beckett-Childs method” based on the DFT-predicted partial charge transferred from phosphine oxide (OPH_3) to a Lewis acid. This descriptor allowed us to predict the catalytic behavior of metal triflate and triflimide salts for the direct amination reaction of benzyl alcohol. This study led us to report the first synthesis of Ti triflimide complex which proved to be a promising catalyst. The exact nature of this catalyst is complex as it is a mixture of Ti(III) and Ti(IV) triflimides. Our results highlight the important impact of poorly coordinating anions, such as triflimides, as well as of Ti(III) on the catalytic activity for the amination reaction. This combination proved to be efficient for the nucleophilic substitution of activated alcohols.

We hope that the settlement of a handy theoretical descriptor of Lewis acidity, readily obtained from a single structure optimization will stand out in the future to rank Lewis acids for catalyzed reactions and that triflimide will pave the way for future breakthrough developments in catalysis.

4. Iron Triflate Salts for Oxidation of Cyclohexane

Recently, iron triflates, i.e. Fe^{II}(OTf)₂ and Fe^{III}(OTf)₃, have been reported as active catalysts in poorly-coordinating solvents for a variety of Lewis-acid catalyzed reactions, including imination of sulfoxides,²⁶¹ aziridination of enol silyl ethers,²⁶² hydroaddition to unsaturated C-C bonds,²⁶³ etherification and transesterification of alcohols,²⁶⁴ and glycosylation of sugar derivatives.²⁶⁵ Despite the potentials of iron triflates for C-H activation in C-N,²⁶⁶ C-C,²⁶⁷ and C-X (X = F, Cl, D)²⁶⁸ coupling reactions, few reports are available on oxidation reactions.²⁶⁹

4.1. Industrial Synthesis of Cyclohexanone and Cyclohexol

The oxidation of cyclohexane (CyH) to cyclohexanol (CyOH) and cyclohexanone (CyONE), also termed as Ketone-Alcohol (KA) oil, is a well-known industrial process for the production of adipic acid.²⁷⁰ This process comprises two consecutive oxidation steps (**Scheme 52**): (i) non-catalytic autooxidation of CyH by O₂ yielding cyclohexyl hydroperoxide (CyHP), and (ii) deperoxidation of CyHP to KA oil catalyzed by a transition metal, typically a homogeneous cobalt catalyst, under a radical chain mechanism.²⁷¹ The process is conducted at very low CyH conversion (~5%) with a CyHP selectivity of 60-70% in the first step.²⁷² The industrial challenge is to increase the conversion and KA selectivity while keeping the CyHP concentration as low

²⁶¹ O. G. Mancheño, J. Dallimore, A. Plant, C. Bolm, *Org. Lett.*, **2009**, *11*, 2429-2432.

²⁶² M. Nakanishi, A.-F. Salit, C. Bolm, *Adv. Synth. Catal.*, **2008**, *350*, 1835-1840; A. C. Mayer, A.-F. Salit, C. Bolm, *Chem. Commun.*, **2008**, 5975-5977.

²⁶³ J.-C. Choi, K. Kohno, D. Masuda, H. Yasuda, T. Sakakura, *Chem. Commun.*, **2008**, 777-779; J. R. Cabrero-Antonino, A. Leyva-Pérez, A. Corma, *Adv. Synth. Catal.*, **2012**, *354*, 678-687; *Chem. Eur. J.*, **2012**, *18*, 11107-11114; *Chem. Eur. J.*, **2013**, *19*, 8627-8633.

²⁶⁴ P. K. Sahoo, S. S. Gawali, C. Gunanathan, *ACS Omega*, **2018**, *3*, 124-136.

²⁶⁵ A. Stévenin, F.-D. Boyer, J.-M. Beau, *Eur. J. Org. Chem.*, **2012**, 1699-1702; A. Xolin, S. Norsikian, F.-D. Boyer, J.-M. Beau, *Eur. J. Org. Chem.*, **2016**, 3408-3418.

²⁶⁶ J. Bonnamour, C. Bolm, *Org. Lett.*, **2011**, *13*, 2012-2014; M. A. B. Mostafa, E. D. D. Calder, S. T. Racys, A. Sutherland, *Chem. Eur. J.*, **2017**, *23*, 1044-1047.

²⁶⁷ C. Yao, B. Qin, H. Zhang, J. Lu, D. Wang, S. Tu, *RSC Adv.*, **2012**, *2*, 3759-3764.

²⁶⁸ B. J. Groendyke, D. I. AbuSalim, S. P. Cook, *J. Am. Chem. Soc.*, **2016**, *138*, 12771-12774; M. A. B. Mostafa, R. M. Bowley, D. T. Racys, M. C. Henry, A. Sutherland, *J. Org. Chem.*, **2017**, *82*, 7529-7537; D. T. Racys, C. E. Warrilow, S. L. Pimlott, A. Sutherland, *Org. Lett.*, **2015**, *17*, 4782-4785.

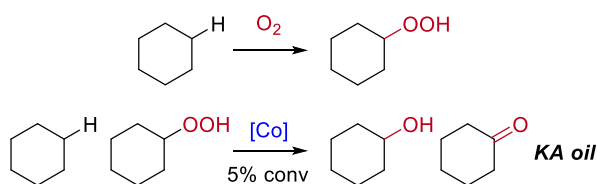
²⁶⁹ G. J. P. Britovsek, J. England, S. K. Spitzmesser, A. J. P. White, D. J. Williams, *Dalton Trans.*, **2005**, 945-955; G. J. P. Britovsek, J. England, A. J. P. White, *Dalton Trans.*, **2006**, 1399-1408; R. Mas-Ballesté, M. Costas, T. van den Berg, L. Que Jr, *Chem. Eur. J.*, **2006**, *12*, 7489-7500; J. England, R. Gondhia, L. Bigorra-Lopez, A. R. Petersen, A. J. P. White, G. J. P. Britovsek, *Dalton Trans.*, **2009**, 5319-5334; M. Lenze, E. B. Bauer, *J. Mol. Catal. A: Chem.*, **2009**, *309*, 117-123.

²⁷⁰ M. T. Musser, *Cyclohexanol and Cyclohexanone*, In: *Ullmann's Encyclopedia of Industrial Chemistry*, **2002** (2nd ed.), Wiley.

²⁷¹ F. Cavani, G. Strukul, (Ed. B. Cornils, W. A. Herrmann, M. Beller, R. Paciello) *Radical Chain Oxidations*, In: *Applied Homogeneous Catalysis with Organometallic Compounds*, Wiley, **2018** (3rd. edition), pp. 510-513.

²⁷² I. Hermans, P. A. Jacobs, J. Peeters, *Chem. Eur. J.*, **2006**, *12*, 4229-4240.

as possible using a clean and safe route. In this context, a fast and selective catalytic pathway using a non-toxic metal would be desirable.



Scheme 52 - Industrial process for the oxidation to CyH to KA oil.

4.2. Iron Catalyzed Oxidation

High-valent iron-oxo complexes (*e.g.*, cytochrome P450) are known to efficiently catalyze oxidation reactions in living systems.²⁷³ Iron-oxo systems have been extended to non-heme bio-inspired catalysts based on Fe centers,²⁷⁴ and to mononuclear iron complexes.²⁷⁵ The most studied and simplest non-heme iron system relies on the so-called Fenton reagent consisting of an aqueous solution of hydrogen peroxide and Fe salt.²⁷⁶ This reagent has been widely used in the oxidation of organic pollutants in liquid waste treatment for environmental applications, as it generates very active and non-selective OH[•] radicals.²⁷⁷ The search for higher selectivity in partial oxidation reactions has led to the development of alternative catalytic systems involving highly oxidized iron-oxo intermediates, Fe(IV) or Fe(V).²⁷⁸

A well-known application of iron complexes as catalysts for CyH oxidation is the pioneering work of Barton, using an iron catalyst combined with metallic zinc and oxygen as oxidant.²⁷⁹ This chemistry was improved by replacing Fe(II)/Zn⁰/O₂ by Fe(II)/superoxide (as KO₂). Using an analogous system based on Fe(III)/TBHP (TBHP = *t*-butyl hydroperoxide) relying on (tris(trimethylacetate))iron(III) [Fe(tma)₃] and (tris(1,1,1,2,2,3,3-heptafluoro-7,7-dimethyl-4,6-

²⁷³ B. Meunier, S. P. de Visser, S. Shaik, *Chem. Rev.* **2004**, *104*, 3947-3980; S. P. de Visser, D. Kumar, S. Shaik, *J. Inorg. Biochem.* **2004**, *98*, 1183-1193.

²⁷⁴ A. L. Feig, S. J. Lippard, *Chem. Rev.* **1994**, *94*, 759-805; R. Mas-Ballesté, M. Costas, T. van den Berg, L. Que, *Chem. Eur. J.* **2006**, *12*, 7489-7500; C. Nguyen, R. J. Guajardo, P. K. Mascharak, *Inorg. Chem.* **1996**, *35*, 6273-6281; C.-W. Chiang, S. T. Kleespies, H. D. Stout, K. K. Meier, P.-Y. Li, E. L. Bominaar, L. Que, E. Münck, W.-Z. Lee, *J. Am. Chem. Soc.* **2014**, *136*, 10846-10849.

²⁷⁵ N. M. F. Carvalho, A. Horn Jr, O. A. C. Antunes, *Appl. Catal. A: Gen.* **2006**, *305*, 140-145.

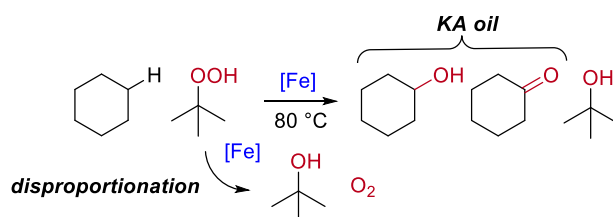
²⁷⁶ H. J. H. Fenton, *J. Chem. Soc., Trans.* **1894**, *65*, 899-910.

²⁷⁷ M. Barbeni, C. Minero, E. Pelizzetti, E. Borgarello, N. Serpone, *Chemosphere* **1987**, *16*, 2225-2237; D. L. Sedlak, A. W. Andren, *Environ. Sci. Technol.* **1991**, *25*, 777-782; I. Casero, D. Sicilia, S. Rubio, D. Pérez-Bendito, *Water Research* **1997**, *31*, 1985-1995; P. L. Huston, J. J. Pignatello, *Water Research* **1999**, *33*, 1238-1246; S. Nam, V. Renganathan, P. G. Tratnyek, *Chemosphere* **2001**, *45*, 59-65; K. Ikehata, M. G. El-Din, *J. Environ. Eng. Sci.* **2006**, *5*, 81-135.

²⁷⁸ W. C. Bray, M. H. Gorin, *J. Am. Chem. Soc.* **1932**, *54*, 2124-2125; W. G. Barb, J. H. Baxendale, P. George, K. R. Hargrave, *Trans. Faraday Soc.* **1951**, *47*, 462-500; P. Mignon, M. Pera-Titus, H. Chermette, *Phys. Chem. Chem. Phys.* **2012**, *14*, 3766-3774.

²⁷⁹ D. H. R. Barton, D. Doller, *Acc. Chem. Res.* **1992**, *25*, 504; D. H. R. Barton, *Tetrahedron* **1998**, *54*, 5805-5817.

octanodionate)iron(III) [Fe(fod)₃], Schuchardt *et al* reported a selectivity of 91% at 11% conversion for CyH oxidation.²⁸⁰ The produced adipic acid (AA) deactivated the catalyst.



Scheme 53 - Oxidation of neat CyH by TBHP catalyzed by iron catalysts.

Herein we report an unprecedented high catalytic activity of Fe^{III}(OTf)₃ over a series of iron-based catalysts for the oxidation of neat CyH towards CyOH and CyONE (KA oil) using TBHP as oxidant in the absence of ligand (**Scheme 53**). The iron activity and selectivity was characterized both in terms of TBHP conversion and KA yield, respectively, as well as the turnover number (TON) after 60 min of reaction and turnover frequency at time zero (TOF₀). Fe^{III}(OTf)₃ behaved as a precursor of the active iron species for CyH oxidation. We provide detailed insight into the structure of the catalyst under the reaction conditions by combining electron paramagnetic resonance (EPR) and DFT calculations.

4.3. Cyclohexane oxidation using TBHP as oxidizing agent

The experimental part of this section (4.3) has been performed by Yu-Ting Zheng under the supervision of Dr Wenjuan Zhou.

Screening of Fe complexes. The catalytic activity of a series of Fe complexes was first investigated using CyH as reactant and solvent and TBHP as an oxidant at 80 °C under reflux (**Scheme 53**).

Table 36 - Conversion of CyH and TBHP, KA selectivity and yield, K/A ratio and TONs as a function of the Fe^{III}(OTf)₃ concentration.

Complex ^b	CyH conv (%)	TBHP conv (%)	KA sel ^c (%)	KA yield (%)	A/K ^d	TON ^e
Fe ^{III} (OTf) ₃	1.9	73	35	25	6.4	1175
Fe ^{II} (OTf) ₂	1.2	74	21	16	3.3	765
Fe ^{III} (NTf ₂) ₃	1.0	69	23	16	3.1	651
Cl-Fe ^{III} TPP	0.9	69	17	12	2.8	574
Fe ^{III} (OTs) ₃	0.7	57	19	11	3.3	455
Fe ^{III} Cl ₃	0.4	30	16	5	5.5	231

^{a)} Reaction conditions: 80 °C, CyH (4.0 g) containing TBHP (7.5 wt%), 60 min.

^{b)} TPP: tetraphenylporphyrine, OTs: OSO₂Tol.

A 7.5 wt% (0.65 mM) solution of TBHP in CyH was used. The products and reactants were analysed after 60 min (**Table 36**). Among the different complexes, the least soluble were

²⁸⁰ U. Schuchardt, R. Pereira, M. C. Rufo, *J. Mol. Catal. A: Chem.* **1998**, *135*, 257-262.

$\text{Fe}^{\text{III}}(\text{OTf})_3$ and $\text{Fe}^{\text{III}}\text{Cl}_3$ with a solubility of 0.59 mM and 0.24 mM at 20 °C and 80 °C, respectively. In light of these results, a Fe concentration of 0.14 mM (10 ppm) was chosen for comparing the catalytic activity of the different complexes. The most active complexes for CyH oxidation were also found to be the most selective towards KA oil (**Table 36**) by minimizing undesired TBHP disproportionation to *t*-butyl alcohol and O_2 (**Scheme 53**). this by-path was favoured at high concentration.

Among the different Fe complexes, $\text{Fe}^{\text{III}}(\text{OTf})_3$ exhibited the highest TBHP conversion and KA yield with values of 81% and 24%, respectively. The TON towards KA formation after 60 min was the highest with a value of *ca.* 1200. The TON decreased in the sense: $\text{Fe}^{\text{III}}(\text{OTf})_3 > \text{Fe}^{\text{II}}(\text{OTf})_2 > \text{Fe}^{\text{II}}(\text{NTf}_2)_3 > \text{Cl-Fe}^{\text{III}}\text{TPP} > \text{Fe}^{\text{III}}(\text{OTf})_3 > \text{Fe}^{\text{III}}\text{Cl}_3$. Noteworthy, the reaction conditions tested, $\text{Fe}^{\text{II}}(\text{OTf})_2$ was slightly less active than $\text{Fe}^{\text{III}}(\text{OTf})_3$. This result is surprising, as Fe(II) ions would readily transform into Fe(III) in oxidative conditions.

Effect of the $\text{Fe}^{\text{III}}(\text{OTf})_3$ concentration. Increasing the Fe concentration (**Table 37**) from 0.014 mM (1 ppm) to 0.56 mM (40 ppm) clearly promoted the CyH and TBHP conversion at the expense of the TON. A $\text{Fe}^{\text{III}}(\text{OTf})_3$ concentration higher than 0.14 mM (10 ppm Fe) was detrimental to the catalytic performance. The highest TON at 60 min (about 2600) was obtained at very low KA yield (5.7%) and at the lowest $\text{Fe}^{\text{III}}(\text{OTf})_3$ concentration (0.014 mM).

Table 37 - Conversion of CyH and TBHP, KA selectivity and yield, K/A ratio and TOFs as a function of the $\text{Fe}^{\text{III}}(\text{OTf})_3$ concentration.^a

C_{Fe} (mM)	CyH conv (%)	TBHP conv (%)	KA sel (%)	KA yield (%)	A/ K	TON _d
0.014	0.43	6.6	86	5.7	82	2658
0.070	1.4	52	34	18	8.6	1670
0.14	1.8	81	29	24	4.0	1140
0.56	2.1	88	30	27	2.3	310
1.95	2.3	96	32	30	2.1	101

^a Reaction conditions: 80 °C, CyH (4.0 g) containing TBHP (7.5 wt%), 60 min.

Besides, the alcohol-to-ketone molar ratio (A/K) decreased at higher Fe concentration with a value of 4.0 at 0.14 mM Fe.

Effect of the reaction temperature. The effect of the reaction temperature was studied in the range 40-100 °C using 0.14 mM $\text{Fe}^{\text{III}}(\text{OTf})_3$ (10 ppm Fe) ensuring high activity and solubility in CyH (

Table 388). TBHP conversion into KA was favored at higher temperature at the expense of disproportionation into *t*-butyl alcohol and O_2 with the product being enriched in CyOH. The high selectivity to CyOH observed at low temperatures (about 40 °C), confirms that CyONE is a secondary oxidation product of CyH.

Table 38 - Conversion of CyH and TBHP, KA selectivity and yield, K/A ratio and TOFs as a function of the reaction temperature at 0.14 mM Fe^{III}(OTf)₃ (10 ppm Fe).^a

T (°C)	CyH conv (%)	TBHP conv (%)	KA sel ^b (%)	KA yield (%)	A/K ^c	TON ^d
40	0.4	30	16	5	5.5	231
45	0.7	57	19	11	3.3	455
50	0.9	69	17	12	2.8	574
55	1.0	69	23	16	3.1	651
60	1.2	74	21	16	3.3	765
65	1.3	78	25	19	3.6	811
70	1.5	80	28	22	3.6	922
80	1.8	81	29	24	4.0	1140
100	1.9	73	35	25	6.4	1175

^a) Reaction conditions: 80 °C, CyH (4.0 g) containing TBHP (7.5 wt%), 60 min

Reactants and products evolution during the reaction. The reaction kinetics was measured during the first 20 min of reaction on Fe^{III}(OTf)₃ and Fe^{III}(NTf₂)₃ in the conditions defined above (**Figure 84**). KA oil formation proceeded rapidly during the first 15 min with a decrease of the K/A ratio. Then, no evolution occurred, even if TBHP was not fully consumed. At first sight, this observation suggests partial catalyst deactivation, which could be due to the KA mixture, or undesirable by-products. Indeed, traces of AA were detected by LC-MS. It is known that AA combined with water might deactivate Fe sites.²⁸¹

²⁸¹ C. Nguyen, R. J. Guajardo, P. K. Mascharak, *Inorg. Chem.* **1996**, *35*, 6273-6281; U. Schuchardt, R. Pereira, M. C. Rufo, *J. Mol. Catal. A: Chem.* **1998**, *135*, 257-262.

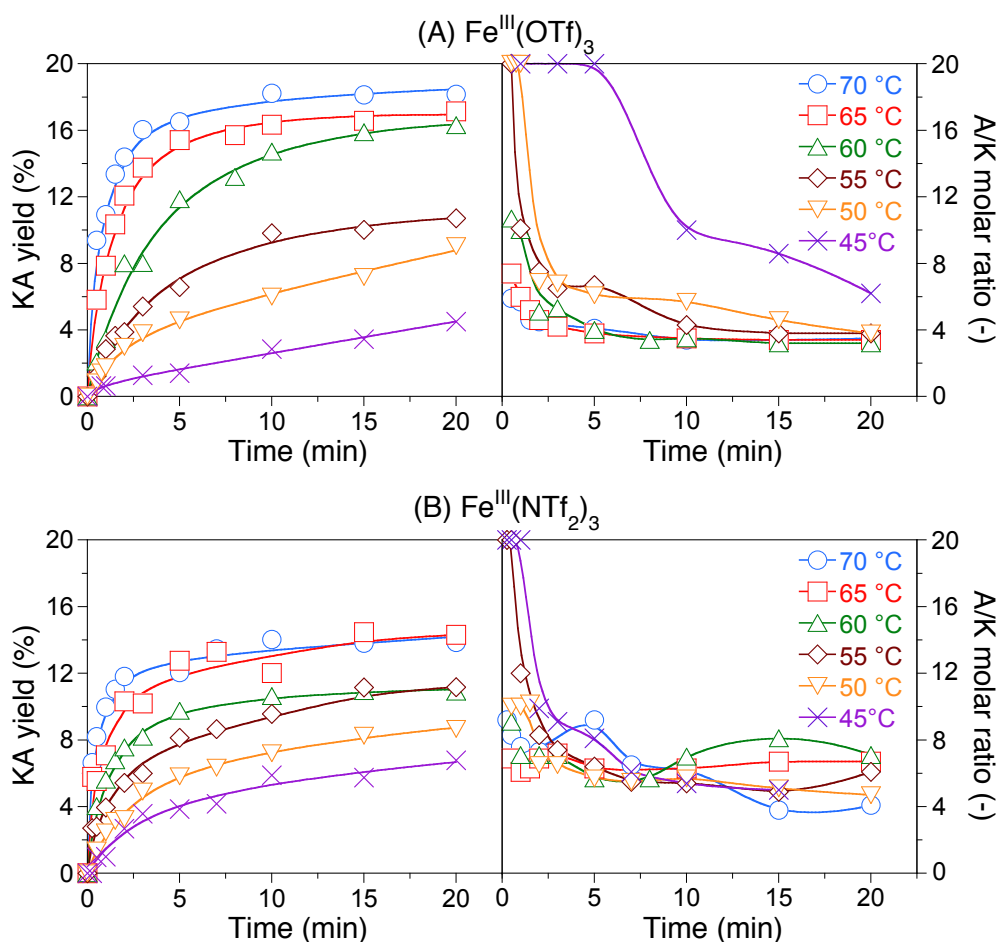


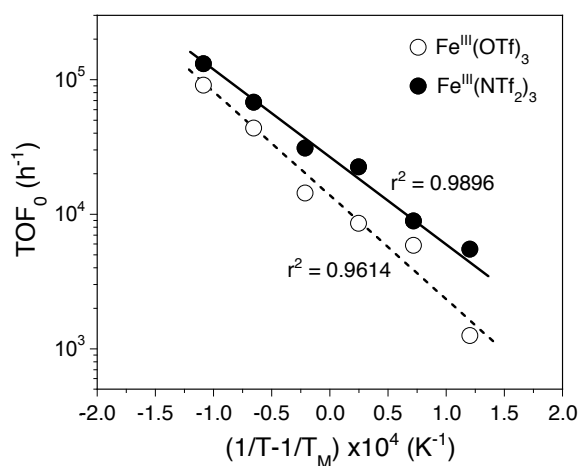
Figure 84 - Evolution of KA yield and the A/K molar ratio with time in CyH oxidation catalyzed by (A) $\text{Fe}^{\text{III}}(\text{OTf})_3$ (top) and (B) $\text{Fe}^{\text{III}}(\text{NTf}_2)_3$ with TBHP as oxidant. Reaction conditions: 45-70 °C, 0.14 mM catalyst (10 ppm Fe), 4 g of CyH containing 7.5 wt% (0.65 mM) TBHP, 0-20 min.

To gain more insight into the mechanism of Fe deactivation, CyOH, CyONE and AA were added to the reaction media at the beginning of the reaction. CyOH was able to enhance the catalytic activity, while CyONE and AA exerted the opposite effect (**Table 39**). Accordingly, the KA mixture produced along the reaction is expected to behave in a complex manner as a function of the A/K selectivity.

The reaction rate (i.e. TOF_0) was measured at time $t = 0$ in the temperature range 45-70 °C for $\text{Fe}^{\text{III}}(\text{OTf})_3$ and $\text{Fe}^{\text{III}}(\text{NTf}_2)_3$. In both cases, very high TOFs were obtained with values about 14,000 h^{-1} and 31,000 h^{-1} , respectively, at 60 °C. The activation energy measured from the Arrhenius plots of $\ln(\text{TOF}_0)$ vs $1/T$ was 145 ± 12 kJ/mol for $\text{Fe}^{\text{III}}(\text{OTf})_3$ and 115 ± 6 kJ/mol for $\text{Fe}^{\text{III}}(\text{NTf}_2)_3$ (**Figure 85**). At all temperatures, the TOF_0 was higher for $\text{Fe}^{\text{III}}(\text{NTf}_2)_3$. However, higher KA yields as well as higher TON at 60 min were achieved for $\text{Fe}^{\text{III}}(\text{OTf})_3$ (**Table 36**). This observation can be explained by a faster deactivation of $\text{Fe}^{\text{III}}(\text{NTf}_2)_3$ during the reaction.

Table 39 - Evolution of the KA yield upon initial addition CyOH, CyONE and AA.^a

Additive	KA	Δ KA
	Yield %	Yield % ^c
-	25	0
CyOH (0.212 mM)	28	+3
CyONE (0.084 mM)	21	-4
AA (0.095 mM)	16	-9
CyOH (0.198 mM) + CyONE (0.045 mM)	22	-2
CyOH (0.220 mM) + AA (0.080 mM)	12	-13
CyONE (0.059 mM) + AA (0.091 mM)	9	-16
CyOH (0.195 mM) + CyONE (0.049 mM) + AA (0.078 mM)	8	-17

**Figure 85** - Arrhenius plots of the TOF₀ for Fe^{III}(OTf)₃ and Fe^{III}(NTf₂)₃ precursors. TM refers to the mean temperature of the series (T_M = 330.7 K).

4.4. EPR investigation

Fe(III) ions having unpaired electrons were investigated by EPR, a sensitive method that is well adapted to very low Fe concentration. In frozen solution, the EPR g -tensor component of Fe(III) can be measured in both low and high spin states providing information about the symmetry and coordination sphere of the species and their evolution during the reaction. In the case of high spin Fe(III), one should also consider the contribution of the zero-field-splitting (ZFS), which can be assessed by the so-called the D tensor. This tensor includes two components (D and E), accounting for the intensity and anisotropy of the interaction.²⁸² As we shall see below, Fe(II) ions that are also paramagnetic are unfortunately silent in conventional X-band (9.6 GHz) spectrometers. Moreover, this technique is useful for detecting the presence of organic radicals.

Structure of Fe(OTf)₃. A CyH solution of Fe^{III}(OTf)₃ exhibited an EPR signal at $g = 2.02$ (**Figure 86**). Since the triflate ion is usually described as a weak ligand, one could reasonably expect Fe to be in high spin state ($S = 5/2$). Indeed, Fe^{III}(OTf)₃ and Fe^{III}(NTf₂)₃ have been described as high spin complexes.²⁸³ In our case, the fitting of the EPR spectrum of Fe^{III}(OTf)₃ using the Matlab[®] routine Easyspin is consistent with a single weakly distorted high-spin Fe centre ($g = 2.012$, $D = 0.01$ cm⁻¹, $E/D = 0.1$).²⁸⁴ The DFT-optimized²⁸⁵ structure for Fe^{III}(OTf)₃ features three bidentate triflate anions interacting with the Fe centre through two oxygen atoms (**Figure 86**). The interaction in Fe^{III}(OTf)₃ is mainly ionic as confirmed by NBO analysis: both Fe and O are strongly charged (+1.7 on Fe and -0.9 on O) and the spin is located mainly on Fe (spin density on Fe: 4.0, on O: 0.1). A $g_x = g_y = g_z = 2.01$ and $D = 0.09$ cm⁻¹ were obtained using the EPR calculation module of ORCA, in good agreement with the experimental spectra.

²⁸² W. R. Hagen, Biomolecular EPR Spectroscopy, **2008**, CRC Press.

²⁸³ J.R. Cabrero-Antonino, A. Leyva-Pérez, A. Corma, *Chem. Eur. J.* **2012**, *18*, 11107-11114

²⁸⁴ S. Stoll, A. Schweiger, EasySpin, a comprehensive software package for spectral simulation and analysis in EPR, *J. Magn. Res.* **2006**, *178*, 42-55.

²⁸⁵ All calculations were performed with the TURBOMOLE 6.6 software using the RI-J approximation and corresponding auxiliary basis sets. Structures and free energy corrections (G_{gas} at $T = 25$ °C and $P = 1$ bar) were calculated at the (DFT) BP86-D3(BJ)/def2-SVP level, while electronic energies (E_e) were calculated at the (DFT) B3LYP-D3(BJ)/def2-TZVP level. The electronic energy contains the electrostatic contribution to the free energy of solvation, as implemented in the COSMO implicit solvation model, using the dielectric constants of cyclohexane ($\epsilon = 1.989$) and default parameters otherwise. NBO charges were calculated from the B3LYP-D3(BJ)/def2-TZVP wave function.

The EPR g -tensor of radical species was calculated on optimized structures at the PBE0/def2-TZVP level using ORCA's default settings for the gauge origin (center of electronic charge). The SO contribution to the D-tensor was estimated using the QRO approach (F. Neese, *J. Am. Chem. Soc.* **2006**, *128*, 10213-10222.) and the SS coupling contribution using ORCA's default settings (uno option) at the same level of theory (PBE0/def2-SVP).

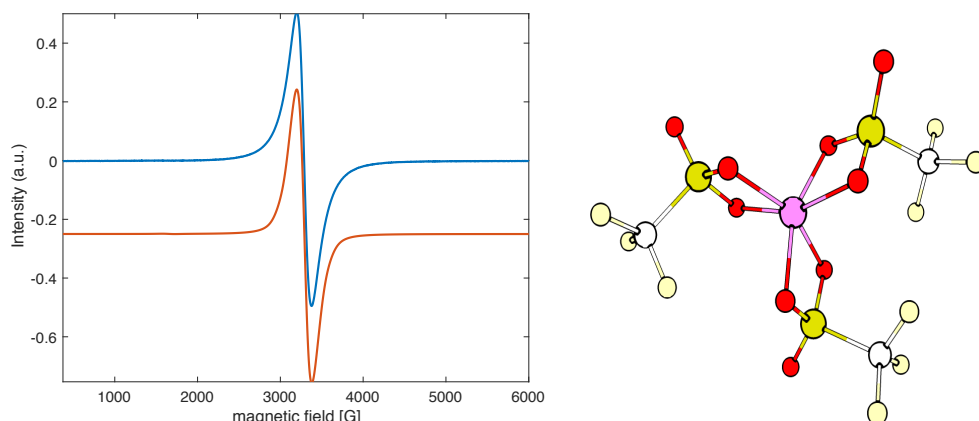


Figure 86 - EPR spectra of $\text{Fe}(\text{OTf})_3$ (solid), recorded at 110 K (blue) and fitting (orange, $S = 5/2$, $g = 2.012$, $|D| = 0.007 \text{ cm}^{-1}$, $E/D = 0.1$, 100%, Gaussian/Lorentzian ratio (G/L): 50%/50%).

Coordination sphere of Fe(III) in the presence of CyOH and CyONE. As pointed out above (**Table 39**), CyONE and CyOH are potential ligands for iron, but showing a contrasting effect on the catalytic activity: CyONE seems to deactivate the catalyst, whereas CyOH enhances its activity. To gain more insight into the coordination of CyONE and CyOH on the iron centre, a dedicated EPR study was performed. The addition of CyONE to a CyH solution of $\text{Fe}^{\text{III}}(\text{OTf})_3$ (10 mM) did not alter the EPR signal (**Figure 87**).

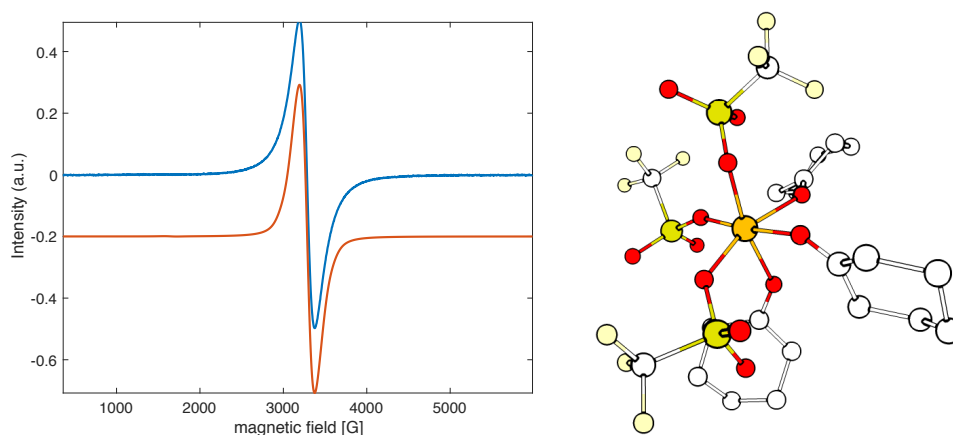


Figure 87 EPR spectra of $\text{Fe}(\text{OTf})_3$ (10 mM in cyclohexane) in the presence of CyONE (10 equiv), recorded at 110 K (blue) and fitting (orange, $S = 5/2$, $g = 2.014$, $|D| = 0.007 \text{ cm}^{-1}$, $E/D = 0.1$, 100%, G/L: 50%/50%).

This result is unexpected, since ketones should interact with $\text{Fe}(\text{III})$, generating a Lewis adduct. Indeed, the free energies of coordination computed by DFT strongly support this idea (**Table 40**): the most stable adduct between $\text{Fe}^{\text{III}}(\text{OTf})_3$ and CyONE, i.e. *mer*- $\text{Fe}^{\text{III}}(\text{OTf})_3(\text{CyONE})_3$, is favoured by more than 100 kJ mol^{-1} . However, the electronic structure of *mer*- $\text{Fe}^{\text{III}}(\text{OTf})_3(\text{CyONE})_3$ is very similar to that of $\text{Fe}^{\text{III}}(\text{OTf})_3$, resulting in almost the same EPR spectrum. A high spin, highly charge iron centre (+1.8) is observed with a spin mainly located on iron (spin density on Fe 4.0). This centre interacts with negatively charged oxygen atoms (O

of OTf -1.0, O of CyONE -0.6). Since the partial charge is slightly lower on the CyONE oxygen atom, the Fe-O bond is slightly longer compared to the Fe-O bond generated with the oxygen atoms of triflates (2.11 Å *vs* 1.94 Å). Accordingly, the adduct geometry is a slightly distorted octahedron. As the coordination of CyONE has little impact on the electronic density on iron, no significant difference is expected for the EPR spectrum. Indeed, the parameters issued from the simulation are close to the previous ones: $g = 2.01$ and $D = 0.05 \text{ cm}^{-1}$ (**Table 40**).

Table 40 - High spin complexes resulting from the coordination of cyclohexanol (CyOH) and cyclohexanone (CyONE) to $\text{Fe}^{\text{III}}(\text{OTf})_3$

Species	ΔG^a (kJ mol ⁻¹)	ΔH (kJ mol ⁻¹)	g	D	E
$\text{Fe}(\text{OTf})_3$ (1)	0	0	2.01	0.087	0.049
$\text{Fe}(\text{OTf})_3(\text{CyONE})$ (2)	-47.6	-104.4	2.01	0,085	0.181
$\text{Fe}(\text{OTf})_3(\text{CyONE})_2$ (3)	-90.8	-214.5	2.01	0.078	0.113
<i>mer</i> - $\text{Fe}(\text{OTf})_3(\text{CyONE})_3$ (4)	-133.3	-307.4	2.01	0.065	0.152
<i>fac</i> - $\text{Fe}(\text{OTf})_3(\text{CyONE})_3$ (5)	-98.9	-276.0	2.01	0.050	0.291
$\text{Fe}(\text{OTf})_3(\text{CyOH})$ (6)	-22.6	-89.4	2.01	0.099	0.320
$\text{Fe}(\text{OTf})_3(\text{CyOH})_2$ (7)	-99.3	-224.7	2.01	0.078	0.300
<i>mer</i> - $\text{Fe}(\text{OTf})_3(\text{CyOH})_3$ (8)	-155.8	-338.0	2.01	0.027	0.305
<i>fac</i> - $\text{Fe}(\text{OTf})_3(\text{CyOH})_3$ (9)	-93.7	-284.4	2.01	0.066	0.095
$\text{Fe}(\text{OTf})_2(\text{CyO})$ (10)	-19.8	-67.1	2.01	0.403	0.212
$\text{Fe}(\text{OTf})_2(\text{CyOH})(\text{CyO})$ (11)	-44.8	-151.7	2.01	0.377	0.065
$\text{Fe}(\text{OTf})_2(\text{CyOH})_2(\text{CyO})$ (12)	-85.3	-247.7	2.01	0.417	0.147

^a Enthalpy and Gibbs free energies of formation were calculated with respect to free $\text{Fe}^{\text{III}}(\text{OTf})_3$, CyOH and CyONE. In the case of complexes **10** to **20**, the formation of $[\text{CyOH}_2]^+$, OTf ion pair was considered ($\Delta G = -6.8 \text{ kJ mol}^{-1}$, $\Delta H = -61.6 \text{ kJ mol}^{-1}$), the formation of triflic acid being less favourable in all cases.

Similarly, the addition of CyOH to $\text{Fe}(\text{OTf})_3$ does not modify the EPR spectra upon addition of up to 3 equiv (**Figure 88-left**). As for CyONE, DFT calculations confirm that simple coordination of CyOH is not expected to modify the signal to an important extent (**Table 40**, complexes **3-5**). Conversely, in the presence of an excess of CyOH, a new signal appeared around 1500 G (**Figure 88-right**), while the solubility of the salt increases significantly. The fitting of the spectrum reveals the presence of at least three different high spin complexes. One complex corresponds to the same above described isotropic signal (**Figure 88-left**), whereas the two other complexes possess a slightly expanded g -tensor [2.008 2.001 2.000] and a higher zero field splitting interaction ($D = 0.5 \text{ cm}^{-1}$; $E/D = 0.33$ and $D = 0.7 \text{ cm}^{-1}$; $E/D = 0.3$). The latter species are responsible for the low-field signal. From these observations, we could assume that both signals appear from the formation of iron-alcoxy complexes. Indeed, the simulated D and E parameters drastically increased when considering an alcoxy as ligand (**Table 40**, complexes **10-12**).

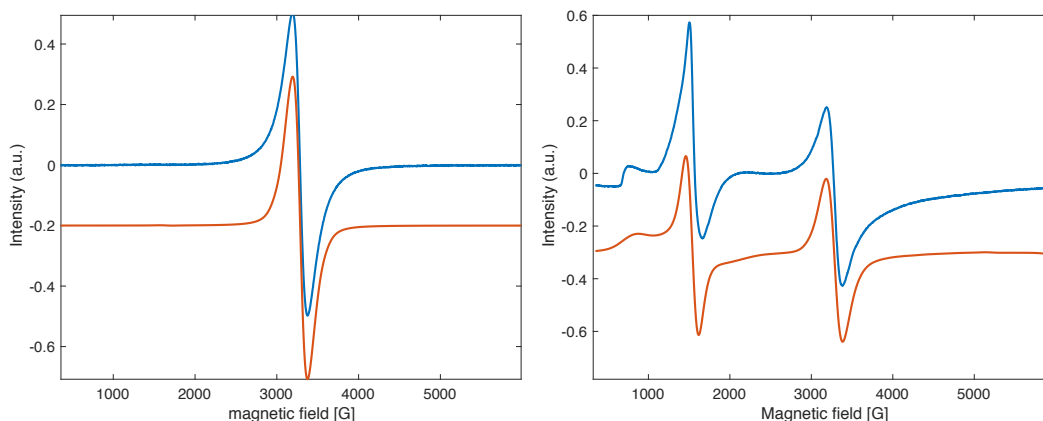


Figure 88 – Left: EPR spectra of $\text{Fe}(\text{OTf})_3$ (10 mM in cyclohexane) in the presence of CyOH (3 equiv), recorded at 110 K (blue) and fitting (orange, $S = 5/2$, $g = 2.014$, $|D| = 0.007 \text{ cm}^{-1}$, $E/D = 0.1$, 100%); **Right:** EPR spectra of $\text{Fe}(\text{OTf})_3$ (10 mM in cyclohexane) in the presence of CyOH (10 equiv), recorded at 110 K (blue) and fitting (orange, $S = 5/2$, $g = 2.014$, $|D| = 0.007 \text{ cm}^{-1}$, $E/D = 0.1$, 43%, G/L: 50%/50%; $S = 5/2$, $g = 2.014$, $|D| = 0.6 \text{ cm}^{-1}$, $E/D = 0.33$, 50%, G/L: 67%/33%; $S = 5/2$, $g = 2.014$, $|D| = 0.7 \text{ cm}^{-1}$, $E/D = 0.09$, 7%, G/L: 80%/20%).

The formation of monoalcoxy species turns out to be thermodynamically favorable ($\text{Fe}(\text{OTf})_3 + (n + 2) \text{CyOH} = \text{Fe}(\text{OTf})_2(\text{CyO})(\text{CyOH})_n + \text{CyOH}_2\cdot\text{OTf}$, with $n = 0, 1$ and 2 , complexes **10-12**), while higher alcoxy species ($\text{Fe}(\text{OTf})(\text{CyO})_2(\text{CyOH})_n$ and $\text{Fe}(\text{CyO})_3(\text{CyOH})_n$ with $n = 0, 1, 2$ and 3 , complexes **13-18**) are less favourable (**Table 41**).

Table 41 - Enthalpy and Gibbs free energy (kJ mol^{-1}) of formation for complexes **13-20**.

complex	ΔG	ΔH
$\text{Fe}(\text{OTf})(\text{CyO})_2$ (13)	+18.8	-78.2
$\text{Fe}(\text{OTf})(\text{CyO})_2(\text{CyOH})$ (14)	-14.9	-170.6
$\text{Fe}(\text{OTf})(\text{CyO})_2(\text{CyOH})_2$ (15)	+5.4	-204.3
$\text{Fe}(\text{OTf})(\text{CyO})_2(\text{CyOH})_3$ (16)	-9.2	-288.2
$\text{Fe}(\text{CyO})_3$ (17)	+87.4	-60.7
$\text{Fe}(\text{CyO})_3(\text{CyOH})$ (18)	+54.3	-144.9
$\text{Fe}(\text{CyO})_3(\text{CyOH})_2$ (19)	+65.5	-197.3
$\text{Fe}(\text{CyO})_3(\text{CyOH})_3$ (20)	+99.2	-224.7

Both aforementioned complexes are predicted to be high spin species (**Table 42**). This result was experimentally confirmed by addition of various amounts of sodium cyclohexanate (CyONa) to $\text{Fe}^{\text{III}}(\text{OTf})_3$ (**Figure 89-left**): by addition of 1 equiv of CyONa , the low field signal immediately appears. However, in the presence of an excess of CyONa , only a single broad signal appears around $g = 2$ (**Figure 89-right**). Interestingly, a similar evolution occurs when heating at $40 \text{ }^\circ\text{C}$ overnight a solution of $\text{Fe}^{\text{III}}(\text{OTf})_3$ with CyOH (10 equiv) in CyH (**Figure 90**).

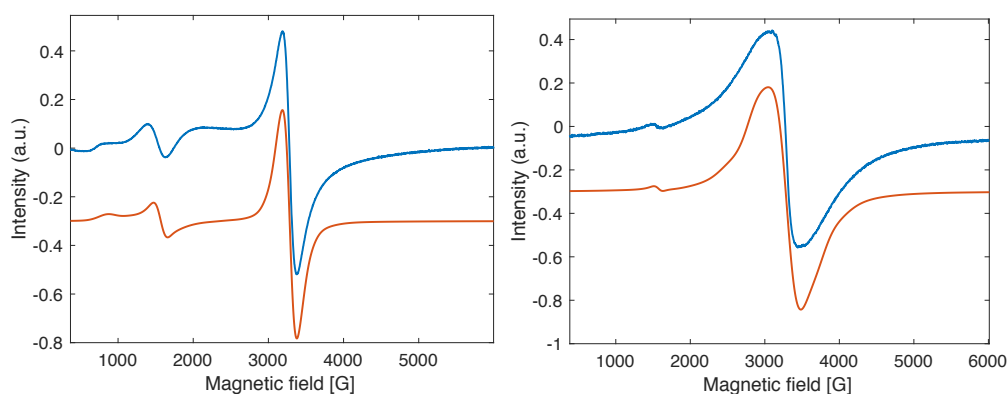


Figure 89 – **Left:** EPR spectra of $\text{Fe}(\text{OTf})_3$ (10 mM in cyclohexane) in the presence of CyONa (1 equiv), recorded at 110 K (blue) and fitting (orange, $S = 5/2$, $g = 2.014$, $|D| = 0.007 \text{ cm}^{-1}$, $E/D = 0.1$, 85%, G/L: 50%/50%; $S = 5/2$, $g = 2.014$, $|D| = 0.3 \text{ cm}^{-1}$, $E/D = 0.33$, 10.5%, G/L: 67%/33%; $S = 5/2$, $g = 2.014$, $|D| = 0.7 \text{ cm}^{-1}$, $E/D = 0.08$, 4.5%, G/L: 80%/20%). **Right:** EPR spectra of $\text{Fe}(\text{OTf})_3$ (10 mM in cyclohexane) in the presence of CyONa (10 equiv), recorded at 110 K (blue) and fitting (orange, $S = 5/2$, $g = 2.02$, $E/D = 0$, $|D| = 0.018 \text{ cm}^{-1}$, 98%, G/L: 42%/58%; $S = 5/2$, $g = 2.02$, $E/D = 0.033$, $|D| = 0.25 \text{ cm}^{-1}$, 2%, L: 0%/100%).

Table 42 - Enthalpy and Gibbs free energy (kJ mol^{-1}) of spin transition ($5/2 \rightarrow 1/2$) for complexes 1-20.

	complex	$\Delta H_{5/2 \rightarrow 1/2}$	$\Delta G_{5/2 \rightarrow 1/2}$
1	$\text{Fe}(\text{OTf})_3$	+115.7	+121.1
2	$\text{Fe}(\text{OTf})_3(\text{CyOH})$	+126.3	+135.7
3	$\text{Fe}(\text{OTf})_3(\text{CyOH})_2$	+121.5	+141.3
4	<i>mer</i> - $\text{Fe}(\text{OTf})_3(\text{CyOH})_3$	+124.2	+145.1
5	<i>fac</i> - $\text{Fe}(\text{OTf})_3(\text{CyOH})_3$	+85.6	+99.6
6	$\text{Fe}(\text{OTf})_3(\text{CyONE})$	+108.6	+127.7
7	$\text{Fe}(\text{OTf})_3(\text{CyONE})_2$	+119.8	+127.4
8	<i>mer</i> - $\text{Fe}(\text{OTf})_3(\text{CyONE})_3$	+114.9	+139.7
9	<i>fac</i> - $\text{Fe}(\text{OTf})_3(\text{CyONE})_3$	+133.7	+155.1
10	$\text{Fe}(\text{OTf})_2(\text{CyO})$	+167.0	+182.0
11	$\text{Fe}(\text{OTf})_2(\text{CyO})(\text{CyOH})$	+139.7	+161.1
12	$\text{Fe}(\text{OTf})_2(\text{CyO})(\text{CyOH})_2$	+119.6	+142.0
13	$\text{Fe}(\text{OTf})(\text{CyO})_2$	+126.5	+137.5
14	$\text{Fe}(\text{OTf})(\text{CyO})_2(\text{CyOH})$	+120.2	+136.0
15	$\text{Fe}(\text{OTf})(\text{CyO})_2(\text{CyOH})_2$	+131.4	+154.8
16	$\text{Fe}(\text{OTf})(\text{CyO})_2(\text{CyOH})_3$	+108.3	+119.6
17	$\text{Fe}(\text{CyO})_3$	+114.4	+116.6
18	$\text{Fe}(\text{CyO})_3(\text{CyOH})$	+131.0	+145.0
19	$\text{Fe}(\text{CyO})_3(\text{CyOH})_2$	+161.4	+166.5
20	$\text{Fe}(\text{CyO})_3(\text{CyOH})_3$	+78.3	+99.4

Since the formation of low spin complexes seems unlikely with only alkoxy ligands, which is confirmed by DFT calculation (**Table 42**), this observation can be explained by the formation of Fe(III) clusters featuring CyO⁻ as bridging ligands. The weak dipolar interaction between localized spin momenta would broaden the signal due to unresolved coupling.^[25] These signals were satisfactorily fitted using an increasing proportion of Gaussian part in the function (**Figure 89** and **Figure 90**).

Catalyst ageing. The broad signal attributed to iron clusters was also observed in the EPR spectrum obtained at the end of the reaction, when the catalyst is supposed to be deactivated (**Figure 90**). The spectrum can be decomposed into a mixture of high spin complexes with high zero field splitting interaction ($D = 0.6 \text{ cm}^{-1}$, $E/D = 0.33$, and $D = 0.7 \text{ cm}^{-1}$, $E/D = 0.21$) in addition of the above mentioned broad signal.²⁸⁶ All these signals may be attributed to alkoxy or hydroxy iron complexes. CyOH plays a dual role: it helps to solubilize the salt, but in excess it may inhibit the catalyst on the long term.

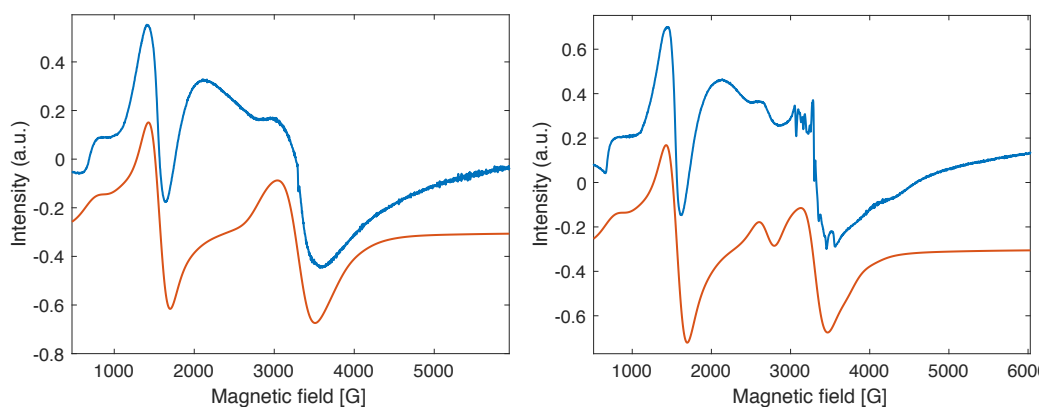


Figure 90 – Left: EPR spectra of Fe(OTf)₃ (10 mM in cyclohexane) in the presence of CyOH (10 equiv) after 24h at 40°C, recorded at 110 K (blue) and fitting (orange, $S = 5/2$, $g = 2.013$, $E/D = 0$, $|D| = 0.018 \text{ cm}^{-1}$, 40%, G/L: 50%/50%, $S = 5/2$, $g = 2.014$, $E/D = 0.33$, $|D| = 0.3 \text{ cm}^{-1}$, 45%, G/L: 60%/40%; $S = 5/2$, $g = 2.014$, $E/D = 0.1$, $|D| = 0.7 \text{ cm}^{-1}$, 15%, G/L: 50%/50%). **Right:** EPR spectra of Fe(OTf)₃ (10 mM in TBHP/cyclohexane) after 24h at 40°C, recorded at 110 K (blue) and fitting (orange, $S = 5/2$, $g = 2.01$, $E/D = 0$, $|D| = 0.018 \text{ cm}^{-1}$, 33%, $S = 1/2$, $g = 2.45$, 2.45 2.4, 11%, $S = 5/2$, $g = 2.014$, $E/D = 0.33$, $|D| = 0.3 \text{ cm}^{-1}$ 44%, $S = 5/2$, $g = 2.014$, $E/D = 0.09$ $|D| = 0.7 \text{ cm}^{-1}$, 12%).

Intermediates and proposed mechanism. When TBHP was added to a solution of Fe^{III}(OTf)₃ in CyH, the signal ascribed to Fe(III) vanished and only sharp signals at $g = [2.024 \ 2.009 \ 2.007]$ and $g = [2.031 \ 2.011 \ 2.003]$ were observed (**Figure 91**). These signals are characteristic of the superoxide radical O₂^{•-}, either free or stabilized on an EPR-silent iron centre (Fe^{II}-OO[•]).²⁸⁷ Surprisingly the signal characteristic for Fe^{III}(OOtBu) complexes was not observed.²⁸⁸

²⁸⁶ The sharp multiple between 3000 and 4000 G is due to Mn(II) impurity resulting from Mn(III) reduction after TBHP addition, $g = [2.03 \ 2.01 \ 1.995]$, $D = 0.008 \text{ cm}^{-1}$, $E/D = 0$, $a_{Mn} = 93 \text{ G}$. The presence of Mn has been confirmed by ICP analysis, the proportion of Mn in Fe(OTf)₃ was estimated to 270 ppm.

²⁸⁷ M. Anpo, M. Che B. Fubini, E. Garrone, E. Giamello, M. C. Paganini, *Top. Catal.*, **1999**, *8*, 189-198; W.-J. Zhou, R. Wischert, K. Xue, Y.-T. Zheng, B. Albel, L. Bonneviot, J.-M. Clacens, F. De Campo, M. Pera-Titus, P. Wu, *ACS Catal.* **2014**, *4*, 53-62.

²⁸⁸ C. Nguyen, R. J. Guajardo, P. K. Mascharak, *Inorg. Chem.* **1996**, *35*, 6273-6281

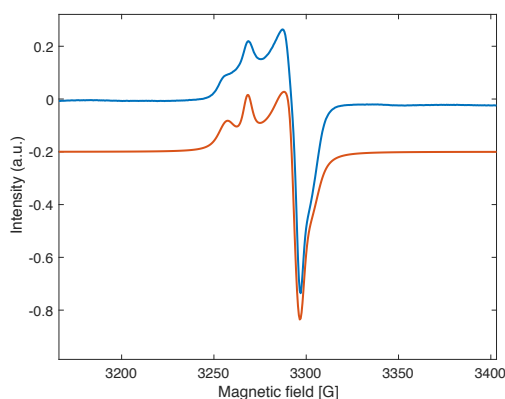


Figure 91 - EPR spectra of $\text{Fe}(\text{OTf})_3$ (10 mM in TBHP/cyclohexane), recorded at 110 K (blue) and fitting (orange, $S = 1/2$, $g = 2.024\ 2.0092\ 2.007$, 70%, $S = 1/2$, $g = 2.031\ 2.011\ 2.003$, 30%).

Radical trapping experiments were also performed using 5,5-dimethyl-1-pyrroline *N*-oxide (DMPO). Spin trap such as DMPO may react with radical to generate persistent radical, allowing the indirect detection of short-live intermediates.²⁸⁹ Under standard reaction conditions, a single radical was observed (**Figure 92**, $S = 1/2$, $g = 2.004$, $a_N = 13.25$ G, $a_H = 9.98, 1.45$ G), corresponding to the adduct formed between DMPO and $(\text{CH}_3)_3\text{CO}^\bullet$ (or $(\text{CH}_3)_3\text{COO}^\bullet$).²⁹⁰ No traces of OH^\bullet , typical of Fenton-type systems, or $(\text{CH}_3)_3\text{C}^\bullet$ trapped by DMPO were detected. Under the same conditions but in the presence of CyONE (10 equiv), the same signal was observed with lower intensity, and a second species appeared (**Figure 92**, $S = 1/2$, $g = 2.006$, $a_N = 7$ G, $a_H = 3.5$ G) due to DMPO oxidation.²⁹¹ This experiment provides clear evidence of iron-poisoning by CyONE, leading to a decrease of the catalytic activity (*vide supra*).

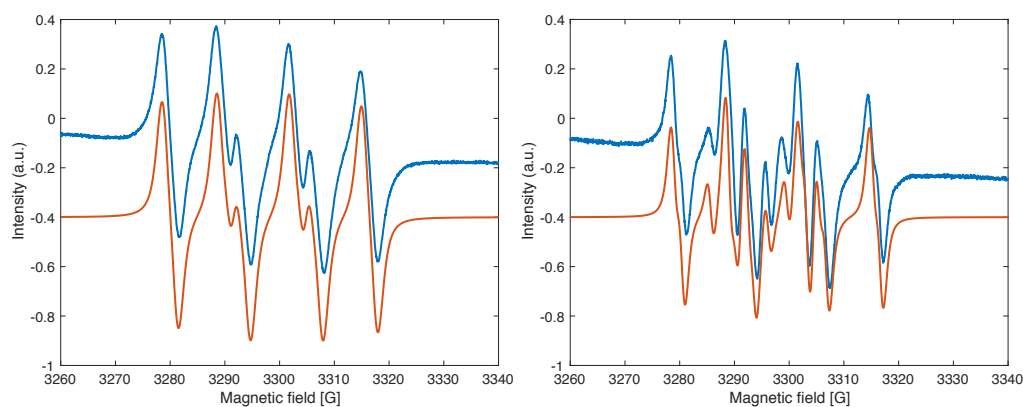


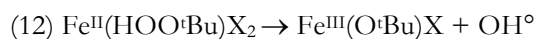
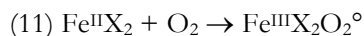
Figure 92 – Left: EPR spectra of $\text{Fe}(\text{OTf})_3$ (10 mM in TBHP/cyclohexane) in the presence of TBHP (5 μL), recorded at 110 K (blue) and fitting (orange, $S = 1/2$, $g = 2.004$, $a_N = 13.25$ G, $a_H = 9.98, 1.45$ G); **Right:** EPR spectra of $\text{Fe}(\text{OTf})_3$ (10 mM in TBHP/cyclohexane) in the presence of TBHP (5 μL) and CyONE (10 equiv), recorded at 110 K (blue) and fitting (orange, $S = 1/2$, $g = 2.004$, $a_N = 13.2$ G, $a_H = 9.9, 1.32$ G, 75%, $S = 1/2$, $g = 2.006$, $a_N = 7$ G, $a_H = 3.5$ G, 25%).

²⁸⁹ F. A. Villamena, *EPR Spin Trapping in Reactive Species Detection in Biology*, 2017, Elsevier, 2017, pp 163-202.

²⁹⁰ L. D. Haire, P. H. Krygsman, E. G. Janzen, U. M. Oehler, *J. Org. Chem.*, 1988, 53, 4535-4542.

²⁹¹ H. G. Aurich, J. Trösken, *Liebigs Annal.*, 1971, 745, 159-163.

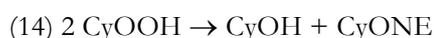
Fe^{II}X₂ may be re-oxidized to Fe(III) or Fe(IV) by O₂ or TBHP by **Eq 11** and **Eq 12**



However, these reactions seem unlikely, since no trace of OH[°] or Fe^{III}O₂[°] was detected.²⁹⁷ On the contrary, **Eq 13** would allow the regeneration of (Fe^{IV}=O)X₂ (X = OTf, ΔG₁₄ = -22 kJ mol⁻¹)



Finally, mechanisms involving the formation of CyOOH and its disproportionation to CyOH and CyONE are unlikely since the KA ratio evolves during our reaction, excluding a termination following **Eq 14**²⁹⁸



4.5. Conclusion

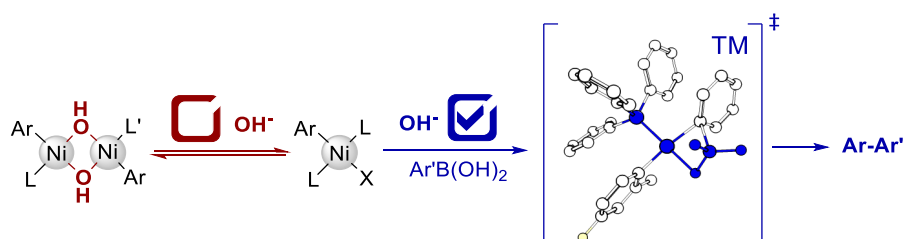
The use of non-coordinating anion ligands – triflates or triflimides – may allow to tune the oxidation potential of a metal and to create potentially interesting reactivity. Iron triflate salts proved experimentally to selectively and efficiently catalyse the oxidation of cyclohexane to cyclohexanol and cyclohexone (KA oil) with very high turnover frequencies. Combined EPR spectroscopy with DFT calculations helped us to propose structures intermediates, as well as to find out possible sources of catalyst deactivation. However, the precise oxidation mechanism is not clear yet and more experiments and calculations are needed to help to understand the particular behaviour of Fe(OTf)₃.

²⁹⁷ L. Deguillaume, M. Leriche, N. Chaumerliac, *Chemosphere*, **2005**, *60*, 718-724.

²⁹⁸ C. Nguyen, R. J. Guajardo, P. K. Mascharak, *Inorg. Chem.*, **1996**, *35*, 6273-6281.

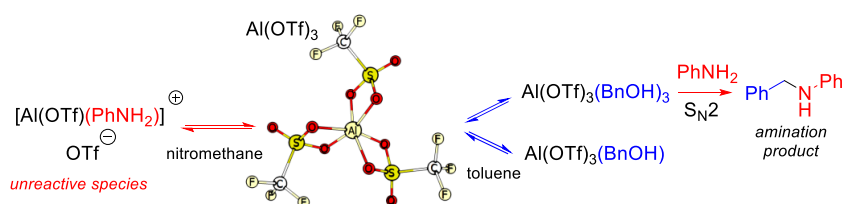
General conclusions and perspectives

The thesis aimed at providing rationales to understand and optimize known reactions but also at developing new methodologies to help predicting the reactivity of unexplored catalysts. Two main projects illustrating this approach are reported in this thesis.



Taming Nickel-Catalyzed Suzuki Coupling: A Mechanistic Study

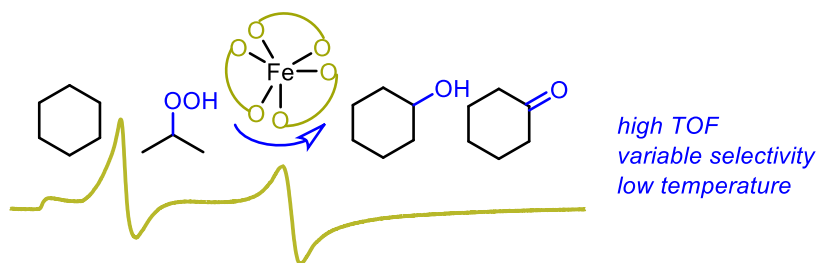
First the nickel-to-boron transmetalation – the key step of the Suzuki-Miyaura cross-coupling – was explored in details. The role played by the base was elucidated and the formation of inactive aryl-nickel dinuclear hydroxo species was evidenced. This observation allows to explain the high sensitivity to experimental conditions (apolar solvent, weak basis ...) of this reaction. The formation this dead-end species can also be modulated by electronic, halides, phosphine and counter-ion effects. We hope that our conclusions will gave the synthetic chemists clues to tune delicate synthesis and eventually leads to the development of rationally-designed catalyst. For instance, the development of heterogeneous catalyst using immobilized single site nickel-catalyst have been recently reported and allows to achieve very low catalyst loadings.²⁹⁹ The extension of this results to boron-to-copper transmetalation and to boron-to-palladium using diphosphine ligands is currently under study in the lab.



Direct Amination of Alcohols Catalyzed by Al(OTf)₃: an Experimental and Computational Study

²⁹⁹ P. Elumalai, H. Mamlouk, W. Yiming, L. Feng, S. Yuan, H.-C. Zhou, S. T. Madrahimov, *ACS Appl. Mater. Interfaces*, **2018**, *10*, 41431-41438; R. J. Key, J. Meynard, M. Tengco, M. D. Smith, A. K. Vannucci, *Organometallics*, **2019**, *38*, 2007-2014.

The second topic developed in this thesis, in collaboration with the E2P2 team in Shanghai, concerns the reactivity of two families of Lewis acids, triflate and triflimide salts. Their reactivity was evaluated on model S_N and oxidation reactions for which mechanisms were studied in detail. A new scale of Lewis acidity based on the charge-transferred to a Lewis base was set-up and compared to existing indicators. This new predicting tool allows to foresee the reactivity of an unprecedented Ti triflimide salts that proved efficient to catalyze the direct amination of alcohols. A huge number of reactions require a Lewis acid catalyst or co-catalyst and its choice is almost never justified. We hope that our rational design of Lewis acid catalyzed reactions will inspire future works.



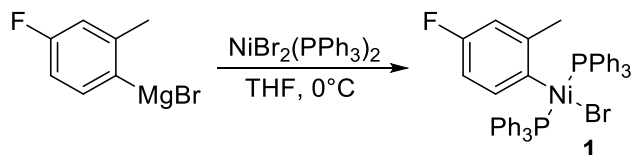
$\text{Fe}(\text{OTf})_3$ as Precursors of Highly Active and Selective Catalyst for the Oxidation of Cyclohexane.

We are convinced that rational design and mechanistic-based reaction optimization strategies relying on a dynamic combination of physical organic chemistry experiments and theoretical modeling can efficiently complement and help to reduce the time-cost of large-scale combinatorial screening algorithms.

Experimental Section

1. Experimental section of CHAPTER I

1.1. Synthesis of trans-[(4-F-2-Me-C₆H₃)NiBr(PPh₃)₂] (1)



NiBr₂(PPh₃)₂ (5.42 g, 7.3 mmol) was placed in a round-bottom flask containing a magnetic stirring bar, the flask was evacuated and filled with argon three times. Dried THF (100 mL) was added, the solution was cooled to 0 °C with an ice bath, and 4-fluoro-2-methylphenylmagnesium bromide (1 equiv, 7.5 mmol, 7.5 mL of a 1 M solution in THF, prepared in the usual way from 2-bromo-5-fluorotoluene and magnesium turnings) was added dropwise with vigorous stirring. The solution was stirred for 15 min at 0 °C, then the stir bar was removed and the solution was evaporated to dryness under reduced pressure. MeOH (100 mL) was added, and the mixture was sonicated until a uniform suspension was obtained (approximately 5 min). After the suspension was cooled to 0 °C, the yellow precipitate was collected by vacuum filtration, washed with two portions of cold MeOH, and dried under high vacuum to yield the title complex (3.03 g, 82%)

¹H NMR (300 MHz, CD₂Cl₂): δ (ppm) = 7.59–7.53 (m, 12H), 7.45–7.26 (m, 18H), 6.96 (t, *J* = 7.3 Hz, 1H), 6.09 (td, *J*₁ = 9.3 Hz, *J*₂ = 2.6 Hz, 1H), 5.75 (dd, *J*₁ = 10.6 Hz, *J*₂ = 2.5 Hz, 1H), 2.14 (br s, 3H).

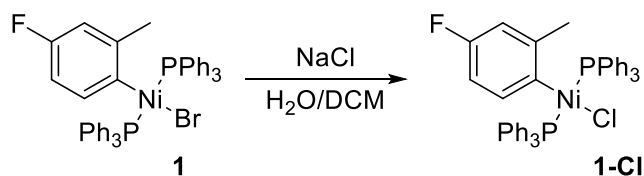
¹H{¹⁹F} NMR (300 MHz, CD₂Cl₂): δ (ppm) = 7.63–7.51 (m, 12H), 7.42–7.25 (m, 18H), 6.97 (d, *J* = 7.3 Hz, 1H), 6.09 (d, *J* = 7.3 Hz, 1H), 5.76 (s, 1H), 2.16 (s, 3H).

¹³C NMR (75 MHz, CD₂Cl₂): δ (ppm) = 161.5 (dt, ¹*J*_{CF} = 237.5 Hz, ⁵*J*_{CP} = 2.7 Hz), 144.7 (dt, ³*J*_{CF} = 6.8 Hz, ³*J*_{CP} = 3.5 Hz), 143.8 (td, ²*J*_{CP} = 33.5 Hz, ⁴*J*_{CF} = 1.6 Hz), 135.6 (dt, ³*J*_{CP} = 6.7 Hz, ³*J*_{CF} = 4.2 Hz), 135.3 (t, virtual coupling, apparent *J*_{CP} = 5.4 Hz), 132.4 (t, virtual coupling, apparent *J*_{CP} = 21.6 Hz), 130.3 (br s), 128.2 (t, virtual coupling, apparent *J*_{CP} = 4.8 Hz), 116.4 (dt, ²*J*_{CF} = 19.3 Hz, ⁴*J*_{CP} = 3.0), 110.7 (dt, ²*J*_{CF} = 19.2 Hz, ⁴*J*_{CP} = 2.3), 26.2 (d, ⁴*J*_{CF} = 2.0 Hz).

¹⁹F{¹H} NMR (282 MHz, CD₂Cl₂): δ (ppm) = -127.8 (br s).

³¹P{¹H} NMR (122 MHz, CD₂Cl₂): δ (ppm) = 21.80 (d, ⁶*J*_{FP} = 2.9 Hz).

1.2. Synthesis of *trans*-[(4-F-2-Me-C₆H₃)NiCl(PPh₃)₂] (**1-Cl**)



A solution of complex **1** (772 mg, 1.0 mmol) in DCM (10 mL) was thoroughly shaken in a separatory funnel with a saturated solution of NaCl in water, acidified with a drop of a 1 M aqueous solution of HCl (5 x 10 mL). The aqueous layer was dried over Na₂SO₄ and the solvent was evaporated *in vacuo*, yielding the title complex as a yellow solid (524 mg, 72%).

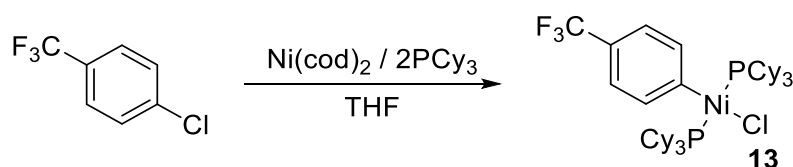
¹H NMR (300 MHz, CD₂Cl₂): δ (ppm) = 7.64–7.54 (m, 12H), 7.42–7.28 (m, 18H), 6.93 (t, $J = 7.5$ Hz, 1H), 6.10 (t, $J = 7.5$ Hz, 1H), 5.79 (d, $J = 9.8$ Hz, 1H), 2.17 (s, 3H).

¹³C NMR (75 MHz, CD₂Cl₂): δ (ppm) = 162.4 (dt, $^1J_{\text{CF}} = 237.5$ Hz, $^5J_{\text{CP}} = 2.7$ Hz), 144.7 (dt, $^3J_{\text{CF}} = 6.7$ Hz, $^3J_{\text{CP}} = 3.4$ Hz), 141.6 (td, $^2J_{\text{CP}} = 34.1$ Hz, $^4J_{\text{CF}} = 1.7$ Hz), 135.7 (dt, $^3J_{\text{CF}} = 6.3$, $^3J_{\text{CP}} = 4.3$ Hz), 135.1 (t, virtual coupling, apparent $J_{\text{CP}} = 5.5$ Hz), 131.9 (t, virtual coupling, apparent $J_{\text{CP}} = 21.3$ Hz), 130.2 (br s), 128.2 (t, virtual coupling, apparent $J_{\text{CP}} = 4.8$ Hz), 116.0 (dt, $^2J_{\text{CF}} = 19.3$ Hz, $^4J_{\text{CP}} = 3.2$ Hz), 110.4 (dt, $^2J_{\text{CF}} = 19.1$, $^4J_{\text{CP}} = 2.2$ Hz), 26.2 (d, $^4J_{\text{CF}} = 2.3$ Hz).

¹⁹F{¹H} NMR (282 MHz, CD₂Cl₂): δ (ppm) = -127.7 (t, $^6J_{\text{FP}} = 3.4$ Hz).

³¹P{¹H} NMR (122 MHz, CD₂Cl₂): δ (ppm) = 20.98 (d, $^6J_{\text{FP}} = 3.4$ Hz).

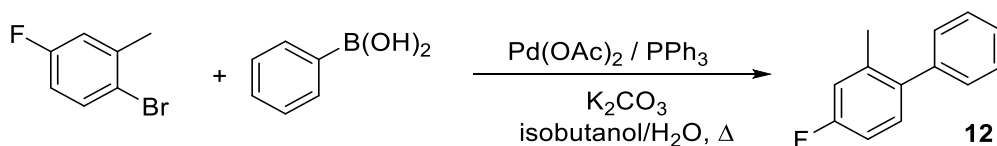
1.3. Synthesis of *trans*-[(4-CF₃-C₆H₄)Ni(PCy₃)₂Cl] (**13**)



A 250-mL round-bottomed flask was charged with bis(1,5-cyclooctadiene) nickel (0.5 g, 1.82 mmol, 1 equiv) and tricyclohexylphosphine (1.53 g, 3 equiv). The flask was evacuated and filled with argon three times, and then dry THF (50 mL) was added. 4-Chlorobenzotrifluoride (1.23 mL, 5 equiv) was introduced by syringe. The mixture was stirred for 24 h at room temperature, the flask was opened to air and the solvent was evaporated *in vacuo*. The residue was triturated with pentane (10 mL) to give a yellow solid which was subsequently filtered (0.94 g, 65%).

Spectral data matched those already reported in the literature (*Organometallics*, **2014**, *33*, 2134-2137).

1.4. Synthesis of 4-fluoro-2-methyl-1,1'-biphenyl (**12**)



A Schlenk flask was charged with 2-bromo-4-fluorotoluene (253 μ L, 2.0 mmol), phenylboronic acid (256 mg, 2.1 mmol) and isobutanol (3.6 mL). The resulting solution was degassed by bubbling argon for 15 minutes. Pd(OAc)₂ (2.0 mg, 0.009 mmol), PPh₃ (7.1 mg, 0.027 mmol) and a degassed solution of Na₂CO₃ (254 mg, 2.4 mmol) in water (1.0 mL) were added. The mixture was stirred at 105 °C for 24 h. The cooled reaction mixture was quenched with brine (10 mL) and extracted with ether (3 x 7 mL). The combined organic extracts were desiccated over MgSO₄ and the residue was purified by flash chromatography (eluent: cyclohexane). The title compound was thus recovered as a colourless oil (372 mg, 81%).

¹H NMR (300 MHz, CDCl₃): δ (ppm) = 7.45-7.35 (m, 3H), 7.32-7.27 (m, 2H), 7.21-7.16 (dd, J = 6.0, 8.4 Hz, 1H), 6.99-6.93 (m, 2H), 2.26 (s, 3H).

¹³C NMR (75.5 MHz, CDCl₃): δ (ppm) = 162.1 (d, ¹ J_{CF} = 245.4 Hz), 141.2, 138.0 (d, ⁴ J_{CF} = 3.3 Hz), 137.8 (d, ³ J_{CF} = 7.5 Hz), 131.3 (d, ³ J_{CF} = 8.3 Hz), 129.4, 128.3, 127.0, 116.9 (d, ² J_{CF} = 20.4 Hz), 112.6 (d, ² J_{CF} = 21.1 Hz), 20.7 (d, ⁴ J_{CF} = 1.5 Hz).

¹⁹F {¹H} NMR (282 MHz, CDCl₃): δ (ppm) = -116.4.

1.5. Typical procedure for kinetic monitoring by $^{19}\text{F}\{^1\text{H}\}$ NMR

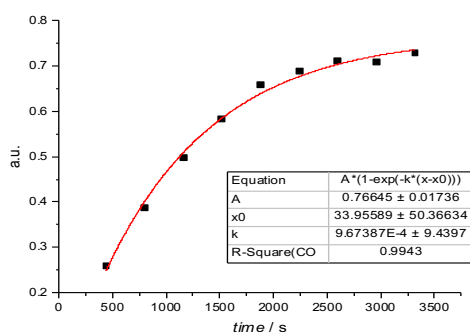
$\text{PhB}(\text{OH})_2$ (10 equiv 24.4 mg) was introduced in a vial stoppered with a rubber septum. A needle connected to a Schlenk line was introduced through the septum and the vessel was evacuated and back-filled with argon three times. Dioxane (1.0 mL) was added by syringe followed by a solution of TBAOH in water (1.5 M, 52 μL , 12.0 mM, 4.0 equiv). The resulting mixture was sonicated for homogeneity.

In the meantime, an NMR tube was charged with *trans*- $[(4\text{-F-2-Me-C}_6\text{H}_4)\text{Ni}(\text{PPh}_3)_2\text{Br}]$ (**1**, 20 mmol), stoppered with a septum of appropriate size and evacuated and filled back with argon for three times. The solution of $\text{PhB}(\text{OH})_2$ and TBAOH previously prepared was transferred to the NMR tube by syringe, and after thorough shaking the sample was introduced in an NMR spectrometer for kinetic monitoring.

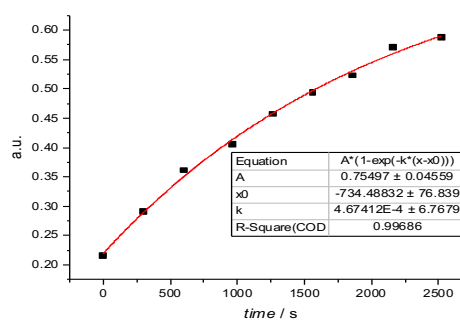
1.6. Raw kinetic data for the reaction of complex **1** with $\text{PhB}(\text{OH})_2$

a) Variation of base concentration

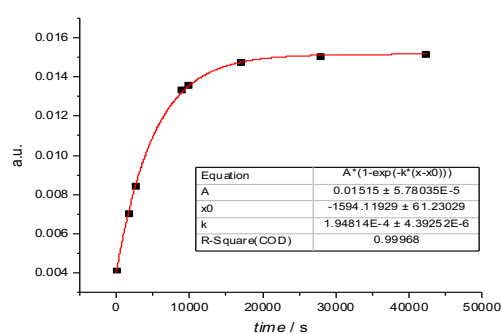
Here follow the kinetic curves and the associated first-order rate law fittings used to construct Figure 4a in the main text. For all reactions, the initial concentration of complex **1** was 20 mM and the initial concentration of $\text{PhB}(\text{OH})_2$ was 200 mM (solvent: dioxane). The amount of TBAOH (dispensed as a 1.5 M solution in water) was varied as specified below each kinetic curve. All the experiments were performed at 20 °C.



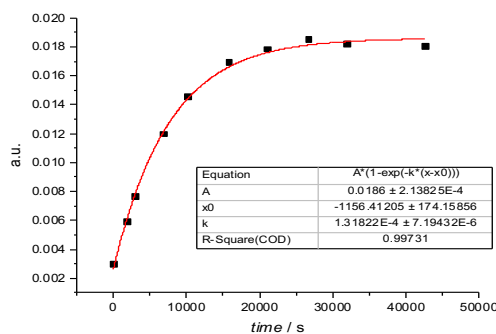
TBAOH (2 equiv)/ $\text{PhB}(\text{OH})_2$ (10 equiv)



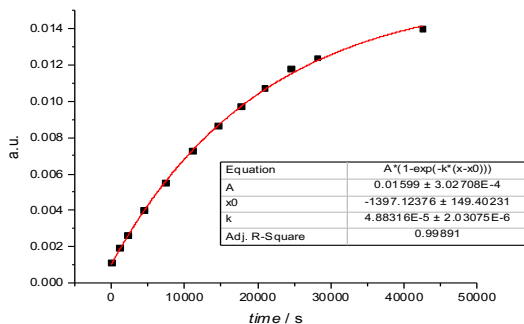
TBAOH (2.2 equiv)/ $\text{PhB}(\text{OH})_2$ (10 equiv)



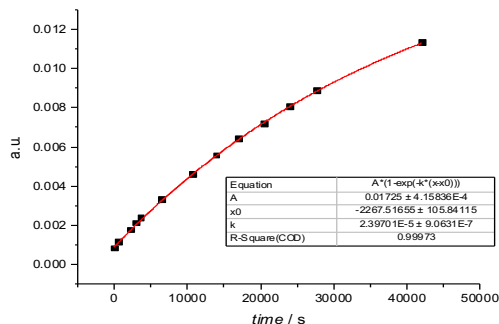
TBAOH (3 equiv)/ $\text{PhB}(\text{OH})_2$ (10 equiv)



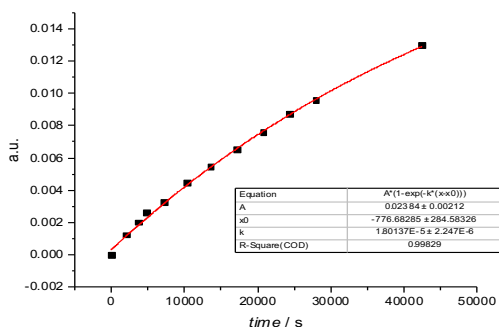
TBAOH (4 equiv)/ $\text{PhB}(\text{OH})_2$ (10 equiv)



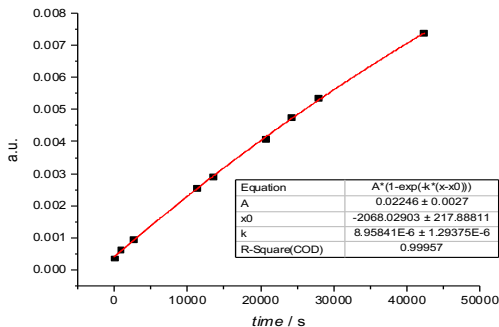
TBAOH (5 equiv)/PhB(OH)₂ (10 equiv)



TBAOH (6 equiv)/PhB(OH)₂ (10 equiv)



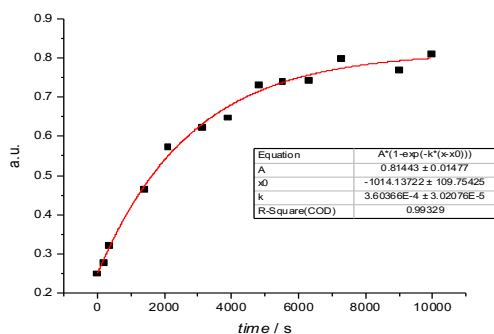
TBAOH (7 equiv)/PhB(OH)₂ (10 equiv)



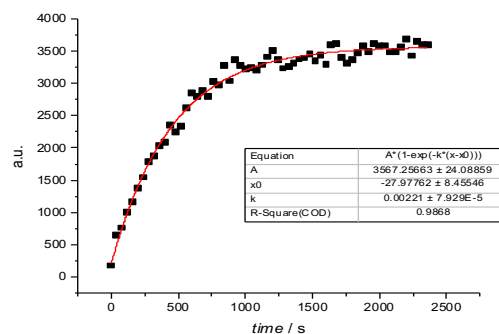
TBAOH (8 equiv)/PhB(OH)₂ (10 equiv)

b) Variation of PhB(OH)₂ concentration

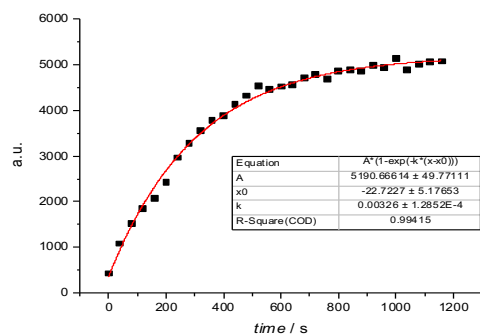
Here follow the kinetic curves and the associated first-order rate law fittings used to construct Figure 4b in the main text. For all the reactions, the initial concentration of complex **1** was 10 mM and the initial concentration of TBAOH (dispensed as a 1.5 M solution in water) was 20 mM (solvent: dioxane). The amount of PhB(OH)₂ was varied as specified below each kinetic curve. All the experiments were performed at 20 °C.



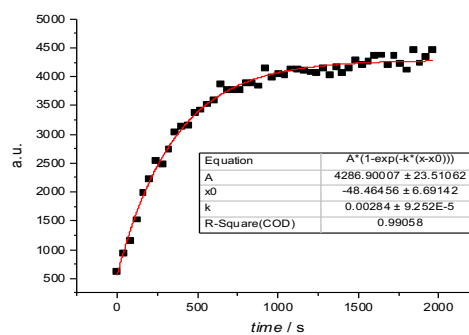
TBAOH (2 equiv)/PhB(OH)₂ (10 equiv)



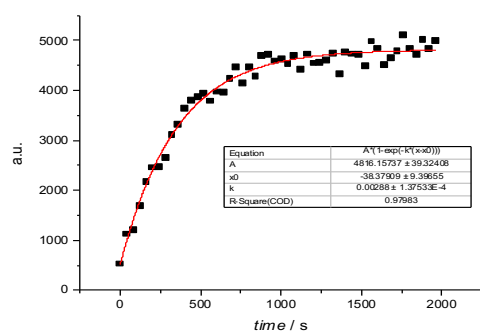
TBAOH (2 equiv)/PhB(OH)₂ (15 equiv)



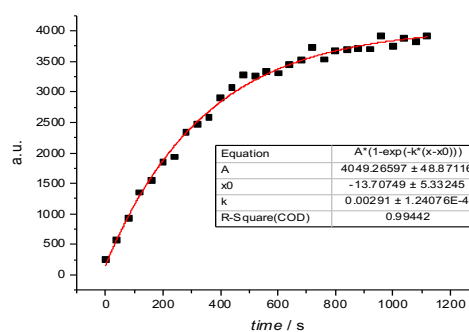
TBAOH (2 equiv)/PhB(OH)₂ (20 equiv)



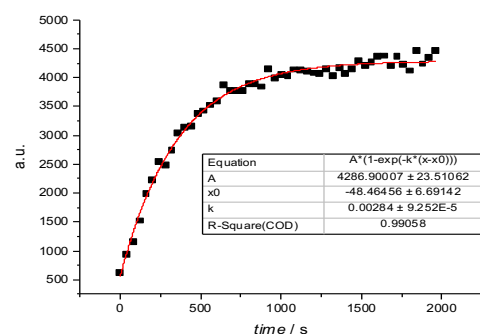
TBAOH (2 equiv)/PhB(OH)₂ (22.5 equiv)



TBAOH (2 equiv)/PhB(OH)₂ (24 equiv)



TBAOH (2 equiv)/PhB(OH)₂ (27.5 equiv)

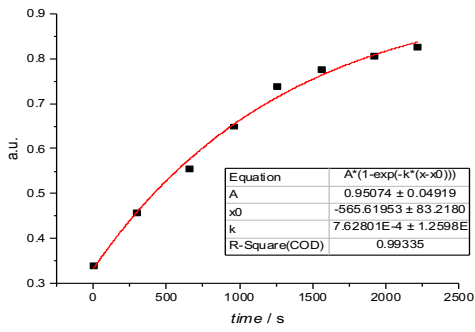


TBAOH (2 equiv)/PhB(OH)₂ (30 equiv)

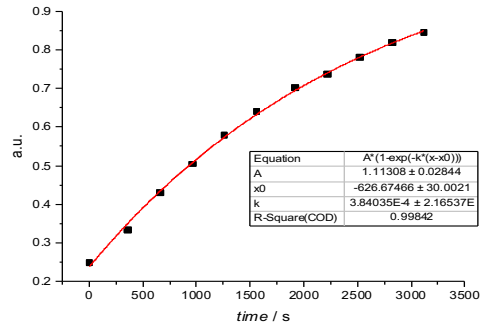
c) Effect of cations

Here follow the kinetic curves and the associated first-order rate law fittings used to construct Figure S30 and all the other kinetics performed with bases different from TBAOH. For all the reactions, the initial concentration of complex **1** was 20 mM (solvent: dioxane) and the amounts of base and PhB(OH)₂ are specified below each kinetic curve.

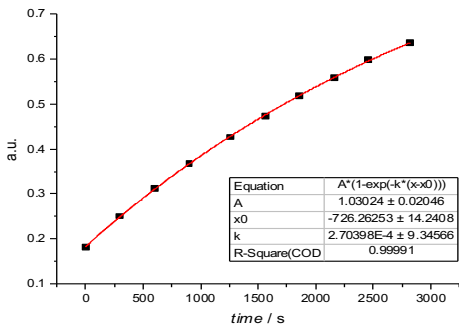
K⁺



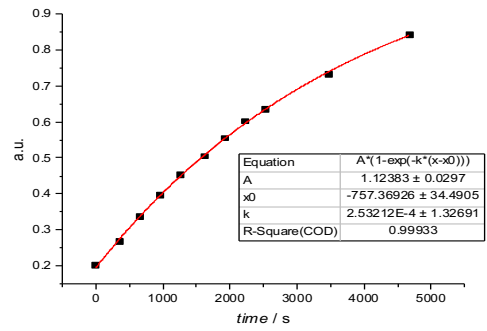
KOH (1.7 equiv) / PhB(OH)₂ (10 equiv)



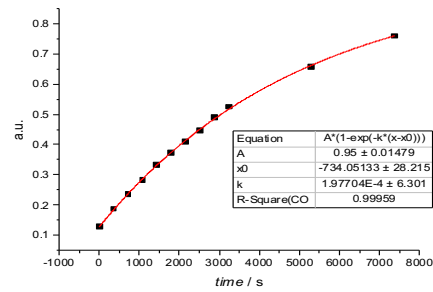
KOH (2.12 equiv) / PhB(OH)₂ (10 equiv)



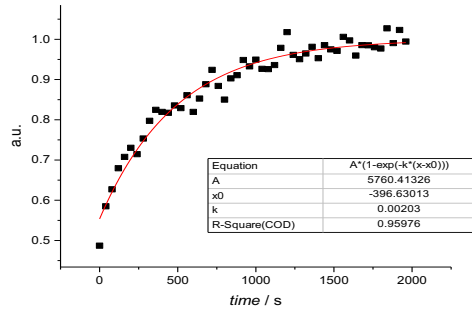
KOH (2.55 equiv) / PhB(OH)₂ (10 equiv)



KOH (3.4 equiv) / PhB(OH)₂ (10 equiv)

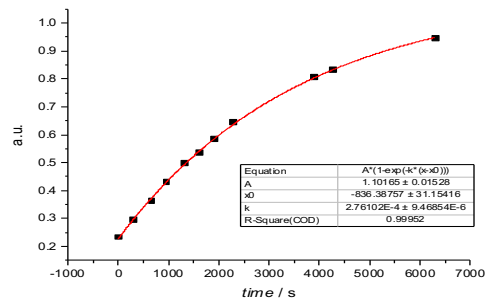
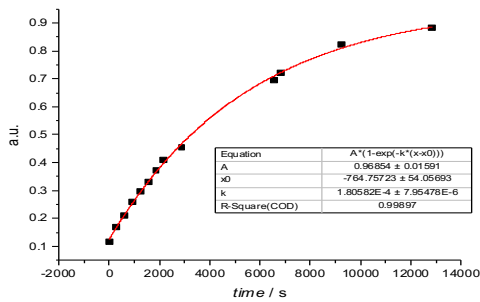


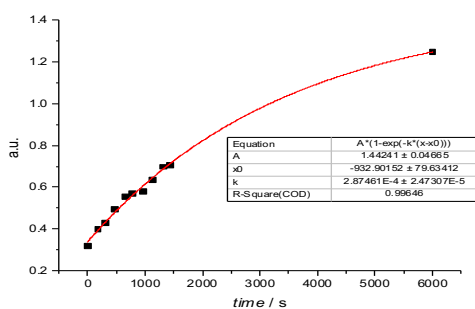
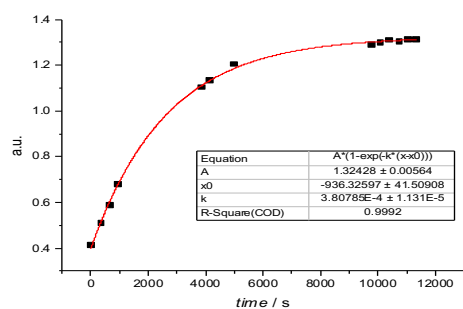
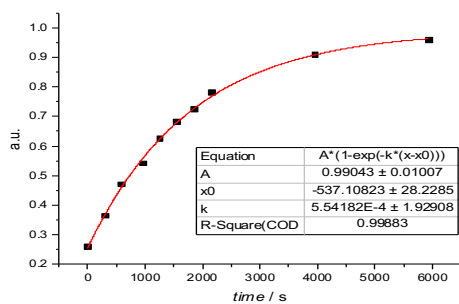
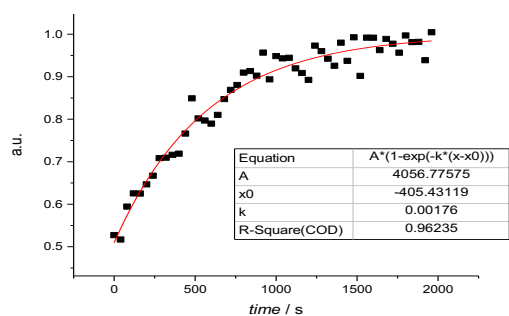
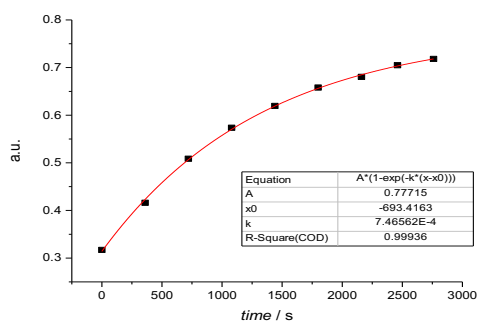
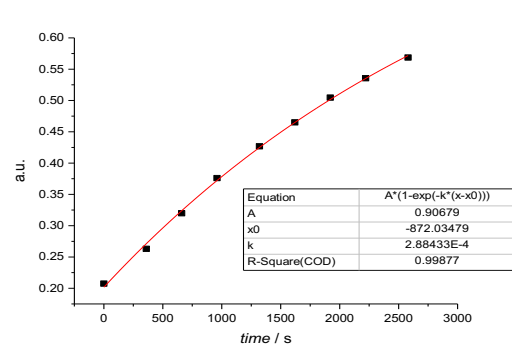
KOH (6.7 equiv) / PhB(OH)₂ (10 equiv)

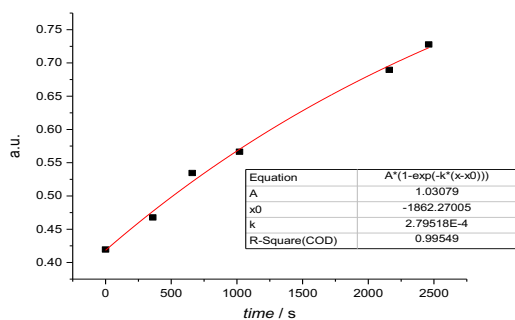


KOH (2 equiv) / PhB(OH)₂ (25 equiv)

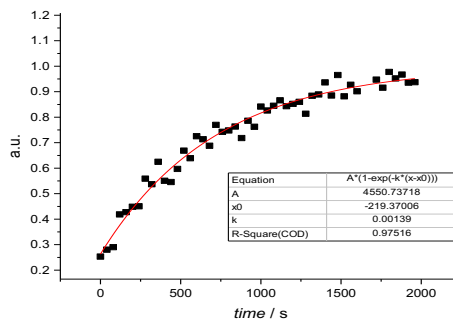
Cs⁺



CsOH (8 equiv) / PhB(OH)₂ (10 equiv)CsOH (5 equiv) / PhB(OH)₂ (10 equiv)CsOH (4 equiv) / PhB(OH)₂ (10 equiv)CsOH (3 equiv) / PhB(OH)₂ (10 equiv)CsOH (2 equiv) / PhB(OH)₂ (10 equiv)CsOH (2 equiv) / PhB(OH)₂ (25 equiv)Na⁺NaOH (2 equiv) / PhB(OH)₂ (10 equiv)NaOH (2.5 equiv) / PhB(OH)₂ (10 equiv)



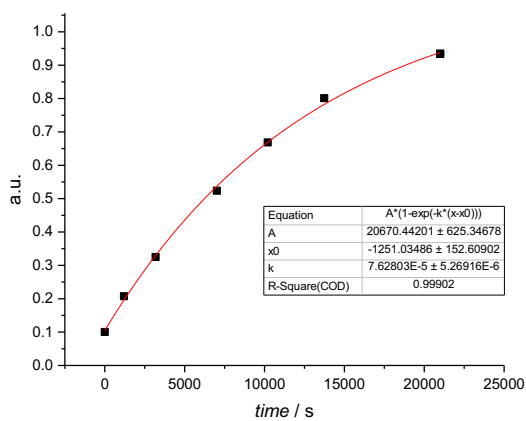
NaOH (4 equiv) / PhB(OH)₂ (10 equiv)



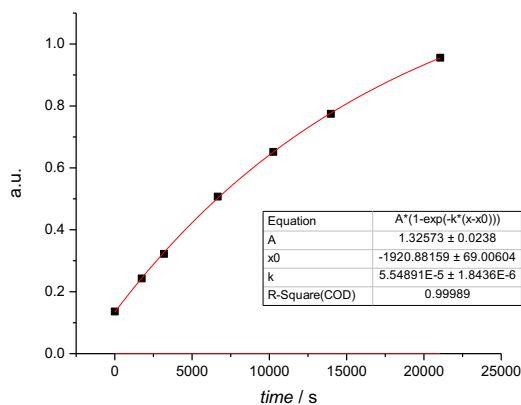
NaOH (2 equiv) / PhB(OH)₂ (20 equiv)

1.7. Effect of Br⁻

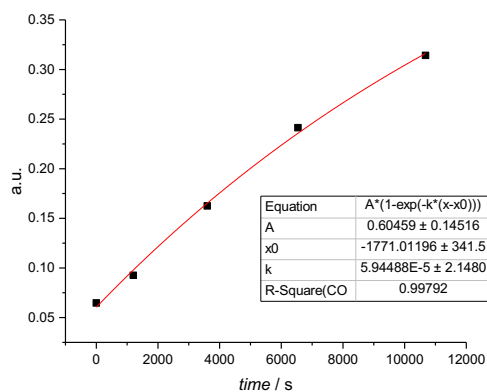
Here follow the kinetic curves and the associated first-order rate law fittings used to construct Figure S20. For all the reactions, the initial concentration of complex **1** was 20 mM, the initial concentration of TBAOH (dispensed as a 1.5 M solution in water) was 80 mM and the initial concentration of PhB(OH)₂ was 200 mM (solvent: dioxane). The amount of tetrabutylammonium bromide (TBABr) was varied as specified below each kinetic curve. All the experiments were performed at 20 °C.



Br⁻ (2 equiv)



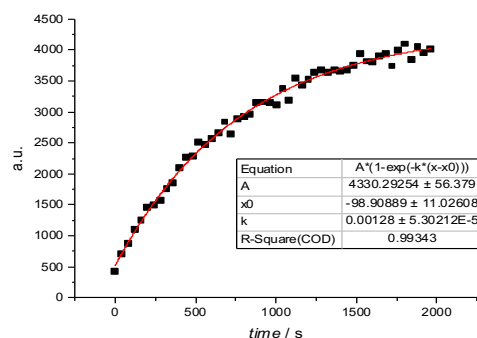
Br⁻ (5 equiv)



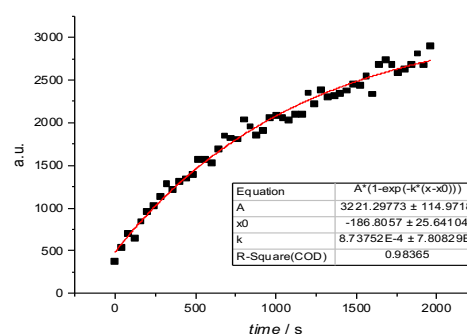
Br⁻ (10 equiv)

1.8. Effect of PPh₃

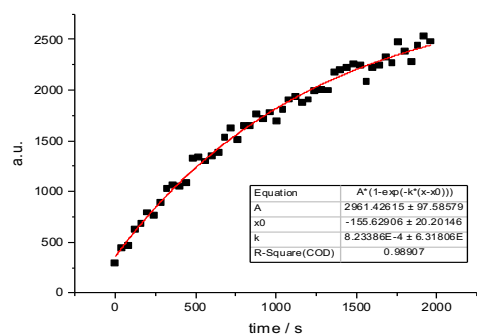
Here follow the kinetic curves and the associated first-order rate law fittings used to construct Figure S21. For all the reactions, the initial concentration of complex **1** was 20 mM, the initial concentration of TBAOH (dispensed as a 1.5 M solution in water) was 40 mM and the initial concentration of PhB(OH)₂ was 200 mM (solvent: dioxane). The amount of PPh₃ was varied as specified below each kinetic curve. All the experiments were performed at 20 °C.



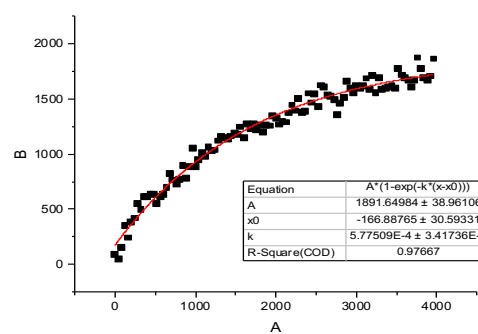
PPh₃ (0.25 equiv)



PPh₃ (0.5 equiv)



PPh₃ (1 equiv)

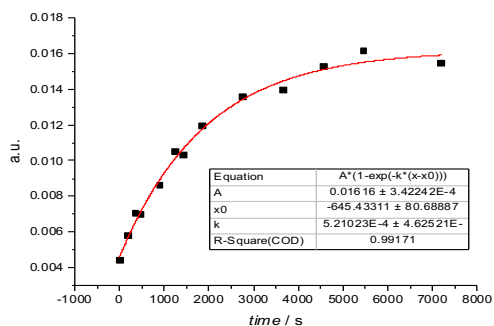


PPh₃ (2 equiv)

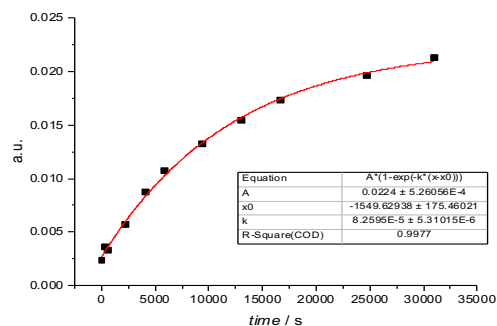
1.9. Raw kinetic data for the reaction of complex **1** with substituted phenylboronic acids (Hammett correlation)

Hammett plot – high TBAOH/ArB(OH)₂ ratio

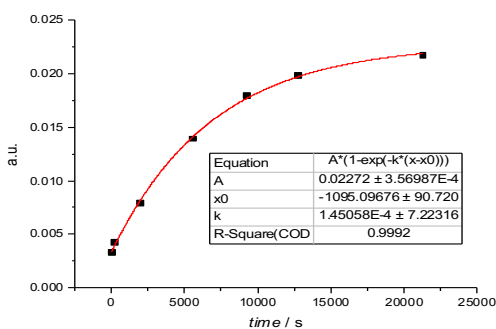
Here follow the kinetic curves and the associated first-order rate law fittings used to construct Figure 8a in the main text. For all the reactions, the initial concentration of the reactants were as follows: complex **1** – 20 mM; TBAOH (dispensed as a 1.5 M solution in water) – 80 mM (solvent: dioxane); ArB(OH)₂ – 200 mM. The phenylboronic acid substituents are specified below each kinetic curve. All the experiments were performed at 20 °C.



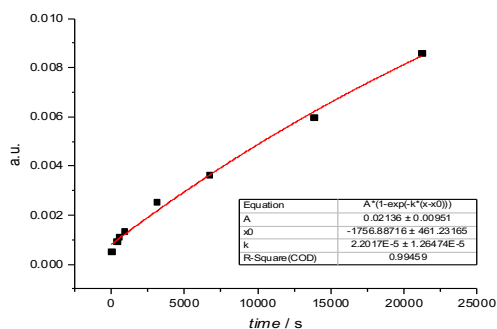
p-NC ($\sigma_p = 0.66$)



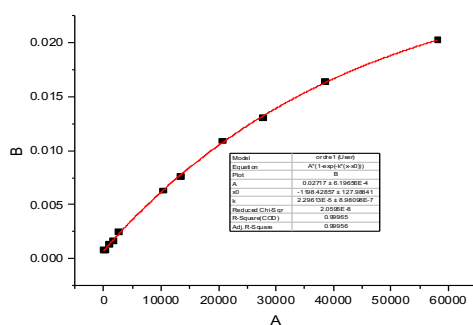
p-F ($\sigma_p = 0.06$)



p-OHC ($\sigma = 0.42$)



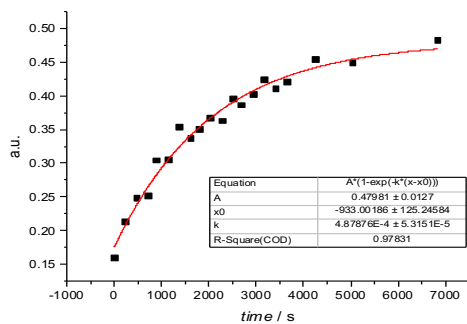
p-Me ($\sigma = -0.17$)



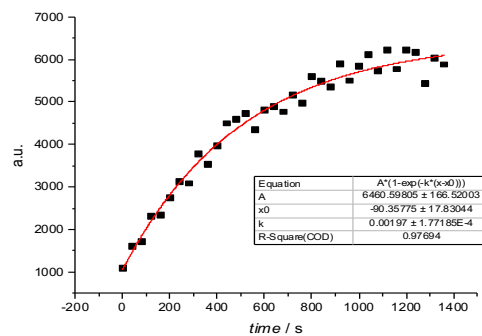
H ($\sigma = 0$)

Hammett plot – low TBAOH/ArB(OH)₂ ratio

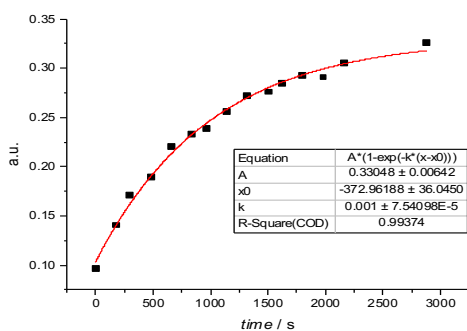
Here follow the kinetic curves and the associated first-order rate law fittings used to construct Figure 8b in the main text. For all the reactions, the initial concentration of the reactants were as follows: complex **1** – 20 mM; TBAOH (dispensed as a 1.5 M solution in water) – 40 mM (solvent: dioxane); ArB(OH)₂ – 400 mM. The phenylboronic acid substituents are specified below each kinetic curve. All the experiments were performed at 20 °C.



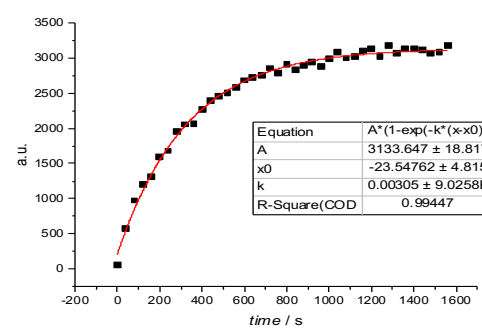
p-NC ($\sigma_p = 0.66$)



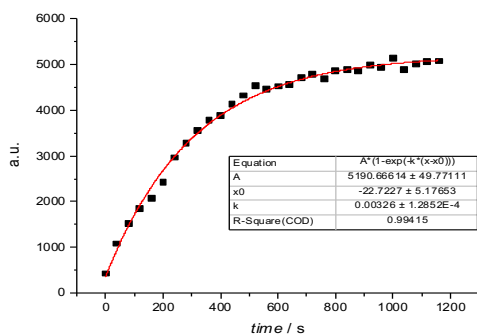
p-F ($\sigma_p = 0.06$)



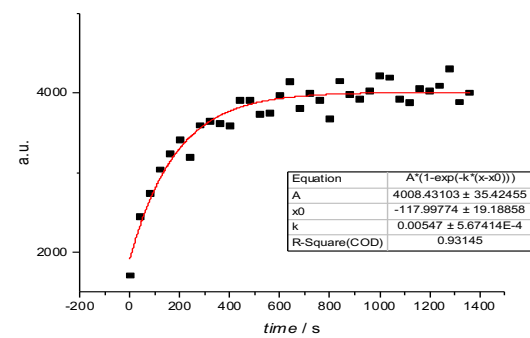
p-OHC ($\sigma_p = 0.42$)



p-Me ($\sigma_p = -0.17$)



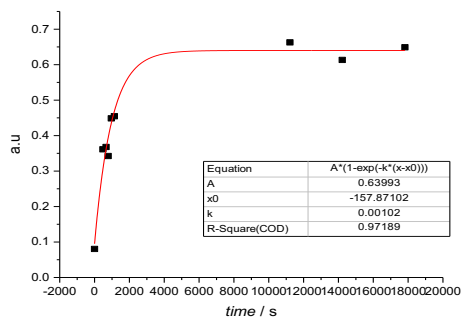
H ($\sigma_p = 0$)



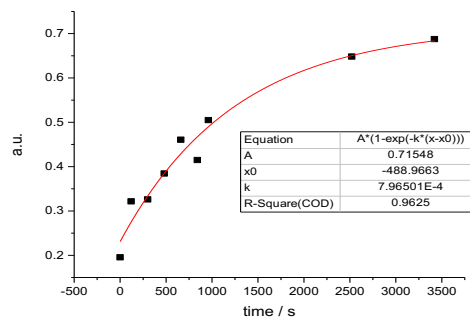
p-MeO ($\sigma_p = -0.27$)

1.10. Raw kinetic data for the reaction of complex 1-Cl with PhB(OH)₂

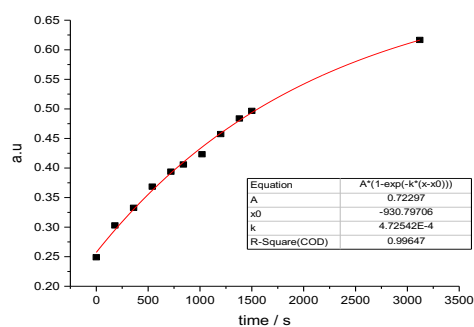
Here follow the kinetic curves and the associated first-order rate law fittings used to construct Figure 10 in the main text. For all the reactions, the initial concentration of complex 1-Cl was 10 mM and the initial concentration of PhB(OH)₂ was 200 mM (solvent: dioxane). The initial amount of TBAOH (added as a 1.5 M solution in water) is specified below each kinetic curve. All the experiments were performed at 20 °C.



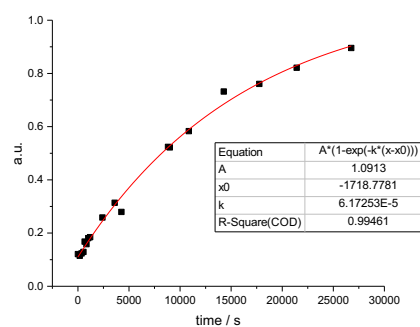
TBAOH (2 equiv)/PhB(OH)₂ (20 equiv)



TBAOH (3 equiv)/PhB(OH)₂ (20 equiv)



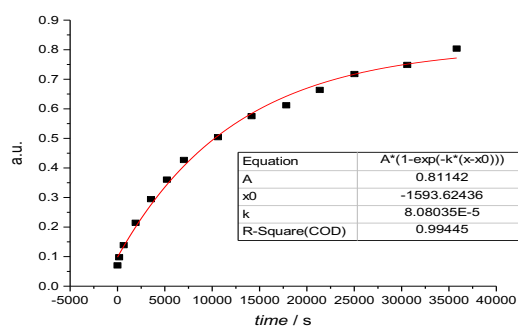
TBAOH (4 equiv)/PhB(OH)₂ (20 equiv)



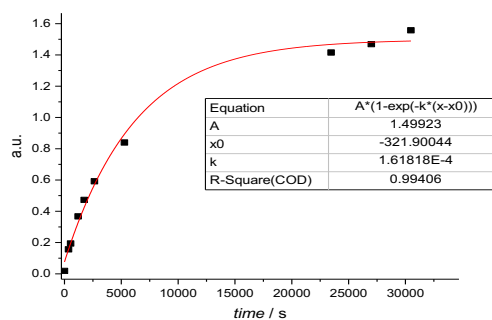
TBAOH (6 equiv)/PhB(OH)₂ (20 equiv)

1.11. Raw kinetic data for the reaction of complex **13** with PhB(OH)₂

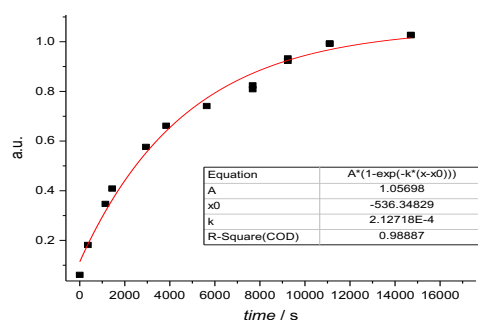
Here follow the kinetic curves and the associated first-order rate law fittings used to construct Figure 11 in the main text. For all the reactions, the initial concentration of complex **13** was 10 mM and the initial concentration of PhB(OH)₂ was 200 mM (solvent: dioxane). The initial amount of TBAOH (added as a 1.5 M solution in water) is specified below each kinetic curve. All the experiments were performed at 20 °C.



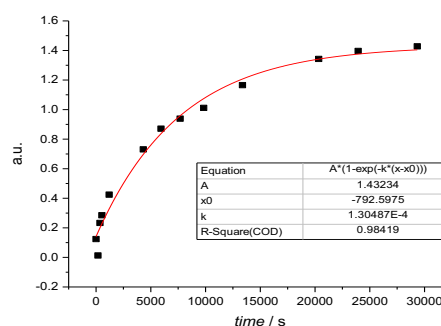
TBAOH (4 equiv)/PhB(OH)₂ (20 equiv)



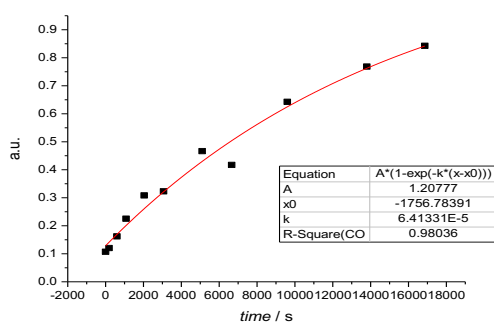
TBAOH (6 equiv)/PhB(OH)₂ (20 equiv)



TBAOH (8 equiv)/PhB(OH)₂ (20 equiv)



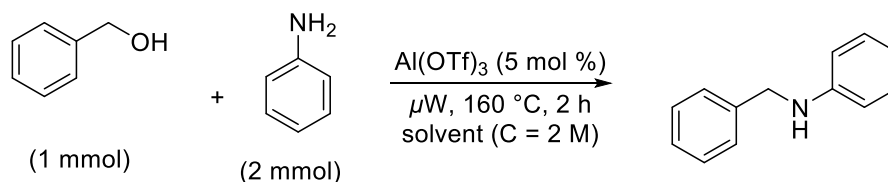
TBAOH (10 equiv)/PhB(OH)₂ (20 equiv)



TBAOH (14 equiv)/PhB(OH)₂ (20 equiv)

2. Experimental section of CHAPTER II

2.1. Typical procedure for amination reactions



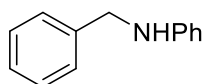
The BnOH (1 mmol) and aniline (2 mmol, 2 equiv) were subsequently added at room temperature to a 5 mL microwave vial equipped with a magnetic stirrer and a solution of $\text{Al}(\text{OTf})_3$ (0.05 mmol, 5 mol %) in toluene or in nitromethane (0.5 mL) (C = 2 M). The vial was then capped, placed in a microwave and heated for 2 h at an adjusted temperature of $160\text{ }^\circ\text{C}$. The conversion and yield were estimated by GC analysis using biphenyl as an internal standard.

^1H NMR (300 MHz, CDCl_3): δ_{H} = 7.42-7.23 (m, 5H), 7.21-7.16 (m, 2H), 6.78-6.66 (m, 3H), 4.36 (s, 2H), 3.92 (br s, 1H) ppm.

^{13}C NMR (75 MHz, CDCl_3): δ_{C} = 148.0, 139.4, 129.2, 128.4, 127.4, 127.1, 117.5, 112.8, 48.2 ppm.

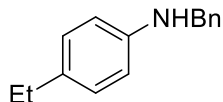
All spectral data are in agreement with the reported ones.^[3]

2.2. Characterization data



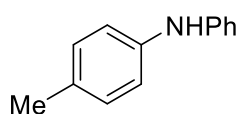
N-Benzylaniline (3aa): 4 (7.5 mol%), $T = 160\text{ }^{\circ}\text{C}$, $t = 1\text{ h}$, 90% yield.

$^1\text{H NMR}$ (300 MHz, CDCl_3): $\delta_{\text{H}} = 7.42\text{--}7.23$ (m, 5H), 7.21–7.16 (m, 2H), 6.78–6.66 (m, 3H), 4.36 (s, 2H), 3.92 (br, 1H) ppm. $^{13}\text{C NMR}$ (75 MHz, CDCl_3): $\delta_{\text{C}} = 148.0, 139.4, 129.2, 128.4, 127.4, 127.1, 117.5, 112.8, 48.2$ ppm. All spectral data are in accordance with the reported ones.³⁰⁰



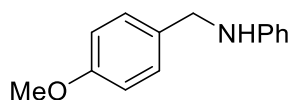
N-Benzyl-4-ethylaniline (3ac): 4 (7.5 mol%), $T = 160\text{ }^{\circ}\text{C}$, $t = 1\text{ h}$, 96% yield.

$^1\text{H NMR}$ (300 MHz, CDCl_3): $\delta_{\text{H}} = 7.48\text{--}7.40$ (m, 5H), 7.16–7.13 (m, 2H), 6.71–6.68 (m, 2H), 4.40 (s, 2H), 3.92 (br, 1H), 2.71–2.64 (q, $J = 7.5\text{ Hz}$, 2H), 1.35–1.30 (t, $J = 7.5\text{ Hz}$, 3H) ppm. $^{13}\text{C NMR}$ (75 MHz, CDCl_3): $\delta_{\text{C}} = 146.3, 139.9, 133.5, 128.7, 127.7, 127.3, 113.2, 48.7, 28.2, 16.2$ ppm. All spectral data are in accordance with the reported ones.³⁰¹



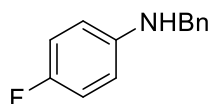
N-Benzyl-4-methylaniline (3ad): 4 (5 mol%), $T = 180\text{ }^{\circ}\text{C}$, $t = 2\text{ h}$, 20% yield (100% NMR yield).

$^1\text{H NMR}$ (300 MHz, CDCl_3): $\delta_{\text{H}} = 7.3\text{--}7.2$ (m, 5H), 6.9 (d, $J = 6.7\text{ Hz}$, 2H), 6.5 (d, $J = 6.7\text{ Hz}$, 6.49), 4.24 (s, 2H), 3.85 (br, 1H), 2.1 (s, 3H) ppm. $^{13}\text{C NMR}$ (75 MHz, CDCl_3): $\delta_{\text{C}} = 148.5, 137.1, 136.9, 129.5, 128.8, 128.1, 120.8, 113.5, 48.0, 21.3$ ppm. All spectral data are in accordance with the reported ones.³⁰²



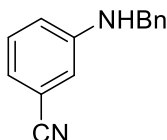
N-Benzyl-4-Methoxyaniline (3ae): 4 (5 mol%), $T = 180\text{ }^{\circ}\text{C}$, $t = 2\text{ h}$, 60% yield (100% NMR yield).

$^1\text{H NMR}$ (300 MHz, CDCl_3): $\delta_{\text{H}} = 7.3\text{--}7.2$ (m, 5H), 6.7 (d, $J = 6.6\text{ Hz}$, 2H), 6.5 (d, $J = 6.6\text{ Hz}$, 2H), 4.2 (s, 2H), 3.69 (br, 1H), 3.67 (s, 3H) ppm. $^{13}\text{C NMR}$ (75 MHz, CDCl_3): $\delta_{\text{C}} = 153.2, 142.5, 139.7, 128.6, 127.6, 127.2, 114.9, 11.1, 55.8, 49.3$ ppm. All spectral data are in accordance with the reported ones.¹



N-Benzyl-4-fluoroaniline (3af): 4 (7.5 mol%), $T = 160\text{ }^{\circ}\text{C}$, $t = 1\text{ h}$, 98% yield.

$^1\text{H NMR}$ (300 MHz, CDCl_3): $\delta_{\text{H}} = 7.42\text{--}7.25$ (m, 5H), 6.97–6.88 (m, 2H), 6.66–6.56 (m, 2H), 4.32 (s, 2H), 3.92 (br, 1H) ppm. $^{13}\text{C NMR}$ (75 MHz, CDCl_3): $\delta_{\text{C}} = 157.6, 154.5, 144.7, 139.5, 128.9, 127.7, 127.5, 116.0, 115.7, 113.9, 113.8, 49.1, 38.2$ ppm. All spectral data are in accordance with the reported ones.³⁰³



3-(Benzylamino)benzonitrile (3ag): 4 (7.5 mol%), $T = 140\text{ }^{\circ}\text{C}$, $t = 8\text{ h}$, 75% yield.

$^1\text{H NMR}$ (300 MHz, CDCl_3): $\delta_{\text{H}} = 7.36\text{--}7.17$ (m, 6H), 6.96 (d, $J = 7.5\text{ Hz}$, 1H), 6.81–6.78 (m, 2H), 4.33 (s, 2H) ppm. $^{13}\text{C NMR}$ (75 MHz, CDCl_3): $\delta_{\text{C}} = 148.0, 138.0, 129.7,$

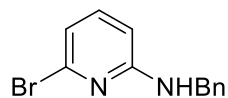
³⁰⁰ Y. Zhao, S. W. Foo, S. Saito, *Angew. Chem., Int. Ed.* **2011**, *50*, 3006–3009.

³⁰¹ F. Meng, C. Wang, J. Xie, X. Zhu, Y. Wan, *Appl. Organometal. Chem.*, **2011**, *25*: 341-347.

³⁰² D. B. Bagal, R. A. Watile, M. V. Khedkar, K. P. Dhake, B. M. Bhanage, *Catal. Science & Tech.* **2012**, *2*, 354-358.

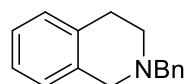
³⁰³ H. Kato, I. Shibata, Y. Yasaka, S. Tsunoi, M. Yasudaa and A. Baba, *Chem. Commun.*, **2006**, *0*, 4189-4191

128.6, 127.3, 127.3, 120.6, 119.4, 117.2, 115.0, 112.5, 47.5 ppm. All spectral data are in accordance with the reported ones.¹



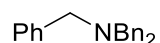
N-Benzyl-6-bromopyridin-2-amine (3ah): 4 (7.5 mol%), $T = 160\text{ }^{\circ}\text{C}$, $t = 8\text{ h}$, 86% yield.

¹H NMR (300 MHz, CDCl₃): $\delta_{\text{H}} = 7.33\text{--}7.18$ (m, 6H), 6.74 (d, $J = 7.6$ Hz, 1H), 6.26 (d, $J = 8.1$ Hz, 1H), 5.31 (br, 1H), 4.48 (d, $J = 5.9$ Hz, 2H) ppm. **¹³C NMR (75 MHz, CDCl₃):** $\delta_{\text{C}} = 158.7$, 140.0, 139.3, 138.2, 128.4, 127.5, 127.0, 115.7, 104.8, 46.0 ppm. All spectral data are in accordance with the reported ones.¹



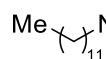
2-Benzyl-1,2,3,4-tetrahydroisoquinoline (3ai): 4 (7.5 mol%), $T = 180\text{ }^{\circ}\text{C}$, $t = 12\text{ h}$, 91% yield.

¹H NMR (300 MHz, CDCl₃): $\delta_{\text{H}} = 7.46\text{--}7.31$ (m, 5H), 7.16–7.12 (m, 3H), 7.03 (d, $J = 7.5$ Hz, 1H), 3.73 (s, 2H), 3.68 (s, 2H), 2.95 (t, $J = 5.7$ Hz, 2H), 2.79 (m, 2H) ppm. **¹³C NMR (75 MHz, CDCl₃):** $\delta_{\text{C}} = 138.1$, 134.7, 134.2, 128.9, 128.5, 128.17, 126.9, 126.4, 125.9, 125.4, 62.2, 55.9, 50.4, 28.9 ppm. All spectral data are in accordance with the reported ones.¹



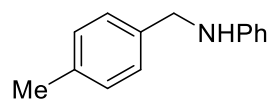
Tribenzylamine (3aj): 4 (7.5 mol%), $T = 180\text{ }^{\circ}\text{C}$, $t = 12\text{ h}$, 96% yield.

¹H NMR (300 MHz, CDCl₃): $\delta_{\text{H}} = 7.52\text{--}7.38$ (m, 6H), 7.34–7.22 (m, 6H), 7.31–7.29 (m, 3H), 3.66 (s, 6H) ppm. **¹³C NMR (75 MHz, CDCl₃):** $\delta_{\text{C}} = 139.5$, 128.6, 128.3, 126.7, 57.8 ppm. All spectral data are in accordance with the reported ones.¹



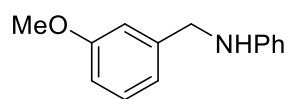
N-Benzyl-dodecan-1-amine (3ak): 4 (7.5 mol%), $T = 190\text{ }^{\circ}\text{C}$, $t = 8\text{ h}$, 36% yield.

¹H NMR (300 MHz, CDCl₃): $\delta_{\text{H}} = 7.34\text{--}7.08$ (m, 5H), 3.78 (s, 2H), 2.62 (t, $J = 6.9$ Hz, 2H), 1.59–1.56 (m, 2H), 1.48–1.21 (m, 18H), 0.88 (t, $J = 6.6$ Hz, 3H) ppm. **¹³C NMR (75 MHz, CDCl₃):** $\delta_{\text{C}} = 140.7$, 128.1, 127.1, 126.7, 54.4, 42.4, 32.3, 31.7, 29.4, 29.2, 29.1, 25.5, 13.9 ppm. All spectral data are in accordance with the reported ones.³⁰⁴



N-(4-Methylbenzyl)aniline (3ca): 4 (7.5 mol%), $T = 160\text{ }^{\circ}\text{C}$, $t = 1\text{ h}$, 61% yield.

¹H NMR (300 MHz, CDCl₃): $\delta_{\text{H}} = 7.42\text{--}7.03$ (m, 6H), 6.79–6.74 (bt, 1H), 6.69 (d, $J = 7.8$ Hz, 2H), 4.29 (s, 2H), 3.98 (br, 1H), 2.38 (s, 3H) ppm. **¹³C NMR (75 MHz, CDCl₃):** $\delta_{\text{C}} = 148.5$, 137.1, 136.9, 129.5, 128.8, 128.1, 120.8, 113.5, 48.0, 21.3 ppm. All spectral data are in accordance with the reported ones.³⁰⁵

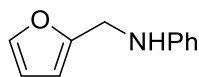


N-(3-Methoxybenzyl)benzenamine (3da): 4 (7.5 mol%), $T = 160\text{ }^{\circ}\text{C}$, $t = 2\text{ h}$, 93% yield.

³⁰⁴ P. R. Likhar, R. Arundhathi, M. L. Kantam, P. S. Prathima, *Eur. J. Org. Chem.*, **2009**, 5383–5389.

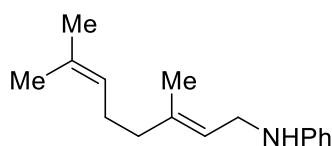
³⁰⁵ A. S. Gajare, K. Toyota, M. Yoshifuji, F. Ozawa, *J. Org. Chem.*, **2004**, *69*, 6504–6506

¹H NMR (300 MHz, CDCl₃): δ_{H} = 7.33–7.22 (m, 3H), 7.04–7.01 (d, 2H), 6.79–6.78 (bd, 1H), 6.71 (bt, 1H), 6.68–6.67 (2H), 4.35 (s, 2H), 3.91 (br, 1H), 3.85 (s, 3H) ppm. **¹³C NMR (75 MHz, CDCl₃):** δ_{C} = 159.6, 147.9, 141.0, 129.4, 129.0, 119.4, 117.3, 112.7, 112.6, 112.3, 54.9, 48.0 ppm. All spectral data are in accordance with the reported ones.¹



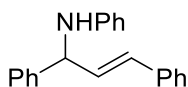
***N*-(Furan-2-ylmethyl)aniline (3ea):** **4** (7.5 mol%), $T = 100\text{ }^{\circ}\text{C}$, $t = 2\text{ h}$, 98% yield.

¹H NMR (300 MHz, CDCl₃): δ_{H} = 7.38–7.37 (m, 1H), 7.23–7.17 (m, 2H), 6.77–6.71 (m, 1H), 6.75–6.67 (m, 2H), 6.33–6.32 (m, 1H), 6.24–6.23 (m, 1H), 4.33 (s, 2H), 4.01 (bs, 1H). **¹³C NMR (75 MHz, CDCl₃):** δ_{C} = 152.6, 147.5, 141.8, 129.1, 117.9, 113.0, 110.2, 106.9, 41.3 ppm. All spectral data are in accordance with the reported ones.



***(E)*-N-(3,7-Dimethylocta-2,6-dienyl)aniline (3fa):** **4** (7.5 mol%), $T = 80\text{ }^{\circ}\text{C}$, $t = 16\text{ h}$, 81% yield.

¹H NMR (300 MHz, CDCl₃): δ_{H} = 7.21–7.13 (m, 2H), 6.71–6.57 (m, 3H), 5.35 (t, $J = 5.6\text{ Hz}$, 1H), 5.13–5.10 (m, 1H), 3.71 (d, $J = 6.9\text{ Hz}$, 2H), 3.54 (br, 1H), 2.18–2.07 (m, 4H), 1.74 (s, 3H), 1.69 (s, 3H), 1.60 (s, 3H) ppm. **¹³C NMR (75 MHz, CDCl₃):** δ_{C} = 148.4, 139.1, 132.1, 129.1, 123.8, 122.3, 117.2, 112.8, 41.6, 32.1, 26.5, 25.7, 23.3, 17.6 ppm. All spectral data are in accordance with the reported ones.¹



***(E)*-N-(1,3-Diphenylallyl)aniline (3ga):** **4** (7.5 mol%), $T = 120\text{ }^{\circ}\text{C}$, $t = 0.5\text{ h}$, 99% yield.

¹H NMR (300 MHz, CDCl₃): δ_{H} = 7.37–7.15 (m, 7H), 6.72–6.58 (m, 4H), 6.42–6.34 (m, 1H), 4.85 (d, $J = 5.9\text{ Hz}$, 1H), 3.62 (br, 1H) ppm. **¹³C NMR (75 MHz, CDCl₃):** δ_{C} = 144.51, 143.8, 137.1, 133.1, 130.6, 129.1, 128.9, 128.3, 128.2, 128.1, 126.9, 125.9, 118.2, 114.9, 53.0 ppm. All spectral data are in accordance with the reported ones.¹

***N*-Cinnamylaniline (3ha):** **4** (7.5 mol%), $T = 120\text{ }^{\circ}\text{C}$, $t = 2\text{ h}$, 98% yield.

¹H NMR (300 MHz, CDCl₃): δ_{H} = 7.43–7.22 (m, 7H), 6.81–6.64 (m, 4H), 6.42 (td, $J = 15.9, 5.8\text{ Hz}$, 1H), 3.98 (d, $J = 1.2\text{ Hz}$, 2H), 3.70 (br, 1H) ppm. **¹³C NMR (75 MHz, CDCl₃):** δ_{C} = 147.9, 136.7, 131.4, 129.2, 128.5, 127.4, 126.9, 126.1, 117.5, 112.9, 45.9 ppm. All spectral data are in accordance with the reported ones.³⁰⁶

2.3. Extraction of TBHP from water to cyclohexane

A cyclohexane solution containing TBHP (7.5 wt% or 0.65 mM, result from titration) was prepared from previous report.^[27b] Briefly, a TBHP solution (5 mL, 70 wt% in water) and cyclohexane (22 mL) were introduced each in a separatory funnel. The funnel was stoppered and shaken to mix both solutions. Then, the funnel was placed stillly until the separation of two solutions. The cyclohexane phase was taken and introduced in centrifuge tube and fresh cyclohexane (7 mL) was added. The above solution was centrifuged

³⁰⁶ T. Ohshima, Y. Miyamoto, J. Ipposhi, Y. Nakahara, M. Utsunomiya, K. Mashima, *J. Am. Chem. Soc.* **2009**, *131*, 14317

at 8,000 rpm for 10 min to separate water from cyclohexane. After removing the water phase, fresh cyclohexane (7 mL) was added again in the centrifuge tube. The above solution was centrifuged again at 8,000 rpm for 10 min. This procedure was repeated for another time. The final TBHP concentration in cyclohexane was determined by iodometric titration using Na₂S₂O₃ solution (0.1 M Na₂S₂O₃ solution, Sinopharm).

2.4. Catalytic oxidation of cyclohexane using TBHP

The as-prepared cyclohexane solution (4.0 g) containing TBHP was introduced into a sealed tube under air together with the iron catalyst (0.014-1.95 mM or 1-140 ppm Fe) on a preheated hot plate at a given temperature chosen between 40 °C and 100 °C and subjected to mild stirring for a given time between few seconds to one hour. Prior to the reaction, water was extracted from TBHP using cyclohexane. After cooling down to room temperature, the reacting solution was removed from the tube and divided into two volumes for analysis. One volume was used for measuring the TBHP conversion after titration, while a given amount of 1,2-dichlorobenzene (DCB) was added to the second volume together with TPP to consume the unreacted TBHP for further analysis. The analyses were carried out in a GC (Agilent 7820A) equipped with a DB-FFAP column and a flame ionization detector. Mass balances were accurate to within 5% in all the catalytic tests.

The KA selectivity was defined as the molar ratio between the produced KA compared to the converted TBHP by combining the iodometric titration and GC analytical methods, whereas the KA yield was defined as the molar ratio between the produced KA compared to the initial TBHP. The turnover number (TON) was computed as the molar ratio between the KA formed and the number of iron centres after 1 h of reaction. Finally, the turnover frequency at time zero (TOF₀) was computed as the slope of the kinetic curve plotting the KA yield divided by the number of iron centres.

RÉSUMÉ

Cette thèse est consacrée à l'étude de mécanismes de réactions catalysées par des métaux ainsi qu'au développement de nouveaux outils pour la rationalisation et la prévision du comportement catalytique. L'étape de transmétallation entre le bore et le nickel a été étudiée en détail à l'aide de méthodes expérimentales variées (electrochimie, RMN, cinétiques) et par DFT, permettant d'expliquer certaines limitations rencontrées par les expérimentateurs. La seconde partie de cette thèse est dédiée à la rationalisation du comportement d'une famille d'acides de Lewis : les sels de triflate et de triflimidate. Leur comportement a été étudié sur des réactions modèles d'amination et d'oxydation et une nouvelle échelle théorique d'acidité de Lewis basée sur l'estimation du transfert de charge vers l'acide a permis de reproduire et prévoir l'activité catalytique.

MOTS CLÉS

acide de Lewis, amination, étude mécanistique, catalyse, couplage de Suzuki-Miyaura, DFT, transmétallation, triflate, triflimidate

ABSTRACT

In this thesis mechanistic studies of metal-catalyzed reactions as well as development of new tools to predict and rationalize the catalytic properties are presented. The boron-to-nickel transmetalation step was thoroughly studied by experimental technics (electrochemistry, NMR, kinetics) and DFT calculations, allowing us to solve some of the limitation encountered by the synthetic chemists. In the second part of this thesis the behavior of a family of Lewis acids (triflates and triflimides) is rationalize. Two model reactions (SN and redox) were studied and a new theoretical scale of Lewis acidity was developed based on the charge transferred to the acid allowing us to reproduce and predict the catalytic activity of these salts.

KEYWORDS

amination, catalysis, DFT, Lewis acid, mechanistic study, Suzuki-Miyaura coupling, transmetalation, triflates, triflimides

